



Instituto de Química

Programa de Pós-Graduação em Química

**UNDERSTANDING THE INFLUENCE OF COLD PLASMA TREATMENT
ON THE ELECTROANALYTICAL PERFORMANCE OF CARBON-BASED
ELECTRODES**

JIAN FELIPE DA SILVA PEREIRA

Tese de Doutorado

UBERLÂNDIA

2023

Ficha Catalográfica Online do Sistema de Bibliotecas da UFU
com dados informados pelo(a) próprio(a) autor(a).

P436
2023
Pereira, Jian Felipe da Silva, 1994-
UNDERSTANDING THE INFLUENCE OF COLD PLASMA TREATMENT
ON THE ELECTROANALYTICAL PERFORMANCE OF CARBON-BASED
ELECTRODES [recurso eletrônico] / Jian Felipe da Silva
Pereira. - 2023.

Orientador: Rodrigo Alejandro Abarza Muñoz.

Coorientador: Osmando Ferreira Lopes.

Tese (Doutorado) - Universidade Federal de Uberlândia,
Pós-graduação em Química.

Modo de acesso: Internet.

Disponível em: <http://doi.org/10.14393/ufu.te.2023.512>

Inclui bibliografia.

1. Química. I. Muñoz, Rodrigo Alejandro Abarza, 1980-,
(Orient.). II. Lopes, Osmando Ferreira, 1989-,
(Coorient.). III. Universidade Federal de Uberlândia.
Pós-graduação em Química. IV. Título.

CDU: 54

Bibliotecários responsáveis pela estrutura de acordo com o AACR2:
Gizele Cristine Nunes do Couto - CRB6/2091
Nelson Marcos Ferreira - CRB6/3074



UNIVERSIDADE FEDERAL DE UBERLÂNDIA
 Coordenação do Programa de Pós-Graduação em Química
 Av. João Naves de Ávila, 2121, Bloco 5I - Bairro Santa Mônica, Uberlândia-MG, CEP 38400-902
 Telefone: (34) 3239-4385 - www.cpgquimica.iq.ufu.br - cpgquimica@ufu.br



ATA

Programa de Pós-Graduação em:	Química				
Defesa de:	Defesa de Doutorado Acadêmico, 140, PPGQUI				
Data:	Vinte e cinco de agosto de dois mil e vinte e três	Hora de início:	9:00	Hora de encerramento:	14:30
Matrícula do Discente:	11923QMI014				
Nome do Discente:	Jian Felipe da Silva Pereira				
Título do Trabalho:	"UNDERSTANDING THE INFLUENCE OF COLD PLASMA TREATMENT ON THE ELECTROANALYTICAL PERFORMANCE OF CARBON-BASED ELECTRODES"				
Área de concentração:	Química				
Linha de pesquisa:	Eletroquímica Aplicada				
Projeto de Pesquisa de vinculação:	"Sensores eletroquímicos de alto desempenho: novos materiais, e estratégias de produção"				

Reuniu-se, no auditório Prof. Manuel Gonzalo Hernandez Terrones, Banca Examinadora, designada pelo Colegiado do Programa de Pós-graduação em Química, assim composta: Professores Doutores: André Luiz dos Santos, da Universidade Federal de Uberlândia; Rodrigo Amorim Bezerra da Silva, da Universidade Federal de Uberlândia; Tiago Araújo Matias, da Universidade Federal do Espírito Santo; Bruna Cláudia Lourenção, da Universidade do Estado de Minas gerais, e Rodrigo Alejandro Abarza Muñoz, orientador do candidato.

Iniciando os trabalhos o presidente da mesa, Dr. Rodrigo Alejandro Abarza Muñoz, apresentou a Comissão Examinadora e o candidato, agradeceu a presença do público e concedeu ao Discente a palavra para exposição do seu trabalho. A duração da apresentação do Discente e o tempo de arguição e de resposta foram conforme as normas do Programa.

A seguir o senhor(a) presidente concedeu a palavra, pela ordem sucessivamente, aos(às) examinadores(as), que passaram a arguir o(a) candidato(a). Ultimada a arguição, que se desenvolveu dentro dos termos regimentais, a Banca, em sessão secreta, atribuiu o resultado final, considerando o(a) candidato(a):

Aprovado.

Esta defesa faz parte dos requisitos necessários à obtenção do título de Doutor.

O competente diploma será expedido após cumprimento dos demais requisitos, conforme as normas do Programa, a legislação pertinente e a regulamentação interna da UFU.



Documento assinado eletronicamente por **Bruna Cláudia Lourenção, Usuário Externo**, em 18/09/2023, às 09:27, conforme horário oficial de Brasília, com fundamento no art. 6º, § 1º, do [Decreto nº 8.539, de 8 de outubro de 2015](#).



Documento assinado eletronicamente por **Rodrigo Alejandro Abarza Munoz, Professor(a) do Magistério Superior**, em 18/09/2023, às 09:58, conforme horário oficial de Brasília, com fundamento no art. 6º, § 1º, do [Decreto nº 8.539, de 8 de outubro de 2015](#).



Documento assinado eletronicamente por **Andre Luiz dos Santos, Professor(a) do Magistério Superior**, em 18/09/2023, às 10:16, conforme horário oficial de Brasília, com fundamento no art. 6º, § 1º, do [Decreto nº 8.539, de 8 de outubro de 2015](#).



Documento assinado eletronicamente por **Rodrigo Amorim Bezerra da Silva, Professor(a) do Magistério Superior**, em 18/09/2023, às 12:34, conforme horário oficial de Brasília, com fundamento no art. 6º, § 1º, do [Decreto nº 8.539, de 8 de outubro de 2015](#).



Documento assinado eletronicamente por **Tiago Araujo Matias, Usuário Externo**, em 18/09/2023, às 14:26, conforme horário oficial de Brasília, com fundamento no art. 6º, § 1º, do [Decreto nº 8.539, de 8 de outubro de 2015](#).



A autenticidade deste documento pode ser conferida no site https://www.sei.ufu.br/sei/controlador_externo.php?acao=documento_conferir&id_orgao_acesso_externo=0, informando o código verificador **4829112** e o código CRC **905B8ABC**.

UNIVERSIDADE FEDERAL DE UBERLÂNDIA

Instituto de Química

Programa de Pós-Graduação em Química

**UNDERSTANDING THE INFLUENCE OF COLD PLASMA TREATMENT
ON THE ELECTROANALYTICAL PERFORMANCE OF CARBON-BASED
ELECTRODES**

Tese de Doutorado apresentada ao Programa de Pós-Graduação do Instituto de Química da Universidade Federal de Uberlândia, como requisito para obtenção do título de Doutor em Química.

Aluno: Jian Felipe da Silva Pereira

Orientador: Prof. Dr. Rodrigo Alejandro Abarza Muñoz

Coorientador: Prof. Dr. Osmando Ferreira Lopes

Área de Concentração: Química Analítica

UBERLÂNDIA

2023

Agradecimentos

Agradeço a todos que participaram desta jornada, direta ou indiretamente.

A minha família. Aos meus pais, Ana e Rildo, aos meus irmãos Larissa e Andrey, pelo amor, carinho e apoio.

A minha família. A minha noiva, Adriana, pelo amor, carinho, paciência, companheirismo e por estar comigo durante todos os períodos de angústia e incerteza que o doutorado traz. Os meus companheiros de noites em claro, e de caminhadas aos fins de tarde, Floki e Nandinho.

Aos meus orientadores Rodrigo, Osmando, e Eduardo, pelas várias discussões que geraram crescimento, e pela contribuição na formação do profissional que me tornei.

Aos professores membros das bancas de qualificação e defesa, Ricardo Brocenschi, André Luiz dos Santos, Rodrigo Amorim Bezerra, Tiago Matias e Bruna Lourenção, pela colaboração no trabalho.

Aos meus inúmeros colegas e amigos de NuPE, onde estive presente em várias gerações (de 2014 a 2023), e pude aprender um pouco (em alguns casos muito) com cada um.

Aos meus amigos que (cada um do seu jeito) estiveram presentes em todas as etapas, sempre presentes, mesmo que de longe.

Ao Instituto de Química da Universidade Federal de Uberlândia, e todos seus funcionários de todos os níveis.

Aos órgãos de fomento CNPq, CAPES e FAPEMIG, em especial ao projeto CAPES pelo provimento de bolsa de estudos, e financiamento do projeto de doutorado sanduiche por meio do programa CAPES PrInt.

O presente trabalho foi realizado com apoio da Coordenação de Aperfeiçoamento de Pessoal de Nível Superior – Brasil (CAPES)

“I said: remember this moment, in the back of my mind (...) It was the end of a decade, but the start of an age (...) One day, we will be remembered.”

RESUMO

Esta tese de doutorado avaliou o emprego de plasmas frios no tratamento superficial de eletrodos de carbono como forma de melhorar a resposta eletroquímica destes materiais que, comumente, são empregados como eletrodos de trabalho em eletroanálise. Um eletrodo fabricado por impressão 3D usando filamento polimérico composto por Carbon-Black/PLA foi submetido ao tratamento com plasma frio dos gases CO₂ e O₂. Foi possível, além da geração de grupos funcionais superficiais, uma maior remoção do material plástico (quando comparado a métodos descritos na literatura), gerando eletrodos com menores resistências à transferência de carga e, conseqüentemente, melhores respostas eletroquímicas. Também como forma de verificar se tais diferenças proporcionam melhora do material quando usado como sensor, foram desenvolvidos métodos para determinação de nitrito, um biomarcador, e dopamina, um neurotransmissor. A partir destes métodos desenvolvidos foi possível observar que o tratamento superficial proporciona melhora no desempenho do CB/PLA. Além disso, os eletrodos foram efetivos para análises em amostras de saliva. O mesmo tratamento também foi utilizado para o tratamento da folha de grafite pirolisado (PGS, do inglês *pyrolytic graphite sheet*), que é bastante reportada na literatura como base para deposição e/ou construção de modificadores de eletrodos, mas raramente apresentada diretamente como eletrodo. Foi demonstrado que o tratamento proporciona aumento da área eletroquimicamente ativa, da rugosidade e da quantidade de grupos funcionais superficiais, menor resistência à transferência de carga, e maior quantidade de defeitos estruturais na superfície, sem que o material perca a característica intrínseca, de camadas empilhadas de grafeno. Como forma de verificar se as modificações superficiais geradas proporcionam melhora na resposta destes materiais como eletrodos de trabalho em eletroanálise, foram desenvolvidos métodos para determinação da droga de interesse forense conhecida como “ecstasy”, e dos antibióticos cloranfenicol, ciprofloxacina e sulfonilamida. A partir dos métodos desenvolvidos foi possível confirmar que o tratamento superficial usando plasma frio de ambos os gases gerou melhora na resposta do PGS. Além disso, os eletrodos foram efetivos nas análises de saliva, de amostras apreendidas pela polícia e de água de torneira.

Palavras-chave: Plasma frio, Eletrodo 3D, Folha de Grafite Pirolisado, MDMA, Antibióticos.

ABSTRACT

This work describes the use of a surface modification procedure to improve the electrochemical response of carbonaceous materials that are commonly used as working electrodes in electroanalysis. A 3D printed electrode (Carbon-Black PLA) was exposed to the cold plasma treatment using CO₂ and O₂, and it was possible to generate surface functional groups at the same time that a higher amount of the insulating material was removed, thus, making electrodes with lower resistance to the charge transfer and, consequently, better electrochemical responses. Also intended to verify if these changes provide a better sensor, the electrodes were used in electrochemical methods to detect Nitrite, a biomarker, and Dopamine, a neurotransmitter. It was possible to confirm that the cold plasma treatments proposed improve the CB/PLA electrodes electrochemical performance, even in real saliva samples.

In another step of this work, Pyrolytic Graphite Sheet (PGS), which is vastly reported in literature as a base substrate for the construction of modified electrodes, but rarely used as a bare electrode, was exposed to the cold plasma treatment using CO₂ and O₂. It was demonstrated that this treatment generates higher surface area, roughness and functional groups concentration, alongside with lower resistance to the charge transfer and higher structural disorder without losing the material intrinsic characteristics of stacked graphene layers. Intended to verify if these changes also provide a better sensor, electroanalytical methods were developed to detect MDMA, a molecule with high forensic interest, and the antibiotics Chloramphenicol, Ciprofloxacin and Sulphanilamide. From the developed methods it was possible to confirm that both surface cold plasma treatments enhanced the performance of PGS electrodes. Also, it was possible to use the electrodes in real samples, such as saliva, seized samples and tap water.

Key-words: Cold plasma, 3D electrode, Pyrolytic Graphite Sheet, Antibiotics, MDMA.

LIST OF FIGURES

Figure 1. Graphical abstract: CHAPTER 2	41
Figure 2. Custom designed microwave plasma-enhanced chemical vapour deposition system.	46
Figure 3. Scanning electron microscopy (SEM) images raised 10,000 x of 3D-printed CB PLA samples before (A) and after CO ₂ -plasma (B) and O ₂ -plasma treatments (C).	47
Figure 4. (A) Raman spectra and (B) I _D /I _G ratio for 3D-printed CB-PLA electrodes before (N-T) and after plasma treatment with CO ₂ (CO ₂ -T) and O ₂ (O ₂ -T).....	48
Figure 5. FTIR spectra for 3D-printed CB-PLA before (N-T, black line) and after plasma treatment with CO ₂ (CO ₂ -T, blue line) and O ₂ (O ₂ -T, magenta line).....	49
Figure 6. High-resolution XPS spectra for C 1 s, O 1 s, and N 1 s for 3D-printed CB-PLA before (untreated, N-T) and after plasma treatment with O ₂ (O ₂ -T) and CO ₂ (CO ₂ -T).	50
Figure 7. Nyquist plots for 3D-printed CB-PLA electrodes acquired in the presence of the redox couple [Fe(CN) ₆] ³⁻ /[Fe(CN) ₆] ⁴⁻ (1 mmol L ⁻¹) using KCl 0.1 mol L ⁻¹ as supporting electrolyte, applying the half-wave potential for each of the electrodes: 0.22 V (O ₂ -T), 0.26 V (CO ₂ -T), and 0.27 V (N-T). Inset shows a zoom out image of a small region indicated by the arrow. Frequency range between 0.1 Hz and 50.000 Hz and signal amplitude of 10 mV.....	52
Figure 8. Cyclic voltammograms for NT (A), CO ₂ -T (B) and O ₂ -T (C) in the presence of 1 mmol L ⁻¹ [Ru(NH ₃) ₆]Cl ₃ in 0.1 mol L ⁻¹ KCl as supporting electrolyte at the scan rates 10, 20, 30, 40, 50, 60, 70, 80, 90 and 100 mV s ⁻¹ , squared root of the scan rate versus peak current for NT (D), CO ₂ -T (E) and O ₂ -T (F), and Log (v) versus Log (i) for NT (G), CO ₂ -T (H) and O ₂ -T (I).	54
Figure 9. Cyclic voltammetric recordings in the presence of 1 mmol L ⁻¹ [Fe(CN) ₆] ³⁻ /[Fe(CN) ₆] ⁴⁻ at the 3D-printed CB-PLA electrode before (N-T, black line) and after plasma treatment with CO ₂ (blue line) and O ₂ (magenta line). The dashed lines correspond to the respective blank signals. Electrolyte: 0.1 mol L ⁻¹ KCl; scan rate: 50 mV s ⁻¹ ; step potential: 5 mV; starting potential: -0.5 V; upper vertex potential: 1.0 V. The inset shows amplification of the response obtained on untreated 3D-printed CB-PLA.	55
Figure 10. (A) Successive cyclic voltametric response (n =100) obtained for 1 mmol L ⁻¹ [Fe(CN) ₆] ^{3-/4-} at the 3D-printed CB-PLA electrode after plasma treatment with O ₂ and (B)	

respective current for anodic and cathodic peak. Background electrolyte: 0.1 mol L ⁻¹ KCl; scan rate: 50 mV s ⁻¹ ; step potential: 5 mV.	58
Figure 11. Cyclic voltammetric response in the presence of 1 mmol L ⁻¹ dopamine (A) and 2 mmol L ⁻¹ sodium nitrite (B) at the 3D-printed CB-PLA electrode before (N-T, black line) and after plasma treatment with CO ₂ (blue line) and O ₂ (magenta line). The dashed lines correspond to the respective blank signals. Experimental conditions in (A): supporting electrolyte: 0.1 mol L ⁻¹ HClO ₄ ; scan rate: 50 mV s ⁻¹ ; step potential: 5 mV. The inset figure in (A) shows the amplification the lower y-axis. Experimental conditions in (B): supporting electrolyte: 0.12 mol L ⁻¹ BR buffer (pH = 2); scan rate: 50 mV s ⁻¹ ; step potential: 5 mV.	59
Figure 12. Baseline-corrected SWV response for increasing concentrations of dopamine in 0.1 mol L ⁻¹ HClO ₄ , using (A) N-T (black), (B) CO ₂ -T (blue) and (C) O ₂ -T (magenta) 3D-printed electrodes and (D) comparison between dopamine current response using the proposed treatment in this work. SWV parameters: a = 50 mV; ΔE _s = 5 mV; f = 50 Hz.	61
Figure 13. Baseline-corrected DPV response for increasing concentrations of sodium nitrite in 0.12 mol L ⁻¹ BR buffer (pH = 2), using (A) N-T (black), (B) CO ₂ -T (blue) and (C) O ₂ -T (magenta) 3D-printed electrodes and (D) comparison between sodium nitrite current response using the treatment proposed in this work. DPV parameters: a= 100 mV ΔE _s = 5 mV; t _m = 50 ms.	62
Figure 14. Baseline corrected voltammograms obtained for saliva spiked with (A) dopamine (SWV parameters: a= 50 mV; ΔE _s = 5 mV; f = 50 Hz) and (B) nitrite (DPV parameters: a= 100 mV ΔE _s = 5 mV; t _m = 50 ms). Calibration curves using the standard addition method for dopamine (C) and nitrite (D) using O ₂ T as working electrode.	66
Figure 15. SEM images obtained for GS before (A and D), after (B and E) O ₂ -plasma treatment and after (C and F) CO ₂ -plasma treatment.	71
Figure 16. FTIR spectra for 3D-printed CB-PLA before (GS, black line) and after plasma treatment with CO ₂ (CO ₂ -GS, blue line) and O ₂ (O ₂ -GS, magenta line).	72
Figure 17. XPS survey (A) and spectra of the GS electrodes spectra of the (B) C 1s and (C) O 1s.	73
Figure 18. Contact angle for (A) GS, (B) CO ₂ -GS and (C) O ₂ -GS.	74
Figure 19. Cyclic voltammograms using GS (black line) and O ₂ -GS (red line) in (A) KCl 0.1 mol L ⁻¹ , (B)HCl 0.1 mol L ⁻¹ and (C) NaOH 0.1 mol L ⁻¹ . scan rate of 50 mV s ⁻¹ and step potential of 5 mV.	75

Figure 20. (A) CVs recorded on untreated (black solid line), CO₂ plasma treated (blue solid line) and O₂ plasma-treated GS electrodes (red solid line); Dashed lined correspond the respective blanks. Scan rate of 50 mV s⁻¹ and step potential of 5 mV. (B) Nyquist plots acquired by applying the 0.20 V half-wave potential on the untreated (black dots), CO₂ plasma treated (blue dots) and O₂ plasma-treated GS electrodes (red dots) GS electrodes in the frequency range of 0.1 Hz to 100 KHz with 10 mV amplitude; Inset in (C) is a zoom-in of the recorded data at high frequency. Solution composition in all (A and B) experiments: 0.1 mmol L⁻¹ [Fe(CN)₆]^{3-/4-} in 0.1 mol L⁻¹ KCl. 76

Figure 21. CVs recorded just after treatment (black solid line) and after three years stored (red solid line) using O₂ plasma-treated GS electrode; scan rate of 50 mV s⁻¹ and step potential of 5 mV. Solution composition in all experiments: 0.1 mmol L⁻¹ [Fe(CN)₆]^{3-/4-} in 0.1 mol L⁻¹ KCl. 77

Figure 22. Cyclic voltammograms for GS (A), CO₂ plasma-treated GS (B) and O₂ plasma-treated GS (C) in the presence of 1 mmol L⁻¹ of [Fe(CN)₆]^{3-/4-} using 0.1 mol L⁻¹ KCl as supporting electrolyte at the scan rates 10, 20, 30, 40, 50, 60, 70, 80, 90 and 100 mV s⁻¹, squared root of the scan rate versus peak current for GS (D) CO₂ plasma-treated GS (E) and O₂ plasma-treated GS (F), and Log (v) versus Log (i) for GS (G), CO₂-GS (H) and O₂-GS (I). 79

Figure 23. Cyclic voltammograms for GS (A), CO₂ plasma-treated GS (B) and O₂ plasma-treated GS (C) in the presence of 1 mmol L⁻¹ of [Ru(NH₃)]Cl₃ using 0.1 mol L⁻¹ KCl as supporting electrolyte at the scan rates 10, 20, 30, 40, 50, 60, 70, 80, 90 and 100 mV s⁻¹, squared root of the scan rate versus peak current for GS (D) CO₂ plasma-treated GS (E) and O₂ plasma-treated GS (F), and Log (v) versus Log (i) for GS (G), CO₂-GS (H) and O₂-GS (I)..... 81

Figure 24. 50 consecutives cyclic voltammograms for GS (A), CO₂-GS (B) and O₂-GS (C). Scan rate of 50 mV s⁻¹ and step potential of 5 mV. Solution composition in all experiments: 0.1 mmol L⁻¹ [Fe(CN)₆]^{3-/4-} in 0.1 mol L⁻¹ KCl. 82

Figure 25. Graphical abstract CHAPTER 4 84

Figure 26. Chemical structure of MDMA. 85

Figure 27. Top view from the modelled systems. From left to right: pristine graphene and graphene oxide. Surfaces and MDMA are shown in licorice and vdW representations, respectively. 89

Figure 28. CVs recorded in solutions containing 0.8 mmol L ⁻¹ MDMA and 0.12 mol L ⁻¹ BR buffer (pH 10.0) at bare (black-line) and O ₂ plasma treated (red-line) GS surfaces. Scan rate of 50 mV s ⁻¹ with 5 mV step potential.	91
Figure 29. CVs profiles of O ₂ -GS electrode in 0.5 mmol L ⁻¹ MDMA in the function of pH (2.0 to 12.0) using 0.12 mol L ⁻¹ BR buffer. Scan rate of 50 mV s ⁻¹ with 5 mV step potential.	92
Figure 30. Baseline-corrected DPV responses registered for concentrations of MDMA (0.5 to 70 μmol L ⁻¹) in 0.12 mol L ⁻¹ BR (pH 10.0) using (A) GS and (B) O ₂ -GS electrodes. The insets of figures correspond to the respective linear regression plots. DPV conditions: 9 mV step potential, 100 mV modulation amplitude, 10 ms modulation time.	94
Figure 31. DPVs recorded for 3.5 μmol L ⁻¹ MDMA in BR buffer solution 0.1 mol L ⁻¹ pH 10.0 on O ₂ -GS. DPV conditions: 9 mV step potential, 100 mV modulation amplitude, 10 ms modulation time.	95
Figure 32 Comparison between peak current vs the number of measurements for three different O ₂ -GS electrodes (n = 3), where ▲ is i _{pa1} and ● is i _{pa2} (A), voltammograms for O ₂ -GS electrodes 1 (B), 2 (C) and 3 (D), for MDMA 3.5 μmol L ⁻¹ in BR buffer solution 0.1 mol L ⁻¹ pH 10.0. DPV conditions: 9 mV step potential, 100 mV modulation amplitude, 10 ms modulation time.	96
Figure 33. Peak currents (second oxidation peak only) obtained from sequential voltammograms for 10, 30, 60, 100 and 250 μmol L ⁻¹ of MDMA in 0.12 mol L ⁻¹ BR (pH 10.0) (n=5) using O ₂ -GS electrode. DPV conditions: 9 mV step potential, 100 mV modulation amplitude, 10 ms modulation time.	97
Figure 34. Non-covalent energies between MDMA and the graphitic surfaces.	98
Figure 35. Most interactive conformational state between MDMA (ball and stick representation) and (A) GS and (B) O ₂ -GS. (licorice and lines representations).	99
Figure 36. Number of contacts between MDMA and the graphitic surfaces (A) and Intermolecular distances between MDMA and the graphitic surfaces (B).	100
Figure 37. Volumetric maps shown in purple. Top and bottom rows correspond to different frames from the simulations with GS (A) and O ₂ -GS (B).	102
Figure 38. DPVs recorded for MDMA (red-line) and for (A) other amphetamines (MDA, MDEA, MA, and A), (B) phenylethylamines (25B-NBOMe and 2C-B), (C) synthetic cathinones (ethylone, ephylone, and dibutylone) and (D) other illicit drugs (LSD, AB-FUBINACA, cocaine, and ketamine). All molecules were analyzed using the same O ₂ -GS electrode at a concentration of 3.5 μmol L ⁻¹ in 0.1 mol L ⁻¹ BR buffer solution pH 10.0.	

DPV conditions: 9 mV step potential, 100 mV modulation amplitude, 10 ms modulation time.	104
Figure 39. Voltammograms for MDMA (red line) and caffeine (pink line), paracetamol (gray line), and ibuprofen (black line). All molecules at $3.5 \mu\text{mol L}^{-1}$ in BR buffer solution 0.1 mol L^{-1} pH 10.0 on O ₂ GS. DPV conditions: 9 mV step potential, 100 mV modulation amplitude, 10 ms modulation time.	105
Figure 40. DPVs recorded for MDMA, MDMA + MDEA, MDMA + Ephylone and MDMA + Dibutylone. All molecules were analysed using the same O ₂ -GS electrode at a concentration of $3.5 \mu\text{mol L}^{-1}$ in 0.1 mol L^{-1} BR buffer solution pH 10.0.	106
Figure 41. DPVs recorded at O ₂ -GS in the presence of supporting electrolyte (black line), seized sample solution (red line), and after the two additions of $20 \mu\text{mol L}^{-1}$ of MDMA (blue and magenta lines) for samples 1 (A), 2 (B), 3 (C) and 4 (D). Supporting electrolyte: 0.1 mol L^{-1} BR buffer solution pH 10.0; DPV conditions: 9 mV step potential; 100 mV modulation amplitude; 10 ms modulation time.	109
Figure 42. Electron ionization gas chromatography-mass spectrometry total ion chromatogram (TIC) (1a) and spectra of the compounds found in four seized samples. Samples 1, 2, 3 and 4 contain MDMA. Sample 3 also contains caffeine (CAF) (3b).	110
Figure 43. DPVs recorded for supporting electrolyte (black line), authentic biological samples from (A) voluntary 1 and (B) voluntary 2 (red line) and after the addition of $10 \mu\text{mol L}^{-1}$ (blue line) and $20 \mu\text{mol L}^{-1}$ (magenta line) of MDMA. Supporting electrolyte: 0.1 mol L^{-1} BR buffer solution pH 10.0; DPV parameters: step 9 mV; amplitude: 100 mV; modulation time: 10 ms.	111
Figure 44. Extracted multiple reaction monitoring chromatograms of all analytes detected and/or quantified in oral fluid samples obtained from (A) voluntary 1 and (B) voluntary 2. Both oral fluid samples were diluted 50 times to fit to the MDMA calibration range.	111
Figure 45. Graphical abstract of CHAPTER 5.	114
Figure 46. CVs responses for 0.2 mmol L^{-1} of (A) CHL, (B) CIP and (C) SUL using 0.12 mol L^{-1} BR buffer solution (pH 2.0) as supporting electrolyte on GS (black line) and CO ₂ -GS (blue line).	118
Figure 47. Voltametric profiles of 0.5 mmol L^{-1} CLO (A), CIP (B) and SUL (C) varying the pH from 2.0 to 11.0 using a 0.12 mol L^{-1} BR buffer solution as supporting electrolyte. Scan rate: 50 mV s^{-1} ; step: 5 mV.	120

Figure 48. Cyclic voltammograms for GS (A) and CO ₂ -GS (B) in the presence of 0.5 mmol L ⁻¹ chloramphenicol using 0.12 mol L ⁻¹ of BR buffer solution pH 5.0 as supporting electrolyte at the scan rates 10, 20, 30, 40, 50, 60, 70, 80, 90 and 100 mV s ⁻¹ , squared root of the scan rate versus peak current for GS (C) and CO ₂ -GS (D), and Log (v) versus Log (i) for GS (E) and CO ₂ -GS (F).	121
Figure 49. Cyclic voltammograms for GS (A) and CO ₂ -GS (B) in the presence of 0.5 mmol L ⁻¹ of ciprofloxacin using 0.12 mol L ⁻¹ of BR buffer solution pH 5.0 as supporting electrolyte at the scan rates 10, 20, 30, 40, 50, 60, 70, 80, 90 and 100 mV s ⁻¹ , squared root of the scan rate versus peak current for GS (C) and CO ₂ -GS (D), and Log (v) versus Log (i) for GS (E) and CO ₂ -GS (F).	122
Figure 50. Cyclic voltammograms for GS (A) and CO ₂ -GS (B) in the presence of 0.5 mmol L ⁻¹ of sulphanilamide using 0.12 mol L ⁻¹ of BR buffer solution pH 5.0 as supporting electrolyte at the scan rates 10, 20, 30, 40, 50, 60, 70, 80, 90 and 100 mV s ⁻¹ , squared root of the scan rate versus peak current for GS (C) and CO ₂ -GS (D), and Log (v) versus Log (i) for GS (E) and CO ₂ -GS (F).	123
Figure 51. Current responses for different electrodes (A, C, E, and F) and for consecutive days (B, D, G, H). Cyclic voltammograms performed with 0.1 mmol L ⁻¹ of ■ CHL (A and B) ●CIP (C and D) ▲SUL E and F).	125
Figure 52. Cyclic voltammograms for CHL (A), CIP (B) and SUL (B) in supporting electrolyte (BR 5 for CHL and CIP and BR 11 for SUL) (black line), supporting electrolyte + 0.1 mol L ⁻¹ KCl (red line) and supporting electrolyte + 1.0 mol L ⁻¹ KCl.126	
Figure 53. Baseline corrected SWV responses for increasing concentrations of antibiotics (A, B) CHL, (C, D) CIP and (E, F) SUL using GS (black line) and CO ₂ GS (blue line). SWV conditions: see Table S2. The insets represent the respective linear adjustments.	128
Figure 54. Baseline corrected SWV recordings for CHL (A, B), CIP (C, D) and SUL (E, F) using GS (black line) and CO ₂ -GS (blue line) as working electrodes. SWV conditions: see Table 14.	130
Figure 55. Baseline corrected SWV for CHL in the presence of AA, CAF, CT, NAT, NIT, PAR, SA and UA. All molecules were analysed using the same CO ₂ -GS electrode at a concentration of 100 μmol L ⁻¹ in BR buffer solution 0.1 mol L ⁻¹ pH 5.0. SWV conditions: 9 mV step potential, 10 mV amplitude, 40 Hz frequency.	134
Figure 56. Baseline corrected SWV CHL in the presence of AA and CT. All molecules were analysed using the same CO ₂ -GS electrode at a concentration of 100 μmol L ⁻¹ in BR	

buffer solution 0.1 mol L ⁻¹ pH 5.0. SWV conditions: -9 mV step potential, 10 mV amplitude, 40 Hz frequency.....	135
Figure 57. Baseline corrected SWV for CIP in the presence of AA, CAF, CT, NAT, NIT, PAR, SA and UA. All molecules were analysed using the same CO ₂ -GS electrode at a concentration of 100 μmol L ⁻¹ in BR buffer solution 0.1 mol L ⁻¹ pH 5.0. SWV conditions: 8 mV step potential, 80 mV amplitude, 20 Hz frequency.	136
Figure 58. Baseline corrected SWV for SUL in the presence of AA, CAF, CT, NAT, NIT, PAR, SA and UA. All molecules were analysed using the same CO ₂ -GS electrode at a concentration of 100 μmol L ⁻¹ in BR buffer solution 0.1 mol L ⁻¹ pH 11.0. SWV conditions: 3 mV step potential, 50 mV amplitude, 30 Hz frequency.	137
Figure 59. Baseline corrected SWV for CHL in the presence of CIP and SUL (A), CIP in the presence of CHL and SUL (B), and SUL in the presence of CHL and CIP (C). All molecules were analysed using the same CO ₂ -GS electrode at a concentration of 25 μmol L ⁻¹ in BR buffer solution 0.1 mol L ⁻¹ pH 5.0 (for CHL and CIP) and 11.0 (for SUL). 139	
Figure 60. Baseline corrected SWV of water and synthetic urine samples spiked with CHL (A and B), CIP (C and D) and SUL (E and F) using CO ₂ -GS as working electrode. Water samples were diluted 2 times directly in the supporting electrolyte, while synthetic urine was diluted 100 times. Dashed lines represent the blanks, black lines represent the voltammograms in the presence of tap water and synthetic urine, red line represents previously spiked tap water and synthetic urine samples and blue lines represents susceptible standard additions. SWV conditions: see Table 14. The insets represent the respective linear adjustments.....	141

LIST OF TABLES

Table 1. XPS analysis and element concentration for the as-printed and plasma treated CB-PLA electrode.	51
Table 2. Electrochemical data (E_{pa} , E_{pc} , ΔE_p , I_{pa} , I_{pc}) obtained from cyclic voltammograms of 1 mmol L ⁻¹ [Fe(CN) ₆] ³⁻ /[Fe(CN) ₆] ⁴⁻ (data from Figure 7).	55
Table 3. Comparison of ΔE_p for the [Fe(CN) ₆] ³⁻ /[Fe(CN) ₆] ⁴⁻ obtained after different procedures of 3D-printed carbon surface treatment.	57
Table 4. Electrochemical data (E_{pa} , E_{pc} , ΔE_p , I_{pa} , I_{pc}) obtained from cyclic voltammograms of dopamine and nitrite (data from Figures 5A and B, respectively) using untreated and plasma-treated 3D-printed CB-PLA electrodes.	59
Table 5. Summary of the analytical parameters obtained for dopamine and nitrite using untreated and plasma-treated 3D-printed CB-PLA electrodes.	62
Table 6. Analytical performance of the oxygen plasma-treated (O ₂ -T) 3D-printed CB-PLA electrode for the detection of dopamine and nitrite compared with other 3D-printed-based electrodes.	64
Table 7. Results obtained in recovery experiments with saliva samples spiked with dopamine or nitrite (n = 3) using O ₂ -T as working electrode.	66
Table 8. XPS analysis of the carbon and oxygen and their species concentration for the GS electrodes.	73
Table 9. Details on the contact angle experiment.	74
Table 10. Analytical parameters obtained for MDMA detection by DPV using GS and O ₂ -GS electrodes.	94
Table 11. Summary results of non-covalent energy, number of contacts, and intermolecular distance between MDMA and the respective simulated surfaces.	101
Table 12. Details on the interferent tests.	106
Table 13. Comparison between analytical features obtained from different working electrodes used for MDMA detection.	112
Table 14. Summarized SWV parameter optimized for the detection of antibiotics of three different classes.	126
Table 15. Analytical parameters obtained for the detection of CHL, CIP and SUL by SWV using GS and CO ₂ -GS electrodes.	129

Table 16. Comparison between the electrodes proposed in this work and previous reports.	131
Table 17. Effect of the possible interferents on analyte current. The % values correspond to $[(\text{analyte current} + \text{interferent current}) / \text{analyte current}] \times 100$	138
Table 18. Results obtained from the recovery studies in tap water and synthetic urine samples spiked with CHL, CIP and SUL. (n=3)	142

ACRONYMS LIST

UV-Vis – Ultraviolet-visible Spectroscopy

RE – Reference Electrode

WE – Working Electrode

CE – Counter Electrode

GCE – Glassy Carbon Electrode

PLA – Polylactic Acid

ABS – Acrylonitrile Butadiene Styrene

PG – Pyrolytic Graphite

HOPG – Highly Oriented Pyrolytic Graphite

PGS – Pyrolytic Graphite Sheet

BDD – Boron Doped Diamond

CVD – Chemical Vapour Deposition

PECVD – Plasma Enhanced Chemical Vapour Deposition

MDMA - 3,4-methylenedioxyamphetamine

FDM – Fused Deposition Modeling

CB – Carbon Black

BR – Britton-Robinson Buffer Solution

SEM – Scanning Electron Microscope

FT-IR – Fourier-Transform Infrared Spectroscopy

XPS – X-Ray Photoelectron Spectroscopy

N-T – Non-Treated CB-PLA Electrode

CO₂-T – CO₂ Plasma Treated CB-PLA Electrode

O₂-T – O₂ Plasma Treated CB-PLA Electrode

EIS – Electrochemical Impedance Spectroscopy

E_{PA} – Anodic Peak Potential

E_{PC} – Cathodic Peak Potential

I_{PA} – Anodic Peak Current

I_{PC} – Cathodic Peak Current

ΔE_p – Peak Potential Variation

HET – Heterogeneous Electron Transfer Constant

SWV – Squared Wave Voltammetry

DPV – Differential Pulse Voltammetry

LOD – Limit of Detection

SD – Standard Deviation

NPS – New Psychoactive Substances

UNODOC – United Nations Office on Drugs and Crime

HPLC – High Performance Liquid Chromatography

GC-MS – Gas Chromatography coupled with Mass Spectrometry

LC-MS – Liquid Chromatography coupled with Mass Spectrometry

GS – Graphite Sheet

MA – Methamphetamine

MDA - 3,4-Methylenedioxyamphetamine

MDEA - 3,4-Methylenedioxy-N-ethylamphetamine

ETH – Ethylone

EPH – Ephylone

DIB – Dibutylone

LSD – Lysergic Acid diethylamide

PCDF – Polícia Civil do Distrito Federal

CAAE – Campinas University Ethical Committee

UHPLC – Ultra High-Performance Liquid Chromatography

CV – Cyclic Voltammetry

UHV – Ultra High Vacuum

CO₂-GS – CO₂ Plasma Treated Graphite Sheet Electrode

O₂-GS – O₂ Plasma Treated Graphite Sheet Electrode

R_{ct} – Resistance to the Charge Transfer

LOQ – Limit of Quantification

IUPAC – International Union of Pure and Applied Chemistry

RSD – Relative Standard Deviation

A – Amphetamine

E – Potential

V – Volts

i – Current

TIC – Total Ion Chromatogram

THC – Tetra Hydro Cannabinol

SPE – Screen Printed Electrode

CHL – Chloramphenicol

CIP – Ciprofloxacin

SUL – Sulphanilamide

MLG – Multilayer Graphene

CAF – Caffeine

PAR – Paracetamol

NAT – Nitrate

NIT – Nitrite

SA – Salicylic Acid

UA – Uric Acid

CONTENTS

CHAPTER 1	29
1. INTRODUCTION	29
2. 3D-PRINTED ELECTRODES	33
3. PYROLYTIC GRAPHITE SHEET	34
4. ELECTRODES FUNCIONALIZATION	36
5. COLD PLASMA TREATMENT	38
GOALS	40
General goals	40
Specific goals	40
CHAPTER 2 – CB-PLA	41
REACTIVE OXYGEN PLASMA TREATMENT OF 3D-PRINTED CARBON ELECTRODES TOWARDS HIGH-PERFORMANCE ELECTROCHEMICAL SENSORS	41
1. Introduction	42
2. Experimental	43
2.1. Reagents and solutions	43
2.2. Electrochemical measurements and electrode production	44
2.3. Microscopic and spectroscopic characterization of 3D-printed CB-PLA surfaces	44
2.4. Cold plasma treatment of 3D-printed CB-PLA surfaces	45
3. Results and discussion	46
3.1. Microscopic and spectroscopic characterization of the 3D-printed CB-PLA electrodes	46
3.2. Electrochemical characterization of the 3D-printed CB-PLA electrodes	51
3.3. Electrochemical sensing properties of plasma-treated 3D-printed CB-PLA electrodes	58

3.4. Application of plasma-treated 3D-printed CB-PLA electrodes for saliva analysis.....	64
4. Conclusions	67
CHAPTER 3 – PYROLYTIC GRAPHITE SHEET: CHARACTERIZATION.....	68
MORPHOLOGICAL, STRUCTURAL AND ELECTROCHEMICAL CHARACTERIZATION OF GS SURFACES.....	68
Introduction	68
1. Experimental.....	68
1.1. Reagents, samples and materials	68
1.2. Electrode surface treatment.....	68
1.3. GS Electrodes characterization	69
2. Results and discussion.....	70
CHAPTER 4 – PYROLYTIC GRAPHITE SHEET: MDMA DETECTION.....	84
OXYGEN PLASMA-TREATED GRAPHITE SHEET ELECTRODES: A SENSITIVE AND DISPOSABLE PLATFORM FOR METHAMPHETAMINES.	84
1. Introduction	85
2. Experimental.....	87
2.1. Reagents, samples and materials	87
2.2. Electrode surface treatment.....	88
2.3. Computational Simulations	88
2.3.1. Parameterization	88
2.3.2. Systems Modelling	89
2.3.3. Molecular Dynamics Simulations.....	89
3. Results and discussion.....	91
3.1. Electrochemical behaviour of MDMA on GS electrodes	91
3.2. MDMA detection using O ₂ -GS electrode by DPV	93
3.3. Molecular Dynamics simulations of MDMA and the graphitic surfaces.....	97

3.4. Interference studies	103
3.5. MDMA determination in seized samples and human saliva.....	108
4. Conclusion.....	113
CHAPTER 5 – PYROLYTIC GRAPHITE SHEET: ANTIBIOTICS DETECTION..	114
CO ₂ -PLASMA SURFACE TREATMENT OF GRAPHITE SHEET ELECTRODES FOR DETECTION OF CHLORAMPHENICOL, CIPROFLOXACIN AND SULPHANILAMIDE.....	114
1. Introduction	115
2. Experimental.....	115
2.1. Reagents, samples and materials.....	115
2.2. Electrode surface treatment.....	117
3. Results and discussion.....	117
3.1. Electrochemical behaviour of antibiotics on GS electrodes.....	117
3.2. Antibiotics detection using CO ₂ -GS electrode by SWV.....	126
3.3. Antibiotics determination in water and synthetic urine samples.....	139
4. Conclusion.....	142
GENERAL CONCLUSIONS	143
REFERENCES.....	145

SUMMARY

This thesis is focused on the use of the cold plasma treatment on carbon-based materials (PGS and 3D printed PLA incorporated with carbon black) for electroanalysis and is presented in 5 chapters, in which the first one is an introduction to electroanalytical chemistry, 3D printed electrodes, pyrolytic graphite sheet electrodes, electrodes functionalization and cold plasma treatment.

Then, the second chapter presents an adaption of the published article entitled “Reactive oxygen plasma treatment of 3D-printed carbon electrodes towards high-performance electrochemical sensors”. In this work, cold plasma treatment carbon employing dioxide and oxygen was used, and it was published in the journal *Sensors and Actuators B: Chemical*, and can be found at <https://doi.org/10.1016/j.snb.2021.130651>.

The third chapter presents a detailed characterization of PGS electrodes before and after the cold plasma treatment using either carbon dioxide or oxygen. Surface characterization by spectroscopic and microscopic techniques are thoroughly evaluated and discussed in combination with the electrochemical characterization.

In chapter four, the use of oxygen cold plasma treated PGS electrode was demonstrated for the selective detection of 3,4-Methylenedioxymethamphetamine. This work was published in the journal *Electrochimica Acta*, entitled “Oxygen plasma-treated graphite sheet electrodes: a sensitive and disposable sensor for methamphetamines”. It can be found at <https://doi.org/10.1016/j.electacta.2023.143089>.

The fifth chapter presents the use of carbon dioxide cold plasma treated PGS electrode for determination of chloramphenicol, ciprofloxacin, and sulphanilamide. This work was published in the journal *Microchimica Acta*, named “CO₂-plasma surface treatment of graphite sheet electrodes for detection of chloramphenicol, ciprofloxacin and sulphanilamide”. This work can be found at <https://doi.org/10.1007/s00604-023-05953-2>.

CHAPTER 1

1. INTRODUCTION

Analytical chemistry consists on a group of methods that have great importance in science. Chemical reactions generate responses that are transformed into measurable information, and in a typical analysis, qualitative (the composition of the sample) and quantitative (the amount of each part that compose the sample) information are necessary. A common chemical analysis comprehends sequential steps, such as selecting the analytical method, obtaining and preparing the sample, evaluating the chemical measurable properties, eliminating possible interferences, measuring the chemical property, calculating the results and the reliability of the selected method (Skoog et al., 2006).

A chemical sensor converts chemical information (from the concentration of the species to the total media composition) into a useful analytical signal (Hulanicki et al., 1991). Its selectivity depends directly on the interaction between the sensor (receptor) and the molecules, and the signal amplification depends on the transducer. The measurement of the sensor is then generated by changes in any physical parameter caused by a chemical stimulus. The exact type of physical change depends on the sensor and used platform (Janata, 2009).

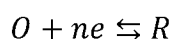
The receptor can work based on different principles: physical, in which there is no chemical reaction (such as absorbance, reflectance, mass or temperature changes); chemical, in which the generated signal comes from a chemical reaction; and biochemical, in which the generated signal originates from a biochemical process (Hulanicki et al., 1991). The chemical sensors can be classified as: optical, where the chemical reaction generates a change in the optical phenomena (absorbance, reflectance, luminescence, fluorescence and refractive index); electric, in which there is no electrochemical reaction, but the chemical reaction causes a change in the electrical properties of the system; gravimetric, where the chemical reaction generates a change in the system's mass (piezoelectric and surface acoustic wave systems); magnetic, where the signal is obtained from changes in the paramagnetic properties of the analytes; thermometric, in which the changes in the system's temperature is what creates the signal;

electrochemical, where the interaction between the receptor and the molecule provokes an electrochemical reaction (Hulanicki et al., 1991).

Chromatographic and spectroscopic methods have dominated and been widely used in various industries and control laboratories (Moudgil et al., 2019). Even though chromatographic methods have many advantages in analysis of various compounds, it involves several difficulties in its application, such as the employment of toxic solvents, relatively slow experimental frequency, difficult sample preparation, especially for drugs and food samples (Engelhardt and Neue, 1982). Spectroscopic methods present no selectivity towards food, pharmaceutical and environmental samples, and the Lambert-Beer Law used in UV-VIS spectroscopy present plenty limitations in analytical application when used in real samples (Karimi-Maleh et al., 2020).

Electrochemical methods provide some advantages when compared with other methods. Firstly, they can present specificity towards particular oxidation/reduction process, thus being possible to determine simultaneously two or more species without any pre-treatment step required. Also, some of the electrochemical methods can provide information about the activity of the species, and not only about its concentration (Skoog et al., 2006). Another important aspect to the choice of electrochemical sensors is the remarkable operational low cost. Additionally, the use of low-cost materials to make electrochemical electrodes have been studied in the last years (Bandodkar and Wang, 2014; Karimi-Maleh et al., 2020; Stefano et al., 2022), and presents an alternative to produce even cheaper apparatus towards portable and fast analysis. Thus, the use of materials that are easily manufactured is of great importance.

Electrochemistry studies the relationship between chemical and physical effects, either applying electric currents and observing the chemical changes, or observing the electric current generated from chemical reactions (Bard et al., 2001). Most electrochemical techniques are based on the electron transfer process (oxidation or reduction), thus, electrochemical sensors must be able to perform as sources (reduction) or “drains” (oxidation) of electrons (Brett and Brett, 1993). These reactions happen according to the following equation, where O is the oxidized species, R is the reduced species and n_e is the number of electrons transferred.



The electrons on the electrode need to be in a minimum energy (sufficiently negative potential compared to the targeted molecule) for the reduction reaction to occur. Likewise, there is a minimum energy in which the lowest unoccupied level of the electrode must be (sufficiently high potential compared to the target molecule) for the oxidation reaction to occur. The potential values can be controlled externally, therefore, it is possible to control the direction of the reaction (Brett and Brett, 1993).

Such processes occur in electrochemical cells that contain a least two electrodes plus the other necessary electrochemical components (electrolyte, analyte, solvent). In two electrodes cells, those are named as cathode (where the reduction reaction occurs) and anode (where the oxidation process happens). Even though it is possible to perform experiments using just these two electrodes, better analytical results are presented when the three electrodes system is used. In a three electrodes system, the electrodes are named as working electrode (where the desired reaction occur), counter or auxiliary electrode (where the opposite potential is applied) and reference electrode (RE) (Brett and Brett, 1993).

It is possible to control and apply either current or potential on the working electrode (WE) when using a three electrodes system, and the response is measured (current, when applying potential, and potential, when applying current). During the experiment, the current flows between the WE and the counter electrode (CE), and the oxidation and reduction reactions happen on both electrodes, since there is no reduction reaction without an oxidation reaction, and *vice-versa* (Brett and Brett, 1993).

From these two electrodes it is possible to perform the desirable reactions, however it is not possible to obtain precise information about the potential in which these reactions occur. Therefore, the RE is placed close to the working electrode in order to correct the voltage drop between the WE and CE, thus providing information to the equipment and enabling adjustments as to the applied potential, achieving higher precision (Brett and Brett, 1993). When using these techniques with analytical purposes, the transducer transforms the information obtained from the electrochemical reaction into a measurable signal, thus, comprehending the electroanalytical techniques (Stradiotto et al., 2022).

The potential window that can be applied depends on one or more of the following factors: solvent decomposition; supporting electrolyte decomposition; formation of a

passive layer in the electrode's surface; stability of the electrode. The selection of the electrode depends then on its stability, and its interactions with the intended analyte, since their interaction is what will provide the signals (Skoog et al., 2006).

Initially, metals were the main materials used as electrochemical sensors due to its innate conductivity and stability. Early works present mercury (dropping mercury electrodes, from polarography) (Koryta, 1972), gold (Groenewald, 1975) and platinum (Feltham and Spiro, 1971; Hubbard et al., 1978). Nowadays, other materials are also used as working electrodes, such as semiconductor solid oxides (George et al., 2018), conductive organic salts (Kempahanumakkagari et al., 2018) and carbon based materials (Brett and Brett, 1993).

Several carbon based materials can be used as WE, such as glassy carbon (GC) (Vieira, 2022; Zittel and Miller, 1965), boron doped diamond (Luong et al., 2009), pyrolytic graphite (Adetayo and Runsewe, 2019) and carbon fiber (Mohammadzadeh Kakhki, 2019). Some composite materials also are reported, such as pencil graphite (Švancara et al., 2009; Švancara et al., 2001), conductive inks (Camargo et al., 2021), screen printed electrodes (SPE) (Taleat et al., 2014; Wang, 1994; Wang and Tian, 1992) and 3D-printed electrodes (Hamzah et al., 2018). These alternative materials are commonly used for their low cost, disposability and relatively easy production.

2. 3D-PRINTED ELECTRODES

Additive manufactured techniques are among the principal pillars of the new industrial revolution. Using these techniques, several parts or entire structures can be rapidly constructed with high precision, thus, a great number of applications have been reported lately (Cardoso et al., 2020a; Liu et al., 2019; Ngo et al., 2018). Therefore, 3D printing technology have gained attention recently for they can offer these exact advantages, associated with low-cost. They are used for the production of artificial organs, jewels, rocket engines, and applied in aviation and food industry (Shahrubudin et al., 2019).

There are different types of 3D printers: material jetting, binder jetting, powder bed fusion, vat photopolymerization, sheet lamination, material extrusion and direct energy deposition. Among all of them, material extrusion is the most known and used technique, and several materials can be employed based on the intended part or structure. Since the shape of the structure is strictly dependent on the thickness of the fused filament, the material's "thermoplasticity" has an important role in the process, once it determines the filament capacity to bind to the previous layer (Aumnate et al., 2018).

Nowadays, the most used products in additive manufacture systems are plastic-polymer filaments (Dizon et al., 2018), and among them, the most used are polylactic acid (PLA) and acrylonitrile butadiene styrene (ABS) (Kristiawan et al., 2021) due to their low cost. Intended to build conductive filaments but still at a low-cost (it is possible to print metals in 3D, but those techniques are highly costly), some carbon composite materials are incorporated in the polymers, such as graphene, carbon black, graphite, carbon nanotubes, among others (Hamzah et al., 2018). More detailed discussion about this material will be presented in CHAPTER 2.

3. PYROLYTIC GRAPHITE SHEET

Among several types of carbon materials used as electrodes (glassy carbon, boron doped diamond, carbon paste, graphite pencil, composite materials), pyrolytic graphite (PG) has gained attention due to its properties, such as light weight, flexibility, high conductivity and low-cost (Pereira et al., 2019). Its name comes from the method of its production, which involves gaseous carbonaceous compounds decomposition in high temperature. If, during the preparation, the pressure is sufficiently high, it is formed the highly ordered pyrolytic graphite (HOPG). Pyrolytic graphite is constituted of parallel stacked graphene layers and its basal and edge planes presents different characteristics, for the exposed structure is different in each case (Brett and Brett, 1993).

The production of PG is barely discussed in literature, however this material have been mentioned in literature since 1951, when Grisdale and co-workers demonstrated its production from thermal decomposition of hydrocarbons. Such procedure happens in inert surfaces, inside a furnace and in the presence of the chosen hydrocarbon. Therefore, there are two possibilities to perform this decomposition or pyrolysis of hydrocarbons: keep the hydrocarbon pressure inside the oven, or use a gaseous carrier to carry the hydrocarbon trough the oven, also in constant pressure. The authors also mentioned that the application of these different possibilities does not produce differences in the resulting material (Grisdale et al., 1951).

In the pyrolysis process, a dehydrogenation of hydrocarbons in gaseous phase occurs, thus, for methane, free radicals, such as methylene, recombine or polymerize resulting in dehydrogenated products (Grisdale et al., 1951). The specific steps to produce thinner films are discussed by Yajima et. al., in which methane and propane are the hydrocarbons used due to their higher thermal stability (Yajima et al., 1965). Pyrolytic Graphite Sheet (PGS) is commercialized by some companies, and a study by Silva compared the commercially-available products and states that the better suited to be used as an electrochemical sensor for ferri-ferrocyanide probe, dopamine, catechol, ciprofloxacin, cadmium and lead is the one offered by Panasonic, with 0.07 mm thickness, 2.5 Ω electric resistance, and 55.6 S cm⁻¹ electric conductivity (Silva et al., 2018).

Its use as electrode is demonstrated for the simultaneous detection of dopamine, ascorbic and uric acid after a mechanical exfoliation using scotch tape (Cai et al., 2014). The use of GS is also reported after chemical, electrochemical and thermal oxidation, in which all proposed treatments enhanced the electrodes surface area and consequently

electrochemical performance. (Cercado et al., 2016) The most common use of this material is as substrate for the construction of modified electrodes, using NiO (Liu et al., 2015), polydiphenylamine (Tkachenko et al., 2022), exfoliated graphene nanosheets (Lee et al., 2010), composites based on polyaniline and/or polyacrylonitrile (Abalyaeva et al., 2020; Ye et al., 2017) carbon nanotubes (Li et al., 2007) sulphur (Dai, 2022), among others.

Pereira and co-workers demonstrated an enhancement on graphite sheets electrochemical performance by applying oxygen and carbon dioxide plasmas, observing a higher surface roughness and consequently decrease on the resistance to the charge transfer (Pereira et al., 2019). Thus, GS seems to be a suitable source to be used directly as an electrode for sensing.

4. ELECTRODES FUNCIONALIZATION

First mentioned by Moses and Murray in 1975, the term chemically modified electrode is widely used to describe electrodes that possess immobilized molecules in its surface (Moses et al., 1975). Since then, several other kinds of modifications were proposed, and the correct way to mention it is “surface modified electrode” (Snell and Keenan, 1979). Modifying electrodes is an advanced way to change an electrodes surface focused in promoting specific interactions with the intended analyte.

There are possibilities to modify and enhance this interaction between the electrode and the analyte: to limit the access of interfering compounds to the electrodes surface, providing better selectivity to the interest molecule; to enhance the electron transfer rate between the electrode and the electrochemical system; to enhance the electrodes superficial and electrochemical active area; to accelerate the molecules diffusion and/or preconcentration into the electrodes surface; to decrease the oxidation/reduction products adsorption in the electrodes surface (Sharma et al., 2018).

It is possible to insert functional groups in the electrodes surface, and the complexity of chemical bonds in carbonaceous materials surface allows a variety of functionalization on its microstructures. Several works demonstrate the addition of carboxyl, carbonyl and hydroxyl groups in carbon nanotubes by acid treatments (Moraes et al., 2011). Functionalization on SPE surfaces is also demonstrated in literature as an important step to enhance its electrochemical performance, shown in the determination of Hg(II) by Bernalte (Bernalte et al., 2011) and Zn²⁺ by da Silva (S. M. da Silva et al., 2020). This process can also be made on a GC electrode by applying a constant potential (+1.8 V) for a period of time in the presence of a buffer solution (pH 7.0), provoking an oxidation of the surface. The film formed is similar to graphene oxide films, with an enhancement in the presence of C-O and C=O groups (Santhiago et al., 2015).

Similarly, boron-doped diamond (BDD) electrodes without any treatment present a hydrophobic surface, and an anodic or cathodic activation can provide better responses, depending on the desired analyte (Suffredini et al., 2004). Additionally, a highly severe cathodic pre-treatment provides higher amount of hydrogen terminated functional groups in it surface (up to 36% of the surface). However, the maximum effect on [Fe(CN)₆]^{3-/4-} redox probe reversibility of this functionalization is achieved when 15% of the surface is covered in H terminated groups (Brocenschi et al., 2016).

Plasma is also applied to functionalize electrodes surfaces. When producing BDD electrodes using a chemical vapour deposition technique (CVD), H₂ and CH₄ plasmas are employed, and the exposure to hydrogen after the end of the gas (methane) flow generates H terminated groups in its surface. Likewise, short time treatments using oxygen plasma and the exposure to a CF-He plasma generates oxygenated groups and fluor terminated hydrophobic groups respectively (Luong et al., 2009).

5. COLD PLASMA TREATMENT

There are four physical states of matter: in solid state, atoms and molecules are restricted as for their movement and are retained into a rigid form; in liquid state, atoms and molecules can move, although their freedom is limited; in gaseous state, atoms and molecules move freely, and their electrons move harmonically inside its orbits, following the quantum mechanics laws; in plasma, however, the electrons are released from the atoms, therefore, ions and electrons move completely free (Frank-Kamenetskii, 1972).

Plasma can be generated by applying energy to a neutral gas, generating a charge carrier. Then, electrons and ions are produced in gaseous phase when electrons or photons with enough energy collide with the neutral atoms of the gas molecules fed in the chamber. There are different ways to provide the necessary energy to generate plasma in a neutral gas: thermal energy, from a flame source; adiabatic compression of a gas with sufficient heat capacity for plasma generation; electric field application; electromagnetic field application (Conrads and Schmidt, 2000).

Usually, Plasma enhanced chemical vapor deposition (PECVD) is used to produce materials or to treat surfaces. A typical PECVD system consists on a reactor, which is a quartz tube and a microwave generator (to generate plasma, with a 2.45 GHz and 500-Watt power), a vacuum pump with a $10 \text{ m}^3 \text{ h}^{-1}$ rate and a gas source. A Pirani gauge directly coupled to the quartz chamber is used to measure the pressure, and the gas flow is controlled by needle-type valves (Carvalho et al., 2015). A cold plasma reaches temperature of around 110° C that are considered “cold plasmas”.

A number of articles in literature demonstrate the use of PECVD systems in various ways, such as the synthesis of nanostructured carbonaceous materials (Carvalho et al., 2015), BDD-like materials (sp^3 bonds) (Grill, 1999), carbon nanotubes and carbon foams (Carvalho et al., 2015; Choi et al., 2006; Hofmann et al., 2003; Löffler et al., 2011; Melechko et al., 2007; Ren et al., 1998), and carbon fibres (Chen et al., 1998; Pham-Huu et al., 2006; Wang and Moore, 2012), as well as for the decrease in membranes hydrophobicity (Gopakumar et al., 2019) and surfaces functionalization (C. C. da Silva et al., 2020; Mahmoud, 2016; Patil et al., 2016; Prabhu et al., 2017; Praveen et al., 2016; Sdrobiş et al., 2012).

When treating GC electrodes with H_2 plasma, lower background currents and limits of detection are observed if compared with a GC polished electrode. This treatment

provides a higher activity to the $[\text{Fe}(\text{CN})_6]^{3-/4-}$ probe (DeClements et al., 1996). Khare et al. evaluated the treatment of a multi-layered graphene electrode using CO_2 , Ar and N_2 plasmas, and the field emission is enhanced (Khare et al., 2015). This effect is caused by a slight change in the hybridization state (sp^2/sp^3) in the treated sample (Patil et al., 2016). The graphene edge plane can be controlled by plasma treatment, reducing in 77% the resistance of the material (Yue et al., 2015). Oxygen plasma treatment can also change a semi-metallic nature of graphene monolayers to semiconductor, depending on the time of exposure, and a bandgap opening is reported caused by the surface functionalization (Nourbakhsh et al., 2010).

Mei et al. demonstrated by combining acid and plasma treatments, functional groups are effectively added to carbon cloths surfaces, creating new active sites. A 34% decrease in the overpotential needed is observed in the treated electrode, achieving a 10 mA cm^{-1} current density (Mei et al., 2021). Oxygen and carbon dioxide plasma treated electrodes also presents higher sensibility towards the detection of dopamine, with higher surface area and lower resistance to the charge transfer (Pereira et al., 2019). So far, despite the potential of applying this technique into modifying surfaces, it has not been explored in electroanalytical works. Thus, we present here the use of cold plasma treatment to modify carbon materials surfaces.

GOALS

General goals

The main goal of this work is to evaluate and understand how O₂ and CO₂ plasma treatments affects disposable carbon-based electrodes materials, and how these changes influence their performances as working electrodes in electrochemical analysis.

Specific goals

- Treat PGS and CB/PLA electrodes using O₂ and CO₂ cold plasma;
- Morphologically and electrochemically characterize the electrodes surfaces;
- Use the CB/PLA cold plasma treated electrodes for the detection and quantification of dopamine and nitrite;
- Use the PGS O₂ cold plasma treated electrodes for selective detection of 3,4-Methylenedioxymethamphetamine (MDMA) in the presence of adulterants;
- Use the PGS O₂ cold plasma treated electrodes for screening of 3,4-Methylenedioxymethamphetamine (MDMA) in seized tablets and in saliva;
- Use the PGS CO₂ cold plasma treated electrodes for detection of antibiotics in tap water and in synthetic urine;

REACTIVE OXYGEN PLASMA TREATMENT OF 3D-PRINTED CARBON ELECTRODES TOWARDS HIGH-PERFORMANCE ELECTROCHEMICAL SENSORS

This chapter contains an adaption of the published article named: “Reactive oxygen plasma treatment of 3D-printed electrodes towards high-performance electrochemical sensors” Jian F. S. Pereira, Raquel G. Rocha, Silvia V. F. Castro, Afonso F. João, Pedro H. S. Borges, Diego P. Rocha, Abner de Siervo, Eduardo M. Richter, Edson Nossol, Rogério V. Gelamo, Rodrigo A. A. Muñoz.

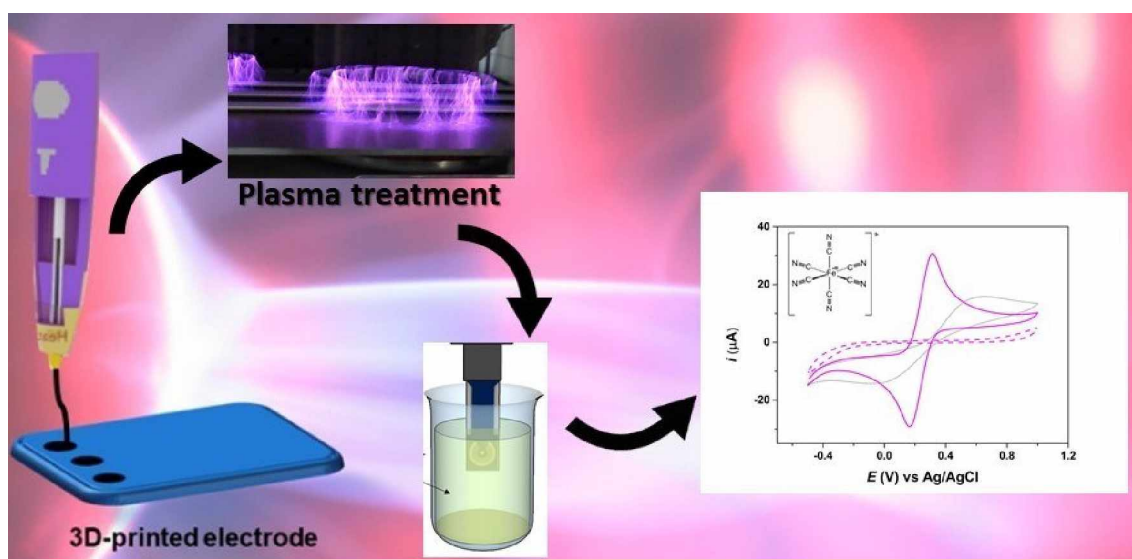


Figure 1. Graphical abstract: CHAPTER 2

1. Introduction

Additive manufacturing technology is one of the major pillars of the new industrial revolution and has been emerging in the last years motivated by the large number of applications in the industry (Ngo et al., 2018). Fused deposition modelling (FDM) is one of the most significant technologies to fabricate plastic materials and is becoming very popular due to the low-cost and wide availability of FDM 3D-printers (Liu et al., 2019). Conductive polymeric filaments have enabled the fabrication of electrochemical devices applied for energy storage and electrochemical sensing (Cardoso et al., 2020a; Tian et al., 2017). Moreover, rapid prototyping, freedom of design, reduced waste generation, low energetic demand, and low cost make this 3D-printing technology greatly advantageous for the large-scale fabrication of electrochemical devices (Silva et al., 2021).

Some works have highlighted the potential applications of 3D-printing for the fabrication of electrochemical sensors using different polymeric filaments which are made of composites containing carbon black (CB), graphene, graphite or metals as the conducting agent (Cardoso et al., 2020a; Giorgini Escobar et al., 2020; Guima et al., 2019; Hamzah et al., 2018; Ngo et al., 2018; Rocha et al., 2020a; Rymansaib et al., 2016; Vaněčková et al., 2020b, 2020a). The need for surface treatment has been emphasized in several works using such 3D-printed electrodes to remove the excess of polymer that hinders the electron transfer process between the target species and electrode as well as to expose the conductive sites within the polymeric matrix (Cardoso et al., 2020a). Different strategies have been proposed, such as the chemical treatment using different solvents (dimethylformamide, acetone, etc.) by simple immersion of the 3D-printed electrodes for 10-30 min (Browne et al., 2018; Gusmão et al., 2019), which is not eco-friendly considering the solvent residues. Protein digestion of the biodegradable polylactic acid (PLA) is a “green” alternative but it takes 24 h at least and results were not satisfactory (Manzanares-Palenzuela et al., 2019a). Thermal annealing has been proposed; however, it requires an oven to be heated at 350 °C for 3 h (gradual temperature increase at 5 °C min⁻¹ and long time to cool down) (Novotný et al., 2019).

Chemical/electrochemical treatment protocols seem to be the most efficient and “green” protocols and thus many different procedures have been proposed (Browne et al., 2018; dos Santos et al., 2019; Kalinke et al., 2020; Richter et al., 2019; Rocha et al., 2020b). In all cases, a specific composition of supporting electrolyte is established and a sequence of potential cycles, which may involve electrolysis, taking around 1 h in most

of the protocols. The use of NaOH seems to give an additional advantage in such protocols as the alkali solution is responsible for the PLA degradation that may be accelerated by the electrochemical treatment. Moreover, the generation of functional groups have been reported (dos Santos et al., 2019; Richter et al., 2019) that may enhance the electron transfer rate.

Herein we demonstrate that a reactive oxygen plasma treatment of 3D-printed carbon back-PLA (CB-PLA) electrodes improves substantially the electron transfer rate, which is essential in the development of any electrochemical device. To the best of our knowledge, this is the first study that shows the potential of the use of cold reactive plasma to improve the electrochemical performance of 3D-printed electrodes. To demonstrate the benefits of such protocol in the development of electrochemical sensors, the voltammetric detection of dopamine and nitrite, important biomarkers present in biological fluids, is presented.

2. Experimental

2.1. Reagents and solutions

All solutions were prepared using ultrapure water obtained from Millipore Direct Q3 (Bedford, USA) purification system ($R \geq 18 \text{ M}\Omega\text{-cm}$). Potassium ferrocyanide, potassium ferricyanide, and potassium chloride were obtained from Synth (Diadema, Brazil). Sodium hydroxide (98% w/w) and boric acid (99 % w/w) were purchased from AppliChem Panreac (Barcelona, Spain). Phosphoric acid (85 % w/v), perchloric acid (70% w/v) and acetic acid were acquired from Synth (Diadema, Brazil). Argon (99.99%), CO₂ (99.99%) and O₂ (99.99%) were obtained from White Martins Co (Brazil). Dopamine (98% w/w) and sodium nitrite (99% w/w) were purchased from Sigma Aldrich (St. Louis, USA). For the dopamine determination, 0.1 mol L⁻¹ perchloric acid solution was used as the supporting electrolyte. Potassium chloride (0.1 mol L⁻¹) was used as the supporting electrolyte for the voltammetric measurements of the redox pair $[\text{Fe}(\text{CN})_6]^{3-}/[\text{Fe}(\text{CN})_6]^{4-}$. A 0.12 mol L⁻¹ Britton-Robinson (BR) buffer solution (pH 2) was used as the supporting electrolyte for the determination of nitrite, as proposed in a previous study that investigated the electrochemical oxidation of nitrite on a 3D-printed carbon-PLA electrode and verified the highest current response using this solution as the supporting electrolyte (Cardoso et al., 2020c). This buffer solution contains a mixture of 0.04 mol L⁻¹ acetic acid, boric acid and phosphoric acid. The pH of BR buffered solutions was

adjusted with 1.0 mol L⁻¹ sodium hydroxide solution. All stock solutions were previously prepared by dissolution in the respective electrolyte. All measurements were performed in the presence of dissolved oxygen and at room temperature ($\pm 25^{\circ}\text{C}$).

Saliva samples were collected from healthy people using the Salivette device (Sarstedt AG & Co; Nümbrecht – Germany). The device has a synthetic swab that was inserted and chewed for two minutes to simulate salivation (Bezerra da Silva et al., 2011). In the next step, the swab with the absorbed saliva was placed inside the Salivette tube and centrifuged at 5000 rpm for 2 min, and about 2 mL was collected. The saliva sample was diluted 50 and 200 times in supporting electrolyte for the determination of nitrite and dopamine, respectively. The collection of authentic human saliva samples is in accordance with the approved procedure from the Research Ethics Committee of the Federal University of Uberlandia (License CEP-UFU No 37370920.6.0000.515).

2.2. Electrochemical measurements and electrode production

Electrochemical recordings (cyclic voltammetry, square-wave voltammetry, differential-pulse voltammetry and Electrochemical Impedance Spectroscopy (EIS)) were made using a AUTOLAB type III potentiostat/galvanostat (Metrohm Autolab B. V., Netherlands) and data acquisition by NOVA 1.11.3 software. Conductive CB-PLA filament (Proto-Pasta® from ProtoPlant Inc., Canada) with resistivity of 30 Ω cm was employed to prototype the conductive parts of the electrodes using a 3D pen (Sanmersen; Shenzhen, China) within 3D-printed template as described elsewhere (Cardoso et al., 2020b; João et al., 2020). These electrodes were fabricated in a cylinder-shape (similar to a conventional disc electrode) using a 3D-printed template. The CB-PLA material was 3Dprinted over the empty pocket left at one end of the 3D-printed cylinder template while at the opposite side a copper wire was used to establish the electric contact of the working electrode. An Ag(s)|AgCl(s)|KCl(sat.) electrode and a platinum wire were used as reference and counter electrodes, respectively, immersed in a 10 mL electrochemical cell.

2.3. Microscopic and spectroscopic characterization of 3D-printed CB-PLA surfaces

The surface morphology was evaluated using a scanning electron microscope (SEM) TESCAN Vega 3 (Czech Republic), with the electron beam energy of 20 kV, controlled by Vega TC software. Raman spectra were obtained in a Horiba Scientific

spectrophotometer LabRAM HR Evolution (Japan), with He-Ne 633 nm (red) laser, controlled by LabSpec 6 software. FT-IR spectrometer with ATR MIR/FIR (PerkinElmer, USA) was used to obtain the infrared spectra. The chemical analysis was performed by X-ray photoelectron spectroscopy (XPS) in a SPECS Phoibos 150 high-resolution hemispherical analyser with multi channeltron detection using an Al K_{α} x-ray source (1486.6 eV) with 180 W, under a base pressure of 10^{-8} mbar, in normal emission, and constant pass energy (20 eV) for all peaks. The sample was glued to a Mo-plate sample-holder with conductive carbon tape. The sample was inserted in a load-lock chamber to degas for 12 h before transferring to the XPS chamber. The obtained data were fitted assuming Shirley-type background and Lorentzian peaks numerically convoluted with a normalized Gaussian function with a fixed full-width half maximum of ~ 1.0 eV that describes the instrumental broadening. The atomic concentrations were obtained using the procedure reported by Wagner et al. (Wagner et al., 1981).

2.4. Cold plasma treatment of 3D-printed CB-PLA surfaces

A custom designed microwave plasma-enhanced chemical vapour deposition system (Figure 2) was used to submit the electrodes through CO_2 ($\text{CO}_2\text{-T}$) and O_2 ($\text{O}_2\text{-T}$) plasma treatments (Khare et al., 2015). Argon was added to the vacuum chamber in order to obtain the plasma discharge at room temperature. The argon gas pressure was 350 mTorr for both cases, and 150 mTorr of CO_2 or O_2 for 2 min. Preliminary studies demonstrated that when exposed to oxygen plasma for more than 2 min, the electrodes were degraded, thus, this was the time chosen to further experiments. The temperature achieved in this process depends on the atmosphere used for the plasma generation. In this case, it reaches a maximum 110°C .

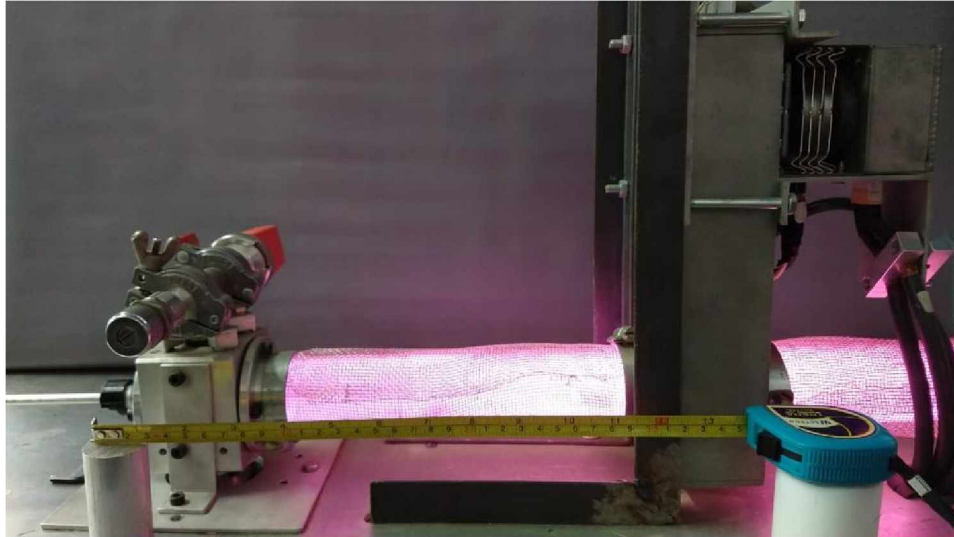


Figure 2. Custom designed microwave plasma-enhanced chemical vapour deposition system.

3. Results and discussion

3.1. Microscopic and spectroscopic characterization of the 3D-printed CB-PLA electrodes

SEM analyses were performed to evaluate the morphological changes caused by the different treatments at the 3D-printed CB-PLA surface. The results are shown in Figure 3. It is possible to note that all treatments provided different levels of grating in the native surface (untreated), in which the CB particles are rarely exposed (Fig. 3A), as previously-reported in the literature (Richter et al., 2019; Rocha et al., 2020b). Figures 3B and 3C show the removal of the insulation material (PLA matrix) generating a surface with high porosity by action of the CO₂- and O₂-plasma treatments, respectively. In addition, it is possible to see rough surfaces due to the crack formation (grooves surfaces), more evident in the O₂-treated sample (Figure 3C).



Figure 3. Scanning electron microscopy (SEM) images raised 10,000 x of 3D-printed CB PLA samples before (A) and after CO₂-plasma (B) and O₂-plasma treatments (C).

Next, Raman spectra were recorded for each surface, non-treated (N-T) and plasma-treated surfaces using CO₂ (CO₂-T) and O₂ (O₂-T), in order to assess possible increase in structural disorder (presence of defects) generated by the treatments proposed in this work and the results are shown in Figure 4A. Carbon materials present well known Raman spectra, with two characteristic bands. The D band at 1338 cm⁻¹ represents the defects on the bidimensional plane caused by the formation of sp³ bonds and oxygenated species. The second signal at 1581 cm⁻¹ corresponds to the G band, which represents the C=C stretch in sp² carbon atoms, composing the bidimensional structure of graphite layers (Rocha et al., 2018b; Silva et al., 2020). All evaluated surfaces presented the same profile, achieving slight variation in the intensities, as can be seen in the Figure 4A. The ratio of intensities between the D and G bands (I_D/I_G) can highlight the concentration of defects in the structure of the material (Rocha et al., 2018b, 2018a; Silva et al., 2020).

Figure 4B provides the I_D/I_G ratio for all surfaces. It can be noted a significant increase in the I_D/I_G ratio (about 35%) when N-T was compared with the surfaces submitted to the plasma treatments (O₂-T and CO₂-T), which indicates that the plasma treatment provided an increase in the defects (increase in disorder). Between the treated surfaces no major changes were observed in the I_D/I_G ratio. Thus, as above-discussed, the increase in the density of defects caused by the plasma treatment, accompanied by an increase in the surface rugosity (evidenced by SEM images), can significantly affect the electrochemical response of these electrodes.

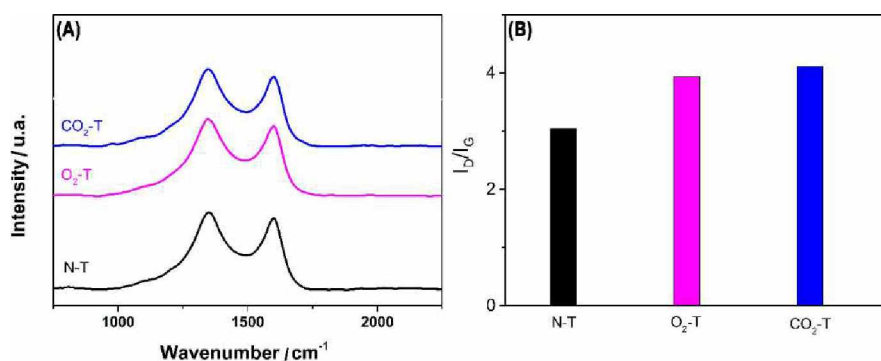


Figure 4. (A) Raman spectra and (B) I_D/I_G ratio for 3D-printed CB-PLA electrodes before (N-T) and after plasma treatment with CO_2 ($\text{CO}_2\text{-T}$) and O_2 ($\text{O}_2\text{-T}$).

It has been reported that cold reactive plasma treatments generate functional groups on different carbon surfaces (Dabhade et al., 2004; Patil et al., 2016; Pereira et al., 2019) and this fact can affect the electrochemical performance of the carbon-based electrodes. In this context, FTIR analyses were conducted and Figure 5 displays the obtained results for each surface. The N-T spectrum exhibits the main vibrational modes that corresponds to PLA material (Cardoso et al., 2018; Rocha et al., 2020b). The low intensity bands at around 2900 and 1415 cm^{-1} are related to symmetrical and unsymmetrical stretching of the CH_3 group. At 1755 cm^{-1} the strong sharp band is attributed to carbonyl group, while the bands at 1180 and 1055 cm^{-1} corresponds to the vibrational modes related to the C-O and C-O-C groups (Cardoso et al., 2018; Rocha et al., 2020b). The $\text{CO}_2\text{-T}$ surface produced similar spectra.

A clear decrease in the intensity of the above-mentioned bands, followed by the pronounciation of a band at 1592 cm^{-1} associated with C=C stretching mode, indicates the elimination of most PLA material which reduces the electrical resistivity by exposing higher CB electroactive sites (Rocha et al., 2020b). The $\text{O}_2\text{-T}$ surface spectrum reveals the absence of some bands related to PLA, indicating the elimination of the polymer from the surface of the electrode, moreover, signals at 1713 (C=O), 1250 (OC=O) and 1015 cm^{-1} (O-C-O) are characteristics of CB treated with oxygen plasma (Rositani et al., 1987). From these results it is supposed that the O_2 plasma effectively eliminates the PLA making the CB more exposed, increasing the electrical conductivity, and functionalizing the CB structure with oxygenated groups, which may improve the electrocatalytic activity of the electrode (Park et al., 2003). It is important to note that $\text{O}_2\text{-T}$ treatment promotes a more effective functionalization of the CB surface with oxygenated groups when compared with $\text{CO}_2\text{-T}$ surface since the amount of oxygen species available in the plasma

discharge to react with the polymer surface is greater when O₂ is used at the same CO₂ pressure (Pérez-Mendoza et al., 1999).

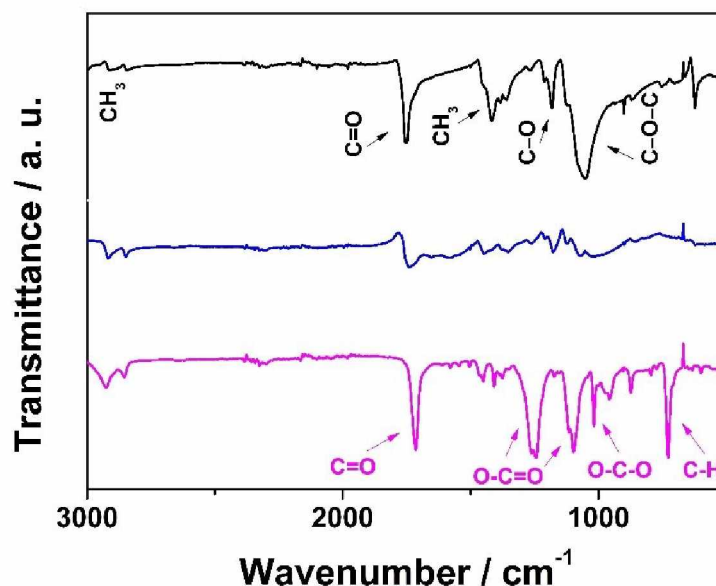


Figure 5. FTIR spectra for 3D-printed CB-PLA before (N-T, black line) and after plasma treatment with CO₂ (CO₂-T, blue line) and O₂ (O₂-T, magenta line).

During XPS analysis we performed survey spectra for all samples which revealed only the presence of C, O, and N in all sample. The pure (non-treated) 3D-printed CBPLA shows small traces of Si that are attributed to sample manipulation. Figure 6 displays the XPS spectra from C1s, O1s, and N1s core-level contributions in all samples. Figure 6 (C 1s) compares the main functional groups revealed by C 1s core level. We have used a comprehensive fitting procedure to constrain peak position and linewidths to values previously reported in the literature for similar materials (Renò et al., 2012; D. P. Rocha et al., 2021a) which suggest at least five components related to O-C=O, C=O/N-C=O, C-O-C, C-H, C-C/C=C. The pure CB-PLA has a majority contribution from C-H groups consistent with the polymeric groups presented in PLA.

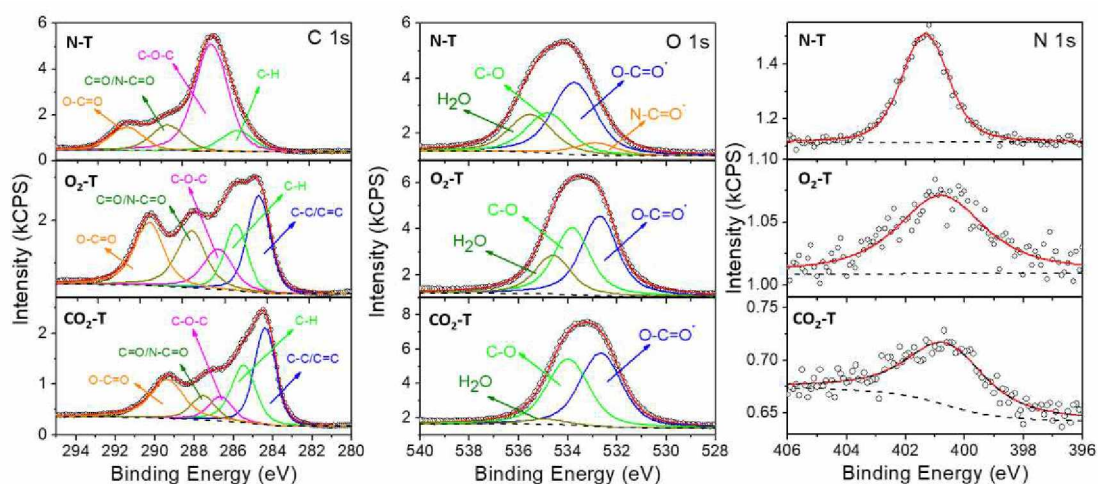


Figure 6. High-resolution XPS spectra for C 1 s, O 1 s, and N 1 s for 3D-printed CB-PLA before (untreated, N-T) and after plasma treatment with O₂ (O₂-T) and CO₂ (CO₂-T).

Moreover, we can also address the typical C-O=O and C-O-C groups already reported in the literature that correspond to PLA (Dias et al., 2008; Renò et al., 2012; D. P. Rocha et al., 2021a). Additionally, C=O, C-C/C=C groups are presented due to carbon black additive in the 3D-printed CB-PLA. The small contribution from N-C=O (close to C=O contribution) is attributed to the adsorption of N by PLA (Bao et al., 2006; Renò et al., 2012; D. P. Rocha et al., 2021a), which is also revealed in the N1s core-level peak (N 1s). The O₂ and CO₂ plasma treatment efficiently displayed the graphitic groups (C-C/C=C) and carbon oxide groups (C=O, O-C=O) presented in the CB additive, and in both cases, a drastic reduction of C-O-C and almost a complete suppression of C-N groups as revealed by N 1s (N 1s) were observed.

These results unequivocally demonstrate that O₂ and CO₂ plasma treatment can efficiently etch the non-conductive PLA on the 3D-printed electrode surface. An extra control on the production of the major functional groups and on the final sensitive properties of the material is obtained when using O₂ or CO₂ plasma treatment. While O₂ plasma strongly increases oxide groups and graphitic groups, CO₂ plasma strongly increases only the graphitic groups. The corresponding functional groups are also revealed by O1s core-level peak shown in Figure 6 (O1s). The relative concentration and binding energy position for each component attributed for C1s, O1s, and N1s are summarized in Table 1.

Table 1. XPS analysis and element concentration for the as-printed and plasma treated CB-PLA electrode.

		N-T		CO ₂ -T		O ₂ -T	
	Comp.	B. E. (eV)	Conc. (%)	B. E. (eV)	Conc. (%)	B. E. (eV)	Conc. (%)
C 1s	O-C=O	290.70	15	289.36	17	289.65	20
	C=O/N-C=O	288.78	17	287.61	13	287.61	18
	C-O-C	286.73	54	286.35	12	286.35	14
	C-H	285.35	14	285.55	23	285.43	20
	C-C/C=C	-	-	284.43	35	284.43	27
C		73.3 at. %		52.7 at. %		66.3 at. %	
O 1s	N-C=O	532.8	8	-	-	-	-
	O-C=O	533.6	44	532.5	50	532.6	43
	C-O	534.7	25	533.9	46	533.7	36
	H ₂ O	535.4	23	534.8	4	534.5	21
O		24.4 at. %		46.5 at. %		32.9 at. %	
N 1s	N-C=O	401.3	100	400.7	100	400.8	100
N		2.2 at. %		0.8 at. %		0.8 at. %	

3.2. Electrochemical characterization of the 3D-printed CB-PLA electrodes

Electrochemical characterization of the surfaces was performed in the presence of the redox couple $[\text{Fe}(\text{CN})_6]^{3-}/[\text{Fe}(\text{CN})_6]^{4-}$ (1 mmol L⁻¹) applying the half-wave potential for each of the electrodes: 0.22V (O₂-T), 0.26V (CO₂-T), and 0.27V (N-T). The EIS measurements presented distinct behaviours between the treatments, as shown in Figure 7 (Nyquist plots (-Z' vs Z'')). All surfaces (untreated and treated) showed a portion of the Nyquist semicircle; however, the great difference is related to the size of the semicircle, which is closely associated to the resistance of charge transfer (R_{ct}). The R_{ct} values were estimated as 394 Ω (O₂-T), 1,915 Ω (CO₂-T), and 245,430 Ω (N-T). From these estimated values, it is possible to conclude that the electron transfer was facilitated for the treated surfaces, corroborating with the Raman data (which presented a greater number of defects for these surfaces) and SEM (which showed higher roughness and higher availability of CB conductive sites).

The N-T showed a higher Rct value among all surfaces (higher resistance to charge transfer), and this can be explained by the great presence of the insulating thermoplastic PLA on its surface (ill-availability of CB nanoparticles) again evidenced by the SEM measurements. Comparable results for the N-T electrode were obtained by Rocha et al. (Rocha et al., 2020b), with a very resistive behaviour (higher impedance). When comparing the O₂-T and CO₂-T surfaces, the first surface provided faster electron transfer (Rct value about 5-fold lower) and these results indicate strong evidence that the electrochemical performance of this electrode will be superior among all proposed here.

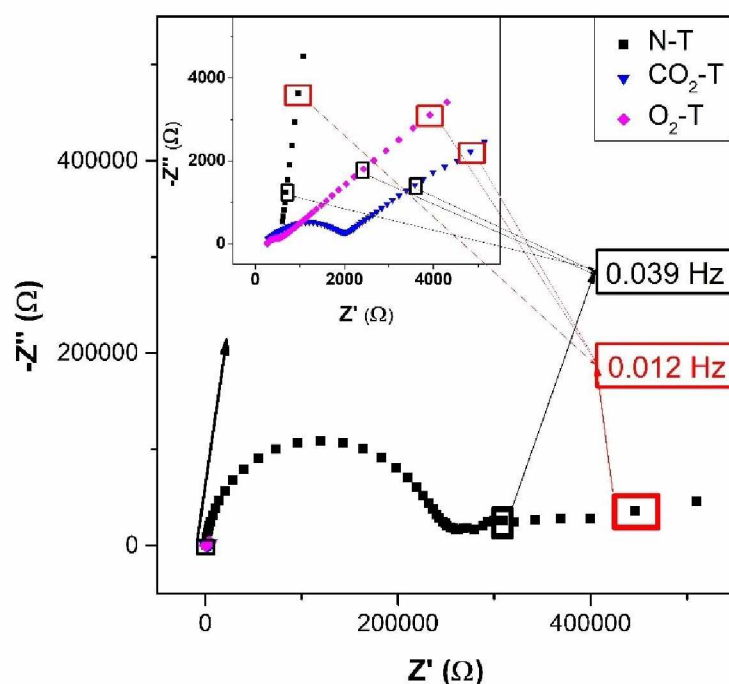


Figure 7. Nyquist plots for 3D-printed CB-PLA electrodes acquired in the presence of the redox couple $[\text{Fe}(\text{CN})_6]^{3-}/[\text{Fe}(\text{CN})_6]^{4-}$ (1 mmol L^{-1}) using $\text{KCl } 0.1 \text{ mol L}^{-1}$ as supporting electrolyte, applying the half-wave potential for each of the electrodes: 0.22 V ($\text{O}_2\text{-T}$), 0.26 V ($\text{CO}_2\text{-T}$), and 0.27 V (N-T). Inset shows a zoom out image of a small region indicated by the arrow. Frequency range between 0.1 Hz and 50.000 Hz and signal amplitude of 10 mV .

According to the Randles-Ševčík equation, there is a relationship between the electroactive area of the electrode and its peak currents for reversible processes, using systems with mass transport controlled by diffusion. For this, cyclic voltammograms were recorded, under different scan rates, in the presence of 1 mmol L^{-1} $[\text{Ru}(\text{NH}_3)_6]\text{Cl}_3$ in 0.1 mol L^{-1} KCl . This choice was made due to the fact that hexaamineruthenium chloride

presents an outer sphere oxidation-reduction process, that is less sensitive to the presence of functional groups in carbon-based electrodes surfaces than the process observed for potassium ferri/ferrocyanide, thus, being more accurate in determining the electroactive surface area of electrodes. (García-Miranda Ferrari et al., 2018)

The Randles–Ševčík equation provides the electroactive area of a working electrode, by knowing the number of electrons involved in the reaction, the species diffusion coefficient and its concentration, scan rate and peak current at a determined temperature (Oldham, 1979; Randles, 1948; Ševčík, 1948). The equation is presented below, in which, A is the electroactive electrode area (cm^2), i_p is the peak current (Ampere), n is the number of electrons transferred, v is the scan rate (Volts s^{-1}), D is the diffusion coefficient of $[\text{Ru}(\text{NH}_3)_6]\text{Cl}_3$ ($\text{cm}^2 \text{s}^{-1}$) and C_0 is the species concentration (mol cm^{-3}).

$$I_p = 2,687 \times 10^5 n^{3/2} A D^{1/2} C_0 v^{1/2}$$

For this, cyclic voltammograms were recorded, under different scan rates, in the presence of 1 mmol L^{-1} $[\text{Ru}(\text{NH}_3)_6]\text{Cl}_3$ in 0.1 mol L^{-1} KCl, and the results are presented in Figure 8. The found values for the electroactive surfaces were 0.75 mm^2 for N-T, 0.89 mm^2 for CO_2 -T and 1.10 mm^2 for O_2 -T. From these values, it is plausible to judge that the results corroborate with that acquired in SEM analyses, in which the O_2 -T provided the higher electroactive area. It is also possible to conclude that such results are also in accordance with the EIS data, since the surface that provides the higher electroactive area (O_2 -T) has a greater number of CB electroactive sites, which facilitates electronic transfer and decreases the resistance observed in the Nyquist plots (Figure 7).

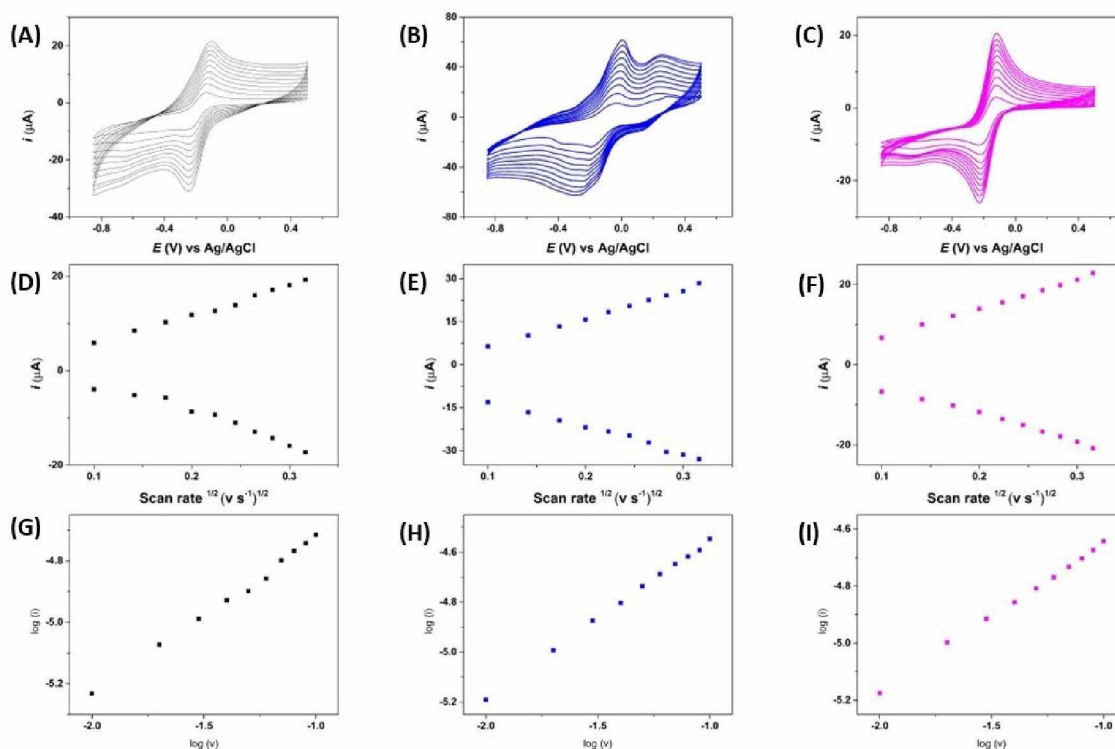


Figure 8. Cyclic voltammograms for NT (A), CO₂-T (B) and O₂-T (C) in the presence of 1 mmol L⁻¹ [Ru(NH₃)₆]Cl₃ in 0.1 mol L⁻¹ KCl as supporting electrolyte at the scan rates 10, 20, 30, 40, 50, 60, 70, 80, 90 and 100 mV s⁻¹, squared root of the scan rate versus peak current for NT (D), CO₂-T (E) and O₂-T (F), and Log (v) versus Log (i) for NT (G), CO₂-T (H) and O₂-T (I).

Cyclic voltammetric recordings for the redox pair [Fe(CN)₆]³⁻/[Fe(CN)₆]⁴⁻ (0.5 mmol L⁻¹ of each) in 0.1 mol L⁻¹ KCl (background electrolyte) at treated and untreated surfaces were obtained. Figure 9 shows these voltammetric scans and Table 2 the electrochemical data extracted from these plots. The peak-to-peak separation (ΔE_p) values were found to be 0.301 V for CO₂-T, and 0.156 V for O₂-T (Table 2). It was not possible to determine the peak separation for the N-T electrodes, as can be seen in the cyclic voltammogram highlighted in the inset of Figure 9 (black line). These results corroborate with the EIS measurements, demonstrating that the charge transfer rate is higher on plasma treated surfaces, in particular on the O₂-T surface, providing a higher electrochemical reversibility than other surface treatments (see peak-to-peak separation in Table 2). Moreover, it is evidenced an increase in current (both I_{pa} and I_{pc}) of about two times for the electrode treated with cold oxygen plasma when compared to CO₂ plasma treatment. When compared with the non-treated 3D-printed CB-PLA electrodes (Table 2), the

current values were dramatically improved after treatment, which may be related to an increase in the surface porosity observed by SEM images and facilitated electron transfer.

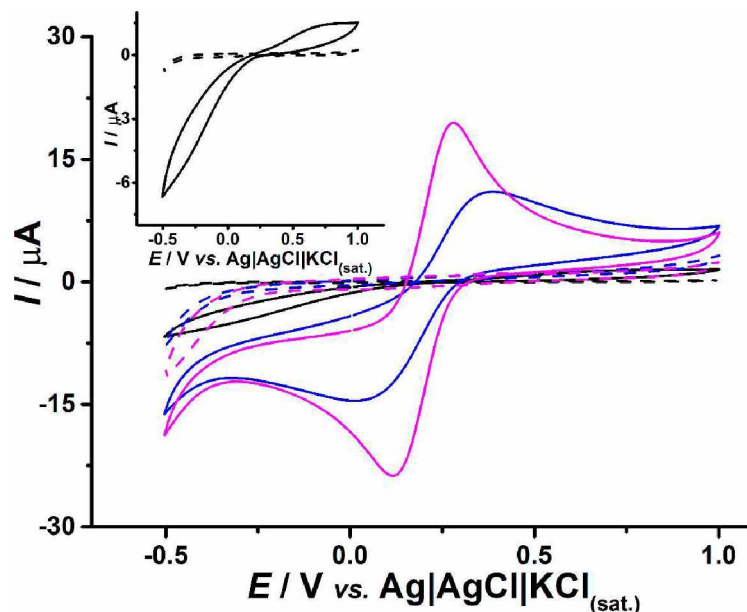


Figure 9. Cyclic voltammograms in the presence of 1 mmol L⁻¹ [Fe(CN)₆]³⁻/[Fe(CN)₆]⁴⁻ at the 3D-printed CB-PLA electrode before (N-T, black line) and after plasma treatment with CO₂ (blue line) and O₂ (magenta line). The dashed lines correspond to the respective blank signals. Electrolyte: 0.1 mol L⁻¹ KCl; scan rate: 50 mV s⁻¹; step potential: 5 mV; starting potential: -0.5 V; upper vertex potential: 1.0 V. The inset shows amplification of the response obtained on untreated 3D-printed CB-PLA.

Table 2. Electrochemical data (E_{pa} , E_{pc} , ΔE_p , I_{pa} , I_{pc}) obtained from cyclic voltammograms of 1 mmol L⁻¹ [Fe(CN)₆]³⁻/[Fe(CN)₆]⁴⁻ (data from Figure 7).

Electrode	[Fe(CN) ₆] ³⁻ /[Fe(CN) ₆] ⁴⁻				
	E_{pa} (V)	E_{pc} (V)	I_{pa} (μ A)	I_{pc} (μ A)	ΔE_p (V)
N-T	0.669	-	0.38	-	-
CO ₂ -T	0.362	0.061	11.1	-10.0	0.301
O ₂ -T	0.277	0.121	22.1	-20	0.156

**versus* an Ag(s)|AgCl(s)|KCl(aq) reference electrode

The ΔE_p value acquired in the cyclic voltammogram registered at the 3D-printed CB-PLA electrode after O₂ plasma treatment for the redox pair [Fe(CN)₆]³⁻/[Fe(CN)₆]⁴⁻ is lower than the values obtained after other surface treatments reported in the literature (Browne et al., 2018; dos Santos et al., 2019; Gusmão et al., 2019; Manzanares-

Palenzuela et al., 2019a; Novotný et al., 2019; Redondo et al., 2021; Wirth et al., 2019), which indicates greater electrochemical reversibility of this treated electrode.

The heterogeneous electron transfer constant (k^0) can be obtained by the Nicholson method (Nicholson, 1965), that can be applied in systems where the electron transfer process is controlled by the diffusion of the species towards the electrodes surface, according to the following equation.

$$\Psi = k^0 [\pi D n \nu F / (RT)]^{-1/2}$$

In which Ψ is a kinetic parameter, determined by the following equation, proposed by Lavagnini (Li et al., 2013).

$$\Psi = (-0.6288 + 0.002 \ln \Delta E_p) / (1 - 0.017 n \Delta E_p)$$

The obtained k^0 values were $4.06 \times 10^{-4} \text{ cm s}^{-1}$ for the CO₂-T and $1.98 \times 10^{-3} \text{ cm s}^{-1}$ for the O₂-T. A higher k^0 value corresponds to a higher electron transfer rate (dos Santos et al., 2019), thus, the O₂-T electrode provided the fastest charge transfer among the studied electrodes, which is in agreement with EIS data and it is evidenced in Figure 9. Therefore, it is possible to conclude that the proposed treatment protocol (using cold oxygen plasma) is an extremely advantageous (fast, environmentally friendly and cheap) and can be considered a fast alternative for improving the electrochemical performance of 3D-printed sensors and increasing electron transfer rates. Furthermore, it can produce devices that are applicable to an *in-situ* analysis.

Table 3 provides a comparison of the obtained results for the same redox probe $[\text{Fe}(\text{CN})_6]^{3-}/[\text{Fe}(\text{CN})_6]^{4-}$ using the proposed reactive plasma treatment with other procedures reported for surface treatment of 3D-printed CB-PLA. These results highlight the improved electrochemical performance of the 3D-printed carbon electrode after the proposed oxygen plasma treatment. Moreover, it is noteworthy to mention that most previous works evaluated 3D-printed graphene/PLA electrodes which present a cost of about 20-fold higher than 3D-printed CB-PLA.

Table 3. Comparison of ΔE_p for the $[\text{Fe}(\text{CN})_6]^{3-}/[\text{Fe}(\text{CN})_6]^{4-}$ obtained after different procedures of 3D-printed carbon surface treatment.

Filament	Procedure	ΔE_p (V)	Reference
Graphene/PLA	Immersion and sonication for 7 min in a) DMF or b) acetone followed by 24 h drying	a) 0.416 b) 0.296	(Gusmão et al., 2019)
Graphene/PLA	Immersion in DMF for 10 min and application of 2 V for 250 s	0.171	(Browne et al., 2018)
Graphene/PLA	Proteinase K-mediated PLA hydrolysis after 24h	0.350	(Manzanares-Palenzuela et al., 2019b)
Graphene/PLA	Electrochemical treatment in PBS: +1.8V for 900s followed by -1.8V vs SCE for 900s	0.200	(dos Santos et al., 2019)
Graphene/PLA	Thermal annealing at 350°C for 3 h (2h to cool down)	0.255	(Novotný et al., 2019)
Graphene/PLA	Electrolysis for 24 h using a 9 V battery	0.350 0.900	(Wirth et al., 2019)
CB/PLA	Mechanical polishing followed by electrochemical treatment: +1.4V for 200s, -1.0V for 200 s in NaOH	0.297	(Rocha et al., 2020b)
CB/PLA	Cold plasma treatment with O ₂ for 2min	0.156	This work

Additionally, the stability of the plasma treatment with O₂ was investigated by cyclic voltammetry in 0.1 mol L⁻¹ KCl, using a redox probe $[\text{Fe}(\text{CN})_6]^{3-}/[\text{Fe}(\text{CN})_6]^{4-}$, according to Figure 10 in the supporting information. The proposed activation showed acceptable stability since the current after 100 cycles varied 2.9% and 3.4% for anodic and cathodic peak, respectively. Moreover, the O₂-plasma-treated electrode can be used for several days without the need of a new treatment process nor polishing (around 7 days, presenting the same electrochemical behaviour for the redox probe $[\text{Fe}(\text{CN})_6]^{3-}/[\text{Fe}(\text{CN})_6]^{4-}$), stocked in the presence of atmospheric air, in room temperature. Thus, the plasma-treated

electrode could be stored for long periods without loss stability and reproducibility in electrochemical tests.

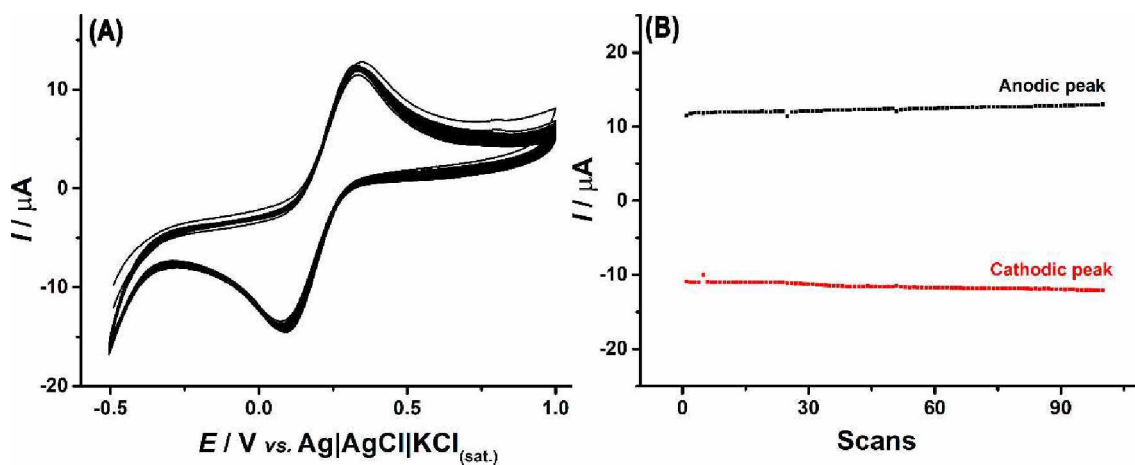


Figure 10. (A) Successive cyclic voltametric response ($n=100$) obtained for 1 mmol L^{-1} $[\text{Fe}(\text{CN})_6]^{3-/4-}$ at the 3D-printed CB-PLA electrode after plasma treatment with O_2 and (B) respective current for anodic and cathodic peak. Background electrolyte: 0.1 mol L^{-1} KCl; scan rate: 50 mV s^{-1} ; step potential: 5 mV .

However, it is important to highlight that such electrodes must be stored in favourable conditions, mainly protected from humidity. Similar results were observed in a study by Charles S. Henry's group (Kava and Henry, 2021) which evaluated the effect of plasma treatment on the surface of stencil-printed carbon electrodes on their electrochemical behaviour. In this work, the authors observed that after activation, the electrode was reproducible for 10 days without needing a new treatment.

3.3. Electrochemical sensing properties of plasma-treated 3D-printed CB-PLA electrodes

As a proof-of-concept, the voltammetric detection of the neurotransmitter dopamine and the biomarker nitrite was utilized to evaluate the proposed treatments (oxygen and carbon dioxide cold plasma) of 3D-printed carbon electrodes and compare with previous works (Cardoso et al., 2020c, 2018; Richter et al., 2019). Both solutions (HClO_4 for dopamine and BR buffer pH 2 for nitrite) used as supporting electrolytes were defined based on previous works that evaluated different conditions for the determination of dopamine (Cardoso et al., 2018) and nitrite (Cardoso et al., 2020c) using 3D-printed carbon-PLA electrodes. Figure 11A shows cyclic voltammograms of 1 mmol L^{-1} dopamine in 0.1 mol L^{-1} HClO_4 which demonstrate that the non-treated electrode

provided an ill-defined irreversible wave at around +0.8 V (inset of Figure 11A) while both plasma-treated electrodes (magenta and blue solid lines in Figure 11A) provided a much better performance, with a decrease of ΔE_p and a dramatic increase of both I_{pa} and I_{pc} when compared to N-T surface (see data in Table 4). When comparing both plasma treatment procedures, the O₂-T electrodes presented superior performance with a ΔE_p value of 171 mV, lower than 283 mV verified on the CO₂-T surface.

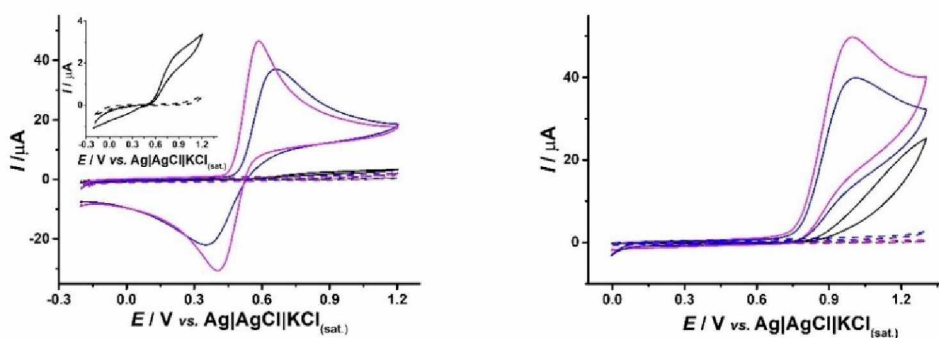


Figure 11. Cyclic voltammetric response in the presence of 1 mmol L⁻¹ dopamine (A) and 2 mmol L⁻¹ sodium nitrite (B) at the 3D-printed CB-PLA electrode before (N-T, black line) and after plasma treatment with CO₂ (blue line) and O₂ (magenta line). The dashed lines correspond to the respective blank signals. Experimental conditions in (A): supporting electrolyte: 0.1 mol L⁻¹ HClO₄; scan rate: 50 mV s⁻¹; step potential: 5 mV. The inset figure in (A) shows the amplification the lower y-axis. Experimental conditions in (B): supporting electrolyte: 0.12 mol L⁻¹ BR buffer (pH = 2); scan rate: 50 mV s⁻¹; step potential: 5 mV.

Similarly, Figure 11B compared the cyclic voltammetric profile of nitrite using untreated and plasma treated 3D-printed CB-PLA electrodes. Once again, an ill-defined oxidation wave was observed on the untreated electrode for nitrite while both plasma-treated electrodes presented an increase in the current response for nitrite at around +1.0 V, whose oxidation process was shifted to less positive potentials in comparison with the untreated electrode (black line). The electrode treated with oxygen plasma (magenta line) presented a higher oxidation current for nitrite. All quantitative data from the voltammetric experiments of Figures 11A and B are presented in Table 4.

Table 4. Electrochemical data (E_{pa} , E_{pc} , ΔE_p , I_{pa} , I_{pc}) obtained from cyclic voltammograms of dopamine and nitrite (data from Figures 5A and B, respectively) using untreated and plasma-treated 3D-printed CB-PLA electrodes.

Electrode	Dopamine				
	E_{pa} / V	E_{pc} / V	$I_{pa} / \mu A$	$I_{pc} / \mu A$	$\Delta E_p / V$
N-T	0.822	-	0.71	-	-
CO ₂ -T	0.646	0.363	30.3	-24.8	0.283
O ₂ -T	0.580	0.409	41.8	-35.1	0.171

Sodium Nitrite					
	E_{pa} / V	E_{pc} / V	$I_{pa} / \mu A$	$I_{pc} / \mu A$	$\Delta E_p / V$
N-T	~1.2 *	-	19.49	-	-
CO ₂ -T	0.995	-	39.89	-	-
O ₂ -T	0.985	-	49.13	-	-

*This value is an approximation since the peak was not well defined.

In summary, the cyclic voltammetric experiments for dopamine and nitrite indicate the oxygen plasma treatment provided was more effective in the surface treatment of 3D-printed CB-PLA electrodes. This result is in agreement with all previous electrochemical data using the redox pair $[Fe(CN)_6]^{3-}/[Fe(CN)_6]^{4-}$. When comparing the data obtained for dopamine and nitrite, the current increase was more intense for dopamine than nitrite which may suggest a stronger interaction of dopamine with the functional groups generated after plasma treatment at the CB-PLA electrode than nitrite. In fact, the electrochemical oxidation of dopamine is a surface adsorption process (Patel et al., 2013) and the plasma treatment enhanced substantially the electron transfer kinetics for this molecule. In the case of nitrite, NO_2^- is oxidized via one electron resulting in NO_2 and negligible adsorption on carbon surface was verified (Patel et al., 2013) which may explain the lower effect of surface groups generated by the plasma treatment on the nitrite oxidation.

Next, square-wave voltammetric (SWV) detection of dopamine using experimental conditions adapted from the literature (Richter et al., 2019) was also evaluated as well as the sensing features using the three different 3D-printed electrodes. Figure 12 shows the corresponding SWV recordings and the obtained calibration curves

on each different electrode for dopamine. Similarly, Figure 13 shows the corresponding differential-pulse voltammetric (DPV) recordings for nitrite detection and the respective calibration curves. DPV was selected based on a preliminary work that proposed a 3D-printed electrode for nitrite detection (Cardoso et al., 2020c). Table 5 compares the analytical features obtained on the different electrodes for the determination of dopamine and nitrite, including the linear concentration range, slope (sensitivity) and limit of detection (LOD) values. The obtained limits of detection were estimated according to the International Union of Pure and Applied Chemistry (IUPAC) (Mocak et al., 1997), $LOD = (B_{SD}) \times 3/S$, in which B_{SD} is the standard deviation of the electrolyte measurement and S is the slope of the analytical curve.

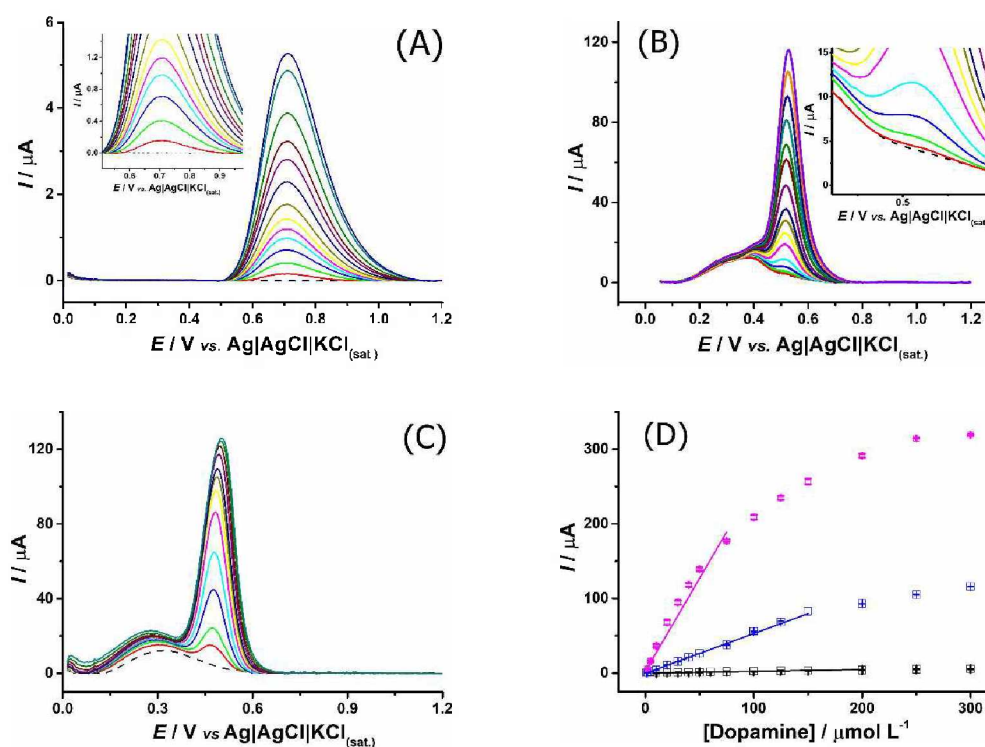


Figure 12. Baseline-corrected SWV response for increasing concentrations of dopamine in 0.1 mol L⁻¹ HClO₄, using (A) N-T (black), (B) CO₂-T (blue) and (C) O₂-T (magenta) 3D-printed electrodes and (D) comparison between dopamine current response using the proposed treatment in this work. SWV parameters: $a = 50$ mV; $\Delta E_s = 5$ mV; $f = 50$ Hz.

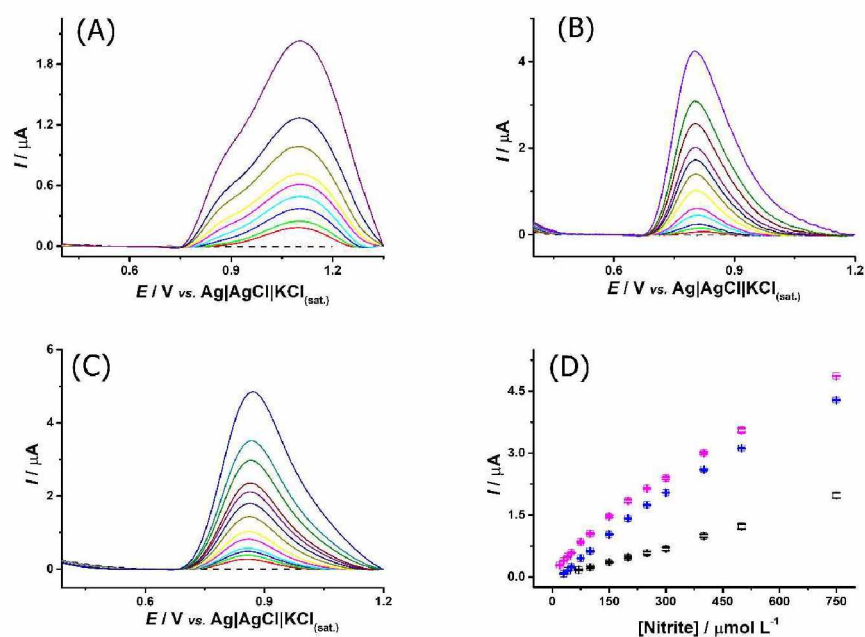


Figure 13. Baseline-corrected DPV response for increasing concentrations of sodium nitrite in 0.12 mol L^{-1} BR buffer ($\text{pH} = 2$), using (A) N-T (black), (B) CO_2 -T (blue) and (C) O_2 -T (magenta) 3D-printed electrodes and (D) comparison between sodium nitrite current response using the treatment proposed in this work. DPV parameters: $a = 100 \text{ mV}$ $\Delta E_s = 5 \text{ mV}$; $t_m = 50 \text{ ms}$.

Table 5. Summary of the analytical parameters obtained for dopamine and nitrite using untreated and plasma-treated 3D-printed CB-PLA electrodes.

Electrode	Dopamine				
	Linear range ($\mu\text{mol L}^{-1}$)	r	Slope ($\mu\text{A L } \mu\text{mol}^{-1}$)	Intercept (μA)	LOD ($\mu\text{mol L}^{-1}$)
N-T	10-200	0.998	0.024	-0.05	0.8
CO_2 -T	1-150	0.999	0.532	-0.35	0.06
O_2 -T	1-75	0.992	2.491	2.33	0.01
Sodium Nitrite					
	Linear range ($\mu\text{mol L}^{-1}$)	r	Slope ($\mu\text{A L } \mu\text{mol}^{-1}$)	Intercept (μA)	LOD ($\mu\text{mol L}^{-1}$)
N-T	70-750	0.997	0.0021	-0.017	2.79
CO_2 -T	30-400	0.998	0.0071	-0.078	0.99
O_2 -T	20-300	0.995	0.0081	0.157	0.86

Both plasma treatment procedures provided a great improvement on the voltammetric sensing properties of 3D-printed CB-PLA electrodes. The O₂-plasma treated electrode provided a more sensitive sensor with improved detection of dopamine and nitrite. The first explanation for such results is the higher electron transfer rate provided by the surface treatment as stated by previous characterization (EIS and cyclic voltammetry for the redox probe), which contributed to a higher density of defects of the carbon structures (Raman spectra) and higher rugosity (SEM images) that may have resulted in the higher exposure of conducting sites within the thermoplastic matrix. The electrochemical oxidation of dopamine depends on a surface adsorption step (Patel et al., 2013) which was facilitated after the plasma treatment by the increase in rugosity and higher exposure of conducting carbon sites. The oxygen plasma treatment provided a great increase in sensitivity and detectability; however, electrode saturation was faster (narrower linear range, as shown in Table 5), which can be explained by electrode fouling by oxidation products whose adsorption was stronger on the oxygen plasma-treated surface.

The nitrite detection was also improved over the oxygen plasma-treated surface; however, not in the same scale, probably because nitrite undergoes an irreversibly electrochemical oxidation not involving adsorption on the electrode surface. This difference of the analytes (dopamine and nitrite) is evident when comparing the current increase observed for dopamine versus nitrite after the plasma treatment (Figures 10A and B, respectively) and the great improvement on sensitivity (slope) and detectability (LOD) for the voltammetric detection of dopamine in comparison with nitrite (see data in Table 2). In fact, previous investigation on the electrochemical sensing of dopamine using carbon-based electrodes have already reported the benefits of surface oxygenated functional groups that contribute to a stronger interaction with dopamine and consequently a facilitated electron transfer at the electrode surface (Hadi and Rouhollahi, 2012).

Table 6 compares the sensing features obtained with the oxygen plasma treatment of 3D-printed CB-PLA electrodes for the detection of dopamine and nitrite. This proposed protocol offers some advantages in comparison with previous electrochemical, chemical and biological treatments, as this protocol is faster (2 min) and reagentless. Nevertheless, the sensing properties were improved as shown in Table 6.

Table 6. Analytical performance of the oxygen plasma-treated (O₂-T) 3D-printed CB-PLA electrode for the detection of dopamine and nitrite compared with other 3D-printed-based electrodes.

Electrode	linear range ($\mu\text{mol l}^{-1}$)	Technique	lod ($\mu\text{mol l}^{-1}$)	Ref.
dopamine				
O ₂ -t CB-PLA	1 – 20	SWV	0.007	This work
3DG _{red}	2 -10	DPV	0.24	(dos Santos et al., 2019)
e-CB-PLA	1 – 250	SWV	0.10	(Richter et al., 2019)
G-PLA	1 – 400	BIA-AMP	0.10	(Cardoso et al., 2018)
G-PLA	10 – 500	CV	3.49	(Kalinke et al., 2020)
	7.0 – 100*	DPV	2.17	
	5.0 – 100*	SWV	1.67	
nitrite				
O ₂ -t CB-PLA	20 - 300	DPV	0.86	This work
G-PLA	50 - 1300	DPV	30	(Cardoso et al., 2020c)

E-CB-PLA - electrochemically treated carbon black; **3DG_{red}** - reduced 3D printed graphene electrode at -1.8V; **G-PLA**- conductive PLA graphene-based filament; **SWV** – square wave voltammetry; **DPV** – differential pulse voltammetry; **BIA-AMP**- batch injection analysis with amperometric detection; *First linear range.

3.4. Application of plasma-treated 3D-printed CB-PLA electrodes for saliva analysis

Using the previous selected voltammetric conditions for the determination of dopamine and nitrite, O₂-plasma treated 3D-printed CB-PLA electrodes were applied for the analysis of human saliva. The concentration values found for dopamine and nitrite in

the sample were below the respective LOD values, therefore the sample was spiked with known concentrations of dopamine and nitrite in parallel experiments and analysed. The saliva samples were doped with 100, 125 and 150 mmol L⁻¹ and diluted 50 times in the electrochemical cell (0.2 mL of the sample and 9.8 mL of supporting electrolyte) for nitrite. As for dopamine, the saliva samples were doped with 200 and 400 mmol L⁻¹ (0.05 mL of the sample and 9.95 mL of supporting electrolyte).

The levels of dopamine and nitrite in saliva of healthy adults can vary significantly, from 1.6 to 5.2 nmol L⁻¹ of dopamine (Malon et al., 2014). Probably, for this reason the concentrations of dopamine in the analysed saliva in this work were situated below the respective LOD values. On the other hand, nitrite can be found in human saliva at abnormal levels from 1.3 to 22 mmol L⁻¹ and the combination of nitrite and amines in the stomach can form nitrosamines, which present well known toxicity and carcinogenicity (Sen et al., 1969; Tannenbaum et al., 1974; Wolff and Wasserman, 1972) while millimolar concentrations of dopamine in saliva may indicate Parkinson disease (Bagheri et al., 1999). Considering the LOD values (Table 5), the proposed O₂-plasma treated 3D-printed CB-PLA electrodes can be used to detect abnormal levels of both dopamine and nitrite. Hence, the saliva sample was spiked with dopamine and nitrite at such abnormal levels to evaluate the sensor based on the recovery values.

Saliva samples were just diluted in the respective supporting electrolyte before analysis. Table 7 shows the recovery values for dopamine and nitrite and Figure 14 presents the recordings for the analysis of a spiked sample and the corresponding calibration curves (the standard addition method was applied for each determination). Recovery values between 78% and 109% were obtained for the analysis of spiked saliva samples, which are considered within acceptable values for the analysis of such biological fluids (Simon and Booth, 2004).

Table 7. Results obtained in recovery experiments with saliva samples spiked with dopamine or nitrite (n = 3) using O₂-T as working electrode.

Analyte	Spiked (mmol L ⁻¹)	Found ± SD (mmol L ⁻¹)	Recovery ± SD (%)
Dopamine	1.0	1.09 ± 0.11	109 ± 10
	2.0	2.08 ± 0.20	104 ± 10
Nitrite	2.0	1.78 ± 0.14	89 ± 7
	2.5	1.96 ± 0.04	78 ± 2
	3.0	3.12 ± 0.03	104 ± 1

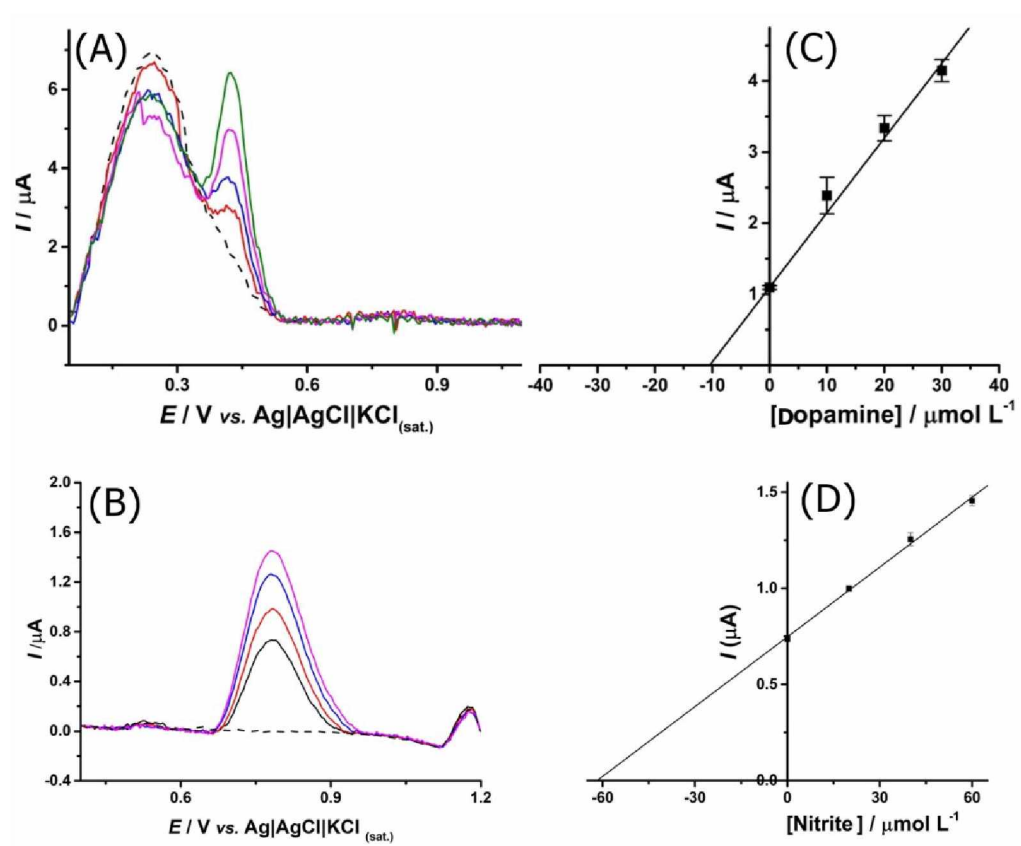


Figure 14. Baseline corrected voltammograms obtained for saliva spiked with (A) dopamine (SWV parameters: $a = 50$ mV; $\Delta E_s = 5$ mV; $f = 50$ Hz) and (B) nitrite (DPV parameters: $a = 100$ mV $\Delta E_s = 5$ mV; $t_m = 50$ ms). Calibration curves using the standard addition method for dopamine (C) and nitrite (D) using O₂T as working electrode.

4. Conclusions

A cold reactive oxygen plasma treatment improves substantially the electron transfer of 3D-printed CB/PLA electrodes, by removing excess of insulating PLA material and exposing conductive CB sites as well as generating oxygenated functional groups on the surface, which probably are responsible for the improved electrochemical characteristics of the 3D-printed electrode. This protocol is faster (2 min), more environmentally friendly (chemical-free and few-step), and provided improved electrochemical performance than any previous method reported in the literature involving electrochemical, chemical, biological treatments. Improved voltammetric sensing of dopamine and nitrite was verified, especially in the case of dopamine for which a 100-fold increase in sensitivity was obtained, resulting in submicromolar detection limits. This protocol is easily implemented in large-scale by combining the plasma treatment with 3D-printing using a hybrid 3D-printing platform. This combination offers great promises for the fabrication of electrochemical devices for bioanalytical applications.

The observer results in this chapter instigated the interest in understand how plasma treatment could modify other potential disposable carbonaceous electrodes. Thus, for the next chapters, the use of CO₂ and O₂ cold plasma treatment in Graphite Sheet (GS) electrodes will be investigated, evaluating the structural changes, as well as its application in real samples.

CHAPTER 3 – PYROLYTIC GRAPHITE SHEET: CHARACTERIZATION

MORPHOLOGICAL, STRUCTURAL AND ELECTROCHEMICAL CHARACTERIZATION OF GS SURFACES.

Introduction

This section presents a complete characterization of GS electrodes before and after the cold plasma treatment using different gases, oxygen and carbon dioxide. This section aims to show the advantages provided by the plasma treatment in the development of electrochemical sensors. The next chapters will show the different applications of the plasma-treated GS electrodes.

1. Experimental

1.1. Reagents, samples and materials

A graphite sheet (GS) of 0.07 mm thickness (115 x 180 x 0.07 mm), electric resistance of 2.5 Ω , and electric conductivity of 55.6 $S\text{ cm}^{-1}$ was acquired from Panasonic (Mansfield, Texas, USA). The positioning procedure of the working electrode (1 x 1 cm) is shown in a video available in a previous work from our research group (Silva et al., 2018). Each GS sheet costs \$ 17.38 and can generate 180 electrodes, therefore, the cost of each electrode is around \$ 0.09. All solutions were prepared using ultrapure water (resistivity $\geq 18\text{ M}\Omega\text{ cm}$) obtained from a purification system Millipore Direct-Q3 (Bedford, USA). Acetic (99.7%) and phosphoric (85.0%) acids were obtained from Vetec (Rio de Janeiro, Brazil); while boric acid was acquired from AppliChem Panreac (Barcelona, Spain). Potassium ferricyanide (99.0%) and potassium ferrocyanide (98.5%) from Synth (Diadema, Brazil) and sodium hydroxide (97.0%) from Dinamica (Diadema, Brazil). Argon (99.99% pure) CO₂ (99.99%), and O₂ (99.99%) were purchased from White Martins Co.

1.2. Electrode surface treatment

The GS was cut into 3 cm diameter discs and subjected to cold plasma discharges using mixtures of argon and O₂, and argon and CO₂ controlled by needle valves at 350 and 100 mTorr, respectively for 2 min. Preliminary studies demonstrated that when

exposed to oxygen plasma for more than 2 min, the electrodes were degraded, thus, this was the time chosen to further experiments. This time was selected due to the fact that GS starts to disintegrate after a longer exposure to the plasma. The plasma-enhanced chemical vapor deposition (PECVD) system (Figure 2) herein applied is assisted by microwaves at a frequency of 2.42 GHz through a 1000 W magnetron (LG Co.), which has been described in details previously (Kannan et al., 2016a).

1.3. GS Electrodes characterization

Electrochemical experiments (cyclic voltammetry (CV), and electrochemical impedance spectroscopy (EIS)) were performed using an Autolab PGSTAT128N potentiostat/galvanostatic (Metrohm Autolab B. V., Netherlands) interfaced to a computer equipped with NOVA 1.11 software, which was responsible for data acquisition. For studies using $[\text{Fe}(\text{CN})_6]^{3-/4-}$, the CV parameters were: step: 5 mV; scan rate: 50 mV s⁻¹; window potential: -0.4 V to +1.2 V. A typical three-electrode system, with a miniaturized $\text{Ag}_{(s)}/\text{AgCl}_{(s)}/\text{Cl}^-_{(aq)}$ electrode (Pedrotti et al., 1996) and a platinum wire were used as reference and counter electrodes, respectively. Treated and untreated GS pieces were evaluated as working electrodes, using an O-ring to delimitate the geometric surface area (0.22 cm²). The 3D-printed electrochemical cell (internal volume of 5 mL) prototyped by our research group (Cardoso et al., 2018) with acrylonitrile butadiene styrene (ABS) filament (GTMax, São Paulo, Brazil) was used for electrochemical analysis.

The GS surfaces, before and after cold-plasma treatments, were characterized by EIS, scanning electron microscopy (SEM), and Raman spectroscopy. EIS measurements were performed using $[\text{Fe}(\text{CN})_6]^{3-/4-}$ redox probe and 0.1 mol L⁻¹ KCl, as supporting electrolyte. These experiments were performed by using a frequency range of 100 kHz to 0.1 Hz and amplitude of 10 mV with 10 data points per frequency decade. The equivalent Randles circuit was applied to fit the experimental data to determine the charge transfer resistance (R_{ct}) related to the $[\text{Fe}(\text{CN})_6]^{3-/4-}$ species. SEM analyses were carried out in a TESCAN Vega 3 (Brunn, Czech Republic), with electron beam energy of 20 kV, controlled by Vega TC software, while Raman spectra were obtained in a Horiba Scientific spectrophotometer, LabRAM HR Evolution (Kyoto, Japan), with He-Ne 633 nm (red) laser, controlled by LabSpec 6 software.

X-ray photoelectron spectroscopy (XPS) was performed using a Scienta Omicron ESCA⁺ spectrometer (Uppsala, Sweden) with a high-performance hemispheric analyzer (EA 125), using monochromatic Al K α ($h\nu = 1486.6$ eV) radiation as an excitation source. The operating pressure in the ultra-high vacuum (UHV) chamber during the analysis was 2×10^{-9} mbar. Energy steps of 0.5 eV and 0.05 eV were used for the survey and high-resolution spectra, respectively. The following peaks were used for quantitative analysis: O 1s, C 1s. The C–(C, H) component of the C 1s peak of adventitious carbon was fixed at 284.8 eV to set the bond energy scale. Data processing was done with the CasaXPS software.

The hydrophilic/hydrophobic surface characteristics of the electrodes were investigated by contact angle measurements using a contact angle meter (KSV Instruments – Helsinki, Finland). Images of a water drop with an estimated volume of 5 μ L were acquired and analyzed by a CCD video camera. The initial ($t = 0$ s) and equilibrium ($t = 10$ s and $t = 20$ s) contact angles were calculated by averaging 5 individual measures ($n = 5$) from 5 different electrode pieces.

2. Results and discussion

SEM images obtained from untreated (GS), CO₂ plasma-treated GS (CO₂-GS) and O₂ plasma-treated GS (O₂-GS) electrodes are exhibited in Figure 15. The carbon material without treatment showed well-defined graphite flakes in a compact morphology (Kwon et al., 2002). On the other hand, as can be seen in Fig. 15B, 15C 15E and 15F, the surface after both cold plasma treatments presented an irregular pattern, mainly, in the edges of the micrometric graphite flakes due to the intense reaction occurred in CO₂-plasma and O₂-plasma discharge. Moreover, it is noted that this activation caused a detachment of the flakes, resulting in an expansion of the material's surface area. Therefore, the plasma treatments provided the availability of more active sites on a GS surface, improving its catalytic properties for application in electroanalysis.

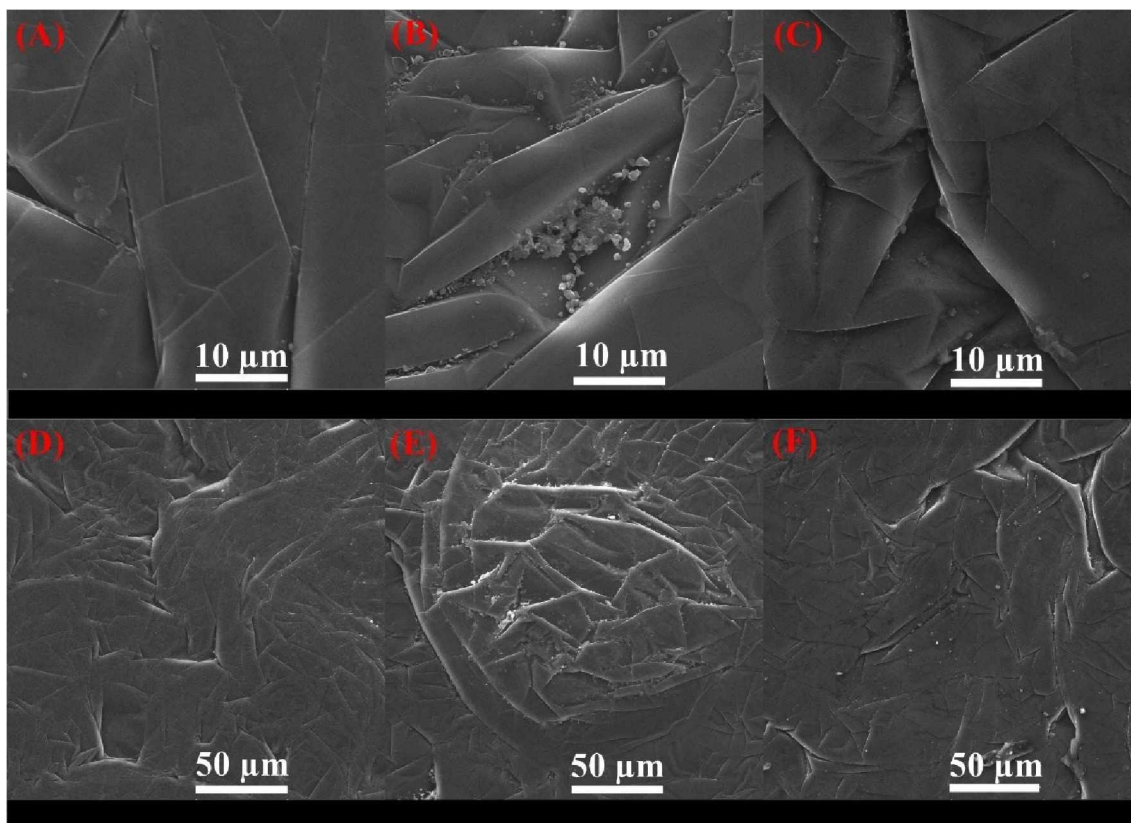


Figure 15. SEM images obtained for GS before (A and D), after (B and E) O₂-plasma treatment and after (C and F) CO₂-plasma treatment.

Furthermore, Figure 16 presents the Raman spectra of both surfaces with typical graphitic bands, where the G band at around 1583 cm⁻¹ is present in every sp²-carbon-based material and it is related to the vibration of the skeletal graphitic structure. On the other hand, the D band (at 1341 cm⁻¹) is active in the presence of lattice defects and structural disorder, while the 2D band (also called G', at approximately 2700 cm⁻¹) is sensitive to the number of stacked graphene monolayers of the sample (Franceschini and Lacconi, 2017). The relationship between the D and G bands intensities (I_D/I_G) provides information about the crystalline disorder degree of the materials and allows the estimation of the crystallite size (L_a). The untreated surface displayed lower I_D/I_G (0.03) than the treated surfaces (0.2 for O₂-GS and 0.067 for CO₂-GS), attesting the both plasmas induced several structural defects in the sp² carbon atoms lattice.

Furthermore, the plasma discharge promoted partial fragmentation of the GS electrode, once the L_a parameter (Cançado et al., 2006) returned a smaller crystallite size of 83 nm and 90 nm for O₂-GS and CO₂-GS respectively, in comparison to the non-treated electrode ($L_a = 493$ nm). It is worth highlighting that the plasma treatment did not promote effective exfoliation and separation of structural graphene monolayers, which is proved

by the I_{2D}/I_G relationship close to 0.35 obtained for all GS electrodes. In other words, these treated GS surfaces maintains its classifications as a multi-layered graphitic material (Papanai et al., 2020).

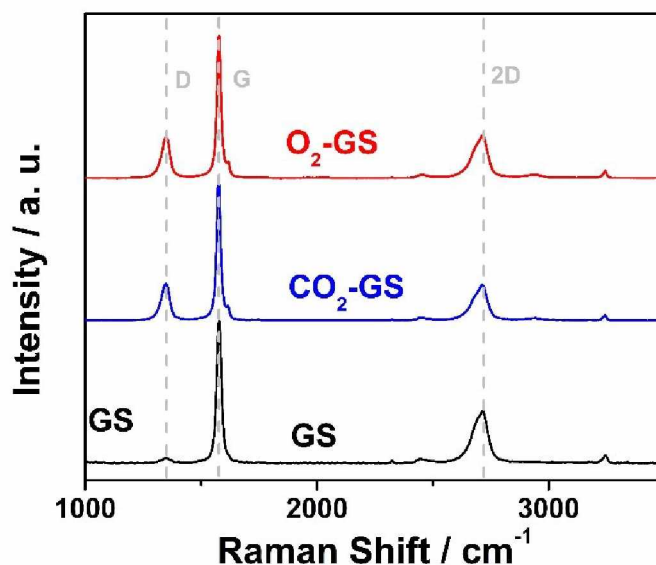


Figure 16. FTIR spectra for 3D-printed CB-PLA before (GS, black line) and after plasma treatment with CO_2 ($\text{CO}_2\text{-GS}$, blue line) and O_2 ($\text{O}_2\text{-GS}$, magenta line).

X-ray photoelectron spectroscopy (XPS) was used to investigate the chemical composition and the kind of carbon and oxygen species in all electrode surfaces. The survey XPS (Figure 17A) spectra of the GS electrodes exhibited C 1s and O 1s peaks, without any contamination. The quantification of the carbon and oxygen species was performed using the survey spectra for both samples (Table 8), the treatment with O_2 and CO_2 plasmas increased 1.6 and 1.5 times respectively the number of oxygen groups in comparison with the untreated electrode. The deconvolution of the C 1s high-resolution spectra of the GS electrodes (Figure 17B) revealed the presence of four peaks related to the following species: C=C, C-C, O-C=O, C-O, as expected for graphitic samples (D. P. Rocha et al., 2021b) with defects as observed by Raman spectroscopy analysis. There is a majority contribution of the C=C groups consistent with the sp^2 hybridization of the graphitic structure (Yue et al., 2010), the presence of O-C=O and C-O groups even in the untreated GS electrode can be attributed to chemisorbed O_2 (Larciprete et al., 2012).

It can be observed that both plasma treatments increased the amount of O-C=O groups in comparison with the untreated sample, due to the oxidation process caused by

the GS electrodes treatment. The deconvolution of the O 1s high-resolution spectra (Figure 17C) revealed the presence of two peaks related to O-C=O and C-O groups for untreated GS electrode, while GS-O₂ and GS-CO₂ electrodes exhibited two peaks related to O-C=O and C-O-C groups. Therefore, we can conclude that plasma treatments induced modification on the GS electrode surface creating oxygen groups, in agreement with Raman spectroscopy analysis.

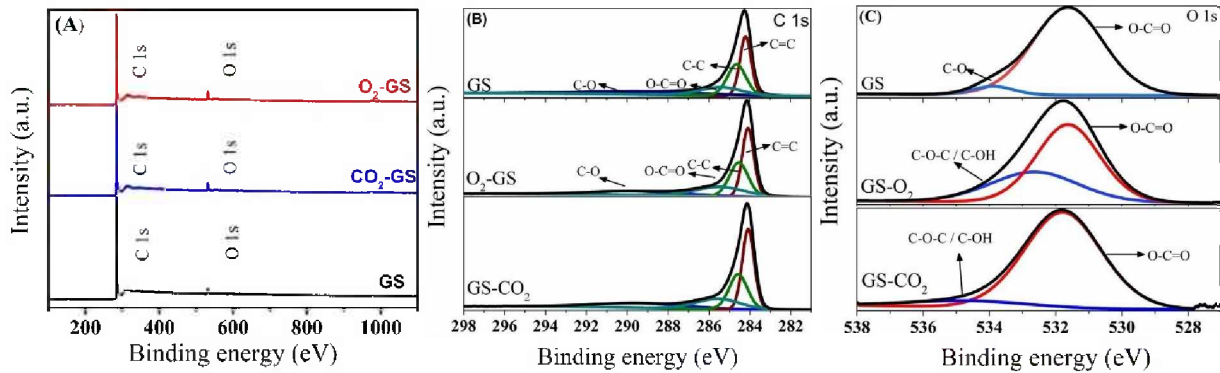


Figure 17. XPS survey (A) and spectra of the GS electrodes spectra of the (B) C 1s and (C) O 1s.

Table 8. XPS analysis of the carbon and oxygen and their species concentration for the GS electrodes.

Species	GS	B.E. (eV)	Conc. (%)	GS-O ₂	Conc. (%)	GS-CO ₂	Conc. (%)
C 1s	C=C	284.2	35	284.1	35	284.2	38
	C-C	284.7	31	284.5	28	284.5	25
	O-C=O	285.4	18	285.4	21	285.4	18
	C-O	288.8	16	289.5	16	288.8	17
Carbon			97.6		96.2		96.4
O 1s	O-C=O	531.6	95	531.6	65	531.6	88
	C-O	533.8	5	*	533.8	12	
	C-O-C		*	532.6	35		
Oxygen			2.4		3.8		3.6

The contact angle of the treated and untreated electrodes was evaluated using a contact-angle meter. The results are presented in Figure 18 and in Table 9. It is possible

to notice that both plasma treatments significantly enhance the electrodes hydrophilicity. The lower contact-angle observed is for O₂-GS electrode, which is slightly lower than the one observed for CO₂-GS. This result is in accordance with previous XPS results and confirms that cold plasma treatment was effective to promote a modification at the electrodes surface. Since the electrode's surface is composed mainly by carbon atoms, and therefore has non-polar characteristics, the enhance in surface oxygenated groups can enhance its polar properties, thus, having a lower contact-angle. This feature possibly provides a better access for the intended analytes on the electrode's electroactive sites.

Table 9. Details on the contact angle experiment.

Electrode	Contact angle (°)	
	10 s	20 s
GS	105.8 ± 6.1	106.1 ± 5.9
CO ₂ -GS	85.5 ± 8.6	85.0 ± 8.5
O ₂ -GS	79.9 ± 7.5	79.7 ± 7.5

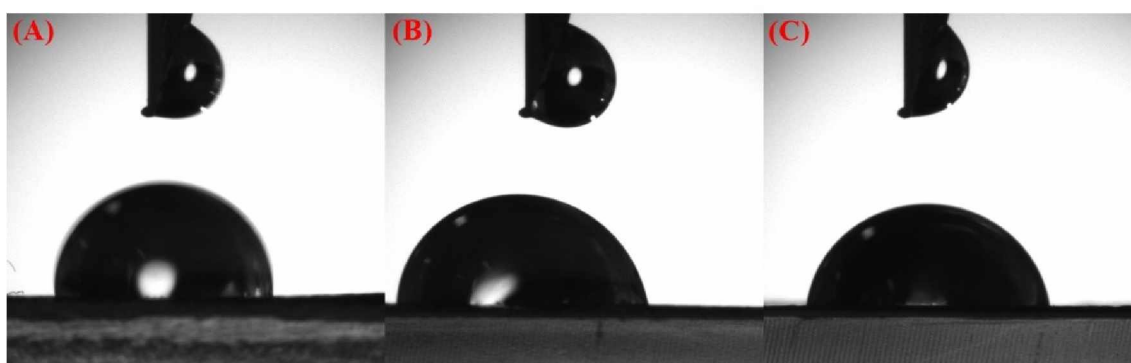


Figure 18. Contact angle for (A) GS, (B) CO₂-GS and (C) O₂-GS.

Additionally, CVs were carried out intended to explore the electrodes potential window. It is noticeable in Figure 19 that in acid media (A) (0.1 mol L⁻¹ HCl), no changes for treated and untreated electrodes were observed. However, in neutral (B) (0.1 mol L⁻¹ KCl) and in alkaline (C) (0.1 mol L⁻¹ NaOH) media, a slightly better window of potential is observed, in the positive region for KCl, and in both (positive and negative) for NaOH. In fact, previous works mentioned that when exposed to an acid treatment, GS electrodes present a behaviour similar to the one observed when applying plasma treatment. Thus, it is possible that by applying extreme potentials, the acid media modifies the electrodes

surface. However, it is important to state that the Rct observed after acid treatment is still higher than the one observed after cold plasma treatment (Pereira et al., 2019).

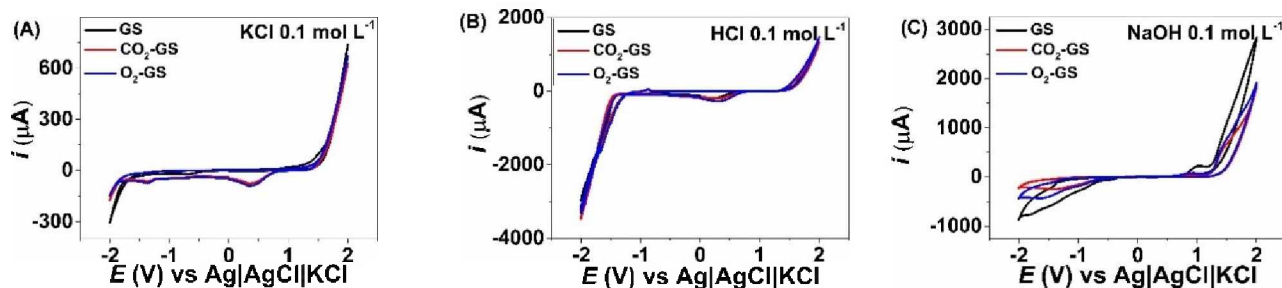


Figure 19. Cyclic voltammograms using GS (black line) and O₂-GS (red line) in (A) KCl 0.1 mol L⁻¹, (B) HCl 0.1 mol L⁻¹ and (C) NaOH 0.1 mol L⁻¹. scan rate of 50 mV s⁻¹ and step potential of 5 mV

To evaluate the behaviour of all GS electrodes, cyclic voltammograms (CVs) were recorded using 1 mmol L⁻¹ [Fe(CN)₆]^{3-/4-} probe in 0.1 mol L⁻¹ KCl as the supporting electrolyte (Figure 20A). Figure 20B shows the EIS measurements also performed in the presence 1 mmol L⁻¹ [Fe(CN)₆]^{3-/4-} coupled probe in 0.1 mol L⁻¹ KCl.

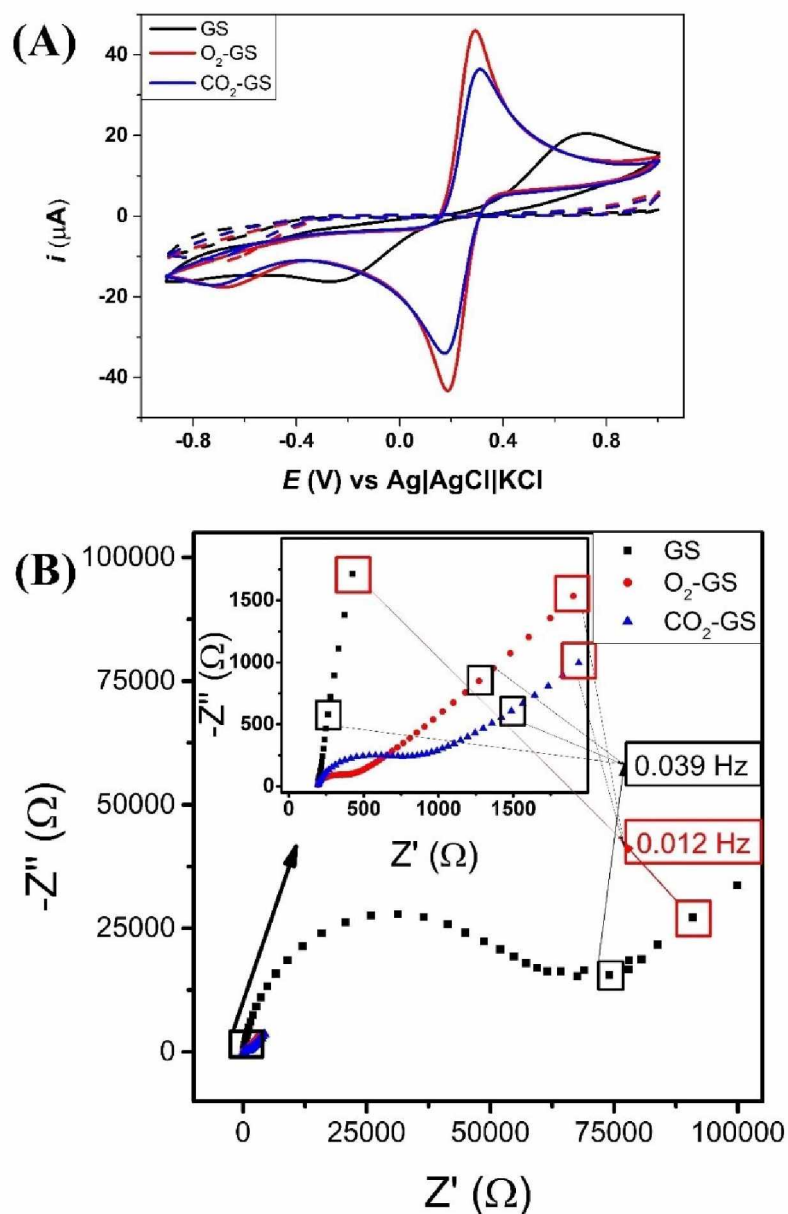


Figure 20. (A) CVs recorded on untreated (black solid line), CO_2 plasma treated (blue solid line) and O_2 plasma-treated GS electrodes (red solid line); Dashed lined correspond the respective blanks. Scan rate of 50 mV s^{-1} and step potential of 5 mV . (B) Nyquist plots acquired by applying the 0.20 V half-wave potential on the untreated (black dots), CO_2 plasma treated (blue dots) and O_2 plasma-treated GS electrodes (red dots) GS electrodes in the frequency range of 0.1 Hz to 100 KHz with 10 mV amplitude; Inset in (C) is a zoom-in of the recorded data at high frequency. Solution composition in all (A and B) experiments: $0.1 \text{ mmol L}^{-1} [\text{Fe}(\text{CN})_6]^{3-/4-}$ in $0.1 \text{ mol L}^{-1} \text{ KCl}$.

As can be seen in Fig 20A, it is evident that a higher peak current and lower peak-to-peak separation ($I_{pa} = 45.9 \mu\text{A}$, $I_{pc} = -43.4 \mu\text{A}$, $\Delta E_{\text{peak}} = 110 \text{ mV}$) were achieved for the O_2 -GS surface when compared to the CO_2 -GS ($I_{pa} = 20.6 \mu\text{A}$, $I_{pc} = -16.4 \mu\text{A}$, $\Delta E_{\text{peak}} = 150 \text{ mV}$) and to the untreated surface ($I_{pa} = 25.1 \mu\text{A}$ and $I_{pc} = 29.3 \mu\text{A}$, $\Delta E_{\text{peak}} = 960 \text{ mV}$). The lower peak-to-peak separation can be associated to a lower resistance to the charge transfer (observed in EIS, Figure 20B) while the higher current can also be related to the higher roughness/surface area, presence of oxide groups and defects caused by both plasma treatments. From the Nyquist plots (Figure 20B), the resistance to the charge transfer (R_{ct}) values for all surfaces were estimated. The R_{ct} values for untreated (black dots), CO_2 -treated (blue dots) and O_2 -treated (red dots) GS electrodes were $129.8 \text{ K}\Omega$, $1.60 \text{ K}\Omega$ and $0.25 \text{ K}\Omega$, respectively, indicating the reduction of the interfacial resistivity for the electron transfer process after cold plasma treatment.

Moreover, an important aspect of this treatment protocol involving specifically O_2 -GS electrode is its great stability for an extended period. As can be noticed in Figure 21, the performance of the treated GS electrode appears to be practically the same, even after three years of the O_2 plasma treatment on its surface. The peak current and ΔE_{peak} remain mostly unchanged, which confirms that the electrode can be stored for a long time.

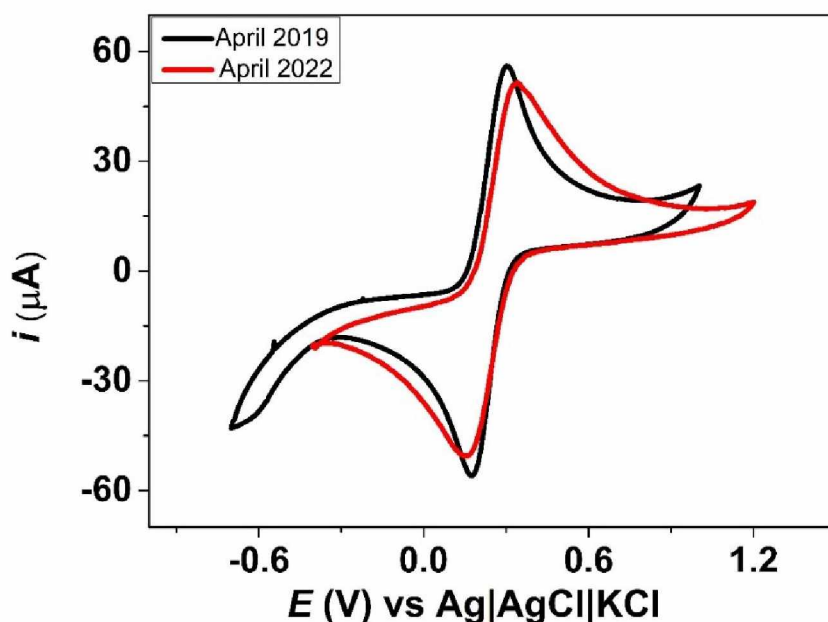


Figure 21. CVs recorded just after treatment (black solid line) and after three years stored (red solid line) using O_2 plasma-treated GS electrode; scan rate of 50 mV s^{-1} and step potential of 5 mV . Solution composition in all experiments: $0.1 \text{ mmol L}^{-1} [\text{Fe}(\text{CN})_6]^{3-/4-}$ in $0.1 \text{ mol L}^{-1} \text{ KCl}$.

To understand the surface electron transfer kinetics and estimate the heterogeneous electron transfer rate constant (k^0) on both surfaces, additional CVs were conducted using $1 \text{ mmol L}^{-1} [\text{Fe}(\text{CN})_6]^{3-/4-}$ in $0.1 \text{ mol L}^{-1} \text{ KCl}$ as the supporting electrolyte with scan rates ranging from 10 to 100 mV s^{-1} (Figure 22). The results showed a linear relationship between the peak current and the square root of the scan rate, indicating that the reaction is controlled by the diffusion of the species towards the electrode surface (Montes et al., 2014, 2012; Sims et al., 2010; Streeter et al., 2008). Log (i) versus Log (v) plots showed a linear adjustment with slopes close to 0.5 for all surfaces, confirming that indeed the diffusion process is the mass transport determinant for the reaction (Gosser, 1994).

Using Nicholson's method (Nicholson, 1965), as mentioned in the previous chapter, K^0 values of $1.46 \times 10^{-6} \text{ cm s}^{-1}$, $1.60 \times 10^{-3} \text{ cm s}^{-1}$, and $2.09 \times 10^{-3} \text{ cm s}^{-1}$ were found for GS, CO_2 -GS and O_2 -GS, respectively, suggesting an electron rate transfer around 1000-fold faster on the treated electrodes. This is in accordance with the previous results, confirming that a lower resistance to the charge transfer, observed in EIS study, provides a higher electron transfer rate.

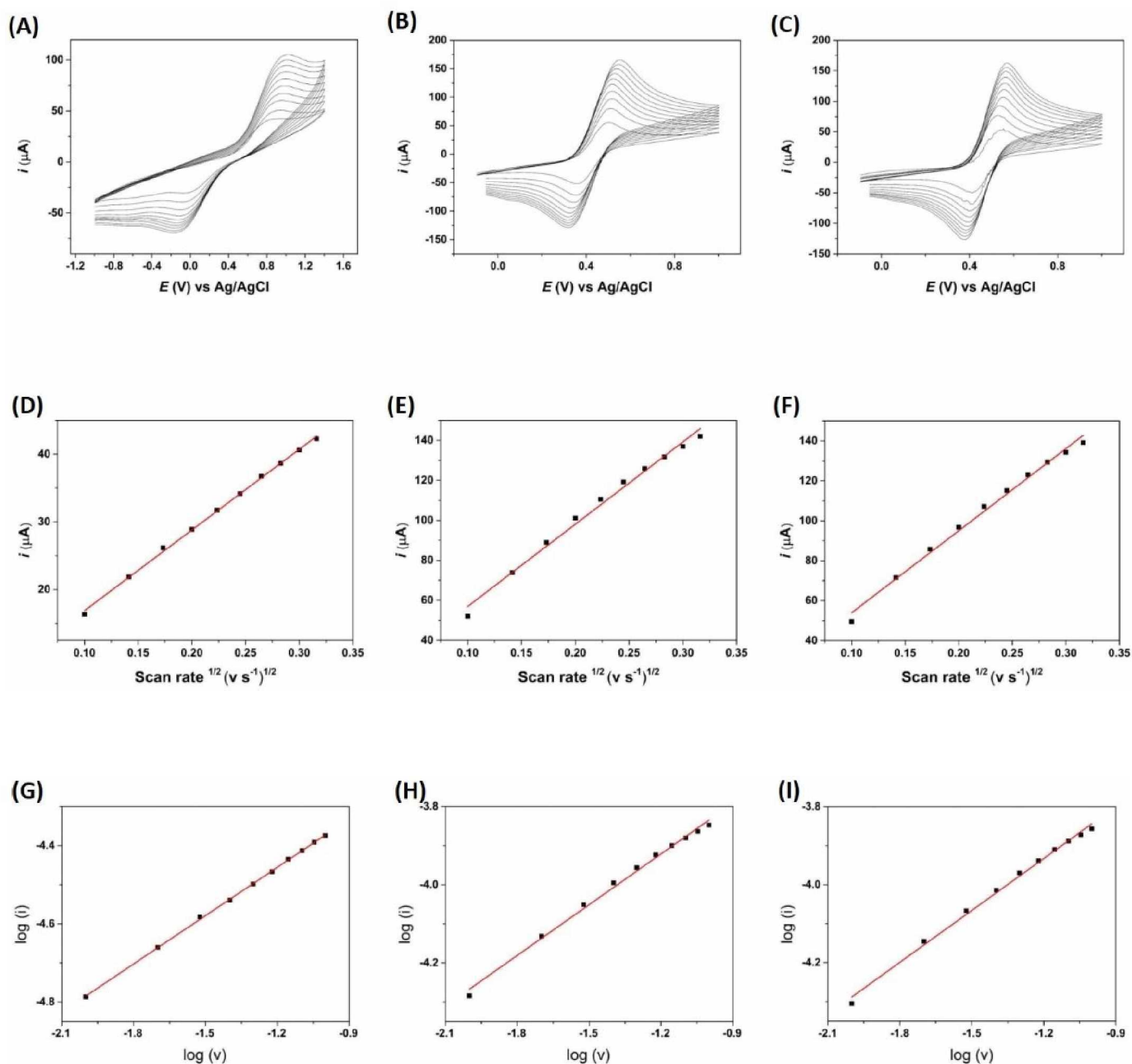


Figure 22. Cyclic voltammograms for GS (A), CO₂ plasma-treated GS (B) and O₂ plasma-treated GS (C) in the presence of 1 mmol L⁻¹ of [Fe(CN)₆]^{3-/4-} using 0.1 mol L⁻¹ KCl as supporting electrolyte at the scan rates 10, 20, 30, 40, 50, 60, 70, 80, 90 and 100 mV s⁻¹, squared root of the scan rate versus peak current for GS (D) CO₂ plasma-treated GS (E) and O₂ plasma-treated GS (F), and Log (v) versus Log (i) for GS (G), CO₂-GS (H) and O₂-GS (I).

The electroactive area is also important information to investigate the effect of the surface treatment. Thus, for this purpose, CVs were recorded in the presence of 1 mmol L⁻¹ of [Ru(NH₃)Cl₃] as redox probe and 0.1 mol L⁻¹ KCl as the supporting electrolyte, using

scan rates in the range of 10 to 100 mV s⁻¹ (Figure 23). The results showed a linear relationship between the peak current and the square root of the scan rate, indicating that the reaction is controlled by the diffusion of the species towards the electrode surface (Montes et al., 2014, 2012; Sims et al., 2010; Streeter et al., 2008). Log (i) versus Log (v) plots showed a linear adjustment with slopes close to 0.5 for all surfaces, confirming that indeed the diffusion process is the mass transport determinant for the reaction (Gosser, 1994). Using the Randles-Sevcik equation (Pacios et al., 2008), which is also detailed in the previous chapter, the electroactive area values were estimated at 198 mm², 231 and 285 mm² for GS, CO₂-GS and O₂-GS, respectively. Such results (electroactive area and K⁰) indicate, once again, that cold plasma surface treatment promotes more catalytic sites and a higher electron rate transfer on the electrode surface.

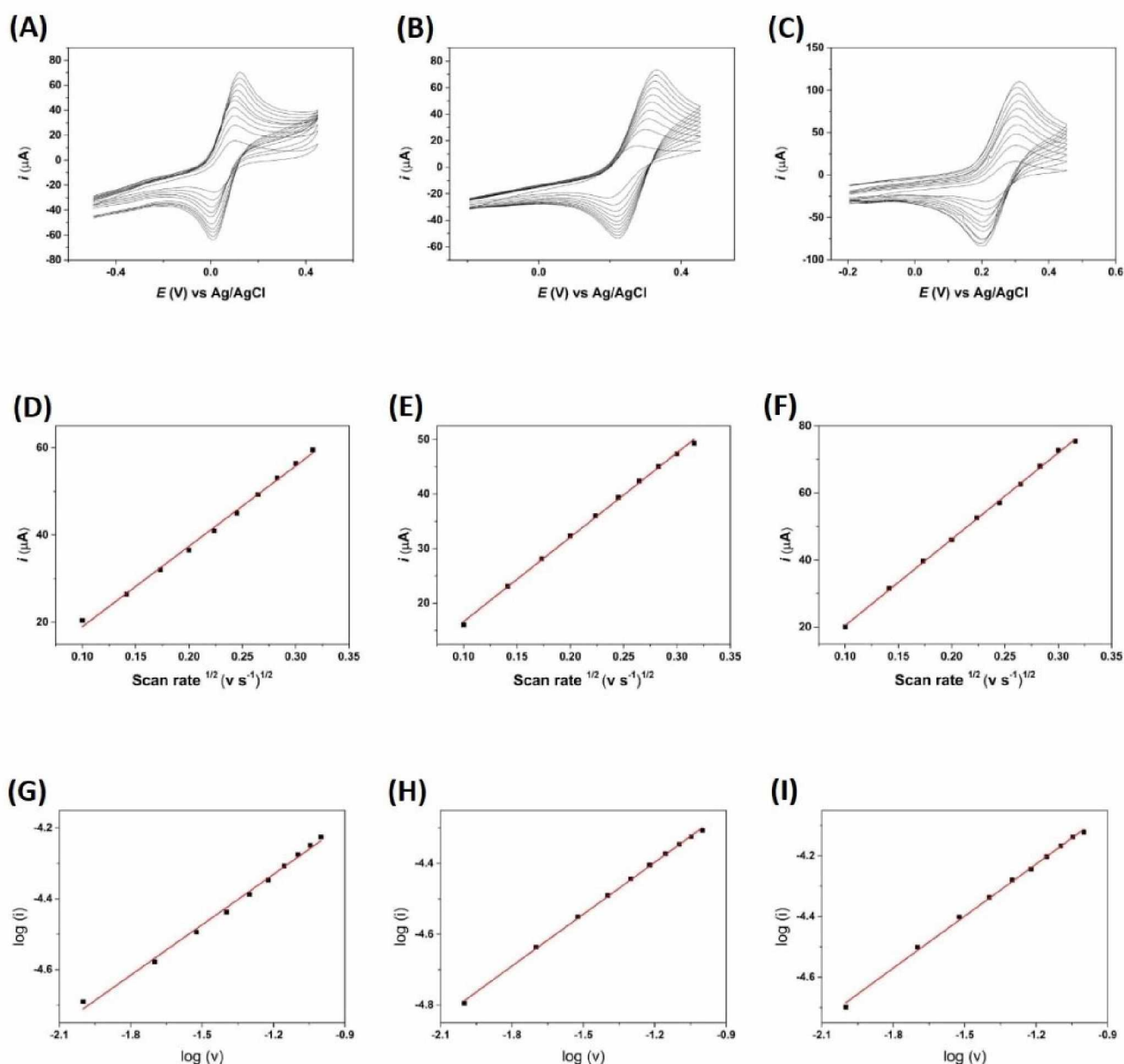


Figure 23. Cyclic voltammograms for GS (A), CO_2 plasma-treated GS (B) and O_2 plasma-treated GS (C) in the presence of 1 mmol L^{-1} of $[\text{Ru}(\text{NH}_3)]\text{Cl}_3$ using 0.1 mol L^{-1} KCl as supporting electrolyte at the scan rates 10, 20, 30, 40, 50, 60, 70, 80, 90 and 100 mV s^{-1} , squared root of the scan rate versus peak current for GS (D) CO_2 plasma-treated GS (E) and O_2 plasma-treated GS (F), and $\text{Log}(v)$ versus $\text{Log}(i)$ for GS (G), CO_2 -GS (H) and O_2 -GS (I).

The enhance on the structural disorder and consequent exposure of graphitic edge planes, associated with a larger electroactive area has a higher effect on the plasma-treated

electrode's conductivity than the slight graphitic oxidation observed. In fact, there have been several studies in the literature examining the effects of cold reactive plasma on graphite/graphene-based electrodes that support the findings presented here. For instance, it was observed by Khare and co-workers (Khare et al., 2015) that O₂, CO₂, Ar and N₂ cold plasma treatments enhance significantly the electrodes conductivities. More specifically, CO₂ and O₂ plasma-treated multilayer graphene (MLG) exhibited enhanced field emission behaviour, characterized by a low turn-on field and high emission current density compared to untreated MLG electrodes. This increase in current density was attributed to the generation of border defects in MLG flakes caused by the plasma treatment.

Furthermore, a study conducted by Kanaan et al. (Kannan et al., 2016b) investigated the effects of cold reactive plasma treatments, using O₂ and CO₂ discharges, on MLG electrodes, and they suggested that during plasma treatment, the MLG layers were peeled off, leading to exfoliation and the formation of very thin graphene flakes with numerous edge sites and defects, which facilitated the acceleration of the electrochemical redox reaction. It is also mentioned by Moura and colleagues (de Moraes Moura et al., 2021) that O₂ and CO₂ discharges induced not only the formation of edge defects but also a significant increase in the electroactive area, leading to a decrease in the resistance to charge transfer (R_{ct}) of the electrodes.

The stability of all electrodes was also checked through 50 consecutive cycles (Figure 24). More stable measurements were observed at both plasma-treated surfaces with relative standard deviations (RSD) below 1.0% for both peak potentials and peak currents, respectively. RSD values of around 5% were observed for the untreated GS electrode.

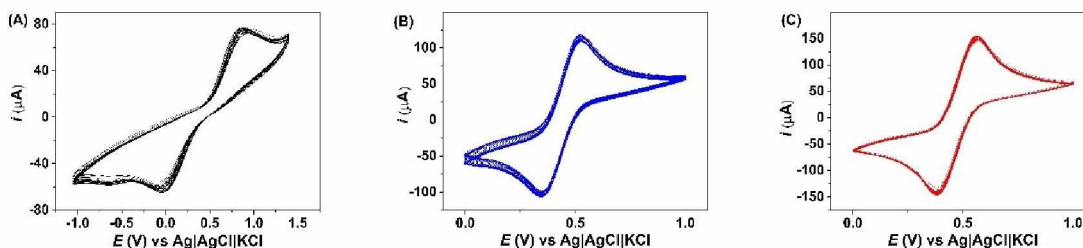


Figure 24. 50 consecutive cyclic voltammograms for GS (A), CO₂-GS (B) and O₂-GS (C). Scan rate of 50 mV s⁻¹ and step potential of 5 mV. Solution composition in all experiments: 0.1 mmol L⁻¹ [Fe(CN)₆]^{3-/4-} in 0.1 mol L⁻¹ KCl.

In light of the above insights, the O₂ plasma-treated GS electrode can be successfully applied in electroanalysis due to its improved properties. Thereby, this electrochemical sensor was evaluated for detection of MDMA in human saliva and seized samples, which application has a great interest in forensic and health-related (monitoring) analysis. In this case, the treatment with oxygen cold plasma treatment presented a slightly higher current for MDMA oxidation processes than carbon dioxide plasma.

Likewise, the CO₂ plasma-treated GS electrode presented higher currents towards the determination of chloramphenicol, ciprofloxacin and sulphamylamide, thus it was evaluated for detection of these antibiotics in tap water and in synthetic urine. Both features are presented in the next chapters.

CHAPTER 4 – PYROLYTIC GRAPHITE SHEET: MDMA DETECTION

OXYGEN PLASMA-TREATED GRAPHITE SHEET ELECTRODES: A SENSITIVE AND DISPOSABLE PLATFORM FOR METHAMPHETAMINES.

This chapter contains an adaption of the published article named: “Oxygen plasma-treated graphite sheet electrodes: a sensitive and disposable platform for methamphetamines” Jian F. S. Pereira, Larissa M. A. Melo, Luciano C. Arantes, Pedro H. S. Borges, Lucas V. Faria, Kelly F. da Cunha, Karla A. O. Souza, William O. Soté, Jose Luiz Costa, Edson Nossol, Rogério V. Gelamo, Eduardo M. Richter, Moacyr C. Jr, Wallans T. P. dos Santos, Osmando F. Lopes, Rodrigo A. A. Muñoz.

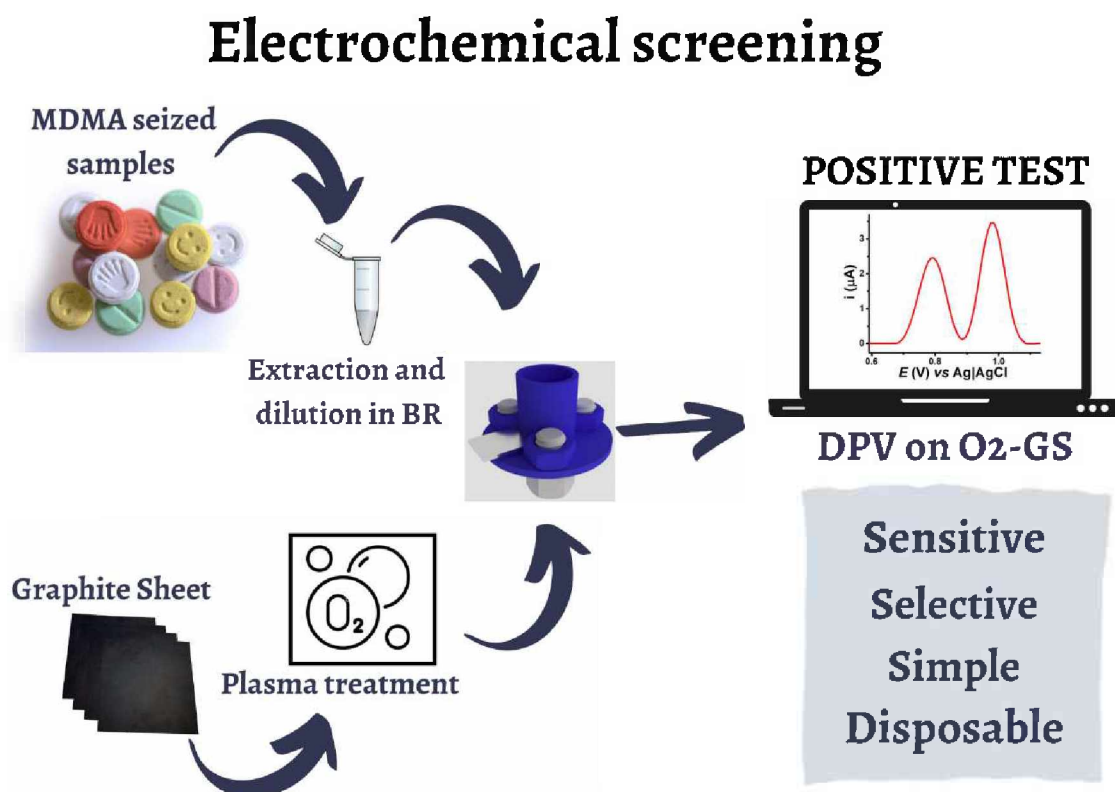


Figure 25. Graphical abstract CHAPTER 4

1. Introduction

Drugs of abuse can be defined as chemical substances for recreational use such as amphetamine-type stimulants, phenethylamine derivatives, synthetic cannabinoids, and synthetic cathinones. Some of these drugs are named as new psychoactive substances (NPS), which term is defined by the United Nations Office on Drugs and Crime (UNODC) for substances of abuse not reported by the Single Convention on Narcotic Drugs, 1961 or by the Convention on Psychotropic Substances, 1971 (UNODOC, 2021).

3,4-methylenedioxymethamphetamine (MDMA) (Figure 26) is an illicit drug also known as “ecstasy”. Although MDMA is not considered an NPS, it is one of the most consumed recreational amphetamines around the world over recent years, especially by young people due to its effects such as euphoria, elevated self-confidence, and heightened sensory awareness (Downing, 1986). However, the indiscriminate abuse of MDMA can lead to sleep disorder, depressed mood, the elevation of anxiety, hostility, impulsiveness, and lack of memory (Morgan, 2000), which may pose a self and public health threat and security issues. On the other hand, some countries like Canada recently authorized limited medicinal use of MDMA (Chénard, 2022). Thereby, monitoring, surveillance and control of MDMA in biological fluids and seized street samples are of great importance for the forensic and health services.

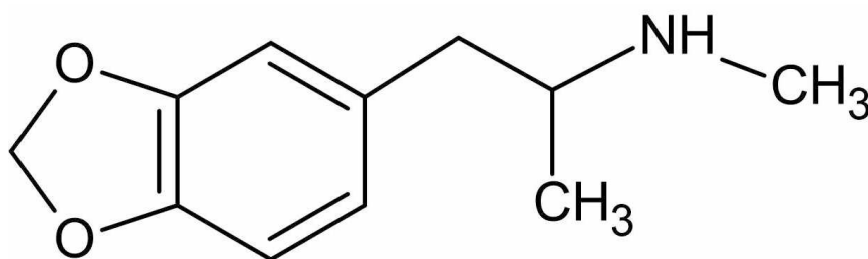


Figure 26. Chemical structure of MDMA.

Several methods have been reported to detect MDMA, such as high-performance liquid chromatography (HPLC) (Concheiro et al., 2005; Tomita et al., 2007) and gas chromatography-mass spectrometry (GC-MS) (Pichini et al., 2003). Although GC-MS and LC-MS are robust and definitive methods for forensic analyses, these are relatively complex, laborious, and high-cost methods for application in preliminary identifications (screening) of MDMA, which is also a crucial step in forensic investigations. The preliminary identification of MDMA in forensic analysis is based on traditional colorimetric methods, such as Marquis and Simon's test (United Nations, 2006). Nevertheless, due to a large number of NPS and adulterants found in seized samples

containing MDMA (Drugs Data, 2022), these colorimetric methods suffer from a lack of specificity and can offer false-negative and false-positive results (Bulcão et al., 2012). Therefore, a more sensitive and selective screening method for MDMA detection in both seized and biological samples, such as human saliva, is required.

In this sense, electroanalysis has emerged as a rapid, low-cost, and effective approach for application in screening tests in forensic analysis (Lima et al., 2020; Pimentel et al., 2021; R. G. Rocha et al., 2021). Among these works, several electroanalytical methods are reported for MDMA detection using different working electrodes (WE) such as bare (or modified) glassy carbon (Cumba et al., 2016; Garrido et al., 2010; Tadini et al., 2014; Zhang et al., 2021), boron-doped diamond (Cumba et al., 2016; Teófilo et al., 2020), carbon paste (Katayama et al., 2020), screen-printed electrodes (Couto et al., 2019; Cumba et al., 2016; Murilo Alves et al., 2021) and 3D-printed electrodes (de Faria et al., 2022).

Although these reported carbon electrodes have been successfully applied for MDMA detection, a simpler, lower-cost, and more stable electrochemical sensor can be even more attractive for an application in routine forensic analysis. Moreover, the reported electrochemical sensors present a low sensitivity for MDMA detection in biological samples. In this context, graphite sheets (GS) have attracted attention because of their characteristics which include flexibility, high conductivity, lightweight, and inexpensiveness.

Herein we present the use of the cold oxygen-plasma treatment on the GS surface for the electrochemical screening of MDMA in seized forensic samples and in human saliva using the differential pulse voltammetry (DPV) technique. Computational simulations using molecular dynamics enabled to investigate the interaction between MDMA molecules and the electrode surface (untreated or plasma-treated surface), which would confirm the enhanced sensing properties provided by the oxygen cold-plasma surface treatment. Moreover, we evaluate the selectivity of the proposed sensor in the presence of amphetamine-type stimulants, phenylethylamine derivatives, synthetic cathinones, as well as other illicit drugs and adulterants that are commonly found in ecstasy-like tablets. Importantly, the proposed sensor was evaluated for the analysis of “real-world” oral fluid samples collected in parties and electronic music festivals, which demonstrates, for the first time, the application of a disposable electrochemical sensing device in real scenarios.

2. Experimental

2.1. Reagents, samples and materials

A graphite sheet (GS) of 0.07 mm thickness (115 x 180 x 0.07 mm), electric resistance of 2.5 Ω , and electric conductivity of 55.6 $S\text{ cm}^{-1}$ was acquired from Panasonic (Mansfield, Texas, USA). The positioning procedure of the working electrode (1 x 1 cm) is shown in a video available in a previous work from our research group (Silva et al., 2018). Each GS sheet costs \$ 17.38 and can generate 180 electrodes, therefore, the cost of each electrode is around \$ 0.09. All solutions were prepared using ultrapure water (resistivity $\geq 18\text{ M}\Omega\text{ cm}$) obtained from a purification system Millipore Direct-Q3 (Bedford, USA). Acetic (99.7%) and phosphoric (85.0%) acids were obtained from Vetec (Rio de Janeiro, Brazil); while boric acid was acquired from AppliChem Panreac (Barcelona, Spain). Sodium hydroxide (97.0%) from Dinamica (Diadema, Brazil). Argon (99.99% pure), and O_2 (99.99%) were purchased from White Martins Co.

The analytical standard of MDMA and several candidates as interfering species, such as amphetamine-type stimulants (amphetamine (A), methamphetamine (MA), 3,4-methylenedioxyamphetamine (MDA), and 3,4-methylenedioxy-N-ethylamphetamine (MDEA)), phenethylamine derivatives (25B-NBOMe and 2C-B), synthetic cathinones (ethylone (ETH), ephylone (EPH) and dibutylone (DIB)), synthetic cannabinoid (AB-FUBINACA), and other illicit drugs (LSD, cocaine, and ketamine) were donated by the UNODC.

For electrochemical measurements, Britton-Robinson (BR) buffer (0.12 mol L^{-1} , pH 2.0 to 10.0) solutions were used as the supporting electrolyte. These BR solutions are composed of a mixture of boric, acetic, and phosphoric acids (0.04 mol L^{-1} of each), where the pH values were adjusted with 2.0 mol L^{-1} sodium hydroxide. A stock solution of 10 mmol L^{-1} MDMA was prepared after dissolution in methanol and stored in the refrigerator (4°C). Before electrochemical studies, the stock solution was diluted in an appropriate supporting electrolyte.

A sample of seized tablet was provided by the Federal District Police (Polícia Civil do Distrito Federal, PCDF), Brazil, where the presence of MDMA was previously confirmed by gas chromatography-mass spectrometry (GC-MS) analysis. The seized sample preparation involved a simple extraction step, as recommended by the Instituto de

Criminalística of the PCDF, Brazil. In short, the tablet (around 100 mg) was triturated, homogenized, and transferred to a microcentrifuge tube, where 1 mL methanol was added followed by a sonication process for 10 min in the ultrasonic bath. Subsequently, an amount of this extract was 1000-fold diluted in electrolyte supporting for MDMA detection by the proposed electrochemical method.

Authentic oral fluid samples were collected in parties and electronic music festivals in Brazil using Quantisal™ oral fluid collection devices and in accordance with the ethical standards of the University of Campinas committee (CAAE 88770318.0.0000.5404). Copies of the informed consent form were available to volunteers at all events. The presence of MDMA in these oral fluid samples was analyzed and confirmed using a validated method to detect 104 new psychoactive substances and other drugs of abuse by Nexera UHPLC chromatographic system coupled to a LCMS8060 triple quadrupole mass spectrometer (Shimadzu, Kyoto, Japan) (da Cunha et al., 2021, 2020), while the MDMA and their analogues (MDEA and MDA) quantification were performed using a validated method using a dispersive liquid-liquid microextraction and analyzed by the same LC-MS/MS system (Kahl et al., 2021).

2.2. Electrode surface treatment

The GS was cut into 3 cm diameter round discs and subjected to cold plasma discharges using mixtures of argon and O₂ controlled by needle valves at 350 and 100 mTorr, respectively for 2 min. The plasma-enhanced chemical vapor deposition (PECVD) system (Figure 2) herein applied is assisted by microwaves at a frequency of 2.42 GHz through a 1000 W magnetron (LG Co.), which has been described in details previously (Kannan et al., 2016a).

2.3. Computational Simulations

2.3.1. Parameterization

The initial structure and molecular mechanics parameters for MDMA were obtained using the automatic OPLS/CM1A parameter generator for organic ligands webserver (Dodda et al., 2017a), assigning localized bond-charge corrected CM1A charges for all atoms (Dodda et al., 2017b), consistent to its protonation state at pH 10. The graphitic surfaces were built using the graphene builder tool available on the PolyParGen (YABE et al., 2019) webserver, in which a 65.7x57.6 Å graphene sheet was modelled, corresponding to a 27x27 hexagonal lattice. A pristine graphene sheet was

chosen to represent the untreated surface due to its simplicity. The functionalization was achieved by randomly distributing epoxy bridges and carboxyl groups throughout the surface in a ratio of 1:2, respectively, resulting in 30 epoxy bridges and 60 carboxyl groups (Figure 27). Partial atomic charges were calculated with NWChem (Valiev et al., 2010) using B3LYP (Becke, 1993; Lee et al., 1988) functional with 6-31G (Hehre et al., 1972) basis set, and the remaining molecular mechanics parameters were obtained using the OPLS/CM1A parameter webserver.

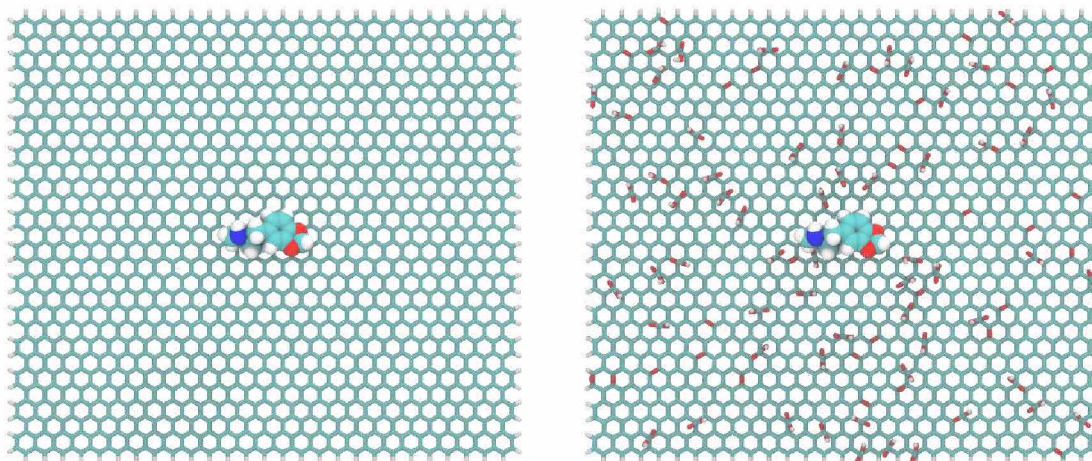


Figure 27. Top view from the modelled systems. From left to right: pristine graphene and graphene oxide. Surfaces and MDMA are shown in licorice and vdW representations, respectively.

2.3.2. Systems Modelling

The initial system configuration was generated using the software PACKMOL (Martínez et al., 2009), with identical parameters applied to both surfaces. It consisted of fixing the center of mass of the surface to the center of the simulation box while placing one MDMA molecule at distance of 5.0 Å from the surface in the z axis in order minimize a position bias relative to its coordinates. A tolerance threshold of 5.0 Å was used to guarantee no superposition occurred between the MDMA and the surface functions. Both systems are shown in Figure S1.

2.3.3. Molecular Dynamics Simulations

All molecular dynamics simulations were carried out using GROMACS (Abraham et al., 2015) package 2019.2 and the OPLS all-atom (Jorgensen et al., 1996) force field. Initially both systems were centered inside a cuboid simulation box, at 10 Å

from its nearest wall, resulting in a total box size of 77.5 x 69.7 x 90.0 Å. The boxes were filled with Three Site Transferrable Intermolecular Potential (Jorgensen et al., 1983) (TIP3P) water model molecules, corresponding to the insertion of 15,330 and 15,239 molecules for the pristine graphene and graphene oxide systems, respectively. To improve the initial systems configurations, in terms of solvent orientation and reducing any steric superposition between models, a steepest descent algorithm was used to find a local energy minimum with a convergence criterion of maximum force smaller than 100 kJ mol⁻¹ Å⁻¹.

Following energy minimization, the systems were simulated in an isochoric-isothermal ensemble (constant NVT), using an annealing treatment to equilibrate temperature. Temperature values were linearly increased from 0 to 298 K for 600 ps, followed by 100 ps at 298 K, both with a time step for integration of 0.002 ps. The velocity rescaling coupling method (Bussi et al., 2007) with a coupling time constant of 0.1 ps was used to manage temperature values. After thermal equilibration, the systems were simulated in an isobaric-isothermal ensemble (constant NPT) during 1,000 ps to achieve proper mass density, using a time step for integration of 0.001 ps. Pressure value was set to 1.0 bar and isotropically coupled using the Parrinello-Rahman method (Nosé and Klein, 1983; Parrinello and Rahman, 1981) with a coupling time constant of 2.0 ps and compressibility of 4.5×10⁻⁵ bar⁻¹. To allow an adequate adjustment of the solvent molecules around the systems, both MDMA and the surfaces were positionally restrained with a force constant of 10 kJ mol⁻¹ Å⁻¹ during thermodynamic equilibrations.

Once properly equilibrated, the molecular events associated with the interactions between MDMA and the surfaces were also sampled in an isobaric-isothermal ensemble (constant NPT) using the same parameters as before, except for a simulation time of 20 ns, time step for integration of 0.002 ps and partially removed position restraints. Notably, no restraints were applied to the MDMA molecule, epoxy bridges or carbonyl groups, while the carbon atoms of the surface remained under restraints, representing the rigidity of an electrode surface. Coordinate and energy values from the final sampling were recorded at 1-ps intervals. Bonds with hydrogen atoms were simulated as rigid constrains using the parallel linear constrain solver algorithm (Hess, 2008) (P-LINCS). A cut-off at 10 Å was used for both short-range Coulomb and Lennard-Jones interactions. Long-range electrostatics were computed using the fast smooth Particle-Mesh Ewald method (Essmann et al., 1995) with cubic interpolation and Fourier spacing of 1.6 Å. In addition,

long-range dispersion corrections were applied for both energy and pressure to account for the repulse term of the Lennard-Jones expression. Periodic boundary conditions were used in all directions and a leap-frog algorithm was used to integrate the equations of motion. Analyses were done with GROMACS and VMD software (Humphrey et al., 1996). Computational details regarding the modelling and simulation steps are provided in the Supplementary material.

3. Results and discussion

3.1. Electrochemical behaviour of MDMA on GS electrodes

Firstly, the electrochemical performance of both treated and untreated GS electrodes for the detection of 0.5 mmol L^{-1} MDMA in 0.12 mol L^{-1} BR buffer (pH 10.0) solution was compared using CV, as shown in Figure 28. This media was chosen based on a previous work that reported this electrolyte condition to result in the highest analytical response for MDMA using carbon electrodes (Teófilo et al., 2020).

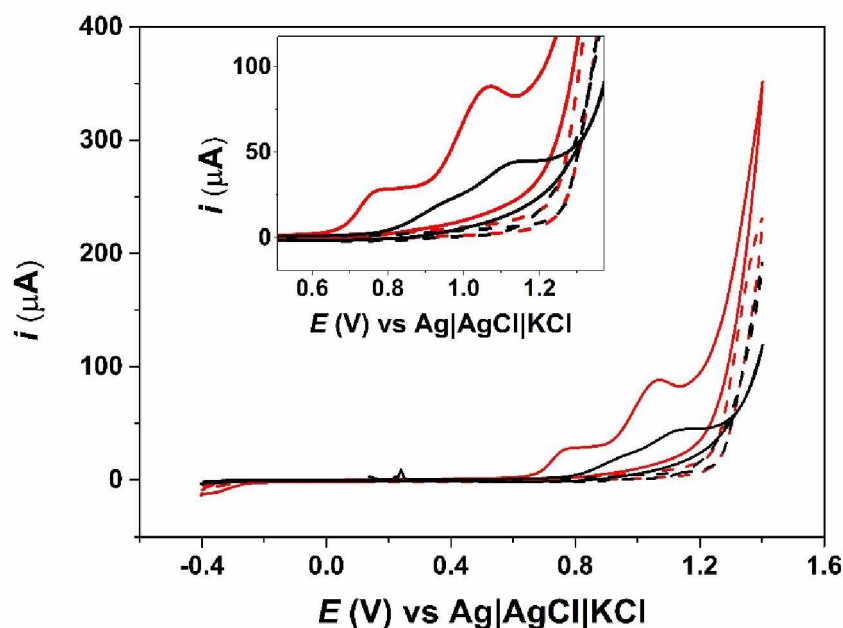


Figure 28. CVs recorded in solutions containing 0.8 mmol L^{-1} MDMA and 0.12 mol L^{-1} BR buffer (pH 10.0) at bare (black-line) and O_2 plasma treated (red-line) GS surfaces. Scan rate of 50 mV s^{-1} with 5 mV step potential.

Figure 28 shows two irreversible oxidation processes between $+0.7$ and $+1.2 \text{ V}$ (vs. Ag/AgCl), at both electrodes. However, well-defined peaks with higher peak currents were obtained on the O_2 plasma-treated GS (red line) when compared with the untreated

one (black line). MDMA electrochemical behaviour on GS surface is in accordance with other electrochemical sensors reported for the detection of this drug such as boron-doped diamond electrode (Teófilo et al., 2020) and glassy carbon electrode (Garrido et al., 2010). These works proposed that the first oxidation process (Ox_1) is related to the removal of one electron from the aromatic ring and the subsequent formation of a cationic radical, while the second process (Ox_2) is associated with the oxidation of a new species formed by dimerization of the initial radical cation.

Next, the influence of pH on the electrochemical response of the GS electrodes using MDMA as the probe (0.8 mmol L^{-1}) was properly evaluated using 0.12 mol L^{-1} BR buffer with pH values ranging from 2.0 to 12.0 (Figure 29). According to Figure 29, only at pH 10 and 12 two oxidation peaks are apparent in the selected potential window, and this feature could present a useful tool to identify MDMA in the presence of other similar methamphetamines. Although higher currents are shown in pH 12, this extreme alkaline condition causes the anticipation of the electrolyte/electrode degradation (see magenta dotted line), which may interfere in the analysis and in the electrode stability. Therefore, pH 10 was selected to further experiments. This pH was also selected as the best electrolyte medium for MDMA detection in another work (Teófilo et al., 2020).

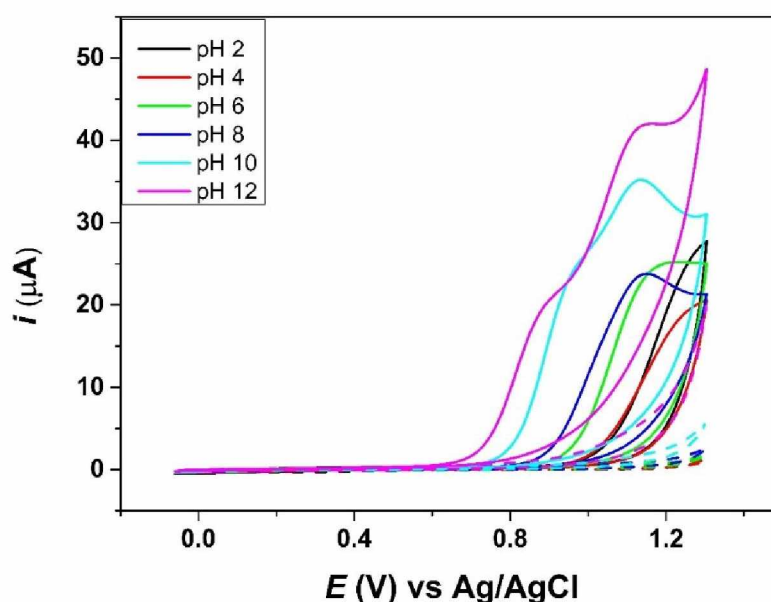
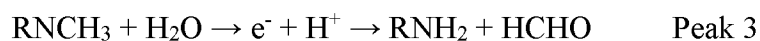
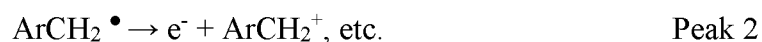


Figure 29. CVs profiles of O_2 -GS electrode in 0.5 mmol L^{-1} MDMA in the function of pH (2.0 to 12.0) using 0.12 mol L^{-1} BR buffer. Scan rate of 50 mV s^{-1} with 5 mV step potential.

This result is in agreement with Garrido and co-workers (Garrido et al., 2010) that observed three pH-dependent oxidation peaks for MDMA related to (1) the oxidation on the aromatic nucleus of the molecule leading to the formation of a cation radical (O1), (2) the oxidation of the species formed by the dimerization of the previous cation (O2), and (3) the oxidation of the secondary amine that is presented in more alkaline media. The proposed mechanism for MDMA oxidation is mentioned in the equations below.



Where Ar is the aromatic nucleus of the molecule (Garrido et al., 2010).

3.2. MDMA detection using O₂-GS electrode by DPV

Although square wave voltammetry (SWV) enables faster analysis than other voltammetric techniques, DPV was used for MDMA detection at the GS electrode because it provided measurements with better resolution (well-defined peaks) than the SWV. The instrumental parameters of the DPV technique were optimized for sensitive and selective detection of MDMA. Under selected conditions (step potential: 9 mV, modulation amplitude: 100 mV, and modulation time: 10 ms), the calibration curves were constructed using increasing concentrations of MDMA between 0.5 and 70 $\mu\text{mol L}^{-1}$ on GS and O₂-GS electrodes, as shown in Figures 30A and 30B, respectively.

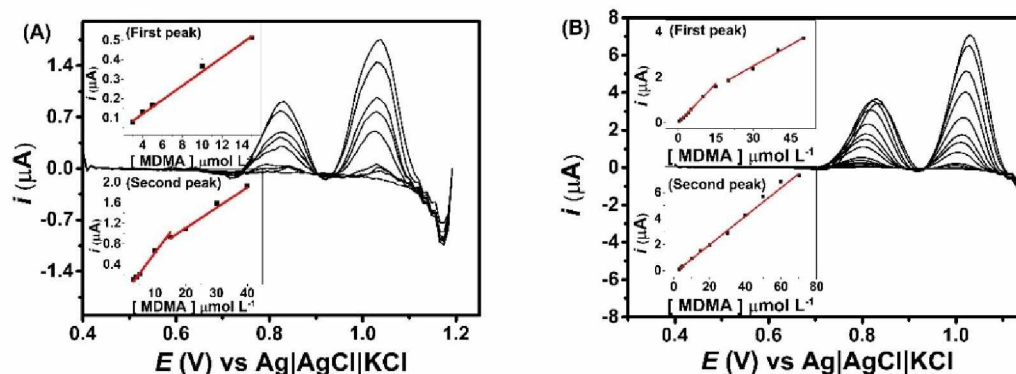


Figure 30. Baseline-corrected DPV responses registered for concentrations of MDMA (0.5 to $70 \mu\text{mol L}^{-1}$) in 0.12 mol L^{-1} BR (pH 10.0) using (A) GS and (B) O_2 -GS electrodes. The insets of figures correspond to the respective linear regression plots. DPV conditions: 9 mV step potential, 100 mV modulation amplitude, 10 ms modulation time.

As can be seen in Figure 30, both GS electrodes (untreated and O_2 plasma treated) presented linear ranges for MDMA detection, which are different for each oxidation process (Ox_1 and Ox_2) of this analyte, as shown in Table 10. Furthermore, the obtained limits of detection (LOD) and quantification (LOQ) for MDMA detection using both GSs are presented in Table 10, which values were estimated according to the International Union of Pure and Applied Chemistry (IUPAC) (Mocak et al., 1997), as mentioned in chapter 2.

Table 10. Analytical parameters obtained for MDMA detection by DPV using GS and O_2 -GS electrodes.

Analytical parameters	Working electrodes			
	GS		O_2 -GS	
	Ox_1	Ox_2	Ox_1	Ox_2
Linear range / $\mu\text{mol L}^{-1}$	3.0 – 15.0	3.0 – 15.0	0.5 – 15.0	3.0 – 70.0
Slope / $\text{A L } \mu\text{mol}^{-1}$	3.64×10^{-8}	8.01×10^{-8}	1.14×10^{-7}	1.09×10^{-7}
r^2	0.996	0.988	0.998	0.998
LOD / $\mu\text{mol L}^{-1}$	0.78	0.35	0.09	0.09
LOQ / $\mu\text{mol L}^{-1}$	2.58	1.16	0.30	0.30

As can be verified in Table 10, good linear ranges were obtained for the two oxidation processes (Ox_1 and Ox_2) of MDMA at both GSs. On the untreated surface, there is two linear ranges observed for the second peak, and this behaviour is also observed on

the second peak when using the treated electrode. Nevertheless, the O₂-GS electrode is more sensitive with better detectability (LOD = 0.09 μmol L⁻¹) for MDMA than the untreated GS (LOD = 0.35 μmol L⁻¹). It is worth highlighting that the lowest measurable signal (0.5 μmol L⁻¹) obtained by O₂-GS is sufficiently low for the application of this sensor in forensic analysis (levels of MDMA usually found in saliva samples are between 9 and 35 μmol L⁻¹) (Pichini et al., 2003; Samyn et al., 2002). As expected, the best sensitivity of the O₂-GS electrode for MDMA detection is due to its higher defect density in the carbon structures, oxygen groups, and roughness than the untreated GS electrode. Thereby, the O₂-GS electrode can offer greater exposure of active sites, allowing a faster electron transfer rate, as shown in the previous electrochemical characterizations.

The stability of the electrochemical response for MDMA (3.5 μmol L⁻¹) oxidation using the same O₂-GS electrode was evaluated after consecutive measurements (n = 20) by the DPV technique (Figure 31). Relative standard deviation (RSD) values lower than 3.83% and 0.12% were obtained for both peak currents and peak potentials of O_{x1} and O_{x2}, respectively. In addition, the inter-electrode precision (different electrodes, n = 3) was also appropriately investigated (Figure 32), where RSD values smaller than 3.16% and 0.23% were also achieved for peak currents and peak potentials, respectively.

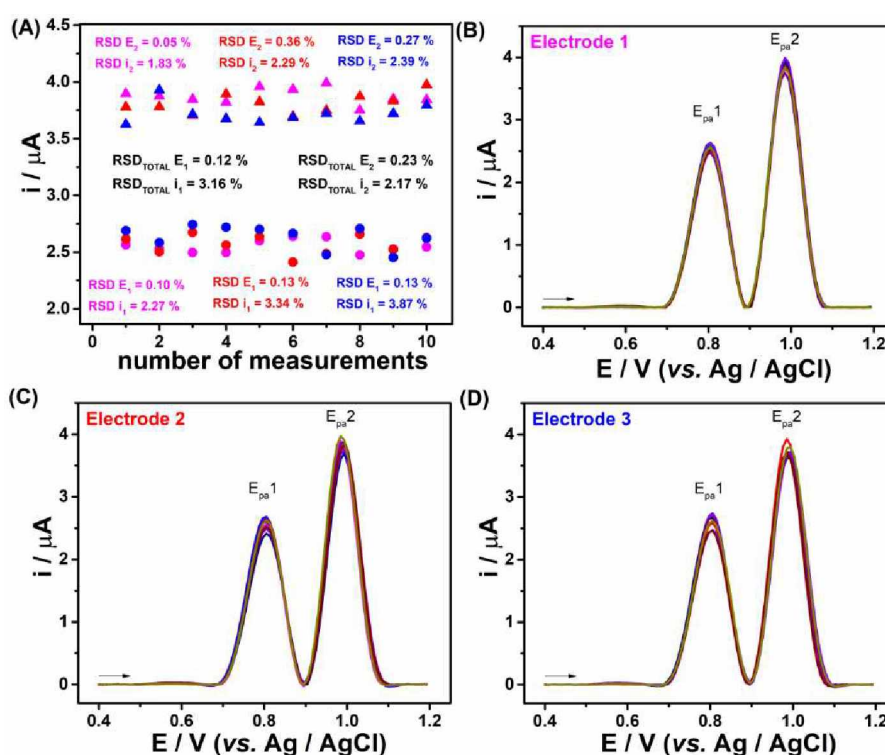


Figure 31. DPVs recorded for 3.5 μmol L⁻¹ MDMA in BR buffer solution 0.1 mol L⁻¹ pH 10.0 on O₂-GS. DPV conditions: 9 mV step potential, 100 mV modulation amplitude, 10 ms modulation time.

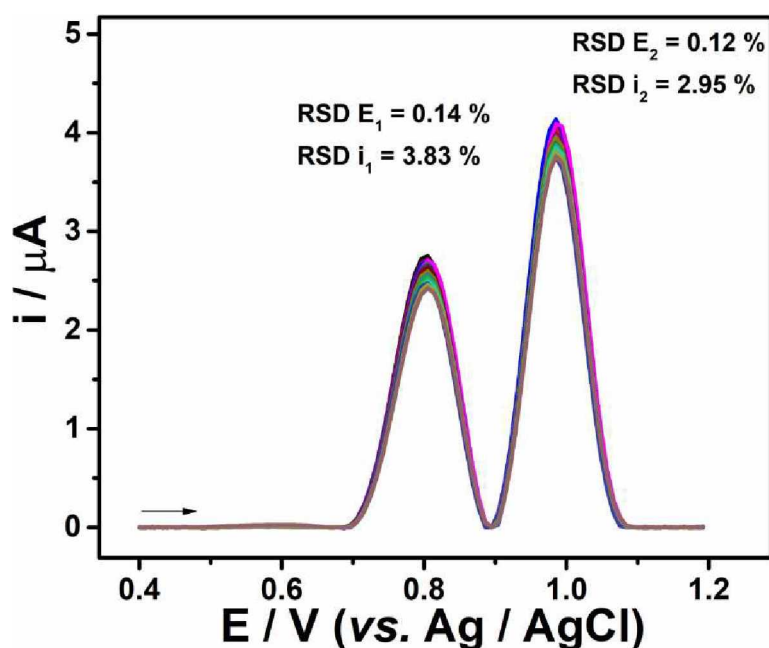


Figure 32 Comparison between peak current vs the number of measurements for three different O₂-GS electrodes (n = 3), where ▲ is i_{pa1} and ● is i_{pa2} (A), voltammograms for O₂-GS electrodes 1 (B), 2 (C) and 3 (D), for MDMA 3.5 $\mu\text{mol L}^{-1}$ in BR buffer solution 0.1 mol L⁻¹ pH 10.0. DPV conditions: 9 mV step potential, 100 mV modulation amplitude, 10 ms modulation time.

Additionally, experiments were carried out intended to evaluate the fouling effect on the electrodes surface. Sequential voltammograms for 10, 30, 60, 100, 250, 500 and 1000 $\mu\text{mol L}^{-1}$ were recorded, and after measuring the higher concentration, the sequence started again, and these procedures were performed 5 times. Figure 33 shows the variation of the peak current (second oxidation peak only) obtained from these experiments including the respective error bars. The results for 500 and 1000 $\mu\text{mol L}^{-1}$ did not presented measurable and distinguished peaks, which was expected considering that such high concentrations are not within the linear range; therefore, they are not represented there. It is possible to notice that up to 100 $\mu\text{mol L}^{-1}$ there is no evident electrode fouling and carryover effects. The RSD values were below 14%, with no clear decrease in concentration from the first to the last measure. These results demonstrate that the electrochemical response for the oxidation processes on the O₂-GS electrode is repeatable, reproducible and there is no fouling effect of the electrodes surface, thus, conferring a good reliability for preliminary identification of MDMA in forensic analysis by the proposed method.

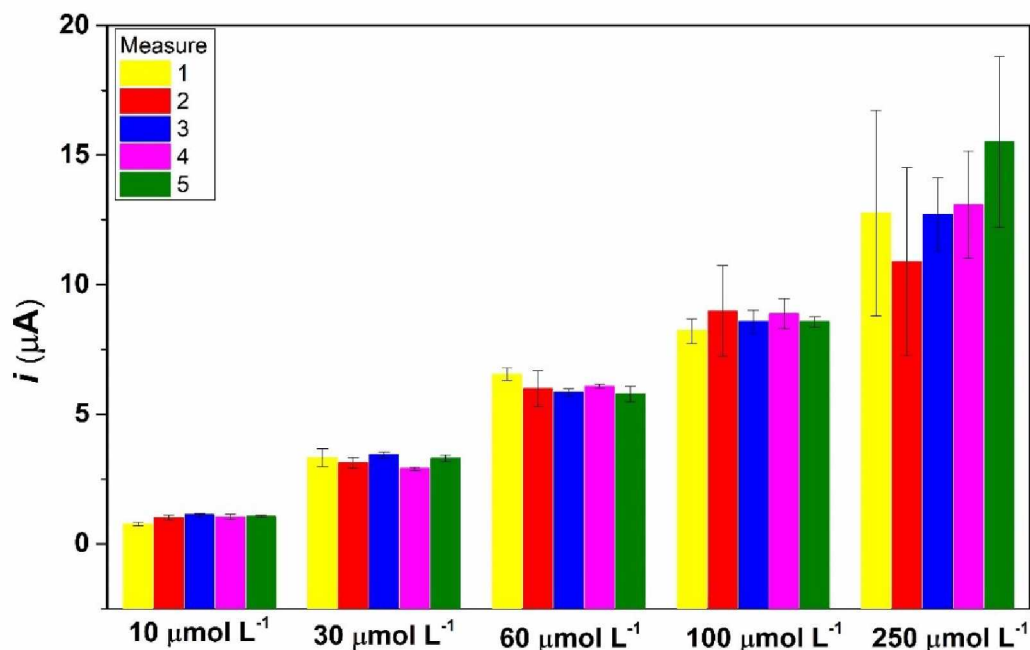


Figure 33. Peak currents (second oxidation peak only) obtained from sequential voltammograms for 10, 30, 60, 100 and 250 $\mu\text{mol L}^{-1}$ of MDMA in 0.12 mol L^{-1} BR (pH 10.0) ($n=5$) using O_2 -GS electrode. DPV conditions: 9 mV step potential, 100 mV modulation amplitude, 10 ms modulation time.

3.3. Molecular Dynamics simulations of MDMA and the graphitic surfaces

To investigate and understand the possible factors contributing to the enhanced interactivity observed between MDMA and the presented graphitic surfaces, classical Molecular Dynamics simulations were used to sample their interactions. The obtained trajectories of the complexes formed between the analyte and surfaces were assessed in terms of non-covalent interaction energy, distance, number of contacts, and volumetric maps.

The calculated non-covalent interaction energy is the sum of short-range Lennard-Jones and Coulomb potentials, defined as:

$$V_{\text{non-covalent}} = V_{\text{Lennard-Jones}} + V_{\text{Coulomb}} \quad (1)$$

$$V_{\text{Lennard-Jones}} = 4\epsilon_{ij} \left[\left(\frac{\sigma_{ij}}{r_{ij}} \right)^{12} - \left(\frac{\sigma_{ij}}{r_{ij}} \right)^6 \right] \quad (2)$$

$$V_{Coulomb} = f \frac{q_i q_j}{\epsilon_r r_{ij}} \quad (3)$$

where ϵ_{ij} is the most negative interactive energy (kJ mol^{-1}) between ij ; σ_{ij} , the distance (\AA) between ij where their interaction energy is zero; r_{ij} , the distance (\AA) between ij ; f , the electric conversion factor ($\text{kJ mol}^{-1} \text{\AA} e^{-2}$); q_n , the partial atomic charge (e) of particle n ; and ϵ_r , the relative dielectric constant of the medium. The results are shown in Figure 34.

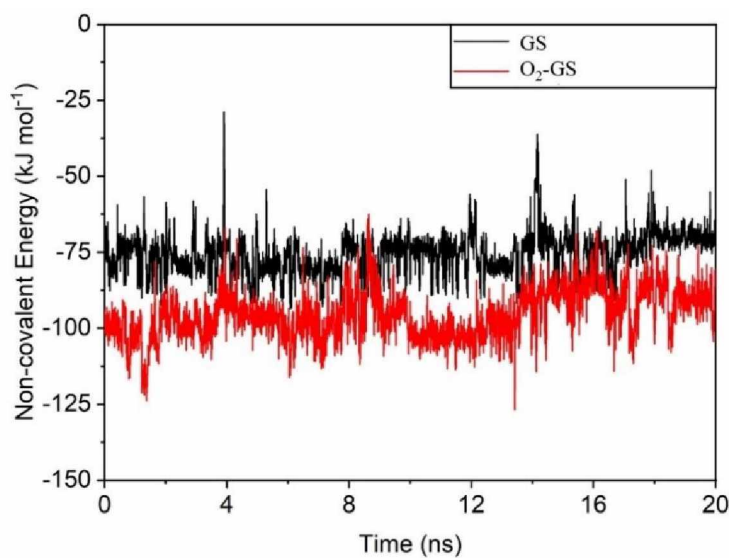


Figure 34. Non-covalent energies between MDMA and the graphitic surfaces.

The median \pm standard deviation (sd) values of the non-covalent interaction energy between MDMA and the graphitic surfaces were -74.93 ± 6.67 and -95.96 ± 8.09 kJ mol^{-1} for pristine GS and O_2 plasma treated GS, respectively, corresponding to a difference of 21.03 ± 10.49 kJ mol^{-1} . This means that there is a higher energy original from a non-covalent bond (where there is no chemical reaction) between the molecule and the treated surface, then between the molecule and the untreated GS. These results agree with the experimental evidence that the interaction of the analyte with the functionalized surface is energetically favourable when compared with the non-functionalized surface. To further examine the differences between the systems, Figure 35 illustrates the conformational states with the strongest interactions sampled during the simulation, corresponding to energy values of -93.80 and -126.78 kJ mol^{-1} for pristine graphene and graphene oxide, respectively.

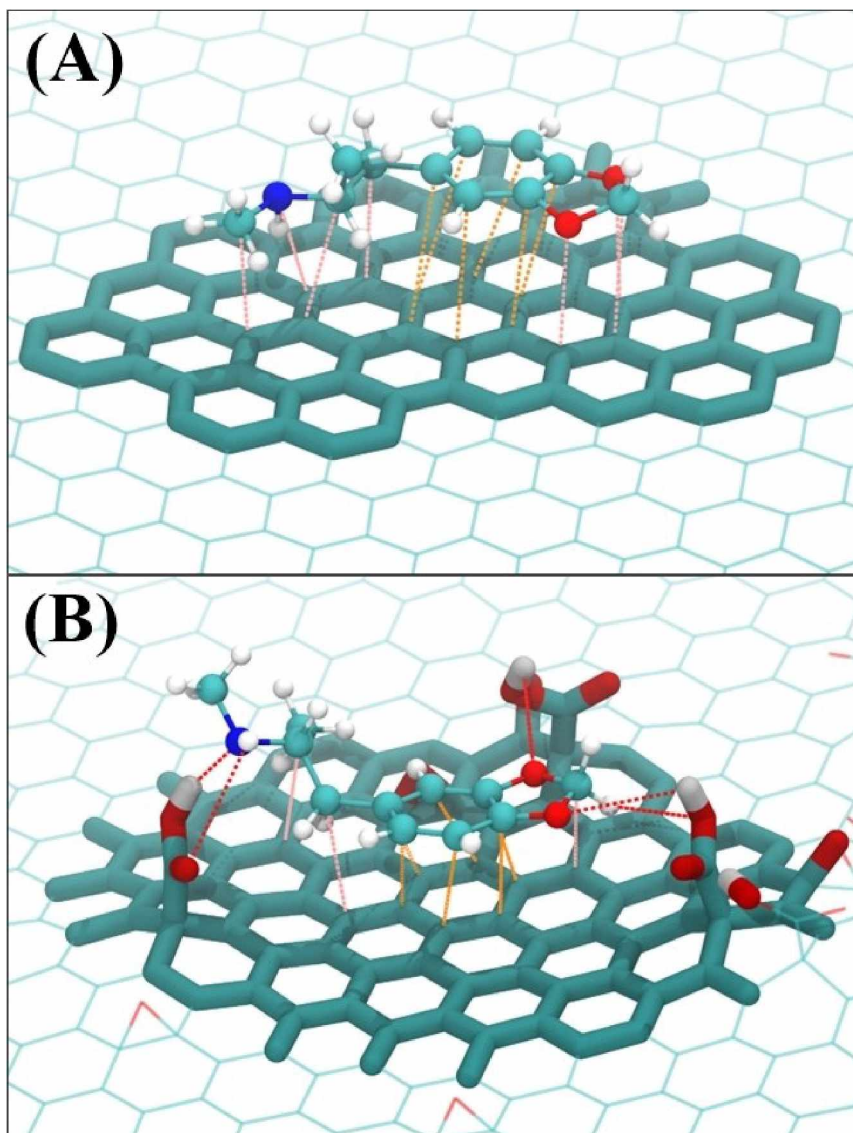


Figure 35. Most interactive conformational state between MDMA (ball and stick representation) and (A) GS and (B) O₂-GS. (licorice and lines representations).

Based on Figure 35, the results suggest the interactions could be the result of up to four types of intermolecular interactions. Both systems presented van der Waals interactions, possibly the dipole-induced dipole-type interactions (shown in pink) with interatomic distances ranging from approximately 3.25 to 3.80 Å, and parallel-displaced π-stacking interaction (shown in orange) with interatomic distances ranging from approximately 3.50 to 4.00 Å. Additionally, both should present slight electrostatic interactions resulted from partial atomic charges. Although in this context they have a less pronounced contribution compared to van der Waals interactions, they would still have a more prominent role on the functionalized surface due to the polar groups. Furthermore, the O₂-GS system presents hydrogen bonding-type interactions (shown in

red) with interatomic distances ranging from 1.88 to 3.49 Å. The sole existence of hydrogen bonding-type interactions could arguably be enough to justify the increase in non-covalent interaction energy between MDMA and the surface; however, it is reasonable to consider the strength of van der Waals interactions in O₂-GS system may also be influenced by the presence of epoxy bridges and carbonyl groups, which can directly impact the permanent and induced dipole moments of the carbon atoms involved in the interactions with MDMA.

To further characterize the interaction energy profiles, the number of contacts between MDMA and both surfaces were calculated. For this analysis, contacts were defined as any overlapping between van der Waals radii of atoms from different molecules within 6.0 Å of each other. All types of contacts were individually computed, regardless of polarity or whether multiple atoms from one molecule interacted with a single atom of another. The results are shown in Figure 36A. The average number of contacts between MDMA and the graphitic surfaces was 643 ± 66 for GS and 835 ± 61 for O₂-GS. This represents a difference of approximately 30% in the number of contacts, consistent with the previous result. Furthermore, when the conformational states of lowest number of contacts were compared, the difference was even more expressive.

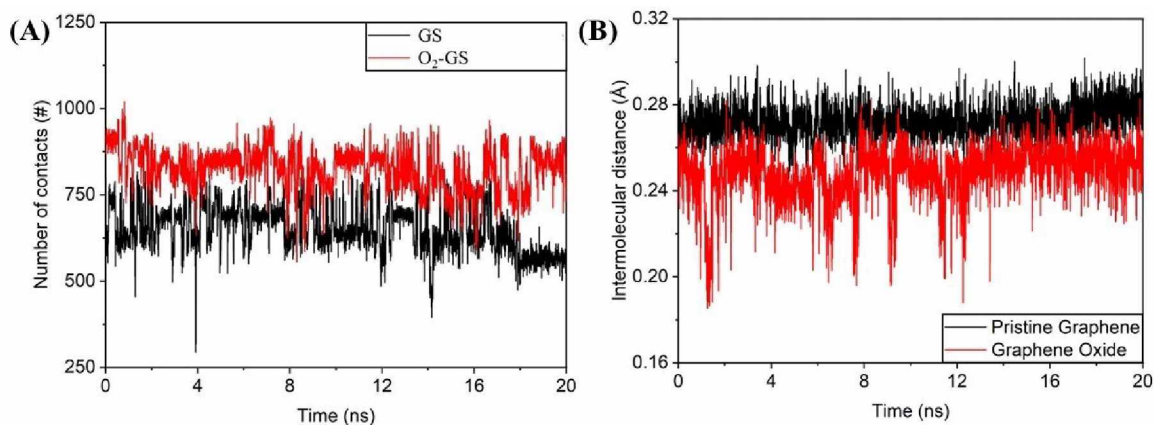


Figure 36. Number of contacts between MDMA and the graphitic surfaces (A) and Intermolecular distances between MDMA and the graphitic surfaces (B).

The untreated GS surfaces had 294 contacts, while the oxygen plasma treated surfaces had 554 contacts, representing a difference of about 88%. For the highest number of contacts, the values for GS and O₂-GS surfaces were 818 and 1019, respectively, corresponding to an increase of approximately 25%. Although the calculation does not

differentiate between types of contacts, the results suggest the increase in interactions with the functionalized surface were predominantly favourable rather than unfavourable.

Given the strong dependence of intermolecular interactions on distances, an analysis of intermolecular distances between analyte and surfaces was made. Minimum, median, and maximum intermolecular distances were calculated considering the closest atom of the surface to MDMA. Results are shown in Figure 36B and Table 11.

Table 11. Summary results of non-covalent energy, number of contacts, and intermolecular distance between MDMA and the respective simulated surfaces.

Non-covalent energy (kJ mol⁻¹)			
	Minimum	Average ± sd	Maximum
GS	-93.80	-74.93 ± 6.67	-28.91
O₂-GS	-126.78	-95.96 ± 8.09	-62.56
Number of contacts (#)			
	Minimum	Average ± sd	Maximum
GS	294	643 ± 66	818
O₂-GS	554	835 ± 61	1019
Intermolecular distance (Å)			
	Minimum	Average ± sd	Maximum
GS	2.39	2.72 ± 0.08	3.02
O₂-GS	1.85	2.50 ± 0.13	2.83

According to the results, MDMA remained at an interacting distance to the surface during the entire simulation, evidence indirectly confirmed by the previous results. However, the analyte remains closer to the O₂GS surface than to the pristine graphene surface, regardless of whether the minimum, median, and maximum intermolecular distances were considered. The median ± sd values of distances were 2.72 ± 0.08 and 2.50 ± 0.13 Å for GS and O₂GS surfaces, respectively. Interestingly, despite the similarity in standard deviation values, a notable difference was observed in the proximity of MDMA with the graphitic surfaces. While the intermolecular distance remained qualitatively

constant during the interaction with GS, there were multiple instances when the analyte interacted with O₂GS surface much closer than the average distance. This closer proximity associated with the surface functionalization strengthens noticed from the previous results, provides further support to suggest the presence of epoxy bridges and carbonyl groups improved the interactions between MDMA and the graphitic surface.

Finally, for the assessment of the interacting dynamics between MDMA and the surfaces, volumetric maps of their interactions were generated. In essence, these maps provide visual representations of spatial distributions, outlining the specific areas above the graphitic surfaces where MDMA interacted. The calculation averaged over all frames from the trajectory and the maps were created using weighted atomic density at each grid point with a resolution of 0.5 Å. Results are shown in Figure 37.

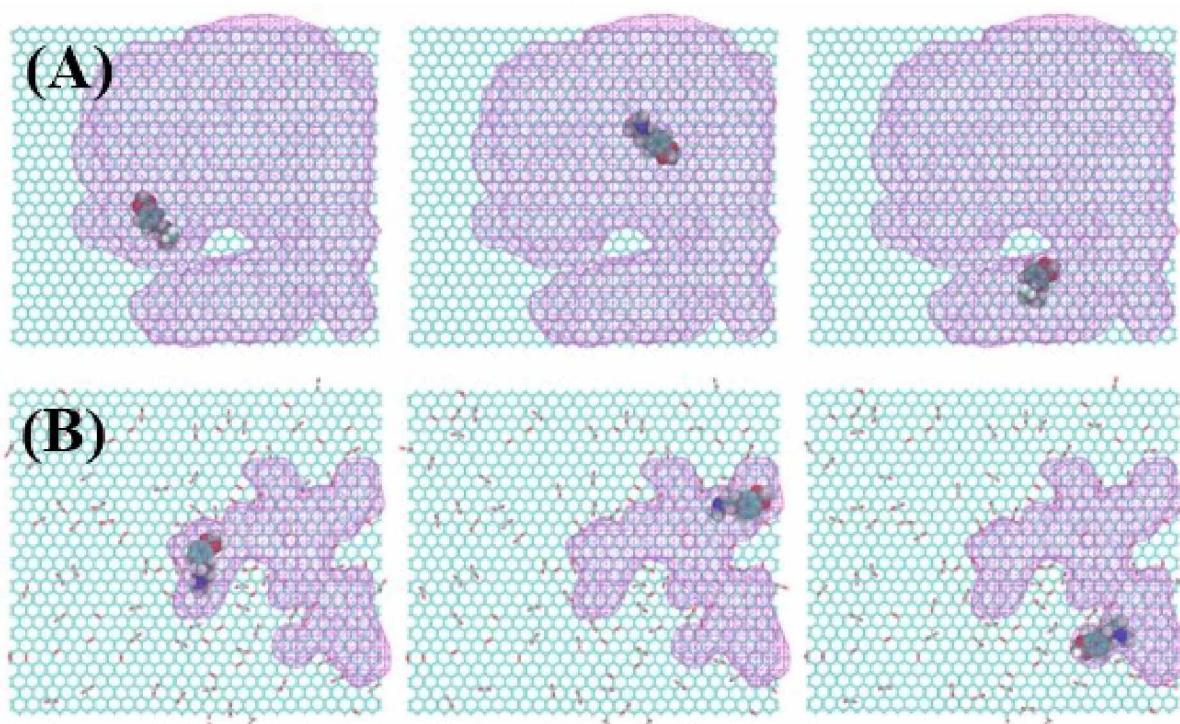


Figure 37. Volumetric maps shown in purple. Top and bottom rows correspond to different frames from the simulations with GS (A) and O₂-GS (B).

According to Figure 37, it is evident the presence of the functional groups narrowed the spatial region where MDMA interacted with the surface. The narrowing resembles the formation of a cage-like region delimited by polar groups. This confinement restricted the movement of the analyte and, more importantly, may have also facilitated more effect interactions with the surface. Although steric effects may contribute to this effect, when taken together, the correlated results of non-covalent

interaction energies, number of contacts, and intermolecular distances strongly suggest the primary factor was the formation of stronger interactions with the O₂-GS surface. Hence, providing substantial arguments to justify and elucidate a reasonable explanation for the observed enhanced interactivity of functionalized graphene surfaces when compared to non-functionalized.

3.4. Interference studies

MDMA is commonly found in the presence of other illicit drugs and adulterants, which are added either to potentialize the psychotropic effect or to reduce the production costs. In fact, according to the literature (Cunha et al., 2023; Drugsdata, 2022), amphetamine-type stimulants (A, MA, MDA, and MDEA), phenylethylamines (25B-NBOMe and 2C-B), synthetic cathinones (ETH, EPH, and DIB) and other illicit drugs (LSD, AB-FUBINACA, cocaine, and ketamine) have been frequently found in ecstasy-like tablets containing MDMA. Therefore, the electrochemical profiles of these substances (3.5 μmol L⁻¹) were investigated by the proposed method, as shown in Figure 38.

As can be seen in Figure 38A, among the amphetamine-type stimulants, only the MDEA (blue-line) can present interference due to their two oxidation processes are practically overlapped with the MDMA oxidation processes (red-line), which is expected, once the difference in the molecules is a methyl group. However, in this case, an ΔE-peak-based strategy could be used to differentiate between both molecules, since the ΔE-peak values for MDMA (0.189 V) and MDEA (0.206 V) are slightly distinct. It is worth mentioning that although the MDA oxidation peak (green line) is overlapping with the second MDMA oxidation peak, the MDMA can be identified in the presence of MDA due to the selectivity of its first oxidation process. As the other amphetamines, MA and A, are not electroactive at the potential range of +0.4 to +1.2 V using an O₂-GS electrode, these drugs are not interferents for MDMA detection by the proposed method.

The electrochemical responses of LSD and phenylethylamine derivatives are presented in Figure 38B. 2C-B (green-line) also exhibited two oxidation processes at the proposed sensor, but similarly to MDA, MDMA can be identified by its first oxidation process. LSD and the other phenylethylamine derivative (25B-NBOMe) are not electroactive at the O₂-GS electrode using the proposed conditions, indicating that MDMA can be easily detected in the presence of these substances.

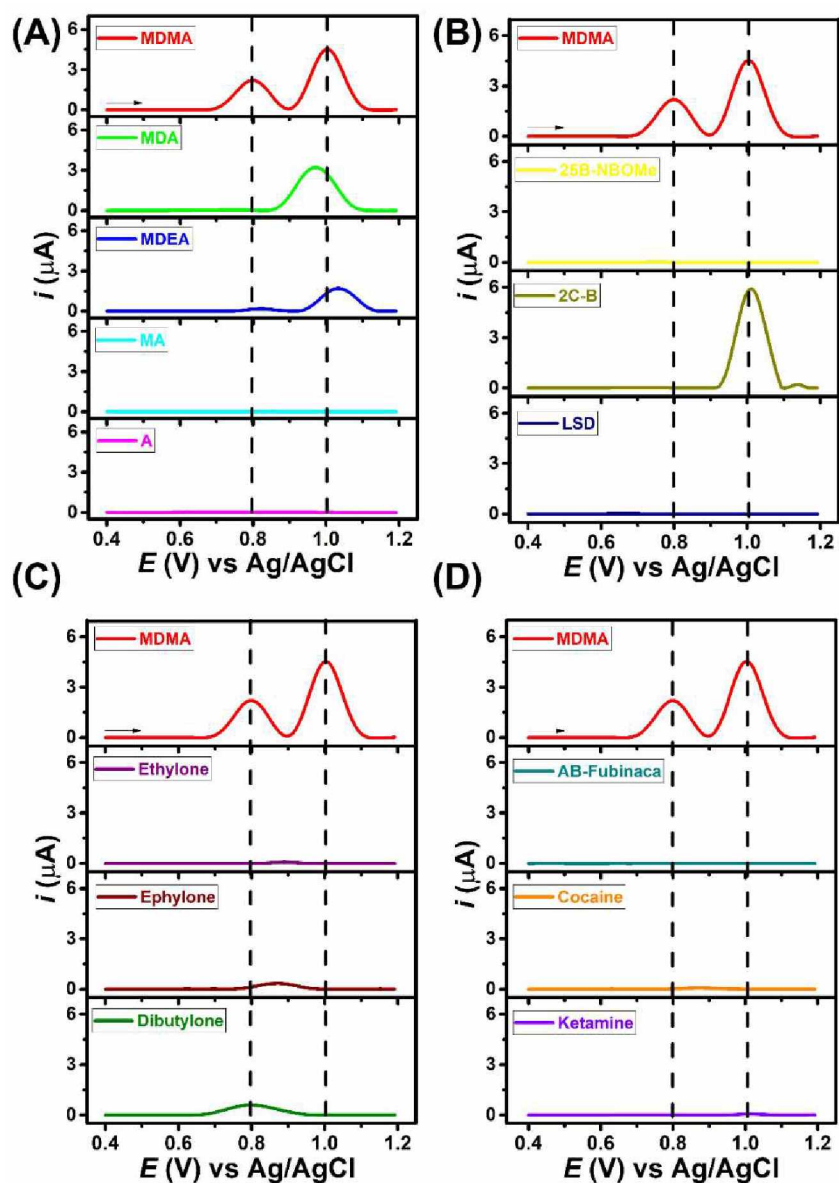


Figure 38. DPVs recorded for MDMA (red-line) and for (A) other amphetamines (MDA, MDEA, MA, and A), (B) phenylethylamines (25B-NBOMe and 2C-B), (C) synthetic cathinones (ethylone, ephylone, and dibutylone) and (D) other illicit drugs (LSD, AB-FUBINACA, cocaine, and ketamine). All molecules were analyzed using the same O₂-GS electrode at a concentration of 3.5 $\mu\text{mol L}^{-1}$ in 0.1 mol L⁻¹ BR buffer solution pH 10.0. DPV conditions: 9 mV step potential, 100 mV modulation amplitude, 10 ms modulation time.

All synthetic cathinones studied (Figure 38C) exhibited an oxidation process with different peak potentials at the O₂-GS electrode, at +0.889 V, +0.868 V, and +0.796 V for ethylone, ephylone, and dibutylone, respectively, with much lower peak currents than the MDMA. This difference in sensitivity can be used for selective detection of MDMA

by the proposed method by diluting the seized sample containing these cathinones. Moreover, in the presence of these cathinones, MDMA can be identified by its second oxidation process.

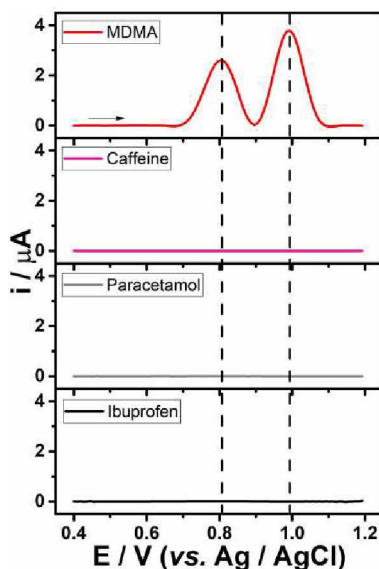


Figure 39. Voltammograms for MDMA (red line) and caffeine (pink line), paracetamol (gray line), and ibuprofen (black line). All molecules at $3.5 \mu\text{mol L}^{-1}$ in BR buffer solution 0.1 mol L^{-1} pH 10.0 on O_2GS . DPV conditions: 9 mV step potential, 100 mV modulation amplitude, 10 ms modulation time.

In addition, it is worth noticing that other illicit drugs (AB-FUBINACA, cocaine, and ketamine, Figure 38D), as well as the adulterants paracetamol, caffeine, and ibuprofen, (Figure 39) commonly found in ecstasy-like tablet samples, are not potential interferences in the identification of MDMA by the proposed method, once they did not provide any electrochemical response at the $\text{O}_2\text{-GS}$ electrode in the evaluated potential range (+0.4 to +1.2 V). More detailed information about the evaluated interferences is described in Table 12.

The molecules that presented electrochemical processes were further evaluated mixed with MDMA to understand their possible interference activity. The results are presented in Figure 40. The molecules (MDEA, ephylone and dibutylone) presented oxidation processes that partially or totally overlapped with MDMA peaks. It is clear that MDEA (peak 2) and ephylone (peak 1) causes a shift in the MDMA peak potential, and dibutylone does not interfere in the E-peak.

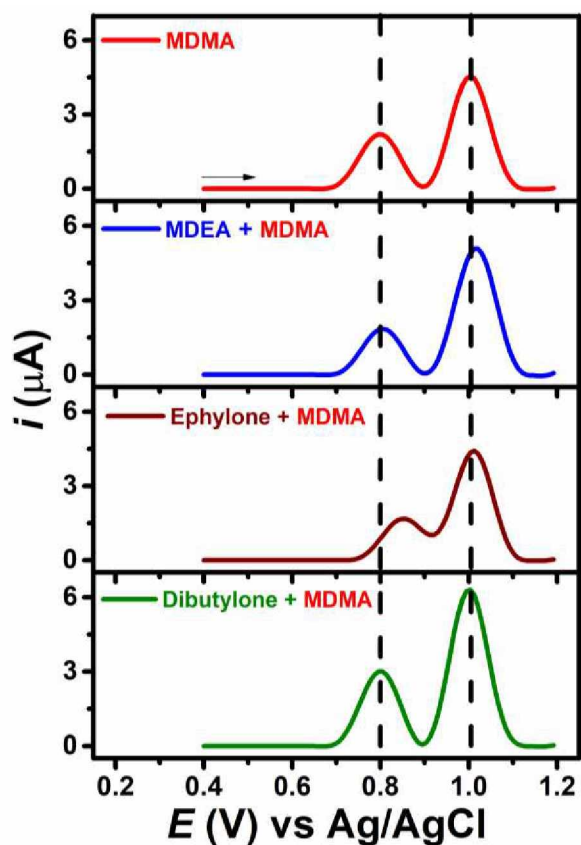
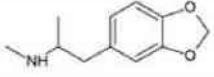
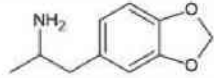
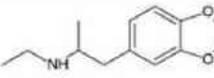
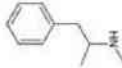
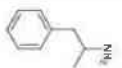
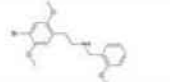
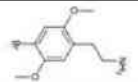
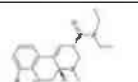
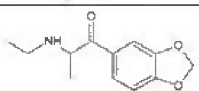
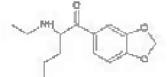
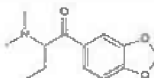
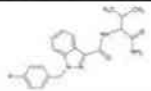
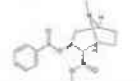
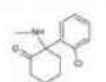
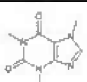
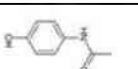
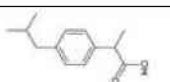


Figure 40. DPVs recorded for MDMA, MDMA + MDEA, MDMA + Ephylone and MDMA + Dibutylone. All molecules were analysed using the same O₂-GS electrode at a concentration of 3.5 μmol L⁻¹ in 0.1 mol L⁻¹ BR buffer solution pH 10.0.

Table 12. Details on the interferent tests.

Substance	Electrode with treatment				Untreated electrode				Chemical structure
	Process 1		Process 2		Process 1		Process 2		
	E/V	i/μA	E/V	i/μA	E/V	i/μA	E/V	i/μA	
MDMA	0.8051	2.6135	0.9941	3.7914	0.8681	0.0319	1.0751	0.4080	
MDA	0.9691	3.2169	-	-	1.0841	0.5023	-	-	
MDEA	0.8236	0.1576	1.0301	1.6995	-	-	-	-	
MA	-	-	-	-	-	-	-	-	
A	-	-	-	-	-	-	-	-	
25B-NBOMe	-	-	-	-	-	-	-	-	
2C-B	1.0121	5.9319	-	-	1.1112	1.1545	-	-	
LSD	-	-	-	-	-	-	-	-	
Ethylone	0.8891	0.1059	-	-	-	-	-	-	
Ephylone	0.8681	0.3336	-	-	-	-	-	-	
Dibutylone	0.7961	0.5913	-	-	0.8951	0.0180	-	-	
AB-Fubinaca	-	-	-	-	-	-	-	-	
Cocaine	-	-	-	-	-	-	-	-	
Ketamine	-	-	-	-	-	-	-	-	
Caffeine	-	-	-	-	-	-	-	-	
Paracetamol	-	-	-	-	-	-	-	-	
Ibuprofen	-	-	-	-	-	-	-	-	

The apprehension of samples containing the association of MDMA with these interferents (MDEA and ephylone) may hinder a discriminatory report of the seized sample; however, it does not change the positive report for MDMA, once the individual profile of the molecules is different. Synthetic cathinone molecules present only one oxidation processes, while amphetamine-like drugs present two processes in the studied conditions. Additionally, only MDMA presents two peaks with similar currents, which differs from MDEA. Therefore, even though it might not be possible to discriminate the compounds present in the seized sample, a positive MDMA report can be assured, added the possibility of the presence of other illicit (and prohibited by UNODOC) drugs.

3.5. MDMA determination in seized samples and human saliva.

To demonstrate the feasibility of the developed method using an O₂-GS electrode for screening tests, four different seized samples (tablets) were examined (Figure 41). After the methanol extraction step (described in the experimental section) and 1000-fold dilution in 0.12 mol L⁻¹ BR buffer pH 10.0, the samples (red-line) displayed two oxidation processes (at around +0.822 V and +1.02 V) using the O₂-GS electrode, which are characteristic of MDMA. Indeed, after the addition of 20 μmol L⁻¹ MDMA (blue-line), there was an increase in the peak currents for both oxidation processes, indicating the presence of this drug in the analysed samples, which was also confirmed by GC-MS, as shown in Figure B9 (page 154). The results demonstrates that this method can be applied to successfully screen MDMA in real seized tablets. By adding MDMA standard in the diluted sample, and observing the increase of both characteristic oxidation peaks of this molecule, we can confirm that it is present in the apprehended tablet.

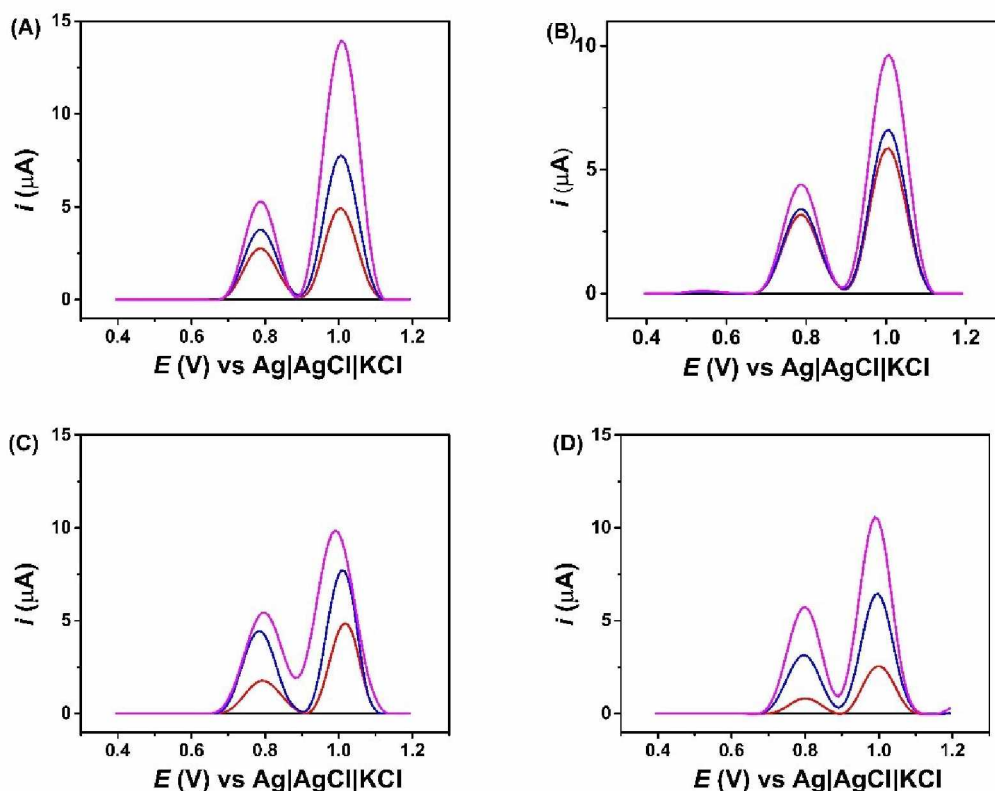


Figure 41. DPVs recorded at O₂-GS in the presence of supporting electrolyte (black line), seized sample solution (red line), and after the two additions of 20 μmol L⁻¹ of MDMA (blue and magenta lines) for samples 1 (A), 2 (B), 3 (C) and 4 (D). Supporting electrolyte: 0.1 mol L⁻¹ BR buffer solution pH 10.0; DPV conditions: 9 mV step potential; 100 mV modulation amplitude; 10 ms modulation time.

Figure 42 shows the total ion chromatogram (TIC) of sample 1, as well as the mass spectra of MDMA detected in samples 1 to 4 and of caffeine detected in sample 3. The TIC of sample 1 exhibits a peak around 5.77 minutes, corresponding to MDMA. The retention times of MDMA differ in samples 1, 2, 3, and 4 due to variations in the GC-MS methods and equipment used for analysis. However, all MDMA mass spectra exhibit similar characteristics, with a prominent base peak at m/z 58 resulting from an α -cleavage reaction involving the carbon-carbon bond of the ethyl linkage between the aromatic ring and the amine. The α -cleavage reaction also produces the 3,4-methylenedioxybenzyl ion at mass 135. Additionally, the molecular ion (m/z 193) is detected but at very low abundance.

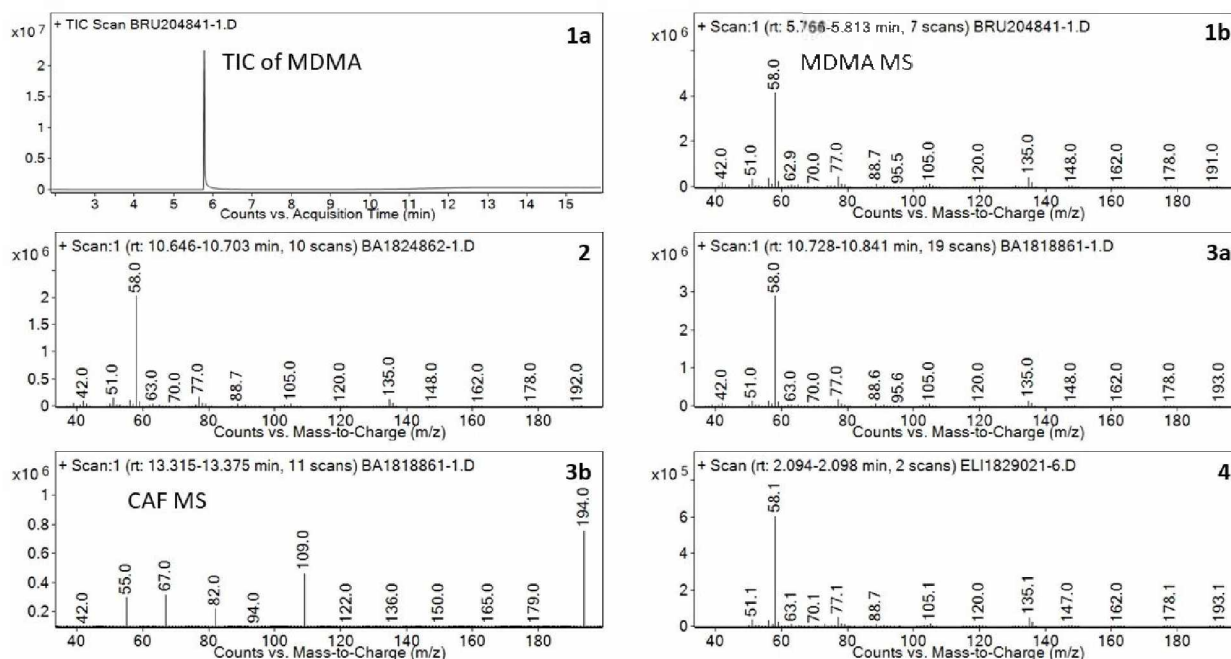


Figure 42. Electron ionization gas chromatography-mass spectrometry total ion chromatogram (TIC) (1a) and spectra of the compounds found in four seized samples. Samples 1, 2, 3 and 4 contain MDMA. Sample 3 also contains caffeine (CAF) (3b).

Likewise, intended to demonstrate another important applicability of this method, two different authentic oral fluid samples, collected from two volunteers, were submitted to extraction process (detailed in experimental part) and diluted 10-fold in the supporting electrolyte for DPV detection (Figure 43). As can be seen in Figure 43, it is possible to notice two oxidation peaks (at around +0.81 V and +1.03V), which are typical from MDMA. In fact, after the addition of 10 $\mu\text{mol L}^{-1}$ (blue line) and 20 $\mu\text{mol L}^{-1}$ (magenta line) MDMA (standard solution) in these two samples, an increase of their two peak currents was observed, indicating the presence of this psychoactive drug in both human oral fluid samples.

It is noteworthy that the presence of MDMA in both oral fluid samples were confirmed by LC-MS/MS system, as shown in Figure 44. Moreover, Figure 44 shows that other drugs (beyond MDMA) were also detected by LC-MS/MS system in these samples, such as in voluntary-1's oral fluid (A): MDMA (79230 ng/mL), MDA (713 ng/mL), MDEA (73 ng/mL) and methylone (2.1 ng/mL); and in voluntary-2's oral fluid (B): MDMA (102486 ng/mL), MDA (1040 ng/mL), MDEA (119 ng/mL), Δ^9 -

tetrahydrocannabinol (THC) and methylone. However, these drugs did interfere in the identification of MDMA using the proposed method.

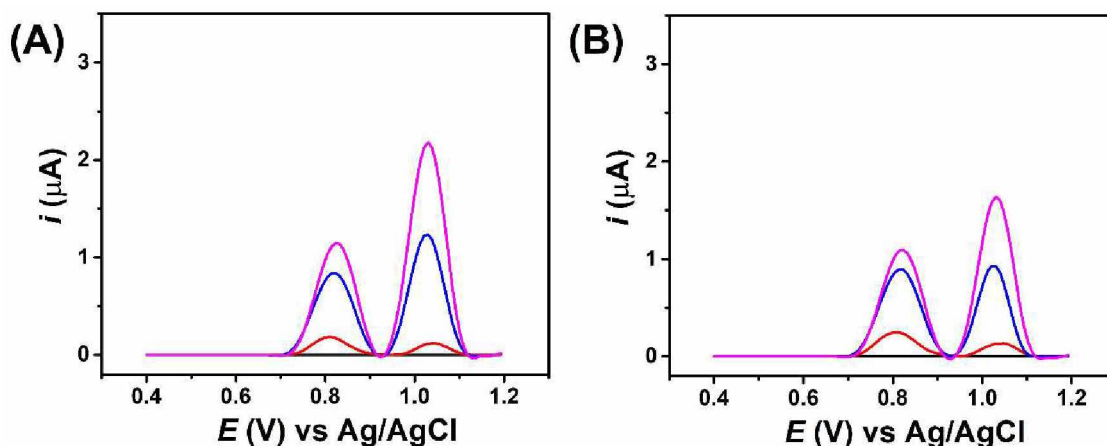


Figure 43. DPVs recorded for supporting electrolyte (black line), authentic biological samples from (A) voluntary 1 and (B) voluntary 2 (red line) and after the addition of $10 \mu\text{mol L}^{-1}$ (blue line) and $20 \mu\text{mol L}^{-1}$ (magenta line) of MDMA. Supporting electrolyte: 0.1 mol L^{-1} BR buffer solution pH 10.0; DPV parameters: step 9 mV; amplitude: 100 mV; modulation time: 10 ms.

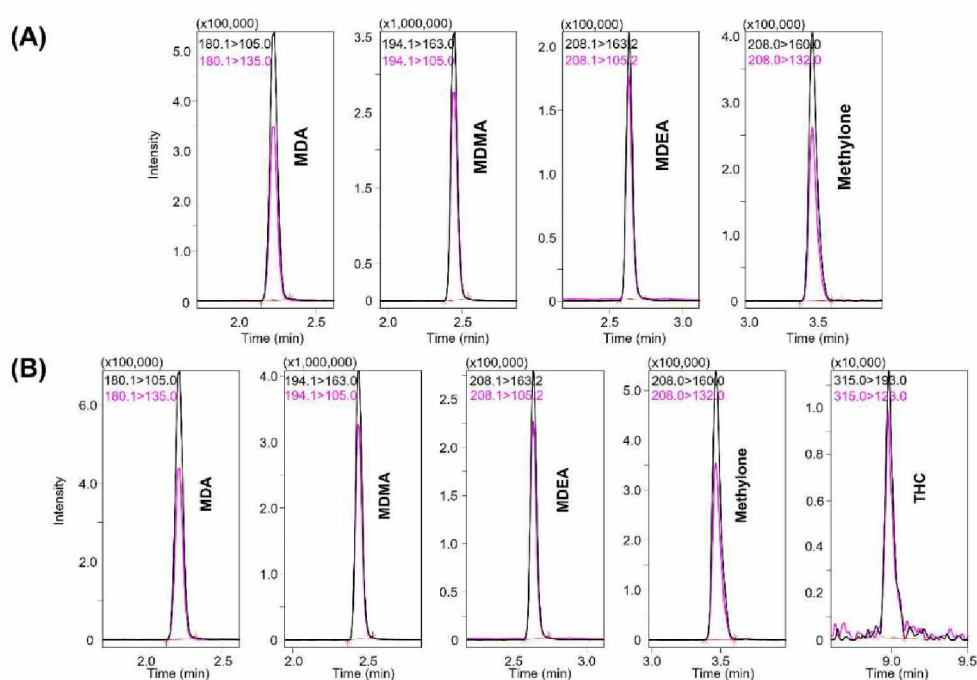


Figure 44. Extracted multiple reaction monitoring chromatograms of all analytes detected and/or quantified in oral fluid samples obtained from (A) voluntary 1 and (B) voluntary 2. Both oral fluid samples were diluted 50 times to fit to the MDMA calibration range.

The analytical performance of the proposed sensor was compared with other electrochemical sensors reported previously (Table 13). Although most of the previous reports have shown good analytical performance for the electrochemical screening of MDMA, the used working electrodes are expensive and not attractive for an application in routine forensic analysis. Likewise, although the SPE is a portable and disposable alternative, it still is costly when compared with the GS electrode (each GS electrode costs \$0.09, while commercial SPEs may cost 55 times more – \$5 each). Moreover, even though carbon paste electrode has a low-cost, it demands a time-consuming preparation step and provides a low detectability. It is worth mentioning that in the proposed method, a simple and fast (2 min) protocol to improve the electrochemical response of MDMA (LOD = 0.09 $\mu\text{mol L}^{-1}$) is presented, which is enough for seized sample screening, once the found concentrations vary between 62 $\mu\text{mol L}^{-1}$ and 175 mmol L^{-1} (Garrido et al., 2010; Green et al., 2003; Maurer et al., 2004; McNamara et al., 2006; Prosser and Nelson, 2012; Togni et al., 2015).

Additionally, its application in human fluid samples is also possible as demonstrated before. Finally, there is another advantage because the protocol for surface treatment proposed here can be performed on a whole GS sheet (11.5 x 18.0 cm) and pieces with different sizes can be cut as needed. Considering the applicability, it is important mentioning that the coupling of the GS electrodes with 3D-printed cells (commercial or lab made) can provide a simple, cheap and efficient sensing platform for *in situ* analysis, as shown in a previous work (Silva et al., 2018), comparable with the easiness of using a SPE electrode.

Table 13. Comparison between analytical features obtained from different working electrodes used for MDMA detection.

Electrode	Technique	LOD ($\mu\text{mol L}^{-1}$)	Linear range ($\mu\text{mol L}^{-1}$)	Sample	Reference
BDD	DPV	0.3	1 - 500	Seized tablets	(Teófilo et al., 2020)
CB-PLA	CSWV	0.6	6 - 35	Seized tablets and saliva	(de Faria et al., 2022)

SPCE	DPV	0.21	3 - 26	Seized tablets	(Cumba et al., 2016)
GCE	SWV	2.4	8 - 45	Seized tablets and serum	(Garrido et al., 2010)
SPCE	SWV	15.0	5 - 1000	Seized tablets	(Thiruvottriyur Shanmugam et al., 2021)
CPE	SWV	9.0*	9 – 870*	Seized tablets	(Naomi Oiye et al., 2020)
AuE	SWV	31	31 - 92	Seized tablets and urine	(Nevescanin et al., 2013)
O ₂ -GS	DPV	0.09	0.5 - 15	Seized tablets and saliva	This work

*Unit of concentration in mmol L⁻¹. BDD: Boron-doped diamond; CB-PLA: Carbon Black doped Polylactic acid; SPCE: Screen Printed Carbon Electrode. GCE: Glassy Carbon Electrode; CPE: Carbon Paste Electrode. AuE: Gold Electrode; DPV: Differential Pulse Voltammetry; CSWV: Cyclic Square Wave Voltammetry; SWV: Square Wave Voltammetry.

4. Conclusion

We demonstrated that the O₂ plasma treatment significantly changed the surface of the graphite sheets, improving its catalytic properties for application in electroanalysis. The O₂-GS electrode with DPV technique presents to be suitable for effective detection of MDMA in very low concentrations (0.5 μmol L⁻¹), allowing the sensitive detection of this analyte in authentic oral fluid. Furthermore, the proposed method shows to be efficient for the selective detection of MDMA in the presence of some NPS, other illicit drugs, and common adulterants, which are usually found in seized samples. Since the plasma treatments here described are conducted in low pressure using lower quantity of reactants (gases) and time, this technique can be considered promising for activation of electrodes in the electroanalytical purposes, thus enabling new strategies and applications.

CHAPTER 5 – PYROLYTIC GRAPHITE SHEET: ANTIBIOTICS DETECTION CO₂-PLASMA SURFACE TREATMENT OF GRAPHITE SHEET ELECTRODES FOR DETECTION OF CHLORAMPHENICOL, CIPROFLOXACIN AND SULPHANILAMIDE.

This chapter contains an adaption of the published article named: “CO₂-plasma surface treatment of graphite sheet electrodes for detection of chloramphenicol, ciprofloxacin, and sulphanimide” Jian F. S. Pereira, Marina Di-Oliveira, Lucas V. Faria, Pedro H. S. Borges, Edson Nossol, Rogério V. Gelamo, Eduardo M. Richter, Osmando F. Lopes, Rodrigo A. A. Muñoz.

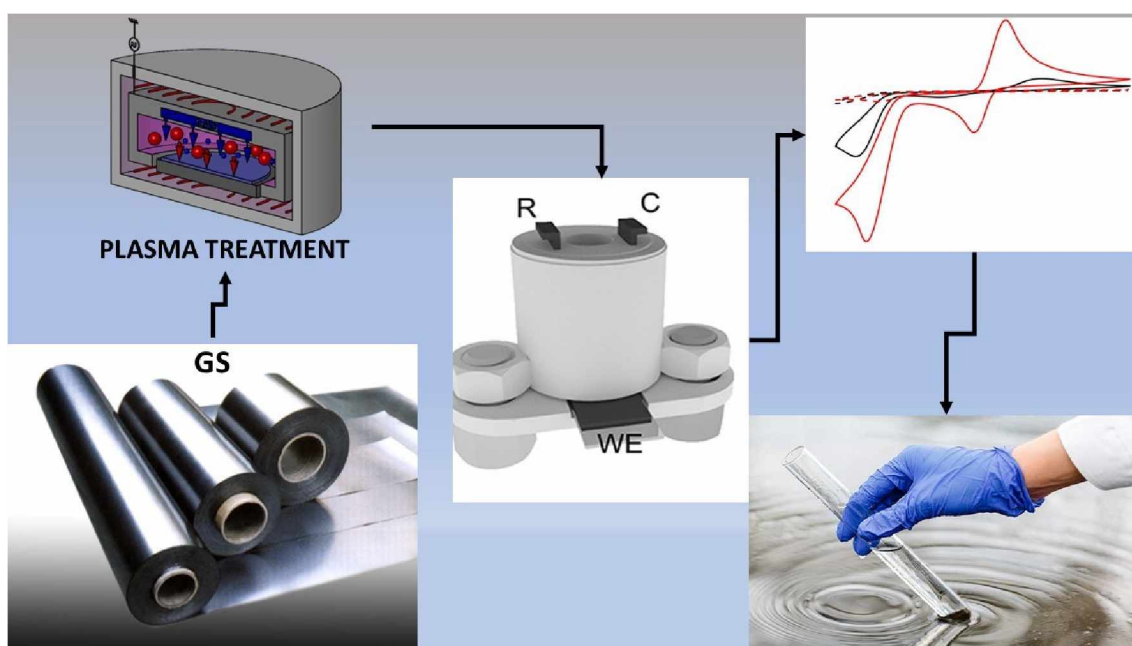


Figure 45. Graphical abstract of CHAPTER 5

1. Introduction

In modern medicine, antibiotics are primarily employed as a prophylactic measure against several infectious diseases, acting as a bactericidal or as a bacteriostatic (by controlling the rate of bacteria growth) (Preda et al., 2022). These drugs can also be classified according to their chemical structure, such as aminoglycosides, amphenicols, β -lactams, macrolides, oxazolidone, quinolones, sulphanilamide, tetracyclines and glycopeptides (Preda et al., 2022). Unfortunately, the overuse of antibiotics can lead to several side effects on human health, such as fever, myalgia, nephrotoxicity and hepatotoxicity, tendon rupture, rash, digestive and cardiovascular disorders, carcinogenicity, among others (Ding et al., 2022; Rebelo et al., 2021; Stoian et al., 2020; Surya et al., 2020; Torkashvand et al., 2016). Another problem associated with antibiotic overdoses is the increase of bacterial resistance (Barton and Hart, 2001), thus, controlling their use and disposal is of high importance. In this sense, the use of electrochemical methods coupled with disposable highly sensitive electrodes can be an interesting tool to monitor the presence of these pollutants in aquatic systems as well as in biological fluids.

Herein, we present for the first-time the use of cold CO₂ plasma treated GS electrodes (preliminary tests demonstrated that carbon dioxide cold plasma treated electrodes presented a slight better response towards antibiotics determination when compared with oxygen treatment, thus, using these electrodes in this work) to detect three antibiotics from different classes, chloramphenicol (CHL), ciprofloxacin (CIP) and sulphanilamide (SUL), species extensively employed in veterinary practices, and considered potential emerging contaminants (de Faria et al., 2021). The electrochemistry of these antibiotics on untreated and treated GS electrodes was investigated to verify if the surface plasma treatment in fact improves the electrochemical activity aiming at the development of highly sensitive sensors for these species. These disposable electrodes were combined with square wave voltammetry (SWV) for fast and portable analysis, which can be useful for on-site applications.

2. Experimental

2.1. Reagents, samples and materials

Pyrolytic GS with 0.07 mm width, 2.5 Ω electrical resistance and 55.6 $S\text{ cm}^{-1}$ electrical conductivity was acquired from Panasonic (Mansfield, Texas, USA). All

solutions were prepared using ultrapure water ($R \geq 18 \text{ M}\Omega\text{cm}$) obtained from a purification system Millipore Direct-Q3 (Bedford, USA). Caffeine (99.9%), paracetamol (99.0%), sodium nitrite (97.8%) salicylic acid (99.0%), calcium chloride (74% to 78%), dihydrogen phosphate (99.7%) and potassium bicarbonate (99.0%) and potassium chloride (99.0%) were obtained from Synth (Diadema, Brazil); SUL (97.0%), acetic (99.7%), ascorbic acid (99.0%), sodium sulphate (99.0%) and phosphoric acids from Vetec (Rio de Janeiro, Brazil); sodium hydroxide (97.0%) from Dinâmica (Diadema, Brazil); CHL (99.0%), uric acid and CIP (98.0%) from Sigma-Aldrich (St. Louis, USA); boric acid (99.0%) from Appli-chem Panreac (Barcelona, Spain); catechol from Acros (Belgium), sodium nitrate from Caal (Araçatuba, Brazil), citric acid from Sandoz (Cambé, Brazil), magnesium sulphate (99.0% and ammonium chloride (99.0%) from Cinética (Itapevi, Brazil). Argon (99.99%) and CO_2 (99.9%) were purchased from White Martins Co.

For electrochemical measurements, 0.12 mol L^{-1} Britton-Robinson buffer solutions (which is a mixture of boric, acetic and phosphoric acids, all at 0.04 mol L^{-1}) with pH ranging from 2 to 12 were used as supporting electrolyte. Stock solutions (10 mmol L^{-1}) of each antibiotic (CHL, CIP and SFL) were prepared separately after dissolution in a 10% alcoholic solution, and stored in a refrigerator (5°C). The water sample was collected from water utilities, and the synthetic urine sample was prepared following the procedure proposed by Brooks and Keevil (Brooks and Keevil, 1997), which consists of a mixture of the following reagents: citric (2.1 mmol L^{-1}) and uric acids (0.4 mmol L^{-1}), urea ($166.5 \text{ mmol L}^{-1}$), sodium bicarbonate (25.0 mmol L^{-1}), calcium chloride (0.4 mmol L^{-1}), sodium chloride (89.0 mmol L^{-1}), sodium sulfate (9.9 mmol L^{-1}), magnesium sulfate (4.1 mmol L^{-1}), ammonium chloride (24.3 mmol L^{-1}), monopotassium phosphate (7.0 mmol L^{-1}), dipotassium phosphate (9.0 mmol L^{-1}) and sodium nitrite (0.7 mmol L^{-1}), whose pH value is around 6.4. An amount of 10 mL of water sample was spiked with 20, 10 and $10 \mu\text{mol L}^{-1}$ of CIP, CHL and SUL, respectively, while 10 mL of synthetic urine was spiked with 1 mmol L^{-1} of each species.

For water sample analyses, 2.5 mL of the sample was directly added to 2.5 mL of BR buffer (0.12 mol L^{-1}) in the electrochemical cell. For urine, $50 \mu\text{L}$ of the sample was diluted in the electrochemical cell in 4.95 mL of the same supporting electrolyte. The measurements using the SWV technique were performed and the presence of CHL, SUL and CIP were checked by oxidation processes at around +0.15, +0.85 V and +1.10 and (*versus* $\text{Ag}|\text{AgCl}|\text{KCl}$), respectively.

2.2. Electrode surface treatment

GS electrodes were cut into squared pieces of 10 cm² and submitted to cold plasma discharges using mixtures of CO₂ and argon controlled by needle valves at 350 and 100 mTorr, respectively, for 2 min each. The reactive plasma here used is composed by a microwave-assisted plasma-enhanced chemical vapor deposition (PECVD) system (Figure 2) described before (Kannan et al., 2016b).

3. Results and discussion

3.1. Electrochemical behaviour of antibiotics on GS electrodes

Firstly, the electrochemical profiles of the three different antibiotics (CHL, CIP and SUL) were evaluated on both GS surfaces by CV using 0.12 mol L⁻¹ BR buffer solution (pH 2.0) as the supporting electrolyte (Figure 46).

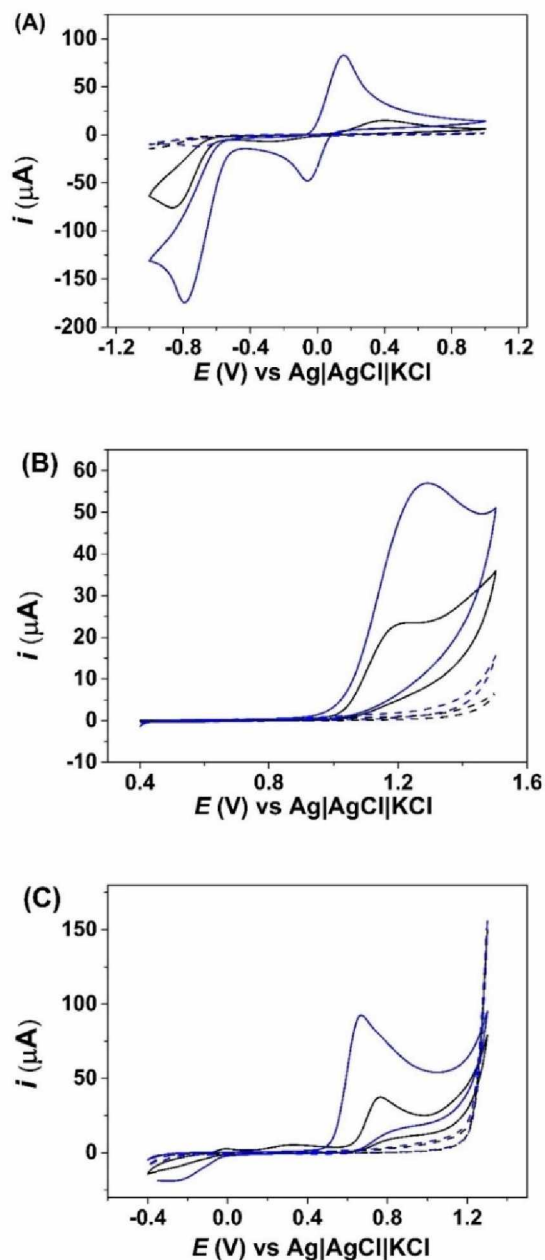


Figure 46. CVs responses for 0.2 mmol L^{-1} of (A) CHL, (B) CIP and (C) SUL using 0.12 mol L^{-1} BR buffer solution (pH 2.0) as supporting electrolyte on GS (black line) and CO_2 -GS (blue line).

It is noticed three electrochemical processes for CHL in both electrodes (Figure 46A), starting by an irreversible reduction peak at around -0.8 V (*versus* $\text{Ag}|\text{AgCl}|\text{KCl}$) followed by two *quasi*-reversible processes at around $+0.2 \text{ V}$ (*versus* $\text{Ag}|\text{AgCl}|\text{KCl}$) (arising from the reduction process). This behaviour has been already studied in the literature using carbon-based electrodes (Di-Oliveira et al., 2022; Vinícius de Faria et al., 2021). It is worth mentioning that the *quasi*-reversible peaks presented a lower ΔE for

CO₂-GS (0.21 V) if compared with GS ($\Delta E = 0.69$ V), and a higher peak current for all peaks was also noticed on treated surface. On the other hand, only one oxidation process is seen for CIP on both electrodes at around +1.2 V (*versus* Ag|AgCl|KCl), which also agrees with previous reports (Chauhan et al., 2020; de Faria et al., 2021), again, with a higher peak current (2.75-fold) for the treated surface (Figure 46B). Likewise, for SUL only one oxidation peak is observed at around +0.8 V (*versus* Ag|AgCl|KCl), also discussed in previous studies (de Faria et al., 2021; Lisboa et al., 2022), with similar enhance of the peak current values for CO₂-GS electrode (Figure 46C). These improvements in the electrochemical responses of the antibiotics can be attributed to the increased surface area, and to the electrocatalytic effects probably conferred by the oxy-functional groups generated by the CO₂ plasma treatment.

The influence of the pH on the electrochemical response of each antibiotic was evaluated using 0.12 mol L⁻¹ BR buffer with pH values between 2.0 to 11.0 (Figure 47). For all species a pH-dependent behavior was observed (as the pH increased, a shift of the peak potentials to the less positive direction occurred), indicating that protons are involved in the redox reactions, as described elsewhere (de Faria et al., 2021). The chosen media for the next experiments were pH 5.0 for CHL and CIP, and pH 11.0 for SUL, which provided higher peak current and a slight shift of potentials to regions closer to 0.0 V, minimizing the effect of possible interfering species.

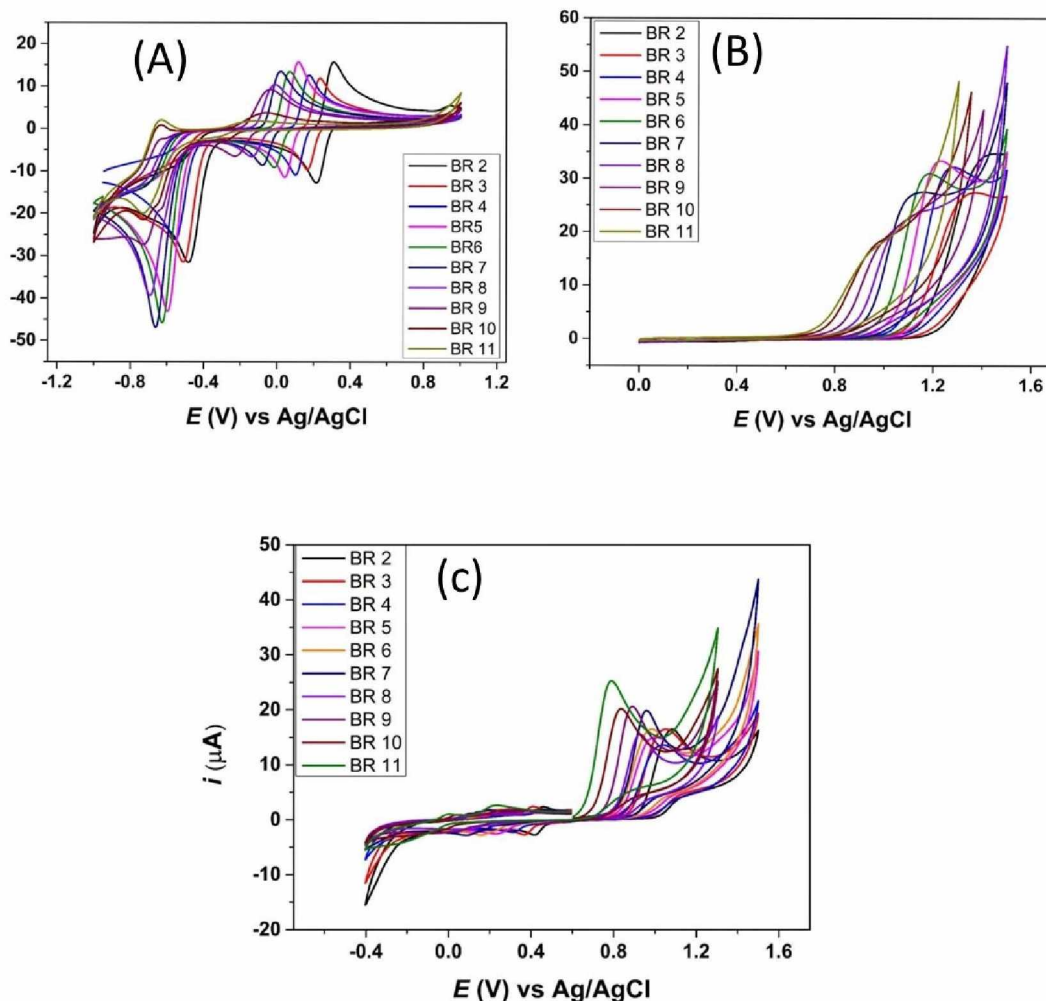


Figure 47. Voltammetric profiles of 0.5 mmol L⁻¹ CLO (A), CIP (B) and SUL (C) varying the pH from 2.0 to 11.0 using a 0.12 mol L⁻¹ BR buffer solution as supporting electrolyte. Scan rate: 50 mV s⁻¹; step: 5 mV.

Also, aiming to investigate the mass transport regime involved in the oxidation of antibiotics on the proposed surfaces, CVs were carried out at different scan rates (from 10 to 100 mV s⁻¹), and the results are presented in Figures 48, 49 and 50. Linear relationships between the squared root of the scan rate and the peak current were found for all molecules studied at both unmodified and modified electrodes, indicating that the diffusion of the species towards the electrodes surface is what control the reaction rate. Likewise, Log (*i*) versus Log (*v*) plots showed a linear adjustment with slopes near 0.5 for both surfaces, which confirms the previous statement (Gosser, 1994; Montes et al., 2014, 2012; Streeter et al., 2008).

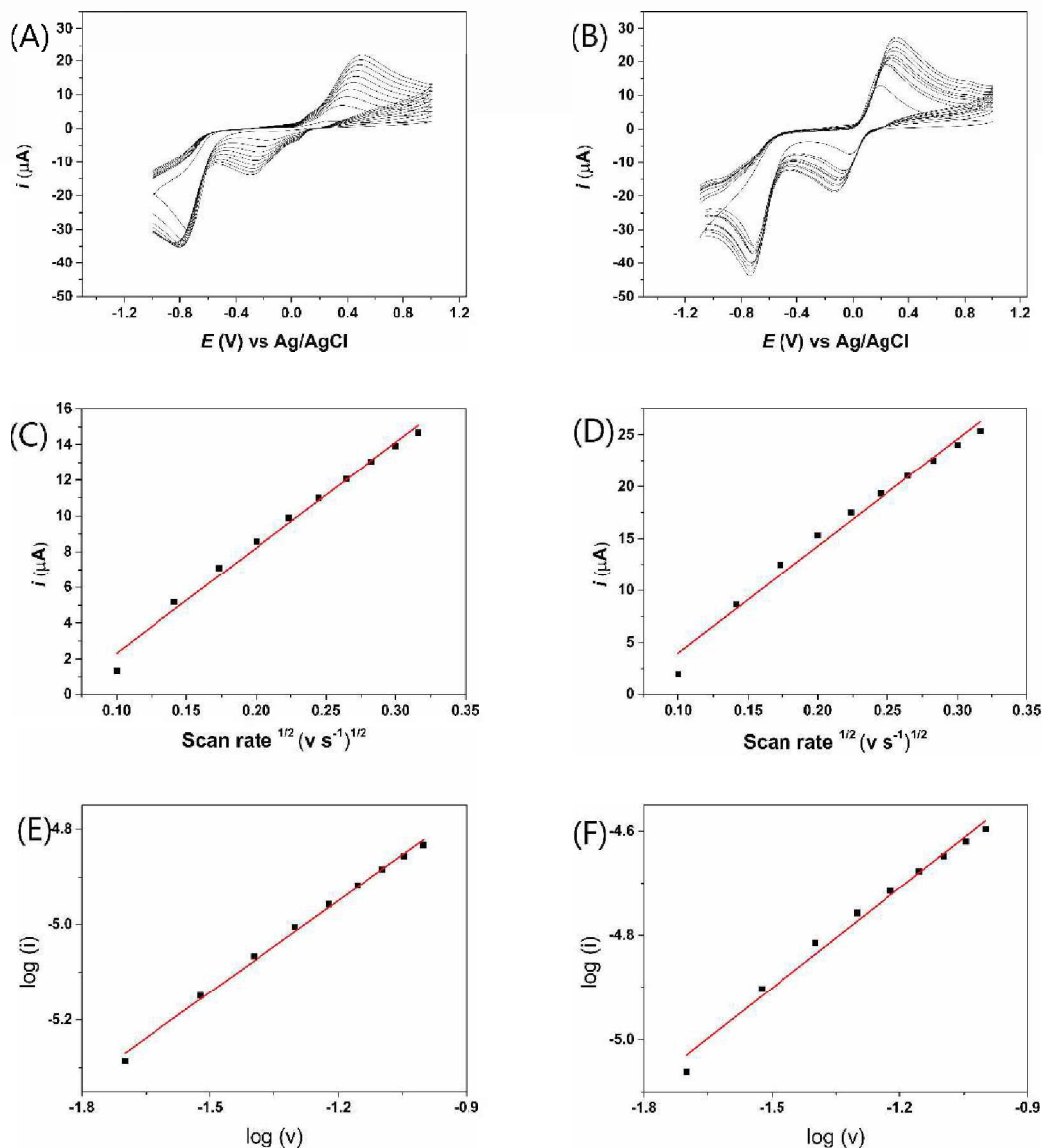


Figure 48. Cyclic voltammograms for GS (A) and CO₂-GS (B) in the presence of 0.5 mmol L⁻¹ chloramphenicol using 0.12 mol L⁻¹ of BR buffer solution pH 5.0 as supporting electrolyte at the scan rates 10, 20, 30, 40, 50, 60, 70, 80, 90 and 100 mV s⁻¹, squared root of the scan rate versus peak current for GS (C) and CO₂-GS (D), and Log (v) versus Log (i) for GS (E) and CO₂-GS (F).

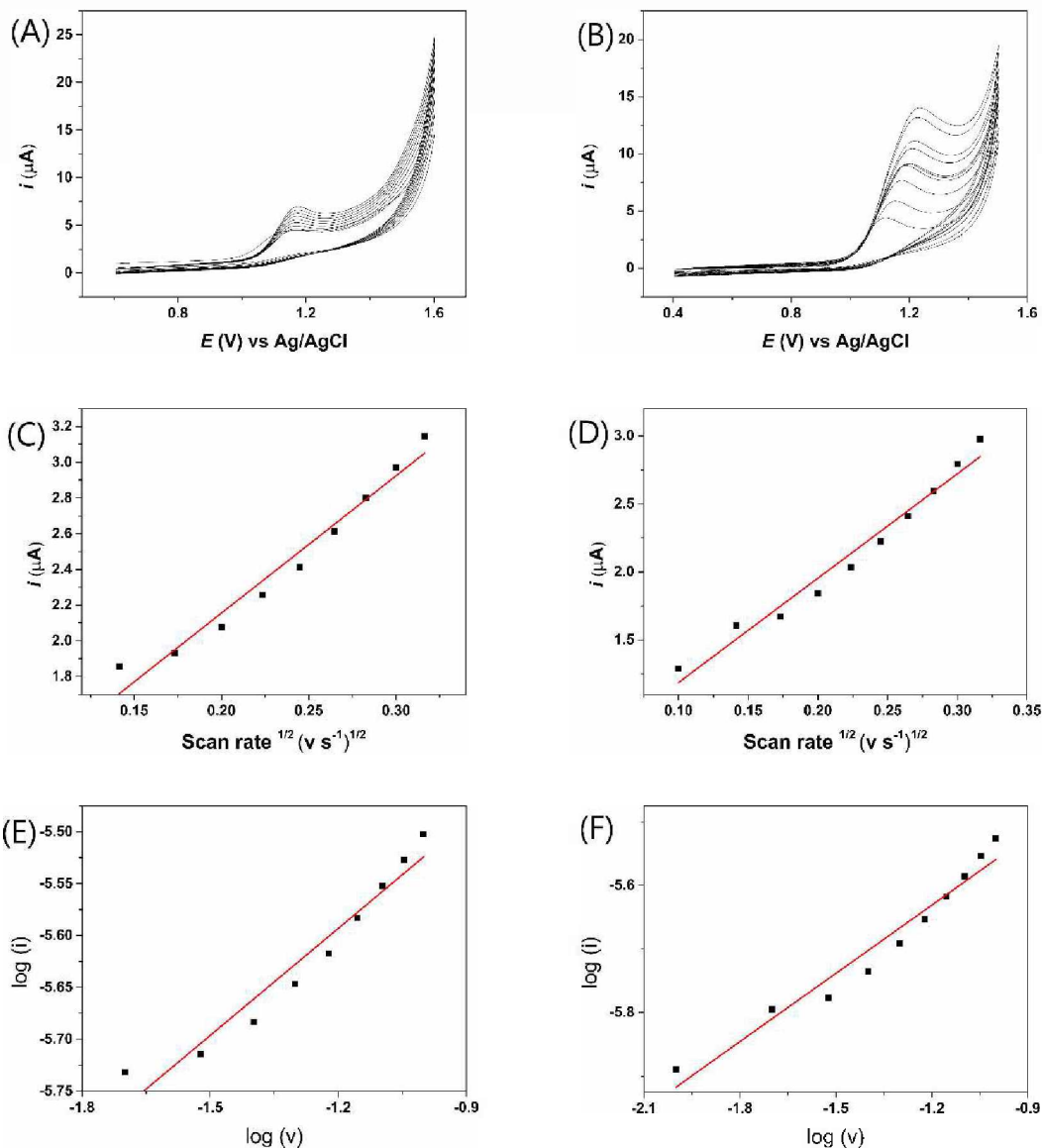


Figure 49. Cyclic voltammograms for GS (A) and CO₂-GS (B) in the presence of 0.5 mmol L⁻¹ of ciprofloxacin using 0.12 mol L⁻¹ of BR buffer solution pH 5.0 as supporting electrolyte at the scan rates 10, 20, 30, 40, 50, 60, 70, 80, 90 and 100 mV s⁻¹, squared root of the scan rate versus peak current for GS (C) and CO₂-GS (D), and Log (v) versus Log (i) for GS (E) and CO₂-GS (F).

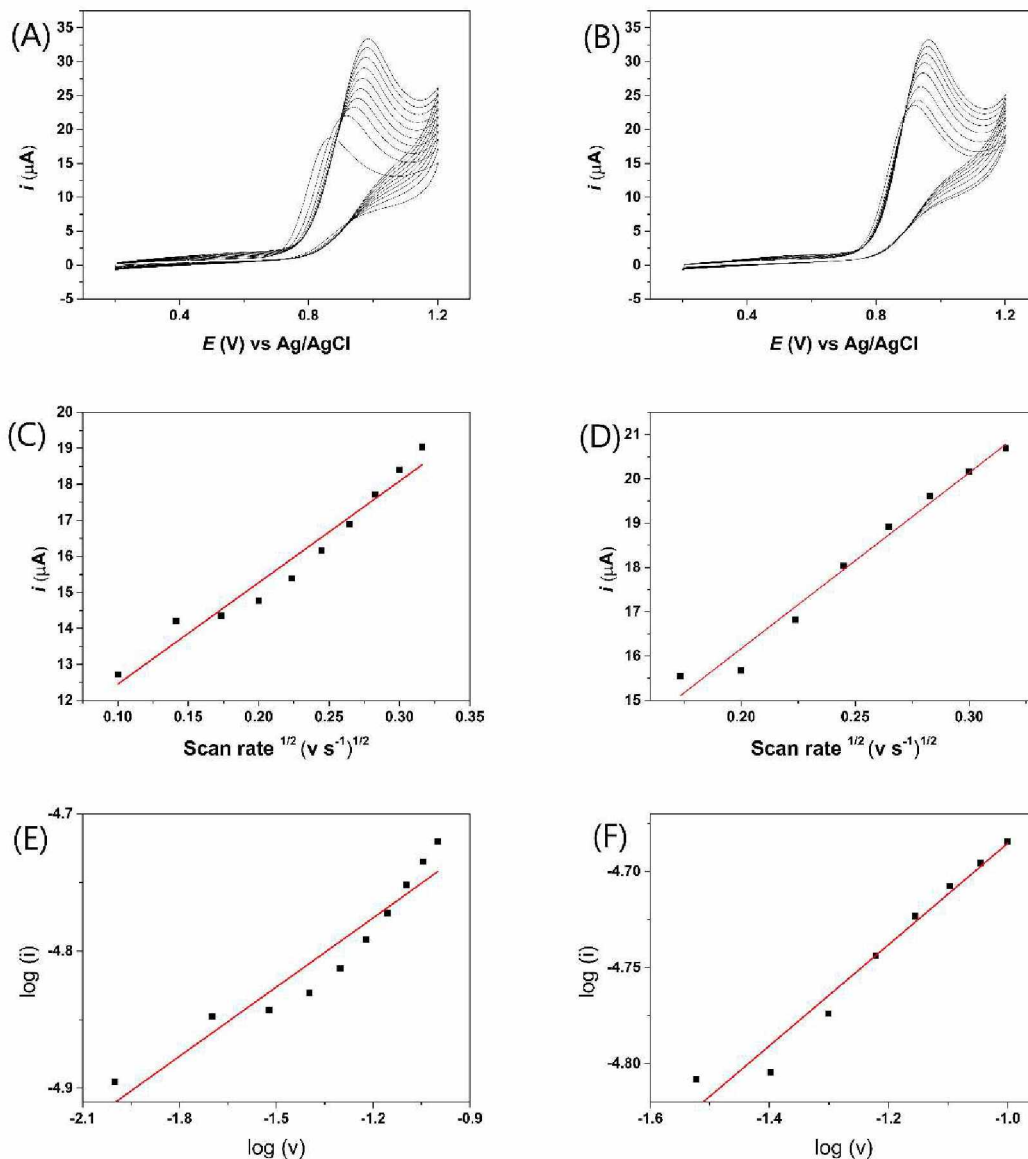


Figure 50. Cyclic voltammograms for GS (A) and CO₂-GS (B) in the presence of 0.5 mmol L⁻¹ of sulphanilamide using 0.12 mol L⁻¹ of BR buffer solution pH 5.0 as supporting electrolyte at the scan rates 10, 20, 30, 40, 50, 60, 70, 80, 90 and 100 mV s⁻¹, squared root of the scan rate versus peak current for GS (C) and CO₂-GS (D), and Log (v) versus Log (i) for GS (E) and CO₂-GS (F).

The sensor stability towards the detection of the proposed molecules was also evaluated by cyclic voltammetry using the same electrode for five consecutive days (Figure 51G) and using 5 different electrodes (Figure 51H). It is important to notice that for CHL (Figures 51A and 51B) the values were satisfactory for both inter-electrode and inter-day experiments (below 2.87% for E_{PEAK} and 1.97% for i_{PEAK}). As for CIP (Figures 51C and 51D), the E_{PEAK} remained below 2.56% in both experiments, however, the

variation observed in oxidation peak currents were above 10%, indicating that the responses either over different electrodes or the same electrode in different days can fluctuate slightly. The same behaviour is observed for SUL (Figures 51E and 51F), in which the peak potential remains with a low variation (below 1.52%) while peak currents slightly varied.

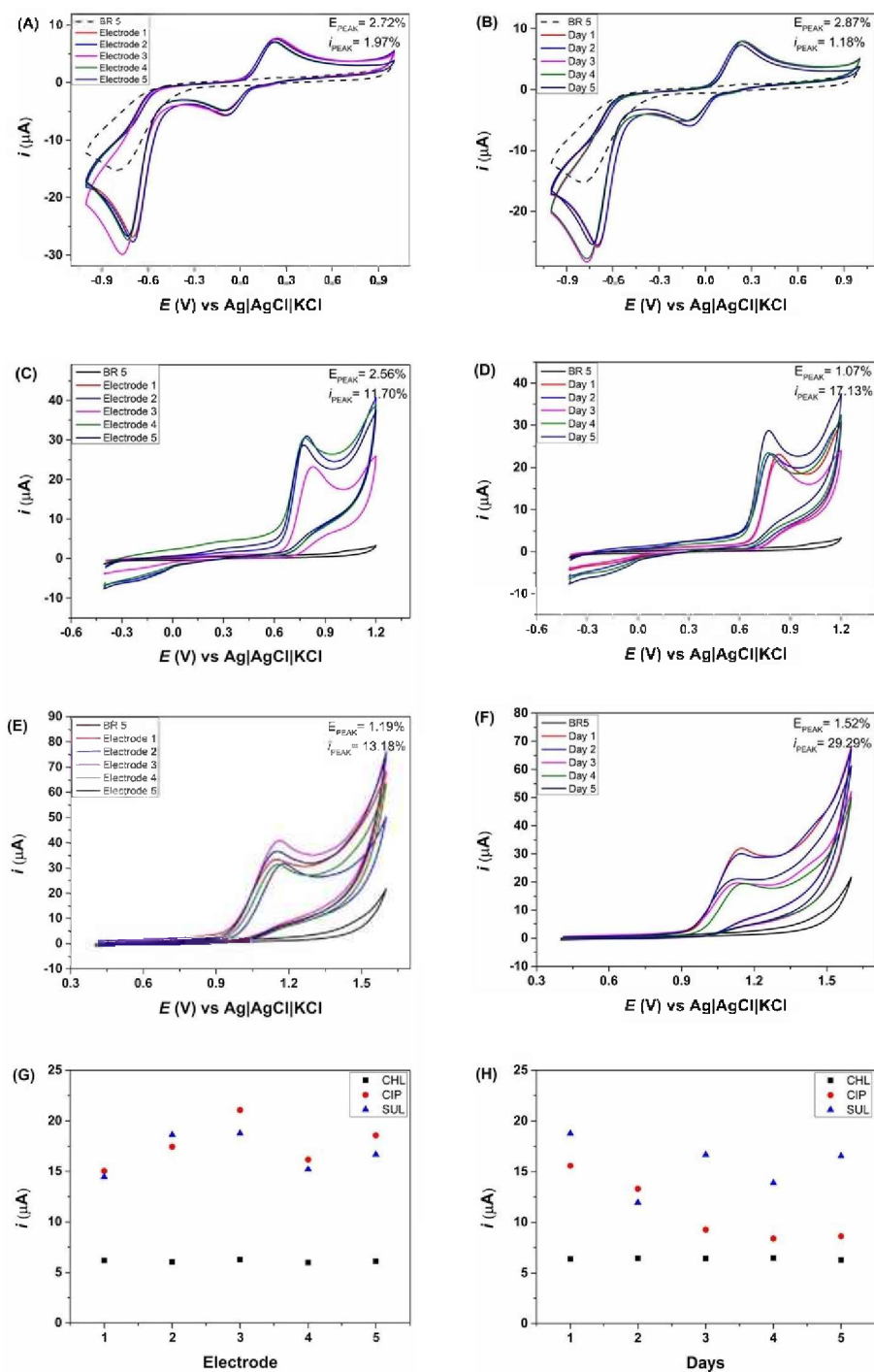


Figure 51. Current responses for different electrodes (A, C, E, and F) and for consecutive days (B, D, G, H). Cyclic voltammograms performed with 0.1 mmol L^{-1} of ■ CHL (A and B) ● CIP (C and D) ▲ SUL E and F).

The effect of the ionic strength was evaluated by adding KCl in two different concentrations, 0.1 and 1.0 mol L^{-1} , into the BR buffer. Figure 52 depicts the results, from which is possible to notice that for CHL a slight decrease in current is observed for a

higher ionic strength, however for both SUL and CIP the variation of ionic strength in the supporting electrolyte did not affect significantly the current responses. Therefore, BR buffer solutions was chosen to carry the next experiments.

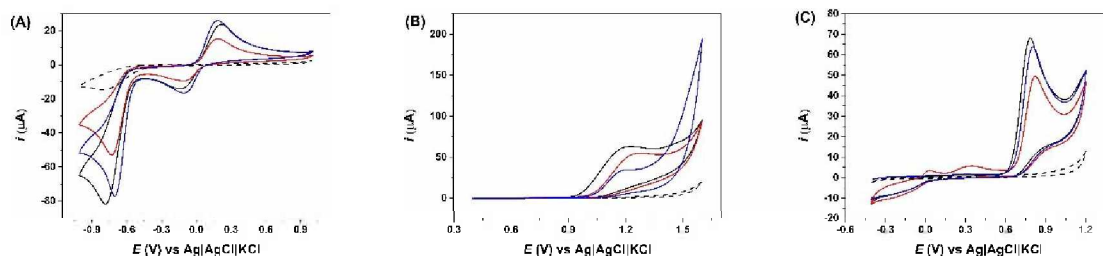


Figure 52. Cyclic voltammograms for CHL (A), CIP (B) and SUL (B) in supporting electrolyte (BR 5 for CHL and CIP and BR 11 for SUL) (black line), supporting electrolyte + 0.1 mol L⁻¹ KCl (red line) and supporting electrolyte + 1.0 mol L⁻¹ KCl.

3.2. Antibiotics detection using CO₂-GS electrode by SWV

The SWV technique was selected because of its speed and ability to minimize the contribution of capacitive current (Granger II et al., 2017), allowing the detection of species even at low concentrations, which is mandatory for emerging contaminants in routine environmental analyses. The SWV parameters, such as step potential, frequency, and amplitude, were properly studied for each molecule, aiming for a better analytical response and resolution. The ranges evaluated and the selected values are presented in Table 14. More specifically for CHL, as it is already well described that the oxidation process (around +0.3 V) is dependent on the reduction step (around -0.8 V), a new strategy using the accumulation step of the reduced species was evaluated for its detection, aiming to increase sensitivity and selectivity (response closer to 0.0 V). Thus, accumulation potential and accumulation time were also studied and the selected values are shown in Table 14.

Table 14. Summarized SWV parameter optimized for the detection of antibiotics of three different classes.

Parameters	Antibiotics		
	CLO	CIP	SUL
pH	5.0	5.0	11.0
Step (mV)	9	8	3

Amplitude (mV)	10	80	50
Frequency (Hz)	40	20	30
Conditioning Potential (V)	-0.7	-	-
Conditioning Time (s)	15	-	-

Subsequently, calibration curves were prepared for each antibiotic using both GS and CO₂-GS electrodes (Figure 53). On the treated electrode, CHL, CIP and SUL were detected around +0.15, +1.10 and +0.85 V (*versus* Ag|AgCl|KCl), respectively. On the other hand, using the non-treated electrode, the same species were oxidized respectively at +0.30, +1.08 and +0.90 V (*versus* Ag|AgCl|KCl).

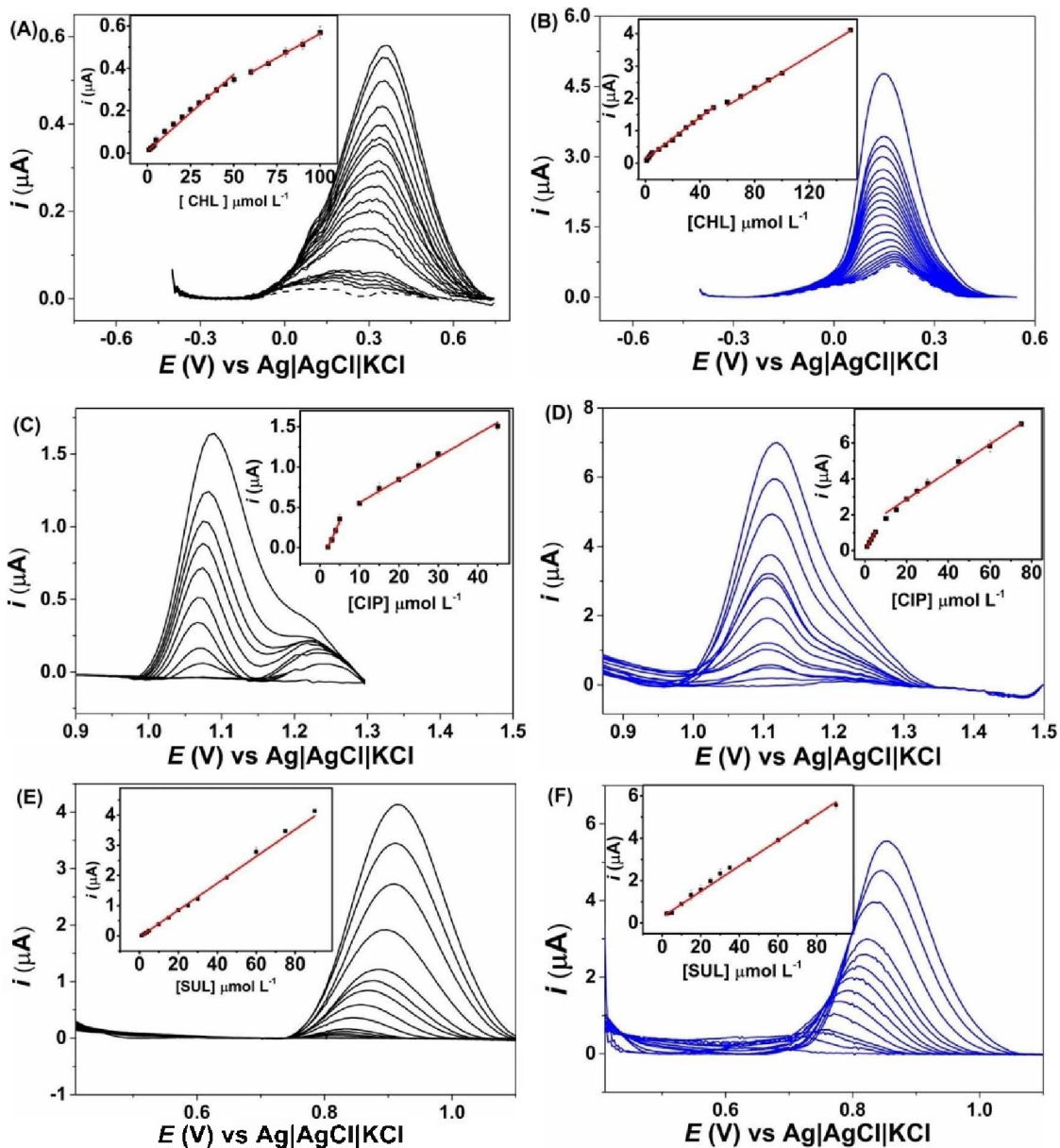


Figure 53. Baseline corrected SWV responses for increasing concentrations of antibiotics (A, B) CHL, (C, D) CIP and (E, F) SUL using GS (black line) and CO₂GS (blue line). SWV conditions: see Table 14. The insets represent the respective linear adjustments.

Note that significantly higher sensitivities were achieved when the treated surface was used, which corroborates with previous CV and EIS studies, suggesting that CO₂ cold plasma treatment is a useful tool to create more catalytic sites and consequently enhance the electrochemical response of different antibiotics. In fact, 4.5, 2.7 and 1.3-fold higher sensitivities were obtained for CHL, CIP and SUL, respectively, using the treated electrode. Also, wider linear working ranges were found for the CO₂-GS electrode.

The limit of detection (LOD) values was calculated following the IUPAC recommendation (Mocak et al., 1997), where $LOD = 3s_B/S$ (s_B is the standard deviation of ten measurements of the blank and S is the slope of the calibration curve). The analytical parameters such as linear range, LOD, and sensitivity are described in Table 15. It is noticeable that GS already provided reasonable LOD values (sub micromolar concentration range), however, after plasma treatment, detectability was dramatically improved, especially for CHL, which can be attributed to a better preconcentration of the reduced species on the porous surface (SEM images) and/or to the functional groups (XPS spectra) generated by the plasma species on the electrode surfaces.

Table 15. Analytical parameters obtained for the detection of CHL, CIP and SUL by SWV using GS and CO₂-GS electrodes.

Analytical parameters	Working electrode					
	GS			CO ₂ -GS		
	CHL	CIP	SUL	CHL	CIP	SUL
Linear range / $\mu\text{mol L}^{-1}$	2-50	2-5	1-90	1-50	1-5	1-90
slope / $\text{A L } \mu\text{mol}^{-1}$	$7.25 \cdot 10^{-9}$	$1.07 \cdot 10^{-7}$	$4.45 \cdot 10^{-8}$	$3.23 \cdot 10^{-8}$	$2.08 \cdot 10^{-7}$	$6.02 \cdot 10^{-8}$
r^2	0.993	0.991	0.991	0.995	0.999	0.999
LOD / $\mu\text{mol L}^{-1}$	0.76	0.05	0.23	0.08	0.01	0.11

Additionally, using SWV technique, consecutive voltammograms ($n = 50$) were recorded intended to evaluate the electrode stabilities for the detection of the studied molecules. The results (Figure 54) demonstrate that E_{PEAK} presented RSD below 3% for all antibiotics on both GS and CO₂-GS. Furthermore, considering the oxidation current, the RSD values observed when using the treated surface (1.51% for CHL, 7.51% for CIP and 6.83% for SUL) were lower than those obtained on the untreated GS (2.59% for CHL, 9.40% for CIP and 44.53% for SUL) for all molecules, confirming that the cold plasma treatment also provides higher stability to the sensing system.

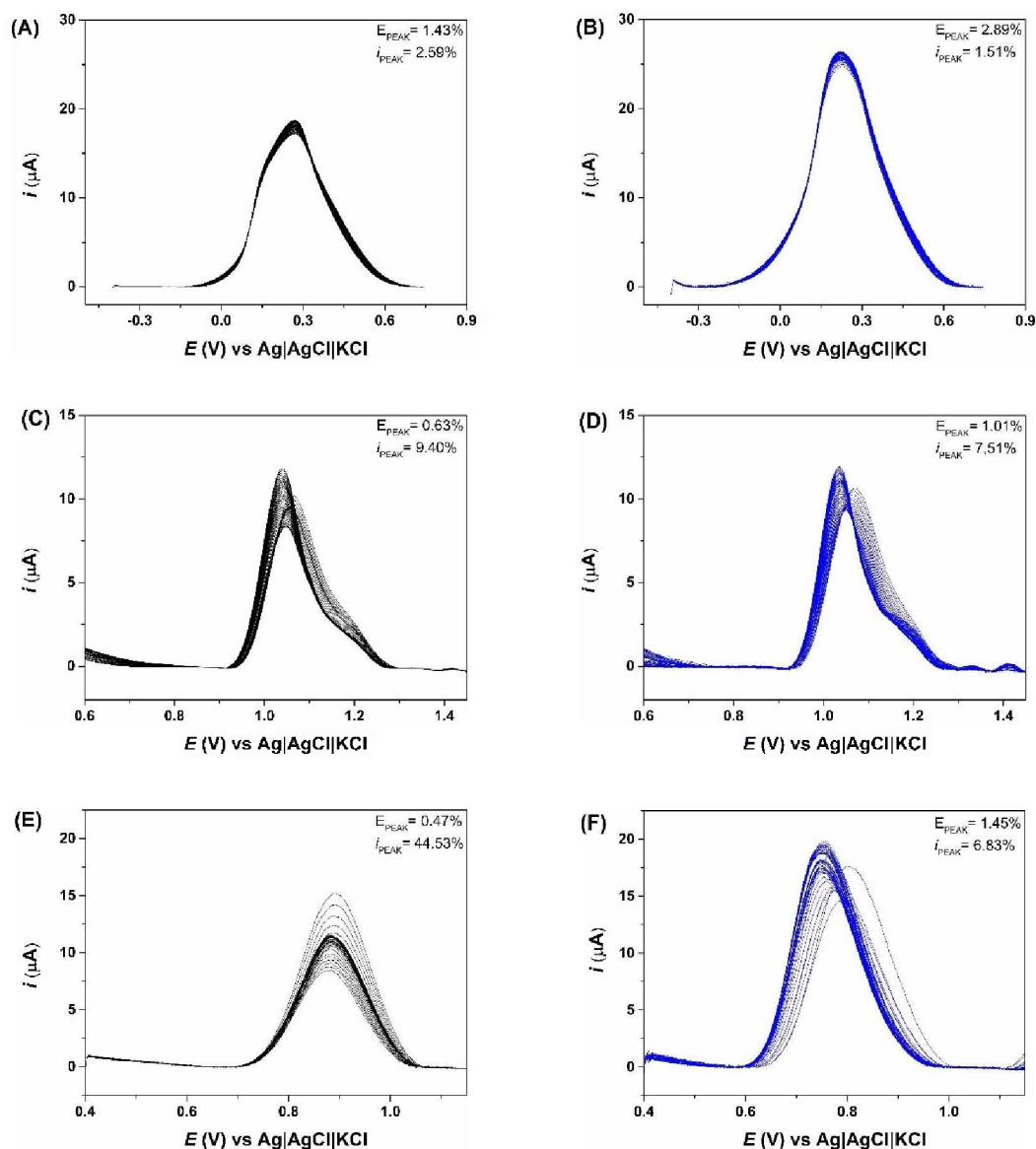


Figure 54. Baseline corrected SWV recordings for CHL (A, B), CIP (C, D) and SUL (E, F) using GS (black line) and CO₂-GS (blue line) as working electrodes. SWV conditions: see Table 14.

The analytical performances of the proposed electrodes in terms of linear range and LOD were compared with previous reports applied to the electrochemical sensing of antibiotics (Table 16). It can be seen that several works provided lower LODs than the ones obtained here for the determination of antibiotics, but it is important to highlight that these works (with very low LODs) use either expensive materials (both as substrate and as modifier) or require laborious and time-consuming steps to build the sensors. Comparatively, considering the time required for the treatments used here (2 min), fewer preparation steps as well as a significant decrease in by-products or waste from the

vacuum plasma process compared to conventional chemical processes that resulting in an approximated cost of each electrode (\$0.09), the approach proposed here can be a promising alternative for large-scale production of improved electrochemical sensors in places with minimal infrastructure.

Table 16. Comparison between the electrodes proposed in this work and previous reports.

Electrode	Method	Antibiotic	LOD ($\mu\text{mol L}^{-1}$)	Linear range ($\mu\text{mol L}^{-1}$)	Ref.
CoMoO₄/GC E	DPV	CHL	0.014	0.06 – 1190	(Vinothkumar et al., 2021)
rGO/PDA/AuNPs/GCE	DPV		0.058	0.1 – 100	(L. Zhang et al., 2022)
Mn₂O₃/TNS/SPCE	DPV		4.3*	15 – 1300*	(Rajaji et al., 2019)
MoN@S-GCN/GCE	DPV		6.9*	0.5 – 2450	(Jaysiva et al., 2020)
CO₂-GS GS	SWV SWV		0.08 0.76	1 – 50 2 – 50	This work This work
MMWCNTs @MIP/CPE	DPV	CIP	1.7*	0.005 – 0.85	(Bagheri et al., 2016)
AuNP/CHI/SPE	SWV		1.0*	0.1 – 150	(Reddy et al., 2018)
TiO₂/PB/AuNPs/CMK-3/Nafion/GE	CV		0.108	1 – 10	(Pollap et al., 2020)
CRGO/GCE	SWV		0.2	6 – 40	(de Faria et al., 2019)
RGO/GCE	FIA-AD		0.1	1,0 – 100	(de Faria et al., 2020)
Au/C₃N₄/GN/GCE	SWV	CIP	0.4	0.6 – 120.0	(Yuan et al., 2018)
CO₂-GS GS	SWV SWV		0.01 0.05	1 – 5 2 – 5	This work This work

N-Cu-MOFs/GCE	DPV	SUL	0.003	0.01 – 58	(Chen et al., 2020)
PE-Si₃Pic⁺Cl⁻/NiTsPc	DPV		12.0	35 – 301	(Vanoni et al., 2019)
Ag@Pt-Rh/GCE	DPV		0.27	2.6 – 320	(Y. Zhang et al., 2022)
MnO₂/NR/CPE	DPV		0.01	0.07 – 100	(Beitollahi et al., 2022)
CO₂-GS	SWV		0.11	1.0 – 90.0	This work
GS	SWV		0.23	1.0 – 90.0	This work

CoMoO₄/GCE – GCE electrode modified with CoMoO₄ nanoparticles film; RGO/PDA/AuNPs/GCE – GCE electrode modified with a film of reduced graphene oxide, polydopamine and gold nanoparticles; MoS₂-rGO/GCE – Mn₂O₃/TNS/SPCE – SPE electrode modified with hierarchical manganese (III) oxide nanostructures; MoN@S-GCN/GCE – GCE electrode modified with sulphur-doped graphitic carbon nitride nanocomposite; MMWCNTs@MIP/CPE – Carbon paste electrode modified with multi-wall magnetic carbon nanotubes; AuNP/CHI/SPE – SPE electrode modified with chitosan and gold nanoparticles; TiO₂/PB/AuNPs/CMK-3/Nafion/GE – graphite electrode modified with titanium dioxide enriched with CMK-3 mesoporous carbon, gold nanoparticles and Nafion; CRGO/GCE – GCE electrode modified with chemically reduced graphene oxide; RGO/GCE – GCE electrode modified with reduced graphene oxide; Au/C₃N₄/GN/GCE – GCE electrode modified with gold nanoparticles, carbon nitride and graphene; N-Cu-MOFs/GCE – GCE electrode modified with nitrogen-doped copper MOF; PE-Si₃Pic⁺Cl⁻/NiTsPc – carbon paste electrode chemically modified with 3-η-propyl(3-methylpyridine) silesquioxanchloride and nickel (II) tetrasulfonic acid tetrasodium phthalocyanine; Ag@Pt-Rh/GCE – GCE electrode modified with trimetallic silver, platinum and rhodium nanocrystals; MnO₂/NR/CPE – Carbon paste electrode modified with manganese dioxide.

The antibiotics studied in this work are commonly found in water samples, as well as in urine. Thus, several other water contaminants and urine contents can interfere in their electrochemical response, and, therefore, the behaviour of CHL, CIP and SUL in the

presence of such contaminants were evaluated. The possible interferents studied were ascorbic acid (AA), caffeine (CAF), catechol (CT), nitrate (NAT), nitrite (NIT), paracetamol (PAR), salicylic acid (SA) and uric acid (UA). The results for CHL, CIP and SUL are presented in Figures 55, 57 and 58 respectively. Both the molecule studied and the possible interferent were in the same concentration ($100 \mu\text{mol L}^{-1}$). The interference was evaluated as for the oxidation potential shift (vs Ag|AgCl|KCl reference electrode), and current variation as a percentage $[(\text{analyte} + \text{interferent current}/\text{analyte current}) \times 100]$, and the results are presented in Table 17.

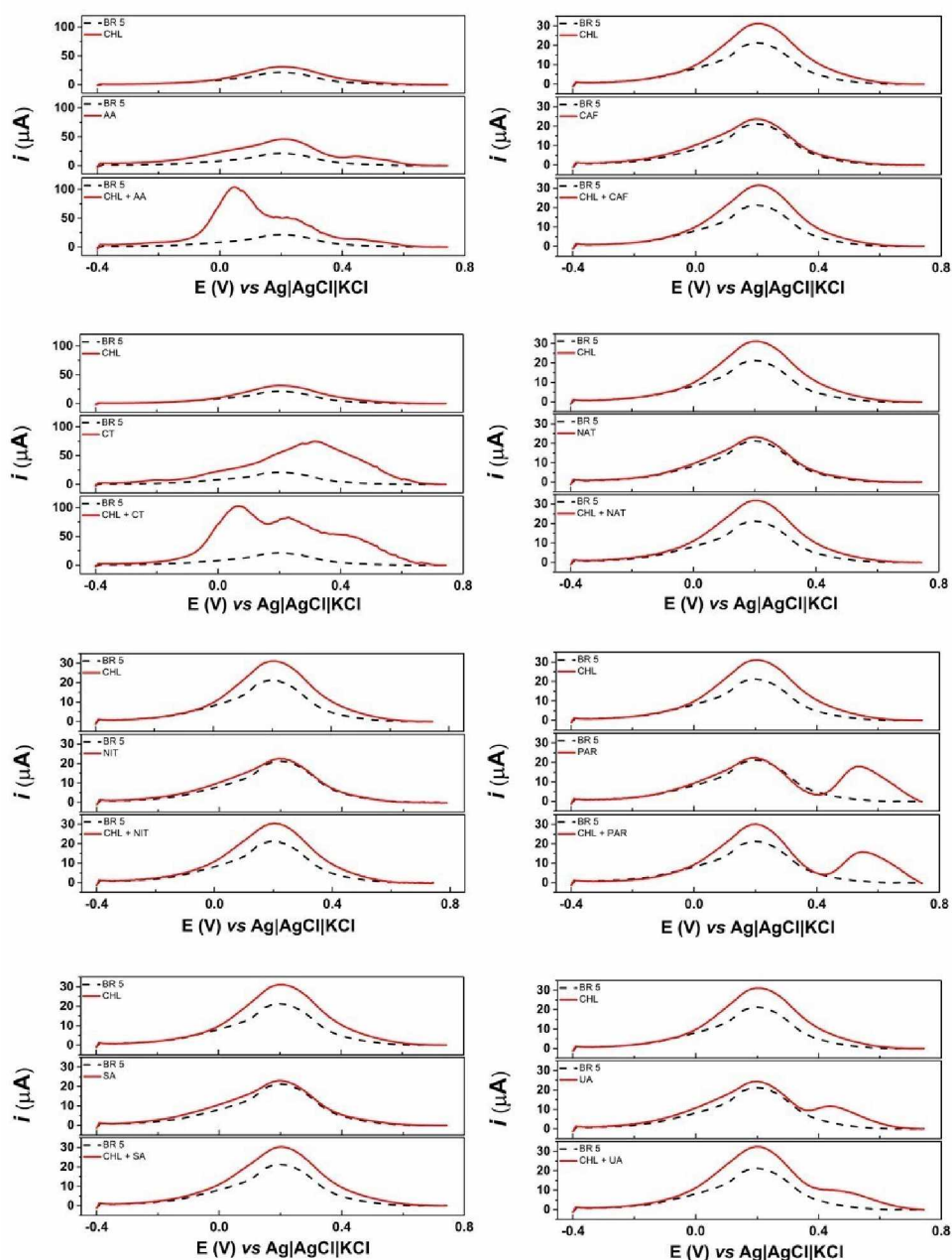


Figure 55. Baseline corrected SWV for CHL in the presence of AA, CAF, CT, NAT, NIT, PAR, SA and UA. All molecules were analysed using the same CO₂-GS electrode at a concentration of 100 μmol L⁻¹ in BR buffer solution 0.1 mol L⁻¹ pH 5.0. SWV conditions: 9 mV step potential, 10 mV amplitude, 40 Hz frequency.

As it can be seen in Figure 55, among the contaminants, only AA and CT can present an interference due to their oxidation processes that are practically overlapped with the CHL oxidation process. However, CHL presents a reduction process at around -0.8 V (*versus* Ag|AgCl|KCl) that can be used to overcome this interference. In fact, when performing SWV using the previous selected parameters in the negative window (from

0 V to -1.5 V) it is possible to see only the CHL reduction peak (see Figure 56). In the presence of the other studied contaminants (CAF, NAT, NIT, PAR, SA and UA), the oxidation current varied between 90% and 110% of its initial response (CHL without any interferent), which is acceptable and considered as a non-interferent.

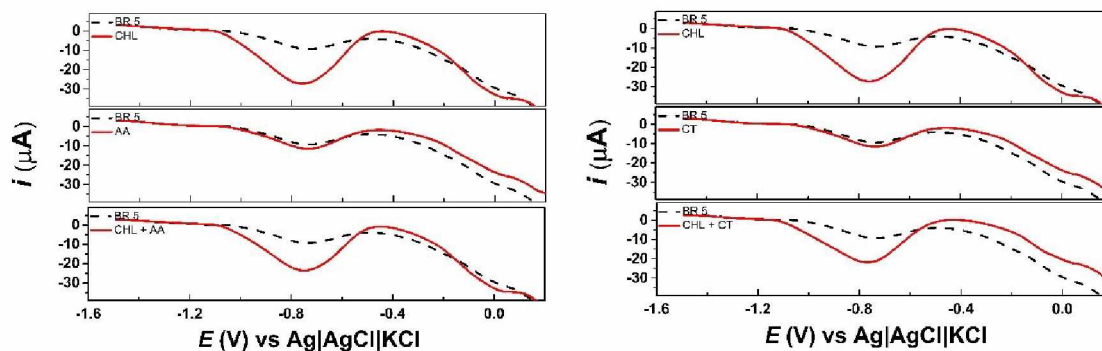


Figure 56. Baseline corrected SWV CHL in the presence of AA and CT. All molecules were analysed using the same CO_2 -GS electrode at a concentration of $100 \mu\text{mol L}^{-1}$ in BR buffer solution 0.1 mol L^{-1} pH 5.0. SWV conditions: -9 mV step potential, 10 mV amplitude, 40 Hz frequency.

For CIP (Figure 57), only NIT presented one oxidation process that could potentially interfere. Although it is still possible to identify the presence of CIP, the quantification is compromised, once the oxidation current exceeds 110%. As for SUL (Figure 58), none of the studied interferents presented redox processes in the same potential observed, demonstrating that they cannot interfere in the identification of SUL in real sample analyses. However, CAF, AS, PAR and NIT interfered in the oxidation current observed (above 110%), thus, they may provoke misled quantifications.

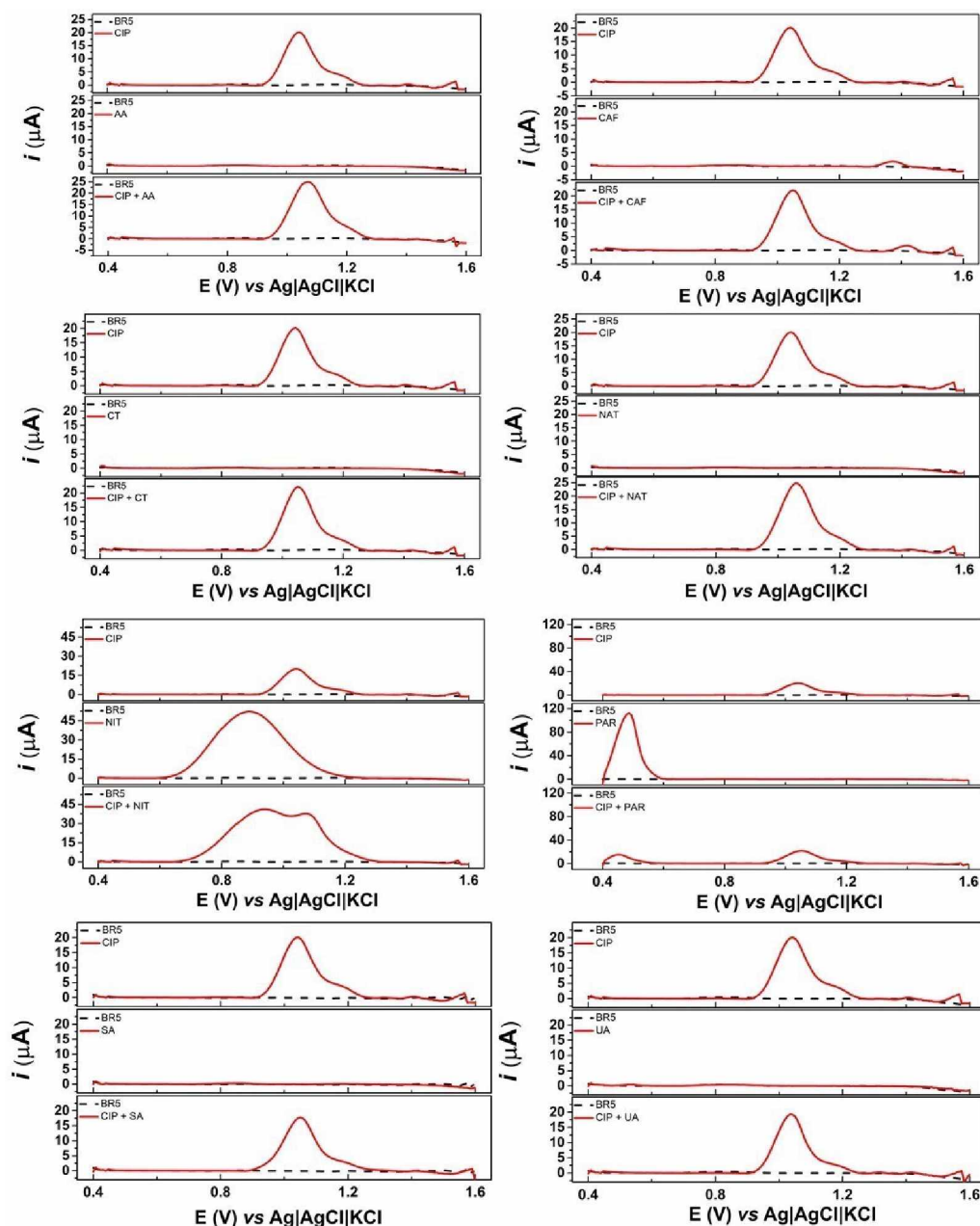


Figure 57. Baseline corrected SWV for CIP in the presence of AA, CAF, CT, NAT, NIT, PAR, SA and UA. All molecules were analysed using the same CO₂-GS electrode at a concentration of 100 μmol L⁻¹ in BR buffer solution 0.1 mol L⁻¹ pH 5.0. SWV conditions: 8 mV step potential, 80 mV amplitude, 20 Hz frequency.

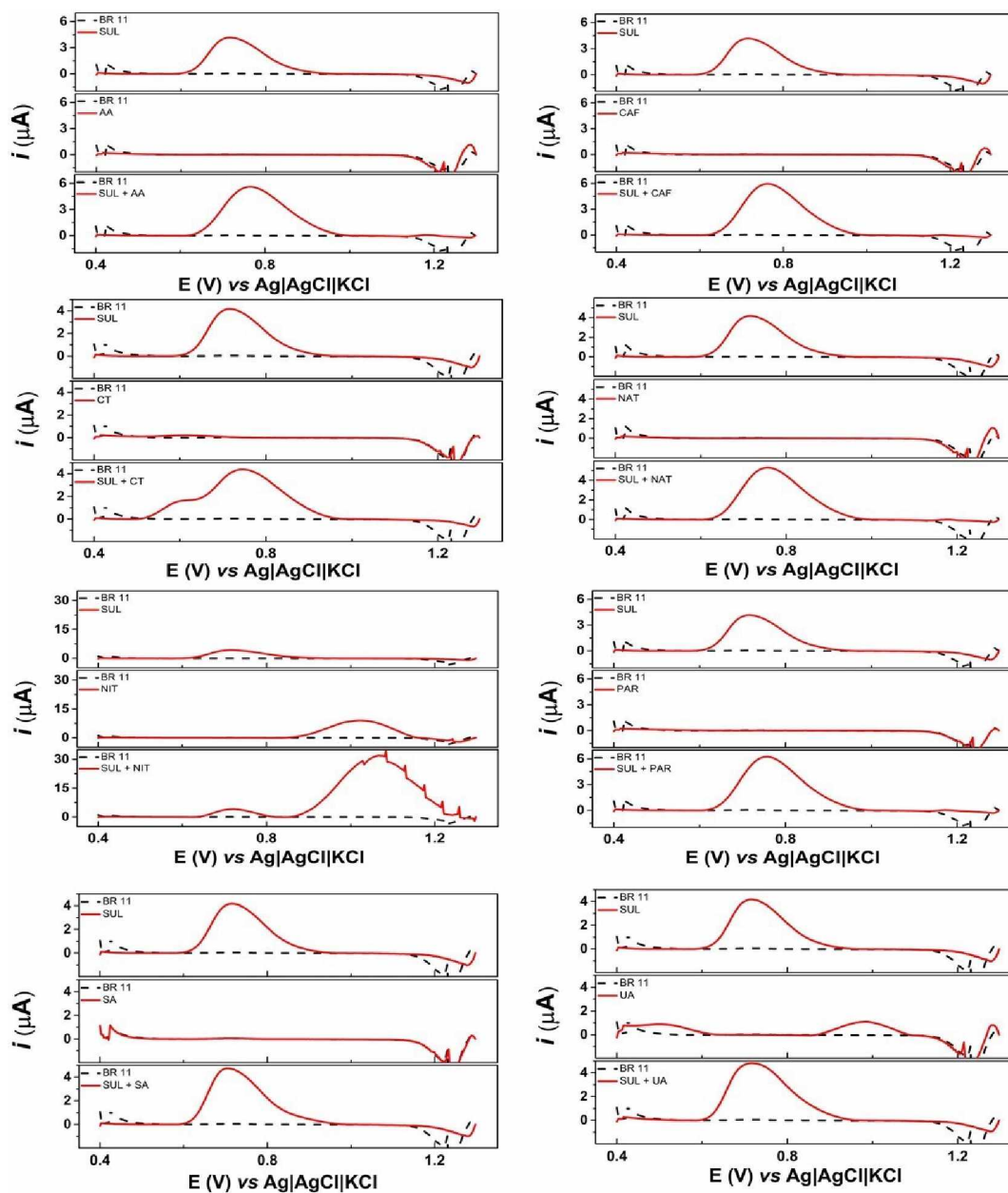


Figure 58. Baseline corrected SWV for SUL in the presence of AA, CAF, CT, NAT, NIT, PAR, SA and UA. All molecules were analysed using the same CO₂-GS electrode at a concentration of 100 μmol L⁻¹ in BR buffer solution 0.1 mol L⁻¹ pH 11.0. SWV conditions: 3 mV step potential, 50 mV amplitude, 30 Hz frequency.

Table 17. Effect of the possible interferents on analyte current. The % values correspond to $[(analyte\ current + interferent\ current)/analyte\ current] \times 100$.

Possible interferents	Antibiotics (analytes)		
	CHL	CIP	SUL
Ascorbic acid	739.0	106.6	133.1
Caffeine	109.6	97.0	141.4
Catechol	570.5	97.7	106.1
Nitrate	102.6	101.5	125.8
Nitrite	95.0	167.9	98.6
Paracetamol	87.5	109.0	148.1
Salicylic acid	92.1	90.5	107.6
Uric acid	109.4	97.0	103.6

Also, the effect on the behaviour of each antibiotic in the presence of the other antibiotics was evaluated using $25\ \mu\text{mol L}^{-1}$ of each. In the presence of CIP and SUL, the CHL peak current diminished 18.8%, however, the oxidation peak potential did not shift. The same behaviour was observed in the same experiment for SUL, in which the current lowered 15.1%. As for CIP, the current enhanced 70.3%, which is probably due to the fact that in this pH (5.0), SUL also has an oxidation process at the same potential. All voltammograms are presented in Figure 59.

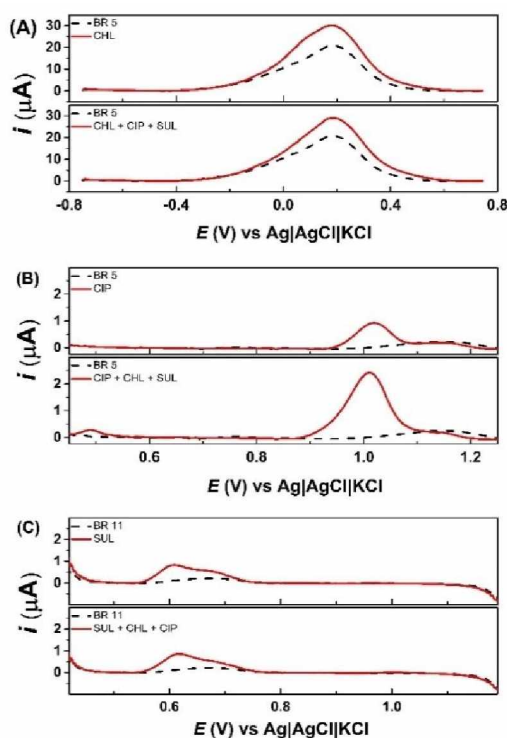


Figure 59. Baseline corrected SWV for CHL in the presence of CIP and SUL (A), CIP in the presence of CHL and SUL (B), and SUL in the presence of CHL and CIP (C). All molecules were analysed using the same CO₂-GS electrode at a concentration of 25 µmol L⁻¹ in BR buffer solution 0.1 mol L⁻¹ pH 5.0 (for CHL and CIP) and 11.0 (for SUL).

3.3. Antibiotics determination in water and synthetic urine samples

Using the previous selected SWV conditions, CO₂-GS was used as working electrode for antibiotics determinations in tap water and in synthetic urine samples. The amount found of CHL, CIP and SUL in water samples was below the respective LOD values. In the case of synthetic urine, CHL, CIP and SUL were not added to the sample, only for the recovery studies when the samples were spiked. Therefore, the samples were spiked with known concentrations of the antibiotics. The spiking concentration values in tap water were 10 µmol L⁻¹ for CHL and SUL, and 20 µmol L⁻¹ for CIP, selected based on a recent survey of antibiotics in natural waters which reported higher amounts of fluoroquinolones (such as CIP) than sulphonamides and chloramphenicol [65]. The spiked samples were then diluted two times in the electrochemical cell. The spiking concentration in synthetic urine was 1 mmol L⁻¹. The spiked samples were then diluted 100 times in the electrochemical cell. Figure 59 presents the recovery studies. From the results it is

possible to know that higher levels of all three antibiotics studied can be found in water using the proposed methods.

These levels can lead to several health issues, as mentioned before. The recovery values were between 94% and 119%, as described in Table 18. These values demonstrate that there is no matrix effect and this electrode can be applied as a simple and portable way to analyse real samples. Pre-concentration procedures, such as liquid-liquid micro-extraction can be coupled to the electrochemical device (Gabbana et al., 2018), aiming to detect low levels of these antibiotics in water environmental samples. On the other hand, the simultaneous determination of these species is a challenge that still needs to be explored. The same results were observed for synthetic urine samples, with recovery values between 88% and 118%, however, a higher dilution ratio was employed to reduce the sample matrix effects.

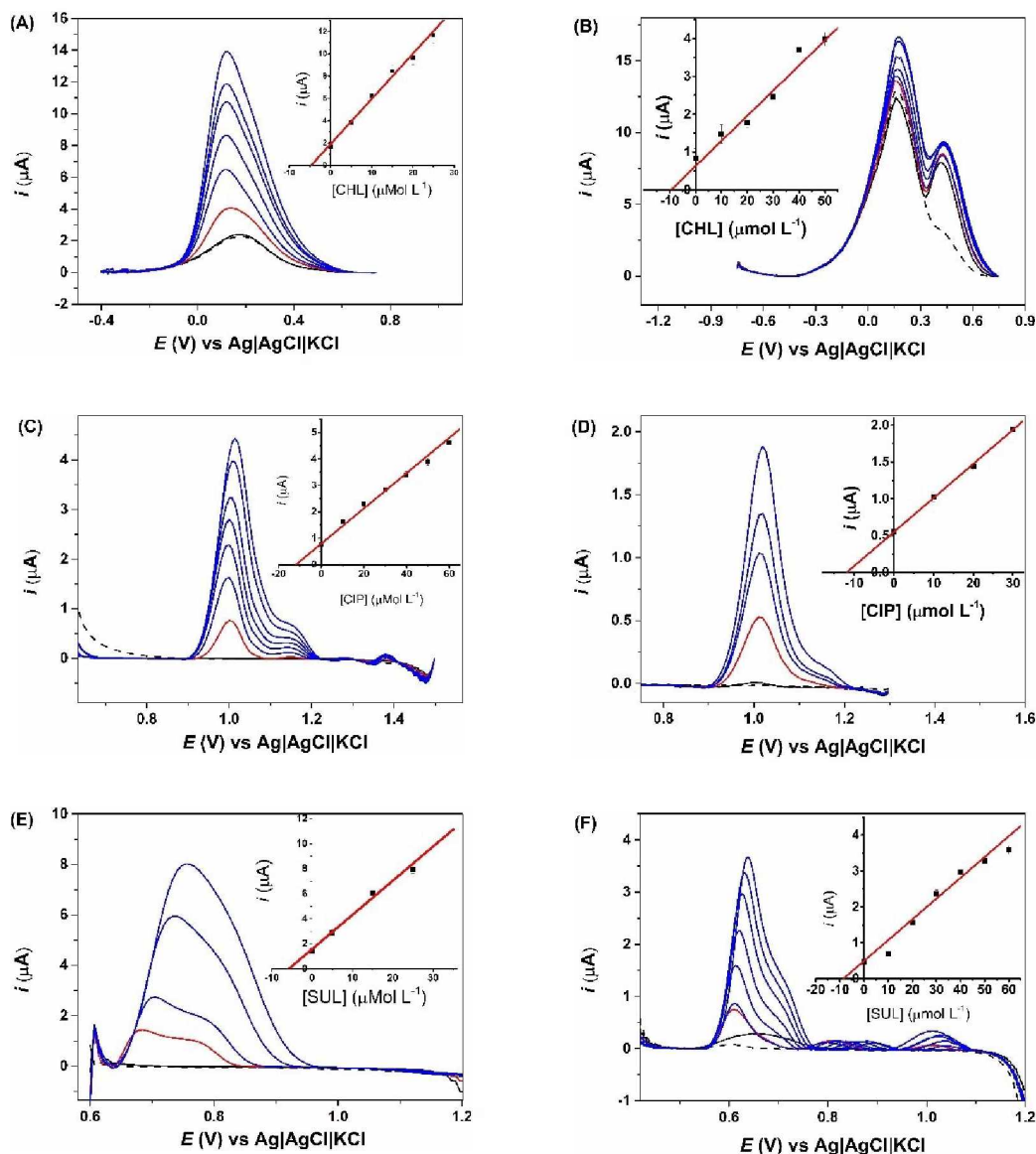


Figure 60. Baseline corrected SWV of water and synthetic urine samples spiked with CHL (A and B), CIP (C and D) and SUL (E and F) using $\text{CO}_2\text{-GS}$ as working electrode. Water samples were diluted 2 times directly in the supporting electrolyte, while synthetic urine was diluted 100 times. Dashed lines represent the blanks, black lines represent the voltammograms in the presence of tap water and synthetic urine, red line represents previously spiked tap water and synthetic urine samples and blue lines represents susceptible standard additions. SWV conditions: see Table 14. The insets represent the respective linear adjustments.

Table 18. Results obtained from the recovery studies in tap water and synthetic urine samples spiked with CHL, CIP and SUL. (n=3)

Analyte	Spiked ($\mu\text{mol L}^{-1}$)	Found ($\mu\text{mol L}^{-1}$)	Recovery (%)	Spiked ($\mu\text{mol L}^{-1}$)	Found ($\mu\text{mol L}^{-1}$)	Recovery (%)
	Tap water			Synthetic urine		
CHL	5.0	4.7 \pm 0.6	94 \pm 13	10.0	9.5 \pm 0.5	95 \pm 5
CIP	10.0	11.9 \pm 0.9	119 \pm 9	10.0	11.8 \pm 0.2	118 \pm 2
SUL	5.0	5.7 \pm 0.8	115 \pm 13	10.0	8.5 \pm 0.7	85 \pm 7

4. Conclusion

We demonstrated that treating graphite sheets with CO₂ plasma, significantly improved electrochemical responses for detecting different classes of antibiotics (amphenicol, sulphanilamide, and fluoroquinolone). This is attributed to the increased surface area, and especially to the structural disorder and presence of oxygen functional groups, which confer electrocatalytic effects. This treatment approach is advantageous compared to other surface modification procedures (drop-casting, spin coating, electrodeposition, among others) because it is reagentless, fast (2 min) and stable. Moreover, the proposed method was able to separately determine CHL, SUL and CIP in water and urine samples, and can also be useful for qualitative proposals (screening tests). However, efforts should be made to achieve simultaneous electrochemical monitoring of these antibiotics, mainly in aquatic environments. On the other hand, this work opens opportunities for the developed electrochemical platform to be explored for other species of antibiotics, in particular, those recently used in the SARS-CoV-2 pandemic.

GENERAL CONCLUSIONS

In this thesis it was demonstrated that CO₂ and O₂ cold plasma treatments significantly change the surfaces of both carbon materials studied. It was possible to characterize its structures and apply both surfaces as electrodes in electroanalysis, and compare the changes in their performances.

- Using the oxygen cold plasma treated 3D-printed CB-PLA electrode it was possible to construct analytical curves for the neurotransmitter Dopamine and the biomarker Nitrite with low limits of detection (0.007 and 0.86 $\mu\text{mol L}^{-1}$ respectively). Additionally, it was possible to detect these molecules in the presence of human saliva, with recovery values between 78% and 109%.
- Using the oxygen cold plasma treated pyrolytic graphite sheet (PGS) electrode, it was possible to create an analytical method for the detection of MDMA, which is a psychoactive substance present in ecstasy tablets, with a limit of detection of 0.09 $\mu\text{mol L}^{-1}$. Theoretical simulations demonstrated that the interaction of the plasma treated GS with the molecule was higher than the one with the untreated electrode. The method allows the detection of this drug even in the presence of other psychoactive substances, illicit drugs and adulterants commonly found in ecstasy tablets. The identification of this analyte in real human saliva and in a real seized sample (provided by Policia Civil – DF and by volunteers) was also possible.
- Using the carbon dioxide plasma treated PGS electrode it was possible to produce analytical methods for the detection and quantification of different antibiotics from different groups. The limit of detection for Chloramphenicol, Ciprofloxacin and Sulphanilamide achieved low limits of detection (0.08, 0.01 and 0.11 $\mu\text{mol L}^{-1}$ respectively). Also, these contaminants were successfully determined and quantified in the presence of tap water, with recovery values between 94% and 119%.

Cold plasma treatment can successfully increase the material's surface functional groups, generate surface defects and enhance both CB-PLA and GS conductivity. Therefore, this treatment can be used in large scale, producing low-cost devices for electrochemical analysis. Additionally, other carbonaceous materials can be studied after

cold plasma treated, intended to understand if this procedure is applicable in other carbon surfaces.

As a perspective, the use of cold plasma to treat carbon materials surfaces generates functional groups, who can enhance the interaction between the electrode and the targeted molecules. Additionally, it can generate fractures that can either expose catalytic active sites or edge conductive planes, depending on the surface. The most impressive feature of cold plasma treatment is the possibility to be applied in large scale. When coupled with additive manufacture, or cheap electrodes commercially available, the proposed techniques presented here can provide highly sensitive and affordable sensors for everyday and portable analysis.

REFERENCES

- Abalyaeva, V.V., Efimov, M.N., Efimov, O.N., Karpacheva, G.P., Dremova, N.N., Kabachkov, E.N., Muratov, D.G., 2020. Electrochemical synthesis of composite based on polyaniline and activated IR pyrolyzed polyacrylonitrile on graphite foil electrode for enhanced supercapacitor properties. *Electrochim. Acta* 354, 136671. <https://doi.org/10.1016/j.electacta.2020.136671>
- Abraham, M.J., Murtola, T., Schulz, R., Páll, S., Smith, J.C., Hess, B., Lindahl, E., 2015. GROMACS: High performance molecular simulations through multi-level parallelism from laptops to supercomputers. *SoftwareX* 1–2, 19–25. <https://doi.org/10.1016/j.softx.2015.06.001>
- Adetayo, A., Runsewe, D., 2019. Synthesis and Fabrication of Graphene and Graphene Oxide: A Review. *Open J. Compos. Mater.* 09, 207–229. <https://doi.org/10.4236/ojcm.2019.92012>
- Aumnate, C., Pongwisuthiruchte, A., Pattananuwat, P., Potiyaraj, P., 2018. Fabrication of ABS/Graphene Oxide Composite Filament for Fused Filament Fabrication (FFF) 3D Printing. *Adv. Mater. Sci. Eng.* 2018, 1–9. <https://doi.org/10.1155/2018/2830437>
- Bagheri, H., Damase-Michel, C., Lapeyre-Mestre, M., Cismondo, S., O'Connell, D., Senard, J.-M., Rascol, O., Montastruc, J.-L., 1999. A Study of Salivary Secretion in Parkinson's Disease.
- Bagheri, H., Khoshsafar, H., Amidi, S., Hosseinzadeh Ardakani, Y., 2016. Fabrication of an electrochemical sensor based on magnetic multi-walled carbon nanotubes for the determination of ciprofloxacin. *Anal. Methods* 8, 3383–3390. <https://doi.org/10.1039/C5AY03410H>
- Bandodkar, A.J., Wang, J., 2014. Non-invasive wearable electrochemical sensors: a review. *Trends Biotechnol.* 32, 363–371. <https://doi.org/10.1016/j.tibtech.2014.04.005>
- Bao, L., Dorgan, J.R., Knauss, D., Hait, S., Oliveira, N.S., Maruccho, I.M., 2006. Gas permeation properties of poly(lactic acid) revisited. *J. Memb. Sci.* 285, 166–172. <https://doi.org/10.1016/j.memsci.2006.08.021>
- Bard, A.J., Faulkner, L.R., Bagotsky, V.S., 2001. *Electrochemical Methods*

Fundamentals of Electrochemistry, John Wiley & Sons, Inc.

- Barton, M.D., Hart, W.S., 2001. Public Health Risks: Antibiotic Resistance - Review -. *Asian-Australasian J. Anim. Sci.* 14, 414–422. <https://doi.org/10.5713/ajas.2001.414>
- Becke, A.D., 1993. Density-functional thermochemistry. III. The role of exact exchange. *J. Chem. Phys.* 98, 5648–5652. <https://doi.org/10.1063/1.464913>
- Beitollahi, H., Tajik, S., Di Bartolomeo, A., 2022. Application of MnO₂ Nanorod–Ionic Liquid Modified Carbon Paste Electrode for the Voltammetric Determination of Sulfanilamide. *Micromachines* 13, 598. <https://doi.org/10.3390/mi13040598>
- Bernalte, E., Sánchez, C.M., Gil, E.P., 2011. Determination of mercury in ambient water samples by anodic stripping voltammetry on screen-printed gold electrodes. *Anal. Chim. Acta* 689, 60–64. <https://doi.org/10.1016/j.aca.2011.01.042>
- Bezerra da Silva, R.A., Rodrigues Cunha, R., Coelho da Silva, A.T., Bessa de Oliveira, A.L., Salmen Espindola, F., Abarza Munoz, R.A., Richter, E.M., 2011. Development of a Simple and Fast Electrochemical Method to Evaluate Physical Stress in Athletes. *Electroanalysis* 23, 2601–2606. <https://doi.org/10.1002/elan.201100326>
- Brett, C.M.A., Brett, A.M.O., 1993. *Electrochemical Methods: Fundamentals and Applications*, 1st ed. Oxford University Press Inc., New York.
- Brocenschi, R.F., Hammer, P., Deslouis, C., Rocha-Filho, R.C., 2016. Assessments of the Effect of Increasingly Severe Cathodic Pretreatments on the Electrochemical Activity of Polycrystalline Boron-Doped Diamond Electrodes. *Anal. Chem.* 88, 5363–5368. <https://doi.org/10.1021/acs.analchem.6b00676>
- Brooks, T., Keevil, C.W., 1997. A simple artificial urine for the growth of urinary pathogens. *Lett. Appl. Microbiol.* 24, 203–206. <https://doi.org/10.1046/j.1472-765X.1997.00378.x>
- Browne, M.P., Novotný, F., Sofer, Z., Pumera, M., 2018. 3D Printed Graphene Electrodes' Electrochemical Activation. *ACS Appl. Mater. Interfaces* 10, 40294–40301. <https://doi.org/10.1021/acsami.8b14701>
- Bulcão, R., Garcia, S.C., Limberger, R.P., Baierle, M., Arbo, M.D., Chasin, A.A. da M.,

- Thiesen, F.V., Tavares, R., 2012. Designer drugs: aspectos analíticos e biológicos. *Quim. Nova* 35, 149–158. <https://doi.org/10.1590/S0100-40422012000100027>
- Bussi, G., Donadio, D., Parrinello, M., 2007. Canonical sampling through velocity rescaling. *J. Chem. Phys.* 126. <https://doi.org/10.1063/1.2408420>
- Cai, W., Lai, T., Du, H., Ye, J., 2014. Electrochemical determination of ascorbic acid, dopamine and uric acid based on an exfoliated graphite paper electrode: A high performance flexible sensor. *Sensors Actuators, B Chem.* 193, 492–500. <https://doi.org/10.1016/j.snb.2013.12.004>
- Camargo, J.R., Orzari, L.O., Araújo, D.A.G., de Oliveira, P.R., Kalinke, C., Rocha, D.P., Luiz dos Santos, A., Takeuchi, R.M., Munoz, R.A.A., Bonacin, J.A., Janegitz, B.C., 2021. Development of conductive inks for electrochemical sensors and biosensors. *Microchem. J.* 164, 105998. <https://doi.org/10.1016/j.microc.2021.105998>
- Cançado, L.G., Takai, K., Enoki, T., Endo, M., Kim, Y.A., Mizusaki, H., Jorio, A., Coelho, L.N., Magalhães-Paniago, R., Pimenta, M.A., 2006. General equation for the determination of the crystallite size L_a of nanographite by Raman spectroscopy. *Appl. Phys. Lett.* 88, 163106. <https://doi.org/10.1063/1.2196057>
- Cardoso, R.M., Kalinke, C., Rocha, R.G., dos Santos, P.L., Rocha, D.P., Oliveira, P.R., Janegitz, B.C., Bonacin, J.A., Richter, E.M., Munoz, R.A.A., 2020a. Additive-manufactured (3D-printed) electrochemical sensors: A critical review. *Anal. Chim. Acta* 1118, 73–91. <https://doi.org/10.1016/j.aca.2020.03.028>
- Cardoso, R.M., Mendonça, D.M.H., Silva, W.P., Silva, M.N.T., Nossol, E., da Silva, R.A.B., Richter, E.M., Muñoz, R.A.A., 2018. 3D printing for electroanalysis: From multiuse electrochemical cells to sensors. *Anal. Chim. Acta* 1033, 49–57. <https://doi.org/10.1016/j.aca.2018.06.021>
- Cardoso, R.M., Rocha, D.P., Rocha, R.G., Stefano, J.S., Silva, R.A.B., Richter, E.M., Muñoz, R.A.A., 2020b. 3D-printing pen versus desktop 3D-printers: Fabrication of carbon black/polylactic acid electrodes for single-drop detection of 2,4,6-trinitrotoluene. *Anal. Chim. Acta* 1132, 10–19. <https://doi.org/10.1016/j.aca.2020.07.034>
- Cardoso, R.M., Silva, P.R.L., Lima, A.P., Rocha, D.P., Oliveira, T.C., do Prado, T.M., Fava, E.L., Fatibello-Filho, O., Richter, E.M., Muñoz, R.A.A., 2020c. 3D-Printed

- graphene/polylactic acid electrode for bioanalysis: Biosensing of glucose and simultaneous determination of uric acid and nitrite in biological fluids. *Sensors Actuators B Chem.* 307, 127621. <https://doi.org/10.1016/j.snb.2019.127621>
- Carvalho, F.H.O., Vaz, A.R., Moshkalev, S., Gelamo, R.V., 2015. Synthesis of Carbon Nanostructures Near Room Temperature Using Microwave PECVD. *Mater. Res.* 18, 860–866. <https://doi.org/10.1590/1516-1439.005315>
- Cercado, B., Cházaro-Ruiz, L.F., Trejo-Córdova, G., Buitrón, G., Razo-Flores, E., 2016. Characterization of oxidized carbon foil as a low-cost alternative to carbon felt-based electrodes in bioelectrochemical systems. *J. Appl. Electrochem.* 46, 217–227. <https://doi.org/10.1007/s10800-015-0906-0>
- Chauhan, R., Gill, A.A.S., Nate, Z., Karpoomath, R., 2020. Highly selective electrochemical detection of ciprofloxacin using reduced graphene oxide/poly(phenol red) modified glassy carbon electrode. *J. Electroanal. Chem.* 871, 114254. <https://doi.org/10.1016/j.jelechem.2020.114254>
- Chen, S., Wang, C., Zhang, M., Zhang, W., Qi, J., Sun, X., Wang, L., Li, J., 2020. N-doped Cu-MOFs for efficient electrochemical determination of dopamine and sulfanilamide. *J. Hazard. Mater.* 390, 122157. <https://doi.org/10.1016/j.jhazmat.2020.122157>
- Chen, Y., Guo, L., Johnson, D., Prince, R., 1998. Plasma-induced low-temperature growth of graphitic nanofibers on nickel substrates. *J. Cryst. Growth* 193, 342–346. [https://doi.org/10.1016/S0022-0248\(98\)00538-7](https://doi.org/10.1016/S0022-0248(98)00538-7)
- Chénard, A., 2022. Subsection 56(1) class exemption for practitioners, agents, pharmacists, persons in charge of a hospital, hospital employees, and licensed dealers to conduct activities with psilocybin and MDMA in relation to a special access program authorization [WWW Document]. Subsect. 56(1) Cl. Exempt. Pract. agents, Pharm. Pers. Charg. a Hosp. Hosp. employees, Licens. Deal. to Conduct Act. with psilocybin MDMA Relat. to a Spec. access Progr. Auth. URL <https://www.canada.ca/en/health-canada/services/health-concerns/controlled-substances-precursor-chemicals/policy-regulations/policy-documents/subsection-56-1-class-exemption-conducting-activities-psilocybin-mdma-special-access-program-authorization.html> (accessed 5.10.22).

- Choi, W.S., Choi, S.-H., Hong, B., Lee, J.-H., 2006. Growth of carbon nanotubes on glass substrate by MPECVD. *Mater. Sci. Eng. C* 26, 1215–1218. <https://doi.org/10.1016/j.msec.2005.09.065>
- Concheiro, M., De Castro, A., Quintela, O., López-Rivadulla, M., Cruz, A., 2005. Determination of MDMA, MDA, MDEA and MBDB in oral fluid using high performance liquid chromatography with native fluorescence detection. *Forensic Sci. Int.* 150, 221–226. <https://doi.org/10.1016/j.forsciint.2004.12.041>
- Conrads, H., Schmidt, M., 2000. Plasma generation and plasma sources. *Plasma Sources Sci. Technol.* 9, 441–454. <https://doi.org/10.1088/0963-0252/9/4/301>
- Couto, R.A.S., Costa, S.S., Mounsef, B., Pacheco, J.G., Fernandes, E., Carvalho, F., Rodrigues, C.M.P., Delerue-Matos, C., Braga, A.A.C., Moreira Gonçalves, L., Quinaz, M.B., 2019. Electrochemical sensing of ecstasy with electropolymerized molecularly imprinted poly(o-phenylenediamine) polymer on the surface of disposable screen-printed carbon electrodes. *Sensors Actuators, B Chem.* 290, 378–386. <https://doi.org/10.1016/j.snb.2019.03.138>
- Cumba, L.R., Smith, J.P., Zuway, K.Y., Sutcliffe, O.B., Do Carmo, D.R., Banks, C.E., 2016. Forensic electrochemistry: Simultaneous voltammetric detection of MDMA and its fatal counterpart “dr Death” (PMA). *Anal. Methods* 8, 142–152. <https://doi.org/10.1039/c5ay02924d>
- Cunha, R.L., Oliveira, C. da S.L., de Oliveira, A.L., Maldaner, A.O., do Desterro Cunha, S., Pereira, P.A.P., 2023. An overview of New Psychoactive Substances (NPS) in northeast Brazil: NMR-based identification and analysis of ecstasy tablets by GC-MS. *Forensic Sci. Int.* 344, 111597. <https://doi.org/10.1016/j.forsciint.2023.111597>
- da Cunha, K.F., Oliveira, K.D., Cardoso, M.S., Arantes, A.C.F., Coser, P.H.P., Lima, L. de N., Maluf, A.C.S., Comis, M.A. de C., Huestis, M.A., Costa, J.L., 2021. Prevalence of new psychoactive substances (NPS) in Brazil based on oral fluid analysis of samples collected at electronic music festivals and parties. *Drug Alcohol Depend.* 227, 108962. <https://doi.org/10.1016/j.drugalcdep.2021.108962>
- da Cunha, K.F., Oliveira, K.D., Huestis, M.A., Costa, J.L., 2020. Screening of 104 New Psychoactive Substances (NPS) and Other Drugs of Abuse in Oral Fluid by LC-MS-MS. *J. Anal. Toxicol.* 44, 697–707. <https://doi.org/10.1093/jat/bkaa089>

- da Silva, C.C., de Faria Lima, A., Moreto, J.A., Dantas, S., Alves Henrique, M., Pasquini, D., Cipriano Rangel, E., Scarmínio, J., Gelamo, R.V., 2020. Influence of plasma treatment on the physical and chemical properties of sisal fibers and environmental application in adsorption of methylene blue. *Mater. Today Commun.* 23, 101140. <https://doi.org/10.1016/j.mtcomm.2020.101140>
- da Silva, S.M., Squissato, A.L., Rocha, D.P., Vasconcellos, M.L.S., de Q. Ferreira, R., Richter, E.M., Munoz, R.A.A., 2020. Improved anodic stripping voltammetric detection of zinc on a disposable screen-printed gold electrode. *Ionics (Kiel)*. 26, 2611–2621. <https://doi.org/10.1007/s11581-019-03379-6>
- Dabhade, R. V., Bodas, D.S., Gangal, S.A., 2004. Plasma-treated polymer as humidity sensing material - A feasibility study. *Sensors Actuators, B Chem.* 98, 37–40. <https://doi.org/10.1016/j.snb.2003.08.020>
- Dai, M., 2022. Sulfur-doped Graphene-coated Graphite Foil as Disposable Electrodes for Electrochemical Sensing. *Int. J. Electrochem. Sci.* ArticleID:221033. <https://doi.org/10.20964/2022.10.18>
- de Faria, L., Pereira, J., Azevedo, G., Matos, M., Munoz, R., Matos, R., 2019. Square-Wave Voltammetry Determination of Ciprofloxacin in Pharmaceutical Formulations and Milk Using a Reduced Graphene Oxide Sensor. *J. Braz. Chem. Soc.* <https://doi.org/10.21577/0103-5053.20190108>
- de Faria, L.V., Lisboa, T.P., Alves, G.F., Farias, D.M., Matos, M.A.C., Muñoz, R.A.A., Matos, R.C., 2020. Electrochemical Study of Different Sensors for Simple and fast Quantification of Ciprofloxacin in Pharmaceutical Formulations and Bovine Milk. *Electroanalysis* 32, 2266–2272. <https://doi.org/10.1002/elan.202060211>
- de Faria, L.V., Lisboa, T.P., Campos, N. da S., Alves, G.F., Matos, M.A.C., Matos, R.C., Munoz, R.A.A., 2021. Electrochemical methods for the determination of antibiotic residues in milk: A critical review. *Anal. Chim. Acta* 1173, 338569. <https://doi.org/10.1016/j.aca.2021.338569>
- de Faria, L. V., Rocha, R.G., Arantes, L.C., Ramos, D.L.O., Lima, C.D., Richter, E.M., P dos Santos, W.T., Muñoz, R.A.A., 2022. Cyclic square-wave voltammetric discrimination of the amphetamine-type stimulants MDA and MDMA in real-world forensic samples by 3D-printed carbon electrodes. *Electrochim. Acta* 429, 141002.

<https://doi.org/10.1016/j.electacta.2022.141002>

de Moraes Moura, G., da Silva, C.C., Naves, E.A.A., Moreto, J.A., Ferreira, D.C., de Oliveira, P.R., Kalinke, C., Scarminio, J., de Siervo, A., da Cunha, T.H.R., Gelamo, R.V., 2021. On the physical and electrochemical properties of MLG-based electrode surfaces modified by microwave-assisted reactive plasma. *Mater. Sci. Eng. B* 272, 115346. <https://doi.org/10.1016/j.mseb.2021.115346>

DeClements, R., Swain, G.M., Dallas, T., Holtz, M.W., Herrick, R.D., Stickney, J.L., 1996. Electrochemical and Surface Structural Characterization of Hydrogen Plasma Treated Glassy Carbon Electrodes. *Langmuir* 12, 6578–6586. <https://doi.org/10.1021/la960380v>

Di-Oliveira, M., Rocha, R.G., de Faria, L. V., Richter, E.M., Munoz, R.A.A., 2022. Carbon-Black Integrated Polylactic Acid Electrochemical Sensor for Chloramphenicol Determination in Milk and Water Samples. *J. Electrochem. Soc.* 169, 047517. <https://doi.org/10.1149/1945-7111/ac6454>

Dias, C.I., Mano, J.F., Alves, N.M., 2008. pH-Responsive biomineralization onto chitosan grafted biodegradable substrates. *J. Mater. Chem.* 18, 2493. <https://doi.org/10.1039/b800776d>

Dichtl, C., Sippel, P., Krohns, S., 2017. Dielectric Properties of 3D Printed Polylactic Acid. *Adv. Mater. Sci. Eng.* 2017, 1–10. <https://doi.org/10.1155/2017/6913835>

Ding, R., Chen, Y., Wang, Q., Wu, Z., Zhang, X., Li, B., Lin, L., 2022. Recent advances in quantum dots-based biosensors for antibiotics detection. *J. Pharm. Anal.* 12, 355–364. <https://doi.org/10.1016/j.jpha.2021.08.002>

Dizon, J.R.C., Espera, A.H., Chen, Q., Advincula, R.C., 2018. Mechanical characterization of 3D-printed polymers. *Addit. Manuf.* 20, 44–67. <https://doi.org/10.1016/j.addma.2017.12.002>

Dodda, L.S., Cabeza de Vaca, I., Tirado-Rives, J., Jorgensen, W.L., 2017a. LigParGen web server: an automatic OPLS-AA parameter generator for organic ligands. *Nucleic Acids Res.* 45, W331–W336. <https://doi.org/10.1093/nar/gkx312>

Dodda, L.S., Vilseck, J.Z., Tirado-Rives, J., Jorgensen, W.L., 2017b. 1.14*CM1A-LBCC: Localized Bond-Charge Corrected CM1A Charges for Condensed-Phase

- Simulations. *J. Phys. Chem. B* 121, 3864–3870.
<https://doi.org/10.1021/acs.jpcc.7b00272>
- dos Santos, P.L., Katic, V., Loureiro, H.C., dos Santos, M.F., dos Santos, D.P., Formiga, A.L.B., Bonacin, J.A., 2019. Enhanced performance of 3D printed graphene electrodes after electrochemical pre-treatment: Role of exposed graphene sheets. *Sensors Actuators, B Chem.* 281, 837–848.
<https://doi.org/10.1016/j.snb.2018.11.013>
- Downing, J., 1986. The Psychological and Physiological Effects of MDMA on Normal Volunteers. *J. Psychoactive Drugs* 18, 335–340.
<https://doi.org/10.1080/02791072.1986.10472366>
- Engelhardt, H., Neue, U.D., 1982. Reaction detector with three dimensional coiled open tubes in HPLC. *Chromatographia* 15, 403–408.
<https://doi.org/10.1007/BF02261598>
- Erowid Center, 2022. DrugsData [WWW Document]. DrugsData.org lab Anal. /drug checking Recreat. drugs, (n.d.). URL <https://www.drugsdata.org/> (accessed 2.8.22).
- Essmann, U., Perera, L., Berkowitz, M.L., Darden, T., Lee, H., Pedersen, L.G., 1995. A smooth particle mesh Ewald method. *J. Chem. Phys.* 103, 8577–8593.
<https://doi.org/10.1063/1.470117>
- Feltham, A.M., Spiro, M., 1971. Platinized platinum electrodes. *Chem. Rev.* 71, 177–193. <https://doi.org/10.1021/cr60270a002>
- Franceschini, E.A., Lacconi, G.I., 2017. Spectroelectrochemical analysis of HOPG surface controlled modification. *Appl. Surf. Sci.* 400, 254–261.
<https://doi.org/10.1016/j.apsusc.2016.12.115>
- Frank-Kamenetskii, D.A., 1972. Plasma: The Fourth State of Matter. Springer US, Boston, MA. <https://doi.org/10.1007/978-1-4684-1896-5>
- Gabbana, J.V., de Oliveira, L.H., Pavoglio, G.C., Trindade, M.A.G., 2018. Narrowing the interface between sample preparation and electrochemistry: Trace-level determination of emerging pollutant in water samples after in situ microextraction and electroanalysis using a new cell configuration. *Electrochim. Acta* 275, 67–75.
<https://doi.org/10.1016/j.electacta.2018.04.134>

- García-Miranda Ferrari, A., Foster, C., Kelly, P., Brownson, D., Banks, C., 2018. Determination of the Electrochemical Area of Screen-Printed Electrochemical Sensing Platforms. *Biosensors* 8, 53. <https://doi.org/10.3390/bios8020053>
- Garrido, E.M.P.J., Garrido, J.M.P.J., Milhazes, N., Borges, F., Oliveira-Brett, A.M., 2010. Electrochemical oxidation of amphetamine-like drugs and application to electroanalysis of ecstasy in human serum. *Bioelectrochemistry* 79, 77–83. <https://doi.org/10.1016/j.bioelechem.2009.12.002>
- George, J.M., Antony, A., Mathew, B., 2018. Metal oxide nanoparticles in electrochemical sensing and biosensing: a review. *Microchim. Acta* 185, 358. <https://doi.org/10.1007/s00604-018-2894-3>
- Giorgini Escobar, J., Vaněčková, E., Nováková Lachmanová, Š., Vivaldi, F., Heyda, J., Kubišta, J., Shestivska, V., Španěl, P., Schwarzová-Pecková, K., Rathouský, J., Sebechlebská, T., Kolivoška, V., 2020. The development of a fully integrated 3D printed electrochemical platform and its application to investigate the chemical reaction between carbon dioxide and hydrazine. *Electrochim. Acta* 360, 136984. <https://doi.org/10.1016/j.electacta.2020.136984>
- Gopakumar, D.A., Arumukhan, V., Gelamo, R. V., Pasquini, D., de Moraes, L.C., Rizal, S., Hermawan, D., Nzihou, A., Khalil, H.P. A., 2019. Carbon dioxide plasma treated PVDF electrospun membrane for the removal of crystal violet dyes and iron oxide nanoparticles from water. *Nano-Structures & Nano-Objects* 18, 100268. <https://doi.org/10.1016/j.nanoso.2019.100268>
- Gosser, D.K., 1994. Cyclic Voltammetry; Simulation and Analysis of Reaction Mechanisms. *Synth. React. Inorg. Met. Chem.* 24, 1237–1238. <https://doi.org/10.1080/00945719408001398>
- Granger II, R.M., Yochum, H.M., Granger, J.N., Sienerth, K.D., 2017. *Instrumental Analysis*, 1st ed. Oxford University Press Inc., New York.
- Green, A.R., Mehan, A.O., Elliott, J.M., O’Shea, E., Colado, M.I., 2003. The Pharmacology and Clinical Pharmacology of 3,4-Methylenedioxymethamphetamine (MDMA, “Ecstasy”). *Pharmacol. Rev.* 55, 463–508. <https://doi.org/10.1124/pr.55.3.3>
- Grill, A., 1999. Diamond-like carbon: state of the art. *Diam. Relat. Mater.* 8, 428–434.

[https://doi.org/10.1016/S0925-9635\(98\)00262-3](https://doi.org/10.1016/S0925-9635(98)00262-3)

Grisdale, R.O., Pfister, A.C., Van Roosbroeck, W., 1951. Pyrolytic Film Resistors: Carbon and Borocarbon. *Bell Syst. Tech. J.* 30, 271–314. <https://doi.org/10.1002/j.1538-7305.1951.tb03660.x>

Groenewald, T., 1975. Electrochemical studies on gold electrodes in acidic solutions of thiourea containing gold (I) thiourea complex ions. *J. Appl. Electrochem.* 5, 71–78. <https://doi.org/10.1007/BF00625961>

Guima, K.-E., Souza, V.H.R., Martins, C.A., 2019. Insulating 3D-printed templates are turned into metallic electrodes: application as electrodes for glycerol electrooxidation. *RSC Adv.* 9, 15158–15161. <https://doi.org/10.1039/C9RA01436E>

Gusmão, R., Browne, M.P., Sofer, Z., Pumera, M., 2019. The capacitance and electron transfer of 3D-printed graphene electrodes are dramatically influenced by the type of solvent used for pre-treatment. *Electrochem. commun.* 102, 83–88. <https://doi.org/10.1016/j.elecom.2019.04.004>

Hadi, M., Rouhollahi, A., 2012. Simultaneous electrochemical sensing of ascorbic acid, dopamine and uric acid at anodized nanocrystalline graphite-like pyrolytic carbon film electrode. *Anal. Chim. Acta* 721, 55–60. <https://doi.org/10.1016/j.aca.2012.01.051>

Hamzah, H.H., Shafiee, S.A., Abdalla, A., Patel, B.A., 2018. 3D printable conductive materials for the fabrication of electrochemical sensors: A mini review. *Electrochem. commun.* 96, 27–31. <https://doi.org/10.1016/j.elecom.2018.09.006>

Hehre, W.J., Ditchfield, R., Pople, J.A., 1972. Self—Consistent Molecular Orbital Methods. XII. Further Extensions of Gaussian—Type Basis Sets for Use in Molecular Orbital Studies of Organic Molecules. *J. Chem. Phys.* 56, 2257–2261. <https://doi.org/10.1063/1.1677527>

Hess, B., 2008. P-LINCS: A Parallel Linear Constraint Solver for Molecular Simulation. *J. Chem. Theory Comput.* 4, 116–122. <https://doi.org/10.1021/ct700200b>

Hofmann, S., Ducati, C., Robertson, J., Kleinsorge, B., 2003. Low-temperature growth of carbon nanotubes by plasma-enhanced chemical vapor deposition. *Appl. Phys. Lett.* 83, 135–137. <https://doi.org/10.1063/1.1589187>

- Hubbard, A.T., Ishikawa, R.M., Katekaru, J., 1978. Study of platinum electrodes by means of electrochemistry and low-energy electron diffraction. *J. Electroanal. Chem. Interfacial Electrochem.* 86, 271–288. [https://doi.org/10.1016/S0022-0728\(78\)80003-5](https://doi.org/10.1016/S0022-0728(78)80003-5)
- Hulanicki, A., Glab, S., Ingman, F., 1991. Chemical sensors: definitions and classification. *Pure Appl. Chem.* 63, 1247–1250. <https://doi.org/10.1351/pac199163091247>
- Humphrey, W., Dalke, A., Schulten, K., 1996. VMD: Visual molecular dynamics. *J. Mol. Graph.* 14, 33–38. [https://doi.org/10.1016/0263-7855\(96\)00018-5](https://doi.org/10.1016/0263-7855(96)00018-5)
- Janata, J., 2009. *Principles of Chemical Sensors*, 2nd ed. Springer US, Atlanta.
- Jaysiva, G., Manavalan, S., Chen, S.-M., Veerakumar, P., Keerthi, M., Tu, H.-S., 2020. MoN Nanorod/Sulfur-Doped Graphitic Carbon Nitride for Electrochemical Determination of Chloramphenicol. *ACS Sustain. Chem. Eng.* 8, 11088–11098. <https://doi.org/10.1021/acssuschemeng.0c00502>
- João, A.F., Castro, S.V.F., Cardoso, R.M., Gamela, R.R., Rocha, D.P., Richter, E.M., Muñoz, R.A.A., 2020. 3D printing pen using conductive filaments to fabricate affordable electrochemical sensors for trace metal monitoring. *J. Electroanal. Chem.* 876, 114701. <https://doi.org/10.1016/j.jelechem.2020.114701>
- Jorgensen, W.L., Chandrasekhar, J., Madura, J.D., Impey, R.W., Klein, M.L., 1983. Comparison of simple potential functions for simulating liquid water. *J. Chem. Phys.* 79, 926–935. <https://doi.org/10.1063/1.445869>
- Jorgensen, W.L., Maxwell, D.S., Tirado-Rives, J., 1996. Development and Testing of the OPLS All-Atom Force Field on Conformational Energetics and Properties of Organic Liquids. *J. Am. Chem. Soc.* 118, 11225–11236. <https://doi.org/10.1021/ja9621760>
- Kahl, J.M.M., da Cunha, K.F., Rodrigues, L.C., Chinaglia, K.D.O., Oliveira, K.D., Costa, J.L., 2021. Quantification of amphetamine and derivatives in oral fluid by dispersive liquid-liquid microextraction and liquid chromatography—tandem mass spectrometry. *J. Pharm. Biomed. Anal.* 196. <https://doi.org/10.1016/j.jpba.2021.113928>

- Kalinke, C., Neumsteir, N.V., Aparecido, G.D.O., Ferraz, T.V.D.B., Dos Santos, P.L., Janegitz, B.C., Bonacin, J.A., 2020. Comparison of activation processes for 3D printed PLA-graphene electrodes: Electrochemical properties and application for sensing of dopamine. *Analyst* 145, 1207–1218. <https://doi.org/10.1039/c9an01926j>
- Kannan, P.K., Gelamo, R. V., Morgan, H., Suresh, P., Rout, C.S., 2016a. The electrochemical 4-chlorophenol sensing properties of a plasma-treated multilayer graphene modified photolithography patterned platinum electrode. *RSC Adv.* 6, 105920–105929. <https://doi.org/10.1039/c6ra24136k>
- Kannan, P.K., Gelamo, R. V., Morgan, H., Suresh, P., Rout, C.S., 2016b. The electrochemical 4-chlorophenol sensing properties of a plasma-treated multilayer graphene modified photolithography patterned platinum electrode. *RSC Adv.* 6, 105920–105929. <https://doi.org/10.1039/C6RA24136K>
- Karimi-Maleh, H., Karimi, F., Alizadeh, M., Sanati, A.L., 2020. Electrochemical Sensors, a Bright Future in the Fabrication of Portable Kits in Analytical Systems. *Chem. Rec.* 20, 682–692. <https://doi.org/10.1002/tcr.201900092>
- Katayama, J.M.T., Oiye, E.N., Ribeiro, M.F.M., Ipólito, A.J., De Andrade, J.F., De Oliveira, M.F., 2020. MDMA electrochemical determination in aqueous media containing illicit drugs and validation of a voltammetric methodology. *Drug Anal. Res.* 4, 3–11. <https://doi.org/10.22456/2527-2616.101162>
- Kava, A.A., Henry, C.S., 2021. Talanta Exploring carbon particle type and plasma treatment to improve electrochemical properties of stencil-printed carbon electrodes. *Talanta* 221, 121553. <https://doi.org/10.1016/j.talanta.2020.121553>
- Kempahanumakkagari, S., Vellingiri, K., Deep, A., Kwon, E.E., Bolan, N., Kim, K.-H., 2018. Metal–organic framework composites as electrocatalysts for electrochemical sensing applications. *Coord. Chem. Rev.* 357, 105–129. <https://doi.org/10.1016/j.ccr.2017.11.028>
- Khare, R.T., Gelamo, R. V., More, M.A., Late, D.J., Rout, C.S., 2015. Enhanced field emission of plasma treated multilayer graphene. *Appl. Phys. Lett.* 107. <https://doi.org/10.1063/1.4931626>
- Koryta, J., 1972. Discovery of polarography. *J. Chem. Educ.* 49, 183. <https://doi.org/10.1021/ed049p183>

- Kristiawan, R.B., Imaduddin, F., Ariawan, D., Ubaidillah, Arifin, Z., 2021. A review on the fused deposition modeling (FDM) 3D printing: Filament processing, materials, and printing parameters. *Open Eng.* 11, 639–649. <https://doi.org/10.1515/eng-2021-0063>
- Kwon, S., Vidic, R., Borguet, E., 2002. Enhancement of adsorption on graphite (HOPG) by modification of surface chemical functionality and morphology. *Carbon N. Y.* 40, 2351–2358. [https://doi.org/10.1016/S0008-6223\(02\)00155-0](https://doi.org/10.1016/S0008-6223(02)00155-0)
- Larciprete, R., Lacovig, P., Gardonio, S., Baraldi, A., Lizzit, S., 2012. Atomic Oxygen on Graphite: Chemical Characterization and Thermal Reduction. *J. Phys. Chem. C* 116, 9900–9908. <https://doi.org/10.1021/jp2098153>
- Lee, C., Yang, W., Parr, R.G., 1988. Development of the Colle-Salvetti correlation-energy formula into a functional of the electron density. *Phys. Rev. B* 37, 785–789. <https://doi.org/10.1103/PhysRevB.37.785>
- Lee, S.-H., Seo, S.-D., Jin, Y.-H., Shim, H.-W., Kim, D.-W., 2010. A graphite foil electrode covered with electrochemically exfoliated graphene nanosheets. *Electrochem. commun.* 12, 1419–1422. <https://doi.org/10.1016/j.elecom.2010.07.036>
- Li, K., Eres, G., Howe, J., Chuang, Y.-J., Li, X., Gu, Z., Zhang, L., Xie, S., Pan, Z., 2013. Self-Assembly of Graphene on Carbon Nanotube Surfaces. *Sci. Rep.* 3, 2353. <https://doi.org/10.1038/srep02353>
- Li, N., Chen, X., Stoica, L., Xia, W., Qian, J., Aßmann, J., Schuhmann, W., Muhler, M., 2007. The Catalytic Synthesis of Three-Dimensional Hierarchical Carbon Nanotube Composites with High Electrical Conductivity Based on Electrochemical Iron Deposition. *Adv. Mater.* 19, 2957–2960. <https://doi.org/10.1002/adma.200602625>
- Lima, C.D., Couto, R.A.S., Arantes, L.C., Marinho, P.A., Pimentel, D.M., Quinaz, M.B., da Silva, R.A.B., Richter, E.M., Barbosa, S.L., dos Santos, W.T.P., 2020. Electrochemical detection of the synthetic cathinone 3,4-methylenedioxypropylone using carbon screen-printed electrodes: A fast, simple and sensitive screening method for forensic samples. *Electrochim. Acta* 354, 136728. <https://doi.org/10.1016/j.electacta.2020.136728>
- Lisboa, T.P., Alves, G.F., de Faria, L.V., de Souza, C.C., Matos, M.A.C., Matos, R.C.,

2022. 3D-printed electrode an affordable sensor for sulfanilamide monitoring in breast milk, synthetic urine, and pharmaceutical formulation samples. *Talanta* 247, 123610. <https://doi.org/10.1016/j.talanta.2022.123610>
- Liu, W., Zhang, H., Yang, B., Li, Z., Lei, L., Zhang, X., 2015. A non-enzymatic hydrogen peroxide sensor based on vertical NiO nanosheets supported on the graphite sheet. *J. Electroanal. Chem.* 749, 62–67. <https://doi.org/10.1016/j.jelechem.2015.04.037>
- Liu, Z., Wang, Y., Wu, B., Cui, C., Guo, Y., Yan, C., 2019. A critical review of fused deposition modeling 3D printing technology in manufacturing polylactic acid parts. *Int. J. Adv. Manuf. Technol.* 102, 2877–2889. <https://doi.org/10.1007/s00170-019-03332-x>
- Löffler, R., Häffner, M., Visanescu, G., Weigand, H., Wang, X., Zhang, D., Fleischer, M., Meixner, A.J., Fortágh, J., Kern, D.P., 2011. Optimization of plasma-enhanced chemical vapor deposition parameters for the growth of individual vertical carbon nanotubes as field emitters. *Carbon N. Y.* 49, 4197–4203. <https://doi.org/10.1016/j.carbon.2011.05.055>
- Luong, J.H.T., Male, K.B., Glennon, J.D., 2009. Boron-doped diamond electrode: synthesis, characterization, functionalization and analytical applications. *Analyst* 134, 1965. <https://doi.org/10.1039/b910206j>
- Mahmoud, K.H., 2016. Optical properties of hydroxyethyl cellulose film treated with nitrogen plasma. *Spectrochim. Acta Part A Mol. Biomol. Spectrosc.* 157, 153–157. <https://doi.org/10.1016/j.saa.2015.12.029>
- Malon, R.S.P., Sadir, S., Balakrishnan, M., Córcoles, E.P., 2014. Saliva-Based Biosensors: Noninvasive Monitoring Tool for Clinical Diagnostics. *Biomed Res. Int.* 2014, 1–20. <https://doi.org/10.1155/2014/962903>
- Manzanares-Palenzuela, C.L., Hermanova, S., Sofer, Z., Pumera, M., 2019a. Proteinase-sculptured 3D-printed graphene/polylactic acid electrodes as potential biosensing platforms: Towards enzymatic modeling of 3D-printed structures. *Nanoscale* 11, 12124–12131. <https://doi.org/10.1039/c9nr02754h>
- Manzanares-Palenzuela, C.L., Hermanova, S., Sofer, Z., Pumera, M., 2019b. Proteinase-sculptured 3D-printed graphene/polylactic acid electrodes as potential biosensing platforms: towards enzymatic modeling of 3D-printed structures. *Nanoscale* 11,

- 12124–12131. <https://doi.org/10.1039/C9NR02754H>
- Martínez, L., Andrade, R., Birgin, E.G., Martínez, J.M., 2009. PACKMOL: A package for building initial configurations for molecular dynamics simulations. *J. Comput. Chem.* 30, 2157–2164. <https://doi.org/10.1002/jcc.21224>
- Maurer, H.H., Kraemer, T., Springer, D., Staack, R.F., 2004. Chemistry, Pharmacology, Toxicology, and Hepatic Metabolism of Designer Drugs of the Amphetamine (Ecstasy), Piperazine, and Pyrrolidinophenone Types. *Ther. Drug Monit.* 26, 127–131. <https://doi.org/10.1097/00007691-200404000-00007>
- McNamara, R., Kerans, A., O'Neill, B., Harkin, A., 2006. Caffeine promotes hyperthermia and serotonergic loss following co-administration of the substituted amphetamines, MDMA (“Ecstasy”) and MDA (“Love”). *Neuropharmacology* 50, 69–80. <https://doi.org/10.1016/j.neuropharm.2005.08.006>
- Mei, T., Gao, M., Liu, D., Wang, Y., Huang, Y., 2021. Enhanced electrocatalytic activity of carbon cloth by synergetic effect of plasma and acid treatment. *Plasma Sci. Technol.* 23, 025504. <https://doi.org/10.1088/2058-6272/abd8b4>
- Melechko, A. V., Klein, K.L., Fowlkes, J.D., Hensley, D.K., Merkulov, I.A., McKnight, T.E., Rack, P.D., Horton, J.A., Simpson, M.L., 2007. Control of carbon nanostructure: From nanofiber toward nanotube and back. *J. Appl. Phys.* 102, 074314. <https://doi.org/10.1063/1.2786710>
- Mocak, J., Bond, A.M., Mitchell, S., Scollary, G., 1997. A statistical overview of standard (IUPAC and ACS) and new procedures for determining the limits of detection and quantification: Application to voltammetric and stripping techniques (Technical Report). *Pure Appl. Chem.* 69, 297–328. <https://doi.org/10.1351/pac199769020297>
- Mohammadzadeh Kakhki, R., 2019. A review to recent developments in modification of carbon fiber electrodes. *Arab. J. Chem.* 12, 1783–1794. <https://doi.org/10.1016/j.arabjc.2014.11.058>
- Montes, R.H.O., Richter, E.M., Munoz, R.A.A., 2012. Low-potential reduction of sulfite at a ruthenium-oxide hexacyanoferrate modified electrode. *Electrochem. commun.* 21, 26–29. <https://doi.org/10.1016/j.elecom.2012.05.005>
- Montes, R.H.O., Stefano, J.S., Richter, E.M., Munoz, R.A.A., 2014. Exploring

- Multiwalled Carbon Nanotubes for Naproxen Detection. *Electroanalysis* 26, 1449–1453. <https://doi.org/10.1002/elan.201400113>
- Moraes, F.C., Cabral, M.F., Mascaro, L.H., Machado, S.A.S., 2011. The electrochemical effect of acid functionalisation of carbon nanotubes to be used in sensors development. *Surf. Sci.* 605, 435–440. <https://doi.org/10.1016/j.susc.2010.11.014>
- Morgan, M.J., 2000. Ecstasy (MDMA): a review of its possible persistent psychological effects. *Psychopharmacology (Berl)*. 152, 230–248. <https://doi.org/10.1007/s002130000545>
- Moses, P.R., Wler, L., Murray, R.W., 1975. Chemically Modified Tin Oxide Electrode. *Anal. Chem.* 47, 1882–1886. <https://doi.org/10.1021/ac60362a043>
- Moudgil, P., Bedi, J.S., Aulakh, R.S., Gill, J.P.S., Kumar, A., 2019. Validation of HPLC Multi-residue Method for Determination of Fluoroquinolones, Tetracycline, Sulphonamides and Chloramphenicol Residues in Bovine Milk. *Food Anal. Methods* 12, 338–346. <https://doi.org/10.1007/s12161-018-1365-0>
- Murilo Alves, G., Soares Castro, A., McCord, B.R., de Oliveira, M.F., 2021. MDMA Electrochemical Determination and Behavior at Carbon Screen-printed Electrodes: Cheap Tools for Forensic Applications. *Electroanalysis* 33, 635–642. <https://doi.org/10.1002/elan.202060080>
- Naomi Oiye, É., Midori Toia Katayama, J., Fernanda Muzetti Ribeiro, M., Oka Duarte, L., de Castro Baker Botelho, R., José Ipólito, A., Royston McCord, B., Firmino de Oliveira, M., 2020. Voltammetric detection of 3,4-methylenedioxymethamphetamine (mdma) in saliva in low cost systems. *Forensic Chem.* 20, 100268. <https://doi.org/10.1016/j.forc.2020.100268>
- Nevescanin, M., Avramov-Ivic, M., Petrovic, S., Mijin, D., Banovic-Stevic, S., Jovanovic, V., 2013. The use of a gold electrode for the determination of amphetamine derivatives and application to their analysis in human urine. *J. Serbian Chem. Soc.* 78, 1373–1385. <https://doi.org/10.2298/JSC121228032N>
- Ngo, T.D., Kashani, A., Imbalzano, G., Nguyen, K.T.Q., Hui, D., 2018. Additive manufacturing (3D printing): A review of materials, methods, applications and challenges. *Compos. Part B Eng.* 143, 172–196. <https://doi.org/10.1016/j.compositesb.2018.02.012>

- Nicholson, R.S., 1965. Theory and Application of Cyclic Voltammetry for Measurement of Electrode Reaction Kinetics. *Anal. Chem.* 37, 1351–1355. <https://doi.org/10.1021/ac60230a016>
- Nosé, S., Klein, M.L., 1983. Constant pressure molecular dynamics for molecular systems. *Mol. Phys.* 50, 1055–1076. <https://doi.org/10.1080/00268978300102851>
- Nourbakhsh, A., Cantoro, M., Vosch, T., Pourtois, G., Clemente, F., van der Veen, M.H., Hofkens, J., Heyns, M.M., De Gendt, S., Sels, B.F., 2010. Bandgap opening in oxygen plasma-treated graphene. *Nanotechnology* 21, 435203. <https://doi.org/10.1088/0957-4484/21/43/435203>
- Novotný, F., Urbanová, V., Plutnar, J., Pumera, M., 2019. Preserving Fine Structure Details and Dramatically Enhancing Electron Transfer Rates in Graphene 3D-Printed Electrodes via Thermal Annealing: Toward Nitroaromatic Explosives Sensing. *ACS Appl. Mater. Interfaces* 11, 35371–35375. <https://doi.org/10.1021/acsami.9b06683>
- Oldham, K.B., 1979. Analytical expressions for the reversible randles-sevcik function. *J. Electroanal. Chem.* 105, 373–375.
- Pacios, M., del Valle, M., Bartroli, J., Esplandiú, M.J., 2008. Electrochemical behavior of rigid carbon nanotube composite electrodes. *J. Electroanal. Chem.* 619–620, 117–124. <https://doi.org/10.1016/j.jelechem.2008.03.019>
- Papanai, G.S., Sharma, I., Gupta, B.K., 2020. Probing number of layers and quality assessment of mechanically exfoliated graphene via Raman fingerprint. *Mater. Today Commun.* 22, 100795. <https://doi.org/10.1016/j.mtcomm.2019.100795>
- Park, S.J., Cho, K.S., Ryu, S.K., 2003. Filler-elastomer interactions: Influence of oxygen plasma treatment on surface and mechanical properties of carbon black/rubber composites. *Carbon N. Y.* 41, 1437–1442. [https://doi.org/10.1016/S0008-6223\(03\)00088-5](https://doi.org/10.1016/S0008-6223(03)00088-5)
- Parrinello, M., Rahman, A., 1981. Polymorphic transitions in single crystals: A new molecular dynamics method. *J. Appl. Phys.* 52, 7182–7190. <https://doi.org/10.1063/1.328693>
- Patel, A.N., Tan, S., Miller, T.S., Macpherson, J. V., Unwin, P.R., 2013. Comparison and

- Reappraisal of Carbon Electrodes for the Voltammetric Detection of Dopamine. *Anal. Chem.* 85, 11755–11764. <https://doi.org/10.1021/ac401969q>
- Patil, U. V., Pawbake, A.S., Machuno, L.G.B., Gelamo, R. V., Jadkar, S.R., Rout, C.S., Late, D.J., 2016. Effect of plasma treatment on multilayer graphene: X-ray photoelectron spectroscopy, surface morphology investigations and work function measurements. *RSC Adv.* 6, 48843–48850. <https://doi.org/10.1039/c6ra03046g>
- Pedrotti, J.J., Angnes, L., Gutz, I.G.R., 1996. Miniaturized Reference Electrodes with Microporous Polymer Junctions. *Electroanalysis* 8, 673–675. <https://doi.org/10.1002/elan.1140080713>
- Pereira, J.F.S., Borges, P.H.S., Moura, G.M., Gelamo, R. V., Nossol, E., Canobre, S.C., Richter, E.M., Munoz, R.A.A., 2019. Improved electrochemical performance of pyrolytic graphite paper: Electrochemical versus reactive cold-plasma activation. *Electrochem. commun.* 105, 106497. <https://doi.org/10.1016/j.elecom.2019.106497>
- Pérez-Mendoza, M., Domingo-García, M., López-Garzón, F.J., 1999. Modifications produced by O₂ and CO₂ plasma treatments on a glassy carbon: Comparison with molecular gases. *Carbon N. Y.* 37, 1463–1474. [https://doi.org/10.1016/S0008-6223\(99\)00009-3](https://doi.org/10.1016/S0008-6223(99)00009-3)
- Pham-Huu, C., Vieira, R., Louis, B., Carvalho, A., Amadou, J., Dintzer, T., Ledoux, M.J., 2006. About the octopus-like growth mechanism of carbon nanofibers over graphite supported nickel catalyst. *J. Catal.* 240, 194–202. <https://doi.org/10.1016/j.jcat.2006.03.017>
- Pichini, S., Navarro, M., Pacifici, R., Zuccaro, P., Ortuño, J., Farré, M., Roset, P.N., Segura, J., De la Torre, R., 2003. Usefulness of sweat testing for the detection of MDMA after a single-dose administration. *J. Anal. Toxicol.* 27, 294–303. <https://doi.org/10.1093/jat/27.5.294>
- Pimentel, D.M., Arantes, L.C., Santos, L.M., Souza, K.A.O., Verly, R.M., Barbosa, S.L., dos Santos, W.T.P., 2021. Rapid and simple voltammetric screening method for Lysergic Acid Diethylamide (LSD) detection in seized samples using a boron-doped diamond electrode. *Sensors Actuators B Chem.* 344, 130229. <https://doi.org/10.1016/j.snb.2021.130229>
- Pollap, A., Baran, K., Kuszewska, N., Kochana, J., 2020. Electrochemical sensing of

- ciprofloxacin and paracetamol in environmental water using titanium sol based sensor. *J. Electroanal. Chem.* 878, 114574. <https://doi.org/10.1016/j.jelechem.2020.114574>
- Prabhu, S., Vaideki, K., Anitha, S., 2017. Effect of microwave argon plasma on the glycosidic and hydrogen bonding system of cotton cellulose. *Carbohydr. Polym.* 156, 34–44. <https://doi.org/10.1016/j.carbpol.2016.08.057>
- Praveen, K.M., Thomas, S., Grohens, Y., Mozetič, M., Junkar, I., Primc, G., Gorjanc, M., 2016. Investigations of plasma induced effects on the surface properties of lignocellulosic natural coir fibres. *Appl. Surf. Sci.* 368, 146–156. <https://doi.org/10.1016/j.apsusc.2016.01.159>
- Preda, D., David, I.G., Popa, D.-E., Buleandra, M., Radu, G.L., 2022. Recent Trends in the Development of Carbon-Based Electrodes Modified with Molecularly Imprinted Polymers for Antibiotic Electroanalysis. *Chemosensors* 10, 243. <https://doi.org/10.3390/chemosensors10070243>
- Prosser, J.M., Nelson, L.S., 2012. The Toxicology of Bath Salts: A Review of Synthetic Cathinones. *J. Med. Toxicol.* 8, 33–42. <https://doi.org/10.1007/s13181-011-0193-z>
- Rajaji, U., Muthumariappan, A., Chen, S.-M., Chen, T.-W., Tseng, T.-W., Wang, K., Qi, D., Jiang, J., 2019. Facile sonochemical synthesis of porous and hierarchical manganese(III) oxide tiny nanostructures for super sensitive electrocatalytic detection of antibiotic (chloramphenicol) in fresh milk. *Ultrason. Sonochem.* 58, 104648. <https://doi.org/10.1016/j.ultsonch.2019.104648>
- Randles, J.E.B., 1948. A cathode ray polarograph. The current-voltage curves. *Trans. Faraday Soc.* 44, 327–338.
- Rebelo, P., Pacheco, J.G., Voroshylova, I. V., Melo, A., Cordeiro, M.N.D.S., Delerue-Matos, C., 2021. Rational development of molecular imprinted carbon paste electrode for Furazolidone detection: theoretical and experimental approach. *Sensors Actuators B Chem.* 329, 129112. <https://doi.org/10.1016/j.snb.2020.129112>
- Reddy, K.R., Brahman, P.K., Suresh, L., 2018. Fabrication of high performance disposable screen printed electrochemical sensor for ciprofloxacin sensing in biological samples. *Measurement* 127, 175–186. <https://doi.org/10.1016/j.measurement.2018.05.078>

- Redondo, E., Muñoz, J., Pumera, M., 2021. Green activation using reducing agents of carbon-based 3D printed electrodes: Turning good electrodes to great. *Carbon* N. Y. 175, 413–419. <https://doi.org/10.1016/j.carbon.2021.01.107>
- Ren, Z.F., Huang, Z.P., Xu, J.W., Wang, J.H., Bush, P., Siegal, M.P., Provencio, P.N., 1998. Synthesis of Large Arrays of Well-Aligned Carbon Nanotubes on Glass. *Science* (80-.). 282, 1105–1107. <https://doi.org/10.1126/science.282.5391.1105>
- Renò, F., D'Angelo, D., Gottardi, G., Rizzi, M., Aragno, D., Piacenza, G., Cartasegna, F., Biasizzo, M., Trotta, F., Cannas, M., 2012. Atmospheric Pressure Plasma Surface Modification of Poly(D,L-lactic acid) Increases Fibroblast, Osteoblast and Keratinocyte Adhesion and Proliferation. *Plasma Process. Polym.* 9, 491–502. <https://doi.org/10.1002/ppap.201100139>
- Richter, E.M., Rocha, D.P., Cardoso, R.M., Keefe, E.M., Foster, C.W., Munoz, R.A.A., Banks, C.E., 2019. Complete Additively Manufactured (3D-Printed) Electrochemical Sensing Platform. *Anal. Chem.* 91, 12844–12851. <https://doi.org/10.1021/acs.analchem.9b02573>
- Rocha, D.P., Ataíde, V.N., de Siervo, A., Gonçalves, J.M., Muñoz, R.A.A., Paixão, T.R.L.C., Angnes, L., 2021a. Reagentless and sub-minute laser-scribing treatment to produce enhanced disposable electrochemical sensors via additive manufacture. *Chem. Eng. J.* 425, 130594. <https://doi.org/10.1016/j.cej.2021.130594>
- Rocha, D.P., Ataíde, V.N., de Siervo, A., Gonçalves, J.M., Muñoz, R.A.A., Paixão, T.R.L.C., Angnes, L., 2021b. Reagentless and sub-minute laser-scribing treatment to produce enhanced disposable electrochemical sensors via additive manufacture. *Chem. Eng. J.* 425, 130594. <https://doi.org/10.1016/j.cej.2021.130594>
- Rocha, D.P., Dornellas, R.M., Cardoso, R.M., Narciso, L.C.D., Silva, M.N.T., Nossol, E., Richter, E.M., Munoz, R.A.A., 2018a. Chemically versus electrochemically reduced graphene oxide: Improved amperometric and voltammetric sensors of phenolic compounds on higher roughness surfaces. *Sensors Actuators, B Chem.* 254, 701–708. <https://doi.org/10.1016/j.snb.2017.07.070>
- Rocha, D.P., Foster, C.W., Munoz, R.A.A., Buller, G.A., Keefe, E.M., Banks, C.E., 2020a. Trace manganese detection via differential pulse cathodic stripping voltammetry using disposable electrodes: Additively manufactured nanographite

- electrochemical sensing platforms. *Analyst* 145, 3424–3430. <https://doi.org/10.1039/d0an00018c>
- Rocha, D.P., Silva, M.N.T., Cardoso, R.M., Castro, S.V.F., Tormin, T.F., Richter, E.M., Nossol, E., Munoz, R.A.A., 2018b. Carbon nanotube/reduced graphene oxide thin-film nanocomposite formed at liquid-liquid interface: Characterization and potential electroanalytical applications. *Sensors Actuators B Chem.* 269, 293–303. <https://doi.org/10.1016/j.snb.2018.04.147>
- Rocha, D.P., Squissato, A.L., da Silva, S.M., Richter, E.M., Munoz, R.A.A., 2020b. Improved electrochemical detection of metals in biological samples using 3D-printed electrode: Chemical/electrochemical treatment exposes carbon-black conductive sites. *Electrochim. Acta* 335, 1–11. <https://doi.org/10.1016/j.electacta.2020.135688>
- Rocha, R.G., Silva, I.C.O.F., Arantes, L.C., Stefano, J.S., Lima, C.D., Melo, L.M.A., Munoz, R.A.A., dos Santos, W.T.P., Richter, E.M., 2021. Simple and rapid electrochemical detection of 1-benzylpiperazine on carbon screen-printed electrode. *Microchem. J.* 167, 106282. <https://doi.org/10.1016/j.microc.2021.106282>
- Rositani, F., Antonucci, P.L., Minutoli, M., Giordano, N., Villari, A., 1987. Infrared analysis of carbon blacks. *Carbon N. Y.* 25, 325–332. [https://doi.org/10.1016/0008-6223\(87\)90002-9](https://doi.org/10.1016/0008-6223(87)90002-9)
- Rymansaib, Z., Irvani, P., Emslie, E., Medvidović-Kosanović, M., Sak-Bosnar, M., Verdejo, R., Marken, F., 2016. All-Polystyrene 3D-Printed Electrochemical Device with Embedded Carbon Nanofiber-Graphite-Polystyrene Composite Conductor. *Electroanalysis* 28, 1517–1523. <https://doi.org/10.1002/elan.201600017>
- Samyn, N., De Boeck, G., Wood, M., Lamers, C.T., De Waard, D., Brookhuis, K.A., Verstraete, A.G., Riedel, W.J., 2002. Plasma, oral fluid and sweat wipe ecstasy concentrations in controlled and real life conditions. *Forensic Sci. Int.* 128, 90–97. [https://doi.org/10.1016/S0379-0738\(02\)00157-3](https://doi.org/10.1016/S0379-0738(02)00157-3)
- Santhiago, M., Maroneze, C.M., Silva, C.C.C., Camargo, M.N.L., Kubota, L.T., 2015. Electrochemical Oxidation of Glassy Carbon Provides Similar Electrochemical Response as Graphene Oxide Prepared by Tour or Hummers Routes. *ChemElectroChem* 2, 761–767. <https://doi.org/10.1002/celec.201402387>

- Sdrobiş, A., Ioanid, G.E., Stevanovic, T., Vasile, C., 2012. Modification of cellulose/chitin mix fibers with N -isopropylacrylamide and poly(N -isopropylacrylamide) under cold plasma conditions. *Polym. Int.* 61, 1767–1777. <https://doi.org/10.1002/pi.4268>
- Sen, N.P., Smith, D.C., Schwinghamer, L., 1969. Formation of N-nitrosamines from secondary amines and nitrite in human and animal gastric juice. *Food Cosmet. Toxicol.* 7, 301–307. [https://doi.org/10.1016/S0015-6264\(69\)80366-4](https://doi.org/10.1016/S0015-6264(69)80366-4)
- Ševčík, A., 1948. Oscillographic polarography with periodical triangular voltage. *Collect. Czechoslov. Chem. Commun.* 13, 349–377. <https://doi.org/10.1135/cccc19480349>
- Shahrubudin, N., Lee, T.C., Ramlan, R., 2019. An Overview on 3D Printing Technology: Technological, Materials, and Applications. *Procedia Manuf.* 35, 1286–1296. <https://doi.org/10.1016/j.promfg.2019.06.089>
- Sharma, S., Singh, N., Tomar, V., Chandra, R., 2018. A review on electrochemical detection of serotonin based on surface modified electrodes. *Biosens. Bioelectron.* 107, 76–93. <https://doi.org/10.1016/j.bios.2018.02.013>
- Silva, A.L., Salvador, G.M. da S., Castro, S.V.F., Carvalho, N.M.F., Munoz, R.A.A., 2021. A 3D Printer Guide for the Development and Application of Electrochemical Cells and Devices. *Front. Chem.* 9. <https://doi.org/10.3389/fchem.2021.684256>
- Silva, L.A.J., Stefano, J.S., Melo, R., Prado, N.S., Henrique, P., Soares, T., Nossol, E., Alejandro, R., Munoz, A., Angnes, L., Richter, E.M., 2018. Evaluation of graphite sheets for production of high-quality disposable sensors. *J. Electroanal. Chem.* 833, #pagerange#. <https://doi.org/10.1016/j.jelechem.2018.12.029>
- Silva, V.A.O.P., Fernandes-Junior, W.S., Rocha, D.P., Stefano, J.S., Munoz, R.A.A., Bonacin, J.A., Janegitz, B.C., 2020. 3D-printed reduced graphene oxide/polylactic acid electrodes: A new prototyped platform for sensing and biosensing applications. *Biosens. Bioelectron.* 170, 112684. <https://doi.org/10.1016/j.bios.2020.112684>
- Simon, W., Booth, B., 2004. *Analytical Method Validation.* pp. 165–185. <https://doi.org/10.1201/9780203026427.ch8>
- Sims, M.J., Rees, N. V., Dickinson, E.J.F., Compton, R.G., 2010. Effects of thin-layer diffusion in the electrochemical detection of nicotine on basal plane pyrolytic

- graphite (BPPG) electrodes modified with layers of multi-walled carbon nanotubes (MWCNT-BPPG). *Sensors Actuators B Chem.* 144, 153–158. <https://doi.org/10.1016/j.snb.2009.10.055>
- Skoog, D.A., West, D.M., Holler, F.J., Crouch, S.R., 2006. *Fundamentos de Química Analítica*, 8th ed. Thomson Learning INC., São Paulo.
- Snell, K.D., Keenan, A.G., 1979. Surface modified electrodes. *Chem. Soc. Rev.* 8, 259. <https://doi.org/10.1039/cs9790800259>
- Stefano, J.S., Orzari, L.O., Silva-Neto, H.A., de Ataíde, V.N., Mendes, L.F., Coltro, W.K.T., Longo Cesar Paixão, T.R., Janegitz, B.C., 2022. Different approaches for fabrication of low-cost electrochemical sensors. *Curr. Opin. Electrochem.* 32, 100893. <https://doi.org/10.1016/j.coelec.2021.100893>
- Stoian, I.-A., Iacob, B.-C., Dudaş, C.-L., Barbu-Tudoran, L., Bogdan, D., Marian, I.O., Bodoki, E., Oprean, R., 2020. Biomimetic electrochemical sensor for the highly selective detection of azithromycin in biological samples. *Biosens. Bioelectron.* 155, 112098. <https://doi.org/10.1016/j.bios.2020.112098>
- Stradiotto, N.R., Yamanaka, H., Zanoni, M.V.B., Sotomayor, M.D.P.T., 2022. *Métodos Eletroanalíticos: Conceitos, Experimentos e Aplicações*, 1st ed. Cultura Acadêmica Editora, São Paulo.
- Streeter, I., Wildgoose, G.G., Shao, L., Compton, R.G., 2008. Cyclic voltammetry on electrode surfaces covered with porous layers: An analysis of electron transfer kinetics at single-walled carbon nanotube modified electrodes. *Sensors Actuators B Chem.* 133, 462–466. <https://doi.org/10.1016/j.snb.2008.03.015>
- Suffredini, H.B., Pedrosa, V.A., Codognoto, L., Machado, S.A.S., Rocha-Filho, R.C., Avaca, L.A., 2004. Enhanced electrochemical response of boron-doped diamond electrodes brought on by a cathodic surface pre-treatment. *Electrochim. Acta* 49, 4021–4026. <https://doi.org/10.1016/j.electacta.2004.01.082>
- Surya, S.G., Khatoon, S., Ait Lahcen, A., Nguyen, A.T.H., Dzantiev, B.B., Tarannum, N., Salama, K.N., 2020. A chitosan gold nanoparticles molecularly imprinted polymer based ciprofloxacin sensor. *RSC Adv.* 10, 12823–12832. <https://doi.org/10.1039/D0RA01838D>

- Švancara, I., Vytrás, K., Barek, J., Zima, J., 2001. Carbon Paste Electrodes in Modern Electroanalysis. *Crit. Rev. Anal. Chem.* 31, 311–345. <https://doi.org/10.1080/20014091076785>
- Švancara, I., Vytrás, K., Kalcher, K., Walcarius, A., Wang, J., 2009. Carbon Paste Electrodes in Facts, Numbers, and Notes: A Review on the Occasion of the 50-Years Jubilee of Carbon Paste in Electrochemistry and Electroanalysis. *Electroanalysis* 21, 7–28. <https://doi.org/10.1002/elan.200804340>
- Tadini, M.C., Balbino, M.A., Eleoterio, I.C., De Oliveira, L.S., Dias, L.G., Jean-François Demets, G., De Oliveira, M.F., 2014. Developing electrodes chemically modified with cucurbit[6]uril to detect 3,4-methylenedioxymethamphetamine (MDMA) by voltammetry. *Electrochim. Acta* 121, 188–193. <https://doi.org/10.1016/j.electacta.2013.12.107>
- Taleat, Z., Khoshroo, A., Mazloum-Ardakani, M., 2014. Screen-printed electrodes for biosensing: a review (2008–2013). *Microchim. Acta* 181, 865–891. <https://doi.org/10.1007/s00604-014-1181-1>
- Tannenbaum, S.R., Sinskey, A.J., Weisman, M., Bishop, W., 1974. Nitrite in Human Saliva. Its Possible Relationship to Nitrosamine Formation. *JNCI J. Natl. Cancer Inst.* 53, 75–784. <https://doi.org/10.1093/jnci/53.1.79>
- Teófilo, K.R., Arantes, L.C., Marinho, P.A., Macedo, A.A., Pimentel, D.M., Rocha, D.P., de Oliveira, A.C., Richter, E.M., Munoz, R.A.A., dos Santos, W.T.P., 2020. Electrochemical detection of 3,4-methylenedioxymethamphetamine (ecstasy) using a boron-doped diamond electrode with differential pulse voltammetry: Simple and fast screening method for application in forensic analysis. *Microchem. J.* 157, 105088. <https://doi.org/10.1016/j.microc.2020.105088>
- Thiruvottriyur Shanmugam, S., Van Echelpoel, R., Boeye, G., Eliaerts, J., Samanipour, M., Ching, H.Y.V., Florea, A., Van Doorslaer, S., Van Durme, F., Samyn, N., Parrilla, M., De Wael, K., 2021. Towards Developing a Screening Strategy for Ecstasy: Revealing the Electrochemical Profile. *ChemElectroChem* 8, 4826–4834. <https://doi.org/10.1002/celec.202101198>
- Tian, X., Jin, J., Yuan, S., Chua, C.K., Tor, S.B., Zhou, K., 2017. Emerging 3D-Printed Electrochemical Energy Storage Devices: A Critical Review. *Adv. Energy Mater.* 7,

1–17. <https://doi.org/10.1002/aenm.201700127>

Tkachenko, L.I., Ozkan, S.Z., Efimov, O.N., Karpacheva, G.P., Nikolaeva, G.V., Kostev, A.I., Dremova, N.N., Kabachkov, E.N., 2022. Electrochemical behavior of polydiphenylamine-2-carboxylic acid and its hybrid nanocomposites with single-walled carbon nanotubes on anodized graphite foil in lithium aprotic electrolyte. *React. Funct. Polym.* 173, 105225. <https://doi.org/10.1016/j.reactfunctpolym.2022.105225>

Togni, L.R., Lanaro, R., Resende, R.R., Costa, J.L., 2015. The Variability of Ecstasy Tablets Composition in Brazil. *J. Forensic Sci.* 60, 147–151. <https://doi.org/10.1111/1556-4029.12584>

Tomita, M., Nakashima, M.N., Wada, M., Nakashima, K., 2007. Sensitive determination of MDMA and its metabolite MDA in rat blood and brain microdialysates by HPLC with fluorescence detection. *Biomed. Chromatogr.* 21, 1016–1022. <https://doi.org/10.1002/bmc.839>

Torkashvand, M., Gholivand, M.B., Malekzadeh, G., 2016. Construction of a new electrochemical sensor based on molecular imprinting recognition sites on multiwall carbon nanotube surface for analysis of ceftazidime in real samples. *Sensors Actuators B Chem.* 231, 759–767. <https://doi.org/10.1016/j.snb.2016.03.061>

United Nations, 2006. Recommended Methods for the Identification and Analysis of Amphetamine, Methamphetamine and their Ring-substituted Analogues in Seized Materials [WWW Document]. URL <https://www.unodc.org/unodc/en/scientists/recommended-methods-for-the-identification-and-analysis-of-amphetamine--methamphetamine-and-their-ring-substituted-analogues-in-seized-materials.html> (accessed 2.8.22).

UNODOC, 2021. UNODC Early Warning Advisory on New Psychoactive Substances [WWW Document]. URL <https://www.unodc.org/LSS/Page/NPS>

Valiev, M., Bylaska, E.J., Govind, N., Kowalski, K., Straatsma, T.P., Van Dam, H.J.J., Wang, D., Nieplocha, J., Apra, E., Windus, T.L., de Jong, W.A., 2010. NWChem: A comprehensive and scalable open-source solution for large scale molecular simulations. *Comput. Phys. Commun.* 181, 1477–1489. <https://doi.org/10.1016/j.cpc.2010.04.018>

- Vaněčková, E., Bouša, M., Nováková Lachmanová, Š., Rathouský, J., Gál, M., Sebechlebská, T., Kolivoška, V., 2020a. 3D printed polylactic acid/carbon black electrodes with nearly ideal electrochemical behaviour. *J. Electroanal. Chem.* 857, 113745. <https://doi.org/10.1016/j.jelechem.2019.113745>
- Vaněčková, E., Bouša, M., Vivaldi, F., Gál, M., Rathouský, J., Kolivoška, V., Sebechlebská, T., 2020b. UV/VIS spectroelectrochemistry with 3D printed electrodes. *J. Electroanal. Chem.* 857, 113760. <https://doi.org/10.1016/j.jelechem.2019.113760>
- Vanoni, C.R., Winiarski, J.P., Nagurniak, G.R., Magosso, H.A., Jost, C.L., 2019. A Novel Electrochemical Sensor Based on Silsesquioxane/Nickel (II) Phthalocyanine for the Determination of Sulfanilamide in Clinical and Drug Samples. *Electroanalysis* 31, 867–875. <https://doi.org/10.1002/elan.201800832>
- Vieira, L. de S., 2022. A review on the use of glassy carbon in advanced technological applications. *Carbon* N. Y. 186, 282–302. <https://doi.org/10.1016/j.carbon.2021.10.022>
- Vinícius de Faria, L., Lisboa, T.P., Alves, G.F., Costa Matos, M.A., Abarza Muñoz, R.A., Matos, R.C., 2021. Adsorptive stripping voltammetric determination of chloramphenicol residues in milk samples using reduced graphene oxide sensor. *Anal. Methods* 13, 5711–5718. <https://doi.org/10.1039/D1AY01756J>
- Vinothkumar, V., Abinaya, M., Chen, S.-M., 2021. Ultrasonic assisted preparation of CoMoO₄ nanoparticles modified electrochemical sensor for chloramphenicol determination. *J. Solid State Chem.* 302, 122392. <https://doi.org/10.1016/j.jssc.2021.122392>
- Wagner, C.D., Davis, L.E., Zeller, M. V., Taylor, J.A., Raymond, R.H., Gale, L.H., 1981. Empirical atomic sensitivity factors for quantitative analysis by electron spectroscopy for chemical analysis. *Surf. Interface Anal.* 3, 211–225. <https://doi.org/10.1002/sia.740030506>
- Wang, H., Moore, J.J., 2012. Low temperature growth mechanisms of vertically aligned carbon nanofibers and nanotubes by radio frequency-plasma enhanced chemical vapor deposition. *Carbon* N. Y. 50, 1235–1242. <https://doi.org/10.1016/j.carbon.2011.10.041>

- Wang, J., 1994. Decentralized electrochemical monitoring of trace metals: from disposable strips to remote electrodes. Plenary lecture. *Analyst* 119, 763. <https://doi.org/10.1039/an9941900763>
- Wang, J., Tian, B., 1992. Screen-printed stripping voltammetric/potentiometric electrodes for decentralized testing of trace lead. *Anal. Chem.* 64, 1706–1709. <https://doi.org/10.1021/ac00039a015>
- Wirth, D.M., Sheaff, M.J., Waldman, J. V., Symcox, M.P., Whitehead, H.D., Sharp, J.D., Doerfler, J.R., Lamar, A.A., LeBlanc, G., 2019. Electrolysis Activation of Fused-Filament-Fabrication 3D-Printed Electrodes for Electrochemical and Spectroelectrochemical Analysis. *Anal. Chem.* 91, 5553–5557. <https://doi.org/10.1021/acs.analchem.9b01331>
- Wolff, I.A., Wasserman, A.E., 1972. Nitrates, Nitrites, and Nitrosamines. *Science* (80-). 177, 15–19. <https://doi.org/10.1126/science.177.4043.15>
- YABE, M., MORI, K., UEDA, K., TAKEDA, M., 2019. Development of PolyParGen Software to Facilitate the Determination of Molecular Dynamics Simulation Parameters for Polymers. *J. Comput. Chem. Japan -International Ed.* 5, n/a. <https://doi.org/10.2477/jccjie.2018-0034>
- Yajima, S., Satow, T., Hirai, T., 1965. Mechanism of the pyrolytic graphite formation. *J. Nucl. Mater.* 17, 116–126. [https://doi.org/10.1016/0022-3115\(65\)90028-0](https://doi.org/10.1016/0022-3115(65)90028-0)
- Ye, Y.-J., Huang, Z.-H., Song, Y., Geng, J.-W., Xu, X.-X., Liu, X.-X., 2017. Electrochemical Growth of Polyaniline Nanowire Arrays on Graphene Sheets in Partially Exfoliated Graphite Foil for High-Performance Supercapacitive Materials. *Electrochim. Acta* 240, 72–79. <https://doi.org/10.1016/j.electacta.2017.04.025>
- Yuan, Y., Zhang, F., Wang, H., Gao, L., Wang, Z., 2018. A Sensor Based on Au Nanoparticles/Carbon Nitride/Graphene Composites for the Detection of Chloramphenicol and Ciprofloxacin. *ECS J. Solid State Sci. Technol.* 7, M201–M208. <https://doi.org/10.1149/2.0111812jss>
- Yue, D.W., Ra, C.H., Liu, X.C., Lee, D.Y., Yoo, W.J., 2015. Edge contacts of graphene formed by using a controlled plasma treatment. *Nanoscale* 7, 825–831. <https://doi.org/10.1039/C4NR05725B>

- Yue, L., Li, W., Sun, F., Zhao, L., Xing, L., 2010. Highly hydroxylated carbon fibres as electrode materials of all-vanadium redox flow battery. *Carbon N. Y.* 48, 3079–3090. <https://doi.org/10.1016/j.carbon.2010.04.044>
- Zhang, L., Yin, M., Wei, X., Sun, Y., Chen, Y., Qi, S., Tian, X., Qiu, J., Xu, D., 2022. Synthesis of rGO@PDA@AuNPs for an effective electrochemical chloramphenicol sensor. *Diam. Relat. Mater.* 128, 109311. <https://doi.org/10.1016/j.diamond.2022.109311>
- Zhang, R., Fu, K., Zou, F., Bai, H., Zhang, G., Liang, F., Liu, Q., 2021. Highly sensitive electrochemical sensor based on Pt nanoparticles/carbon nanohorns for simultaneous determination of morphine and MDMA in biological samples. *Electrochim. Acta* 370, 137803. <https://doi.org/10.1016/j.electacta.2021.137803>
- Zhang, Y., Lv, Y., Chen, Y., Li, Y., Wang, Y., Zhao, H., 2022. Trimetallic Ag@Pt-Rh core-shell nanocubes modified anode for voltammetric sensing of dopamine and sulfanilamide. *Chem. Eng. Sci.* 249, 117326. <https://doi.org/10.1016/j.ces.2021.117326>
- Zittel, H.E., Miller, F.J., 1965. A Glassy-Carbon Electrode for Voltammetry. *Anal. Chem.* 37, 200–203. <https://doi.org/10.1021/ac60221a006>

Curricular summary

Complete articles published:

- Oxidative stability and corrosivity of biodiesel produced from residual cooking oil exposed to copper and carbon steel under simulated storage conditions: Dual effect of antioxidants. *Renewable Energy*, Volume 164, February 2021, Pages 1485-1495. <https://doi.org/10.1016/j.renene.2020.10.097>
- Reactive oxygen plasma treatment of 3D-printed carbon electrodes towards high-performance electrochemical sensors. *Sensors and Actuators B: Chemical*, Volume 347, 15 November 2021, 130651. <https://doi.org/10.1016/j.snb.2021.130651>
- In situ electrochemical determination of resorcinol using a fully 3D printed apparatus. *Microchemical Journal*, Volume 191, August 2023, 108810. <https://doi.org/10.1016/j.microc.2023.108810>
- Oxygen plasma-treated graphite sheet electrodes: A sensitive and disposable sensor for methamphetamines. *Electrochimica Acta*, Volume 467, 1 November 2023, 143089. <https://doi.org/10.1016/j.electacta.2023.143089>
- CO₂-plasma surface treatment of graphite sheet electrodes for detection of chloramphenicol, ciprofloxacin and sulphanilamide. *Microchimica Acta*, (2023) 190:379. <https://doi.org/10.1007/s00604-023-05953-2>

Works presented in congress

- 20° ENQA (Encontro Nacional de Química Analítica) e 8° CIAQA (Congresso Ibero-Americano de Química Analítica). Oxygen plasma treated graphite sheet electrodes for MDMA sensing. Oral presentation. September 2022, Bento Gonçalves, RS, Brazil.

Patents deposited

- CASTRO, S. V. F.; MUNOZ, R. A. A.; MONTES, R. H. O.; RICHTER, E. M.; PEREIRA, J. F. S.; CARDOSO, R. M.; ROCHA, R. G. SENSOR ELETROQUÍMICO PARA ANÁLISE DE RESÍDUOS DE DISPARO DE ARMA DE FOGO. 2021, Brazil. Patent: Innovation Privilege. Register number: BR10202101437, title: "SENSOR ELETROQUÍMICO PARA ANÁLISE DE RESÍDUOS DE DISPARO DE ARMA DE FOGO.", register institution: INPI - Instituto Nacional da Propriedade Industrial. Deposit: 21/07/2021.

APENDIX

Publication licenses for the published articles



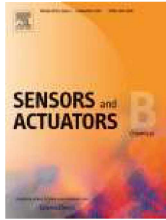
RightsLink

Home

Help ▾

Email Support

Jian da Silva Pereira ▾



Reactive oxygen plasma treatment of 3D-printed carbon electrodes towards high-performance electrochemical sensors

Author:

Jian F.S. Pereira, Raquel G. Rocha, Silvia V.F. Castro, Afonso F. João, Pedro H.S. Borges, Diego P. Rocha, Abner de Siervo, Eduardo M. Richter, Edson Nossol, Rogério V. Gelamo, Rodrigo A.A. Muñoz

Publication: Sensors and Actuators B: Chemical**Publisher:** Elsevier**Date:** 15 November 2021

© 2021 Elsevier B.V. All rights reserved.

Journal Author Rights

Please note that, as the author of this Elsevier article, you retain the right to include it in a thesis or dissertation, provided it is not published commercially. Permission is not required, but please ensure that you reference the journal as the original source. For more information on this and on your other retained rights, please visit: <https://www.elsevier.com/about/our-business/policies/copyright#Author-rights>

BACK

CLOSE WINDOW

© 2023 Copyright - All Rights Reserved | [Copyright Clearance Center, Inc.](#) | [Privacy statement](#) | [Data Security and Privacy](#)
| [For California Residents](#) | [Terms and Conditions](#) Comments? We would like to hear from you. E-mail us at customer-care@copyright.com



RightsLink

Home

Help ▾

Email Support

Jian da Silva Pereira ▾



Oxygen plasma-treated graphite sheet electrodes: A sensitive and disposable sensor for methamphetamines

Author:

Jian F.S. Pereira, Larissa M.A. Melo, Luciano C. Arantes, Pedro H.S. Borges, Lucas V. Faria, Kelly F. da Cunha, Karla A.O. Souza, William O. Soté, Jose Luiz Costa, Edson Nossol, Rogério V. Gelamo, Eduardo M. Richter, Moacyr Comar, Wallans T.P. dos Santos et al.

Publication: Electrochimica Acta**Publisher:** Elsevier**Date:** 1 November 2023

© 2023 Elsevier Ltd. All rights reserved.

Journal Author Rights

Please note that, as the author of this Elsevier article, you retain the right to include it in a thesis or dissertation, provided it is not published commercially. Permission is not required, but please ensure that you reference the journal as the original source. For more information on this and on your other retained rights, please visit: <https://www.elsevier.com/about/our-business/policies/copyright#Author-rights>

BACK

CLOSE WINDOW

© 2023 Copyright - All Rights Reserved | [Copyright Clearance Center, Inc.](#) | [Privacy statement](#) | [Data Security and Privacy](#)
| [For California Residents](#) | [Terms and Conditions](#) Comments? We would like to hear from you. E-mail us at customer care@copyright.com

**SPRINGER NATURE LICENSE
TERMS AND CONDITIONS**

Sep 08, 2023

This Agreement between Dr. Jian da Silva Pereira ("You") and Springer Nature ("Springer Nature") consists of your license details and the terms and conditions provided by Springer Nature and Copyright Clearance Center.

License Number	5624200552949
License date	Sep 08, 2023
Licensed Content Publisher	Springer Nature
Licensed Content Publication	Microchimica Acta
Licensed Content Title	CO ₂ -plasma surface treatment of graphite sheet electrodes for detection of chloramphenicol, ciprofloxacin and sulphanilamide
Licensed Content Author	Jian F. S. Pereira et al
Licensed Content Date	Sep 8, 2023
Type of Use	Thesis/Dissertation
Requestor type	academic/university or research institute
Format	electronic
Portion	full article/chapter
Will you be translating?	no
Circulation/distribution	1 - 29

Author of this Springer Nature content yes

Title UNDERSTANDING THE INFLUENCE OF COLD PLASMA TREATMENT IN CARBON BASED ELECTRODES

Institution name Universidade Federal de Uberlândia

Expected presentation date Sep 2023

Order reference number 4741485

Requestor Location Dr. Jian da Silva Pereira
Rua Antônio Marciano de Ávila
1051
Uberlândia, Minas Gerais 38408-244
Brazil
Attn: Universidade Federal de Uberlândia

Total 0.00 USD

Terms and Conditions

Springer Nature Customer Service Centre GmbH Terms and Conditions

The following terms and conditions ("Terms and Conditions") together with the terms specified in your [RightsLink] constitute the License ("License") between you as Licensee and Springer Nature Customer Service Centre GmbH as Licensor. By clicking 'accept' and completing the transaction for your use of the material ("Licensed Material"), you confirm your acceptance of and obligation to be bound by these Terms and Conditions.

1. Grant and Scope of License

1. 1. The Licensor grants you a personal, non-exclusive, non-transferable, non-sublicensable, revocable, world-wide License to reproduce, distribute, communicate to the public, make available, broadcast, electronically transmit or create derivative works using the Licensed Material for the purpose(s) specified in your RightsLink Licence Details only. Licenses are granted for the specific use requested in the order and for no other use, subject to these Terms and Conditions. You acknowledge and agree that the rights granted to you under this License do not include the right to modify, edit, translate, include in collective works, or create derivative works of the Licensed Material in whole or in part unless expressly stated in your RightsLink Licence Details. You may use the Licensed Material only as permitted under this Agreement and will not reproduce, distribute, display, perform, or otherwise use or exploit any Licensed Material in any way, in whole or in part, except as expressly

permitted by this License.

1. 2. You may only use the Licensed Content in the manner and to the extent permitted by these Terms and Conditions, by your RightsLink Licence Details and by any applicable laws.

1. 3. A separate license may be required for any additional use of the Licensed Material, e.g. where a license has been purchased for print use only, separate permission must be obtained for electronic re-use. Similarly, a License is only valid in the language selected and does not apply for editions in other languages unless additional translation rights have been granted separately in the License.

1. 4. Any content within the Licensed Material that is owned by third parties is expressly excluded from the License.

1. 5. Rights for additional reuses such as custom editions, computer/mobile applications, film or TV reuses and/or any other derivative rights requests require additional permission and may be subject to an additional fee. Please apply to journalpermissions@springernature.com or bookpermissions@springernature.com for these rights.

2. Reservation of Rights

Licensor reserves all rights not expressly granted to you under this License. You acknowledge and agree that nothing in this License limits or restricts Licensor's rights in or use of the Licensed Material in any way. Neither this License, nor any act, omission, or statement by Licensor or you, conveys any ownership right to you in any Licensed Material, or to any element or portion thereof. As between Licensor and you, Licensor owns and retains all right, title, and interest in and to the Licensed Material subject to the license granted in Section 1.1. Your permission to use the Licensed Material is expressly conditioned on you not impairing Licensor's or the applicable copyright owner's rights in the Licensed Material in any way.

3. Restrictions on use

3. 1. Minor editing privileges are allowed for adaptations for stylistic purposes or formatting purposes provided such alterations do not alter the original meaning or intention of the Licensed Material and the new figure(s) are still accurate and representative of the Licensed Material. Any other changes including but not limited to, cropping, adapting, and/or omitting material that affect the meaning, intention or moral rights of the author(s) are strictly prohibited.

3. 2. You must not use any Licensed Material as part of any design or trademark.

3. 3. Licensed Material may be used in Open Access Publications (OAP), but any such reuse must include a clear acknowledgment of this permission visible at the same time as the figures/tables/illustration or abstract and which must indicate that the Licensed Material is not part of the governing OA license but has been reproduced with permission. This may be indicated according to any standard referencing system but must include at a minimum 'Book/Journal title, Author, Journal Name (if applicable), Volume (if applicable), Publisher, Year, reproduced with permission from SNCSC'.

4. STM Permission Guidelines

4. 1. An alternative scope of license may apply to signatories of the STM Permissions Guidelines ("STM PG") as amended from time to time and made available at <https://www.stm-assoc.org/intellectual-property/permissions/permissions-guidelines/>.

4. 2. For content reuse requests that qualify for permission under the STM PG, and which may be updated from time to time, the STM PG supersedes the terms and conditions contained in this License.

4. 3. If a License has been granted under the STM PG, but the STM PG no longer apply at the time of publication, further permission must be sought from the Rightsholder. Contact journalpermissions@springernature.com or bookpermissions@springernature.com for these rights.

5. Duration of License

5. 1. Unless otherwise indicated on your License, a License is valid from the date of purchase ("License Date") until the end of the relevant period in the below table:

Reuse in a medical communications project	Reuse up to distribution or time period indicated in License
Reuse in a dissertation/thesis	Lifetime of thesis
Reuse in a journal/magazine	Lifetime of journal/magazine
Reuse in a book/textbook	Lifetime of edition
Reuse on a website	1 year unless otherwise specified in the License
Reuse in a presentation/slide kit/poster	Lifetime of presentation/slide kit/poster. Note: publication whether electronic or in print of presentation/slide kit/poster may require further permission.
Reuse in conference proceedings	Lifetime of conference proceedings
Reuse in an annual report	Lifetime of annual report
Reuse in training/CME materials	Reuse up to distribution or time period indicated in License
Reuse in newsmedia	Lifetime of newsmedia
Reuse in coursepack/classroom materials	Reuse up to distribution and/or time period indicated in license

6. Acknowledgement

6. 1. The Licensor's permission must be acknowledged next to the Licensed Material in print. In electronic form, this acknowledgement must be visible at the same time as the figures/tables/illustrations or abstract and must be hyperlinked to the journal/book's homepage.

6. 2. Acknowledgement may be provided according to any standard referencing system and at a minimum should include "Author, Article/Book Title, Journal name/Book imprint, volume, page number, year, Springer Nature".

7. Reuse in a dissertation or thesis

7. 1. Where 'reuse in a dissertation/thesis' has been selected, the following terms apply: Print rights of the Version of Record are provided for; electronic rights for use only on institutional repository as defined by the Sherpa guideline (www.sherpa.ac.uk/romeo/) and only up to what is required by the awarding institution.

7. 2. For theses published under an ISBN or ISSN, separate permission is required. Please contact journalpermissions@springernature.com or bookpermissions@springernature.com for these rights.

7. 3. Authors must properly cite the published manuscript in their thesis according to current citation standards and include the following acknowledgement: '*Reproduced with permission from Springer Nature*'.

8. License Fee

You must pay the fee set forth in the License Agreement (the "License Fees"). All amounts payable by you under this License are exclusive of any sales, use, withholding, value added or similar taxes, government fees or levies or other assessments. Collection and/or remittance of such taxes to the relevant tax authority shall be the responsibility of the party who has the legal obligation to do so.

9. Warranty

9. 1. The Licensor warrants that it has, to the best of its knowledge, the rights to license reuse of the Licensed Material. **You are solely responsible for ensuring that the material you wish to license is original to the Licensor and does not carry the copyright of another entity or third party (as credited in the published version).** If the credit line on any part of the Licensed Material indicates that it was reprinted or adapted with permission from another source, then you should seek additional permission from that source to reuse the material.

9. 2. EXCEPT FOR THE EXPRESS WARRANTY STATED HEREIN AND TO THE EXTENT PERMITTED BY APPLICABLE LAW, LICENSOR PROVIDES THE LICENSED MATERIAL "AS IS" AND MAKES NO OTHER REPRESENTATION OR WARRANTY. LICENSOR EXPRESSLY DISCLAIMS ANY LIABILITY FOR ANY CLAIM ARISING FROM OR OUT OF THE CONTENT, INCLUDING BUT NOT LIMITED TO ANY ERRORS, INACCURACIES, OMISSIONS, OR DEFECTS CONTAINED THEREIN, AND ANY IMPLIED OR EXPRESS WARRANTY AS TO MERCHANTABILITY OR FITNESS FOR A PARTICULAR PURPOSE. IN NO EVENT SHALL LICENSOR BE LIABLE TO YOU OR ANY OTHER PARTY OR ANY OTHER PERSON OR FOR ANY SPECIAL, CONSEQUENTIAL, INCIDENTAL, INDIRECT, PUNITIVE, OR EXEMPLARY DAMAGES, HOWEVER CAUSED, ARISING OUT OF OR IN CONNECTION WITH THE DOWNLOADING, VIEWING OR USE OF THE LICENSED MATERIAL REGARDLESS OF THE FORM OF ACTION, WHETHER FOR BREACH OF CONTRACT, BREACH OF WARRANTY, TORT, NEGLIGENCE, INFRINGEMENT OR OTHERWISE (INCLUDING, WITHOUT LIMITATION, DAMAGES BASED ON LOSS OF PROFITS, DATA, FILES, USE, BUSINESS OPPORTUNITY OR CLAIMS OF THIRD PARTIES), AND WHETHER OR NOT THE PARTY HAS BEEN ADVISED OF THE POSSIBILITY OF SUCH DAMAGES. THIS LIMITATION APPLIES NOTWITHSTANDING ANY FAILURE OF ESSENTIAL PURPOSE OF ANY LIMITED REMEDY PROVIDED HEREIN.

10. Termination and Cancellation

10. 1. The License and all rights granted hereunder will continue until the end of the applicable period shown in Clause 5.1 above. Thereafter, this license will be terminated and all rights granted hereunder will cease.

10. 2. Licensor reserves the right to terminate the License in the event that payment is not received in full or if you breach the terms of this License.

11. General

11. 1. The License and the rights and obligations of the parties hereto shall be construed, interpreted and determined in accordance with the laws of the Federal Republic of Germany without reference to the stipulations of the CISG (United Nations Convention on Contracts for the International Sale of Goods) or to Germany's choice-of-law principle.

11. 2. The parties acknowledge and agree that any controversies and disputes arising out of this License shall be decided exclusively by the courts of or having jurisdiction for Heidelberg, Germany, as far as legally permissible.

11. 3. This License is solely for Licensor's and Licensee's benefit. It is not for the benefit of any other person or entity.

Questions? For questions on Copyright Clearance Center accounts or website issues please contact springernaturesupport@copyright.com or +1-855-239-3415 (toll free in the US) or +1-978-646-2777. For questions on Springer Nature licensing please visit <https://www.springernature.com/gp/partners/rights-permissions-third-party-distribution>

Other Conditions:

Version 1.4 - Dec 2022

Questions? customercare@copyright.com.
